FLUORESCENT CHEMOSENSORS FROM HYDRAZIDE DERIVATIVES OF JULOLIDINE

Mr. Warakorn Akarasareenon

จุฬาลงกรณ์มหาวิทยาลัย
CHULALONGKORN UNIVERSITY

A Dissertation Submitted in Partial Fulfillment of the Requirements
for the Degree of Doctor of Philosophy in Chemistry
Department of Chemistry
FACULTY OF SCIENCE
Chulalongkorn University
Academic Year 2022
Copyright of Chulalongkorn University

ฟลูออเรสเซนต์คีโมเซนเซอร์จากอนุพันธ์ไฮดราไซด์ของจูโลลิดีน

นายวรากร อัครเสรีนนท์

วิทยานิพนธ์นี้เป็นส่วนหนึ่งของการศึกษาตามหลักสูตรปริญญาวิทยาศาสตรดุษฎีบัณฑิต
สาขาวิชาเคมี ภาควิชาเคมี
คณะวิทยาศาสตร์ จุฬาลงกรณ์มหาวิทยาลัย
ปีการศึกษา 2565

Thesis Title	FLUORESCENT CHEMOSENSORS FROM HYDRAZIDE DERIVATIVES OF JULOLIDINE
By	Mr. Warakorn Akarasareenon
Field of Study	Chemistry
Thesis Advisor	Professor Dr. PAITOON RASHATASAKHON

Accepted by the FACULTY OF SCIENCE, Chulalongkorn University in Partial Fulfillment of the Requirement for the Doctor of Philosophy

.... Dean of the FACULTY OF SCIENCE

(Professor Dr. POLKIT SANGVANICH)

DISSERTATION COMMITTEE

.... Chairman

(Professor Dr. TIRAYUT VILAIVAN)

.... Thesis Advisor

(Professor Dr. PAITOON RASHATASAKHON)

.... Examiner

(Professor Dr. MONGKOL SUKWATTANASINITT)

.... Examiner

(Professor Dr. THAWATCHAI TUNTULANI)

.... External Examiner

(Associate Professor Dr. Nakorn Niamnont)

วรากร อัครเสรีนนท์ : ฟลูออเรสเซนต์คีโมเซนเซอร์จากอนุพันธ์ไฮดราไซด์ของจูโลลิดีน. (FLUORESCENT CHEMOSENSORS FROM HYDRAZIDE DERIVATIVES OF JULOLIDINE) อ.ที่ปรึกษาหลัก : ศ. ดร.ไพฑูรย์ รัชตะสาคร

อนุพันธ์ของเอ็น-เอซิลไฮดราโซนจูโลลิดีนสามชนิดถูกสังเคราะห์ขึ้นและถูกนำมาศึกษาใน ลักษณะเปรียบเทียบกันถึงความเลือกจำเพาะในการเป็นเซนเซอร์ฟลูออเรสเซนต์ของไอออน โลหะ พบว่าอนุพันธ์ที่มาจากพิโคลิโนไฮดราไซด์สามารถเป็นเซนเซอร์เรืองแสง "แบบเปิด" สำหรับ ไอออน Cu^{2+} ในตัวทำละลาย DMSO ที่มีน้ำ การตรวจสอบทางกลไกแสดงให้เห็นว่า Cu^{2+} ส่งเสริม การเกิดปฏิกิริยาไฮโดรไลซิสของหน่วยพิโคลิโนไฮดราไซด์เพื่อสร้างสารประกอบจูโลลิดีน-9-คาร์ บอกซาลดีไฮด์ที่ให้การเรืองแสงสูง โดยมีสัญญาณการคายแสงสูงสุดที่ 420 นาโนเมตร โพรบนี้ แสดงความเลือกจำเพาะอย่างเด่นชัดต่อไอออน Cu^{2+} เหนือไอออนโลหะอื่น ๆ ด้วยขีดจำกัดการ ตรวจจับที่ 0.1 ppm และภายใต้สภาวะที่เหมาะสม พบว่าประสบความสำเร็จในการวัดปริมาณ ไอออน Cu^{2+} ในตัวอย่างน้ำจริง

นอกจากนี้ อนุพันธ์เอซาคราวน์อีเธอร์ของจูโลลิดีนยังได้ถูกออกแบบสำหรับการนำมาใช้ เป็นเซนเซอร์ไอออนของโลหะด้วย การสังเคราะห์เอซาคราวน์อีเธอร์จะสามารถดำเนินการได้อย่าง ราบรื่น แต่มีอุปสรรคในขั้นตอนการเชื่อมอนุพันธ์เอซาคราวน์อีเธอร์เข้ากับจูโลลิดีน-9-คาร์บอกซาล ดีไฮด์ โดยพบว่าไม่เกิดผลิตภัณฑ์ตามที่ต้องการ ถึงแม้ว่าวิธีการสังเคราะห์และการออกแบบ โครงสร้างจะถูกปรับเปลี่ยนไปหลายครั้งแล้วก็ตาม ดังนั้น งานวิจัยในส่วนนี้จึงถูกนำเสนอเพื่อแสดง ให้เห็นถึงแนวทางการวางแผนการสังเคราะห์ในงานอื่น ๆ ต่อไป

สาขาวิชา	เคมี	ลายมือชื่อนิสิต ....
ปีการศึกษา	2565	ลายมือชื่อ อ.ที่ปรึกษาหลัก ....

6072826623 : MAJOR CHEMISTRY

KEYWORD: Acylhydrazone, Copper ion, Fluorescence, Hydrolysis, Julolidine, Sensor

Warakorn Akarasareenon : FLUORESCENT CHEMOSENSORS FROM HYDRAZIDE DERIVATIVES OF JULOLIDINE. Advisor: Prof. Dr. PAITOON RASHATASAKHON

Three derivatives of *N*-acylhydrazone julolidine are synthesized and comparatively investigated for their selectivities as metal ion fluorescent sensors. The compound derived from picolinohydrazide is found to be a "turn-on" fluorescent sensor for Cu^{2+} in aqueous DMSO media. The mechanistic investigation suggests that Cu^{2+} promotes the hydrolysis reaction of picolinohydrazide moiety to generate a highly fluorescent compound julolidine-9-carboxaldehyde which has a maximum emission signal at 420 nm. This probe shows an extraordinary selectivity for Cu^{2+} over other metal ions with a detection limit of 0.1 ppm. Under optimal conditions, the determinations of Cu^{2+} in real water samples are successfully executed.

In addition, aza crown ether derivatives of julolidine have also been designed for use as metal ion sensors. The synthesis of aza crown ether could be carried out smoothly, but there were many obstacles in the coupling steps of the aza crown ether with the julolidine-9-carboxaldehyde. The desired product could not be obtained even though several different synthesis methods and structural designs were changed. Therefore, this part of the research is presented to illustrate the synthesis planning guidelines in other further works.

Field of Study: Chemistry   Student's Signature ....

Academic Year: 2022   Advisor's Signature ....

ACKNOWLEDGEMENTS

TABLE OF CONTENTS

Page

LIST OF TABLES

LIST OF FIGURES

LIST OF SCHEMES

LIST OF ABBREVIATIONS

HEPES	4-(2-hydroxyethyl)-1-piperazineethanesulfonic acid
ACN	acetonitrile
K_a	association constant
ATR	attenuated total reflectance
Bis-Tris	bis-(2-hydroxyethyl)amino-tris(hydroxymethyl)methane
Calcd.	calculated
cm	centimeter
δ	chemical shifts
decomp.	decompose
DFT	density functional theory
$CDCl_3$	deuterated chloroform
DCM	dichloromethane
DMC	dimethyl carbonate
DMSO	dimethyl sulfoxide
DMF	dimethylformamide
EN	electronegativity
EDTA	ethylenediaminetetraacetic acid
ESIPT	excited-state intramolecular proton transfer
FTIR	fourier-transform infrared
g	gram
HRMS	high resolution mass spectrometry
HOMO	highest occupied molecular orbital
ICP-OES	inductively coupled plasma-optical emission spectrometer
ICT	intramolecular Charge Transfer
LOD	limit of detection

LE	locally excited state
LUMO	lowest unoccupied molecular orbital
λ_{em}	maximum emission wavelength
MHz	megahertz
MΩ	megaohm
MCEF	metal chelation-enhanced fluorescence
µL	microliter
µM	micromolar
mg	milligram
mL	milliliter
mM	millimolar
mmol	millimole
min	minute
M	molar
ε	molar absorptivity
χ	mole fraction
m	multiplet
nm	nanometer
nM	nanomolar
NMR	nuclear magnetic resonance
PBS	phosphate-buffered saline
PET	photo-induced electron transfer
ϕ_{fl}	quantum yields
RPT	reverse proton transfer
s	singlet
SMD	solvation model based on density

THF	tetrahydrofuran
TLC	thin layer chromatography
TD-DFT	time-dependent density-functional theory
t	triplet
tt	triplet of triplets
UV-vis	ultraviolet-visible
v/v	volume/volume

CHAPTER I

INTRODUCTION

1.1 Fluorescence

Fluorescence, a type of luminescence, is the emission of light from a particular chemical compound after being exposed to light that has higher energy. The interaction of light with molecules can be contributed to the transitions of electrons between certain defined states or their molecular orbitals. The transitions between different energy states of a molecule can be illustrated using the Jablonski diagram (**Scheme 1.1**). [1]

Excited Singlet States

S_2 Vibrational Energy States

Internal Conversion

S_1

S_0

Ground State

Excitation (Absorption) 10^{-15} Seconds

Fluorescence (10^{-9} - 10^{-7} Sec)

Internal Conversion and Vibrational Relaxation (10^{-14} - 10^{-11} Sec)

Quenching

Non-Radiative Relaxation
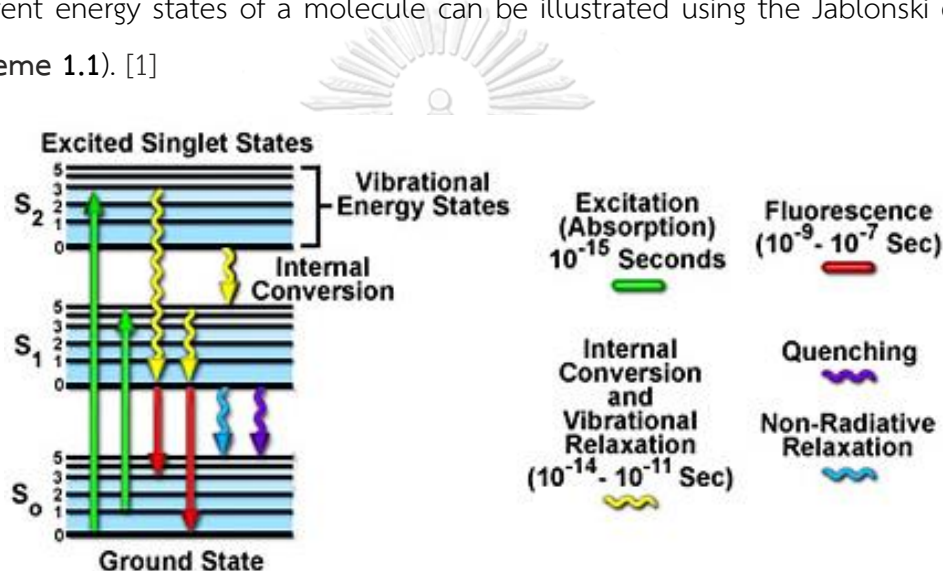
Scheme 1.1 Jablonski diagram. [1]

This diagram shows the various possible quantized energy values available to a molecule on a vertical scale of increasing energy. The types of energy states associated with a molecule include electronic states (denoted as S_0, S_1, S_2) and vibrational state (denoted as $\mathcal{V}$) which is located in each electronic state. Under UV radiation, the excitation of a molecule in an electronic ground state (S_0) is promoted with various transitions such as $S_0 \rightarrow S_1$, $S_0 \rightarrow S_2$, $S_0 \rightarrow S_3$, etc. Although absorption occurs into any higher excited state, the rate of the vibrational and electronic–energy relaxation in excited states is very rapid compared to the rate of fluorescent emission. Therefore, the fluorescence proceeds from the lowest vibrational level of the excited state S_1 ($\mathcal{V}$=0) to one of the S_0 state vibrational levels. [2-4]

This information suggests that the energy of the emission is consistently less than that of absorption, in other words, fluorescence typically occurs at longer wavelengths. The difference between the maxima of the lowest energy absorption and highest energy fluorescence bands is termed Stokes shift. For example, the absorption and emission spectra for quinine are shown in **Figure 1.1**.
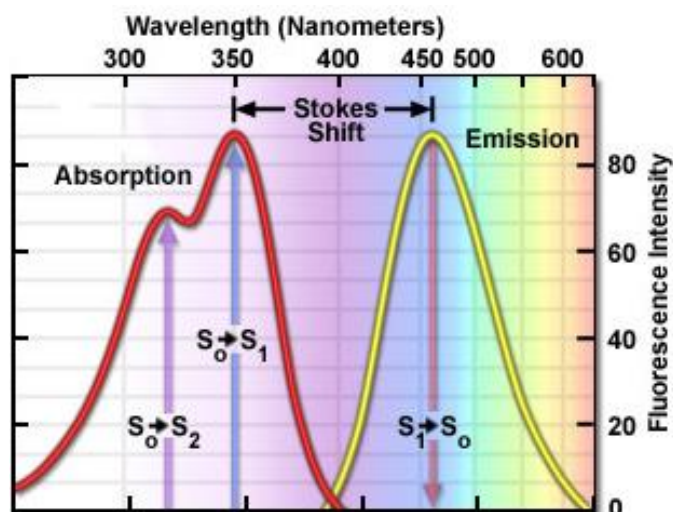
Figure 1.1 The absorption and emission spectra for quinine. [1]

จุฬาลงกรณ์มหาวิทยาลัย

CHULALONGKORN UNIVERSITY

1.2 Fluorescent sensors for metal ions

The toxicity of heavy metal cations in the environment has provoked researchers to design sensors that are selective to a specific cation. Based on the different sensing methods for detecting metal cations, fluorescent probes have several advantages over other methods due to their high sensitivity, selectivity, and real-time monitoring. The general components of the molecular fluorescent sensors for metal ions consist of the signaling unit and metal receptor unit which are covalently bonded together as shown in **Figure 1.2**.
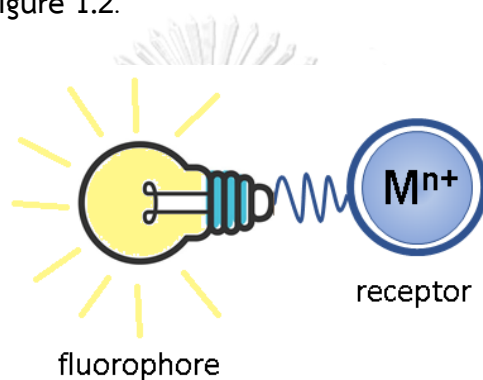
Figure 1.2 Molecular fluorescent sensors diagram. [5]

The signaling unit is referred to as an organic fluorophore which can exhibit fluorescent properties, whereas the receptor unit is a part that has the potential to bind or interact with the metal ion. Once the target metal ion is recognized by the receptor unit, the fluorophore will convert a chemical circumstance at the receptor unit to the desired fluorescent signal response. The change in fluorescence properties of the fluorophore part such as intensity or excitation/emission wavelength could provide both qualitative and quantitative information about the target metal ion. [6-12] Therefore, the selection of fluorophores and well-designed receptor parts are important factors that directly affect a fluorescent sensor's efficiency.

1.3 Sensing mechanism

Based on the sensing mechanism of the sensor toward metal ions, a variety of fluorescent sensors can be divided into two main categories. They are as follows:

(1) M^{n+}-coordination-based sensors.

(2) M^{n+}-promoted reaction-based sensors.

1.3.1 M^{n+}-coordination-based sensors

The characteristic of this type is the metal ion forms a dative covalent bond with the receptor unit of the sensor molecule. This sensor type usually responds quickly to the analyte and is generally reversible. [13] There are several mechanisms for altering the fluorescent signal of M^{n+}-coordination-based sensors. However, the common sensing mechanisms used to design fluorescent sensors include Photo-induced Electron Transfer (PET), Intramolecular Charge Transfer (ICT), Excited-State Intramolecular Proton Transfer (ESIPT), and the restriction of C=N bond isomerization.

1) Photo-induced Electron Transfer (PET)

The fluorescent chemosensors based on PET often have fluorophore-spacer-receptor (**Scheme 1.2**) as their fundamental structure. A spacer between the fluorophore and the receptor will separate them electronically from the π-electron systems. Fluorophores are often electron acceptors, whereas receptors are typically electron donors (such as amino-containing groups). Upon excitation, the electron occupying the highest occupied molecular orbital (HOMO) of the fluorophore can be transferred to the lowest unoccupied molecular orbital (LUMO). If the electron in the receptor's HOMO is located near an orbit of the fluorophore and the energy of the receptor's orbital lies between the HOMO and LUMO of the fluorophore, the electron of the receptor's HOMO can transfer to the HOMO of the excited fluorophore through space, which blocks the emission transition of the excited electron occupying the fluorophore's LUMO to fluorophore's HOMO. The chemosensor frequently undergoes quenching or a decrease in fluorescence intensity as a result of the PET. [14]

However, the energy gap between the two HOMO orbitals can change from positive to negative when the receptor coordinates with the target metal ion. In another word, the receptor's HOMO level can be dropped by metal coordination. As a result, the fluorescence of the probe is recovered. This metal chelation-enhanced fluorescence is also defined as the metal chelation-enhanced fluorescence (MCEF) effect.
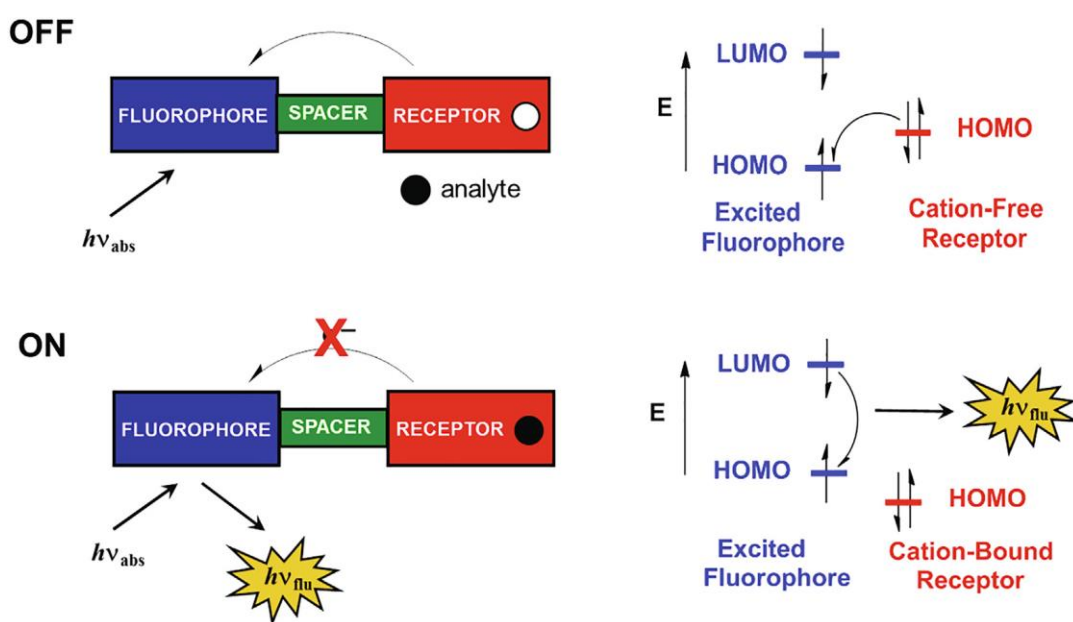
Scheme 1.2 Schematic representation of PET sensor in the sensing process. [14]

2) Intramolecular Charge Transfer (ICT)

The organic compound containing an electron-donor group (such as an amino group, or alkoxy group) and an electron-acceptor group (such as a carbonyl group, or nitrile group) in the same conjugation system is one characteristic of the ICT-based sensor. The ICT process is the transfer of charge from an electron-rich donor moiety to an electron-poor acceptor part located in the same molecule upon the photoexcitation. This process causes the change in electronic charge distribution over the atoms of the molecule in the excited state. As depicted in **Scheme 1.3**, the normal excited state without charge transfer is often referred to as a locally excited (LE) state, while the new state formed due to the rearrangement of its electronic structure in the excited state is called the ICT state.

It appears that the ICT state has lower energy than the LE state resulting in the ICT molecule displaying a large Stokes shift and visible light excitability. Although several ICT-based organic molecules show dual emission in their electronic spectra, some ICT molecules are reported to show emission from either the LE or the ICT species only. [15]
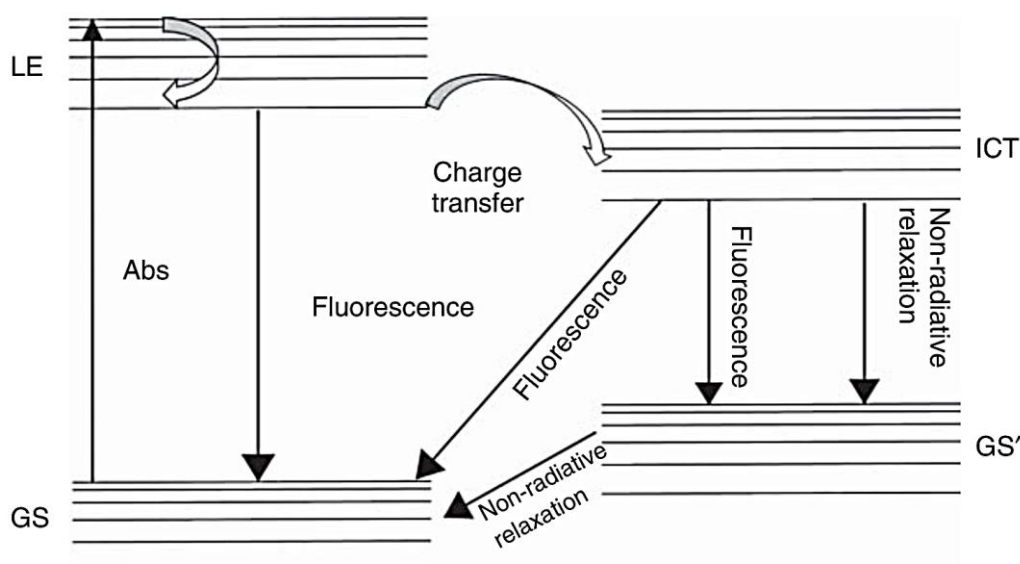
Scheme 1.3 Jablonski diagram showing a molecule undergoing the ICT process. [15]

The strategy for designing the ICT sensor is the ability of a receptor unit that could induce the redistribution of electron density of molecules upon the complexation with the target metal ion. **Scheme 1.4** displays the spectral changes that will be seen upon coordination of the ICT sensor with a metal ion in the cases when the receptor occupies the electron donor or electron acceptor parts of the molecule. In the case of a metal ion interacting with the electron donor group, it reduces the ICT process due to the inhibition of electron-donating ability, which leads to a hypsochromic shift (blue shift) in the absorption and emission spectra. In contrast, when a metal ion binds with the electron acceptor group, a bathochromic shift (red shift) is observed in the absorption and emission spectra due to the encouragement of the ICT process. [16, 17]

The strengths of these sensing characteristics are the self-calibration of two excitation/emission bands which could remove the influence of photobleaching, deviated microenvironments, local probe concentration, and experimental parameters.
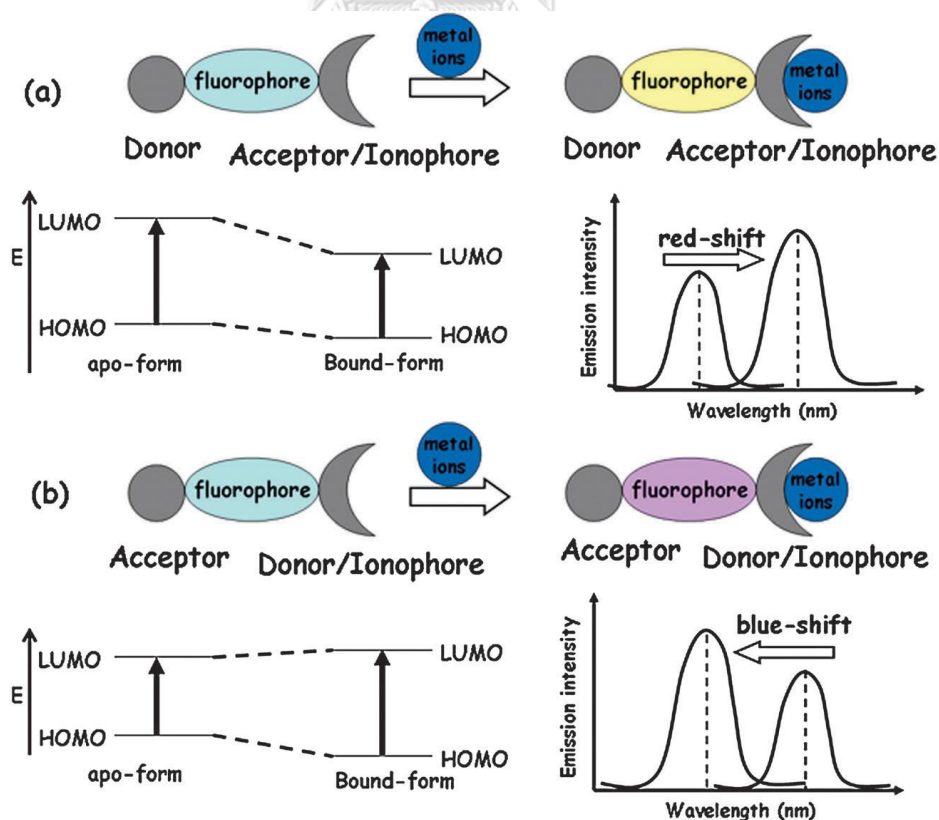
Scheme 1.4 Intramolecular charge transfer mechanism (ICT). [8]

3) Excited-State Intramolecular Proton Transfer (ESIPT)

ESIPT process is commonly found in compounds containing a hydrogen bond donor (hydroxyl or amino group) that can form an intramolecular hydrogen bond with a neighboring heteroatom in the same conjugation system. The examples of ESIPT fluorophores are illustrated in **Figure 1.3**.

A photochemical process of ESIPT molecule containing hydroxyl group as hydrogen bond donor is shown in **Scheme 1.5**. In the ground state, ESIPT molecules usually exist in an enolic form (E). Upon photoexcitation, the hydroxyl proton of the molecule in the enol excited state (E*) migrates to the hydrogen bond acceptor to form the keto excited state (K*). After the release of energy to the ground state of the keto form (K), reverse proton transfer (RPT) will occur to form the initial enolic form. Due to the existence of two excited states, the ESIPT compound's fluorescence spectrum commonly shows two emission maxima from both tautomers. [18-22]

The keto form's emission band displays a large Stokes shift which helps reduce background noise, making it a strong point of ESIPT-based fluorescent sensor. The design of ESIPT-based fluorescent sensors is generally based on inhibiting the formation of an intramolecular hydrogen bond upon the addition of metal ions because the complexation with some metal ions may induce the deprotonation of the hydrogen bond donor. As a result, there are no exchangeable protons available, only enol emission is observed. [23]

benzo[*h*]quinolin-10-ol **(*E*)-2-((phenylimino)methyl)phenol** ***N*-(9,10-dioxo-9,10-dihydro anthracen-1-yl)acetamide**
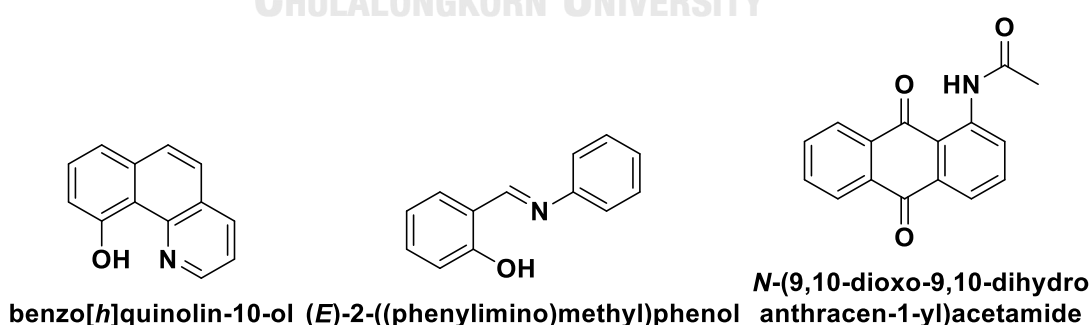
Figure 1.3 Representative examples of commonly used ESIPT fluorophores. [23]
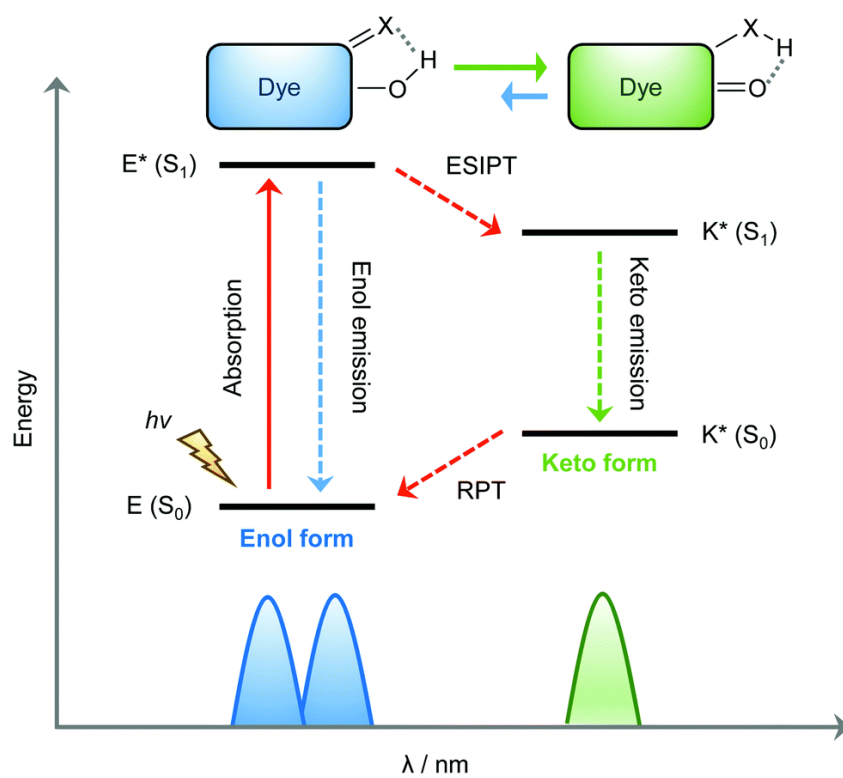
Scheme 1.5 Diagrammatic description of the ESIPT process. [23]

4) C=N Bond Isomerization

Isomerization around the C=N bond can be achieved photochemically with UV and visible light. The evidence suggests that compounds bearing an unbridged C=N bond (see examples in **Figure 1.4**) generally lose fluorescent properties because C=N isomerization is one of the decay processes in the excited state. [24]

However, the C=N isomerization could be inhibited by metal ions through complexation in a fluorescent-sensing molecule as shown in **Figure 1.5**. As a result, the fluorescence of the metal complex enhances dramatically due to the suppression of C=N isomerization in the excited states. [25-27]
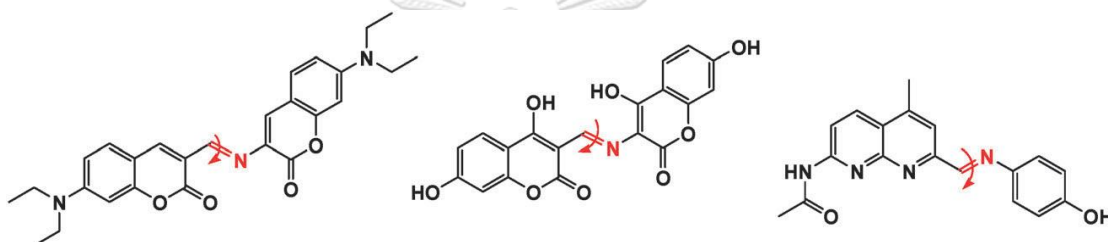
Figure 1.4 Molecular structures of imine derivatives. [26]
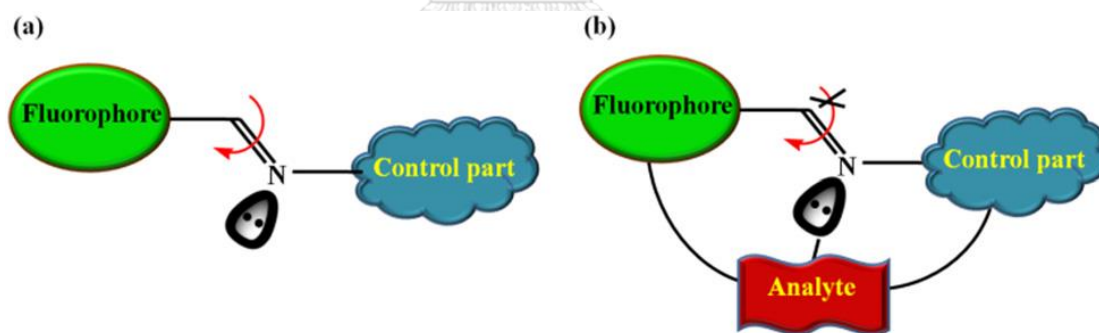
Figure 1.5 (a) Analyte-free and (b) analyte-bond mechanism in the fluorescent sensor for the restriction of C=N isomerization. [27]

1.3.2 M^{n+}-promoted reaction-based sensors

Due to the nature of most transition metals such as the reversibility of metal-ligand bonds for host-guest chemistry, the Lewis acid nature, and the redox flexibility, they sometimes serve as catalysts or reagents in organic transformation. The design of reaction-based sensors involves the chemical reaction of the target metal cation at the reactive functional groups of molecular sensors resulting in both the breaking and forming of the covalent bonds. These types of probes are known as chemodosimeters. The reaction can be controlled by designing the appropriate conditions such as solvent, pH, and temperature. This kind of probe exhibits a slow response and irreversible behavior.

The example reactions involving metal catalysts are hydrolysis reactions as shown in **Scheme 1.6**. Assume that the free probe has no fluorescence signal. When the target metal ion interacts with the reactive site of the molecular sensor (usually located in a receptor unit). If it can accelerate the hydrolysis reaction, the metal complex part is cleaved from the free fluorophore part. In this case, either the fluorophore part or the metal complex which is generated from the reaction exhibits a fluorescence signal to report information.

In other words, the irreversible reactions induced by specific metal ion result in products that have optically different properties from the starting molecular sensor. Therefore, the objective of chemodosimeter research is to find a specific reactivity for the binding site and the target metal ion. [28-30]
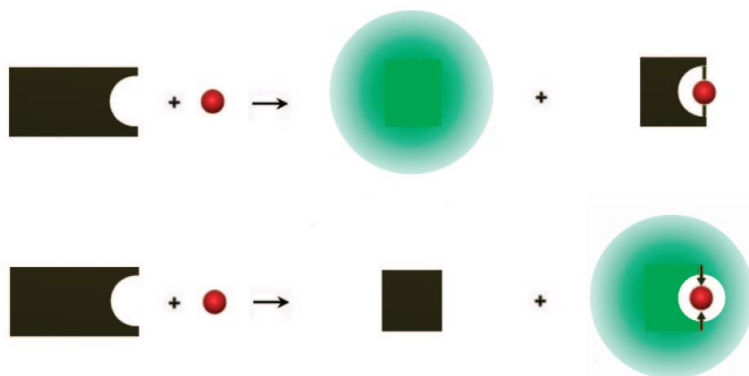
Scheme 1.6 Schematic operating protocols of chemodosimeter. [30]

1.4 Julolidine

One of the fluorescent dye families that have received the greatest research attention is the julolidine derivatives, which are also among the most widely utilized fluorescent substances. Julolidine was first synthesized in 1892 by Pinkus when he reacted 1,2,3,4-tetrahydroquinoline with 3-chloro-1-bromopropane and the name "julolidine" was given by Reissert in 1893. [31] The julolidine ring has a similar chemical structure with *N,N*-alkylated aniline in the former two N-alkyl chains undergo bis-annulation back to the aromatic ring locking the nitrogen lone pair into conjugation with the aromatic cycle. [32]

As depicted in **Figure 1.6**, julolidine derivatives have been shown to have potential in many applications such as for metal sensing [33, 34], dye-sensitized solar cells [35], antidepressants and tranquilizers [36], photoconductive materials [37], chemiluminescent substances [38], and nonlinear optical materials [39].
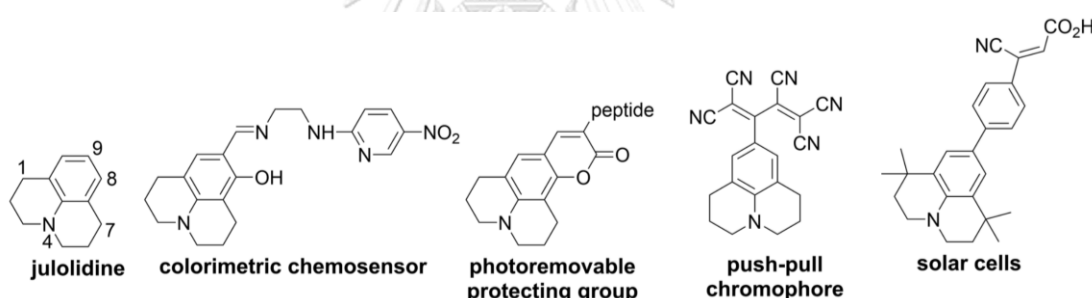
Figure 1.6 Some examples and applications of julolidine derivatives. [40]

1.5 Hydrazone

Hydrazones are compounds containing the structure $R_2C=NNR_2$, (**Figure 1.7**) formally derived from aldehydes or ketones by replacing =O by $=NNH_2$ (or substituted analogs). [41, 42] Hydrazone group is usually found in the receptor part of fluorescent sensors because it has two nitrogen atoms that are Lewis bases in nature and can act as donor atoms in the chelation of metal ions. Meanwhile, the carbon atom of the hydrazone group has both electrophilic and nucleophilic characteristics due to the bonding with the high EN nitrogen atom and the conjugation with a lone pair of electrons on the terminal nitrogen atom. [43, 44] If the substituent at the terminal nitrogen site of hydrazones is an acyl group, the compound is acyl hydrazones. Acyl hydrazones can be synthesized by condensation reaction between aldehydes or ketones and hydrazide. This additional carbonyl group allows electron delocalization within the hydrazone component and increases the denticity of these compounds. [45]
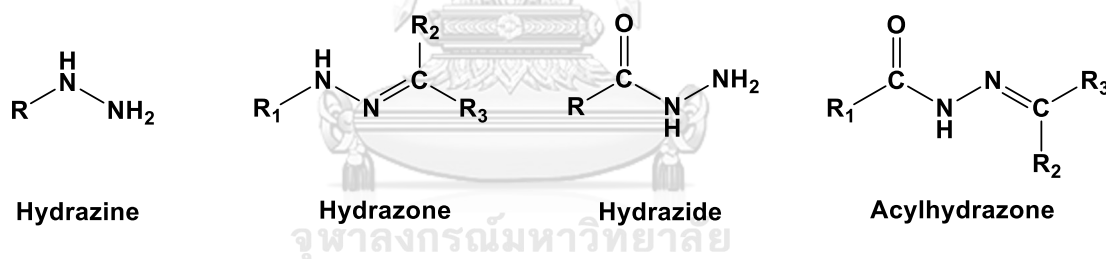
Figure 1.7 The general structure of hydrazine, hydrazone, hydrazide, and acyl hydrazone.

Tautomerism is an interesting feature of acyl hydrazone. They exist as an equilibrium mixture of keto and enol forms in a solution through intramolecular proton transfer. (**Scheme 1.7**) This process causes a change in the π-electronic configuration and extends conjugation. Due to tautomerism, acyl hydrazones could be considered as bidentate ligands in two forms including neutral ligands in keto form and mono-anionic ligands in enolic form. [46, 47]
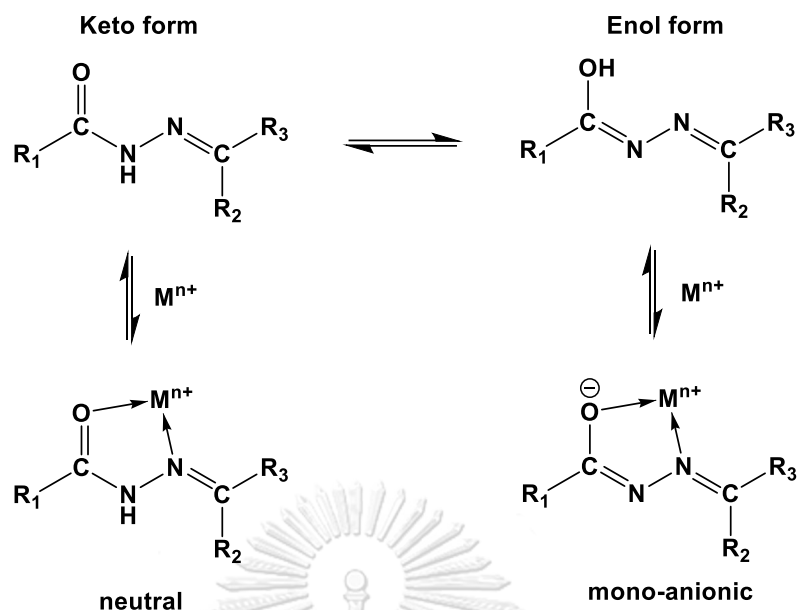
Scheme 1.7 Tautomerism in Acylhydrazone.

However, the addition of an alkyl or aryl group containing one or more heteroatoms might further improve the denticity of these compounds. If the heteroatom exists in a suitable position and can coordinate with a metal ion, the hydrazone behaves as a tridentate ligand. When the coordination number increases, the stability of the complexes increases.

Due to their functional diversity, direct synthesis, stability toward hydrolysis compared to imines, and modularity, acylhydrazones allow their application in the detection of cations and other species.

1.6 Fluorescent sensors from *N*-acylhydrazone derivatives

Since many *N*-acylhydrazone-based fluorescence sensors have been reported in the database, only 62 compounds with the structures related to this work were selected for discussion in this review. The derivatives with the same *N*-acyl unit are grouped for comparing their sensing properties to understand the nature of these compounds. (**Table 1.1**)

Table 1.1 The *N*-acylhydrazone derivatives in the review.

R group	Name of its hydrazide derivative	Compound Number	The study in this work
The acyl of non-heteroatom substituent			
H₃C	Acetohydrazide	1-3	✓
(phenyl)	Benzohydrazide	4-14	-
The acyl of phenyl ring containing heteroatom substituent at 2-position			
(phenyl-OH)	2-Hydroxybenzohydrazide	15-26	✓
(phenyl-NH₂)	2-Aminobenzohydrazide	27-31	-
The acyl of heterocyclic at 2-position			
(pyridine)	2-Pyridinecarbohydrazide	32-48	✓
(furan)	2-Pyrrolecarbohydrazide	49-53	-
(thiophene)	2-Furancarbohydrazide	54-58	-
(pyrrole)	2-Thiophenecarbohydrazide	59-62	-

1.6.1 Derivatives derived from acetohydrazide.

Acetohydrazide is the smallest carbohydrazide that is selected for designing molecular sensors with simple structures.

In 2014, Wang et. al. designed compound **1** [48] which is derived from the condensation reaction of acetohydrazide and 2-hydroxybenzaldehyde. In water, sensor **1** gave very weak green fluorescence (ϕ_{fl} = 0.01), partially attributing to the PET effect from the amide nitrogen. Apparently, the emission of **1** exhibited a large Stocks shift due to the ESIPT process between the hydroxyl group with the adjacent imine bond. They found this sensor could produce a bright blue fluorescent ''turn-on" response upon exposure to Al^{3+} with its ϕ_{fl} reaching as high as 0.73. The evidence from large spectral bathochromic shift and ^{1}H-NMR indicated the deprotonation of the hydroxyl group, because of Al^{3+}-binding to phenol. The strong binding of compound **1** with Al^{3+} suppressed the PET and ESIPT process as shown in **Scheme 1.8**. The complex was assumed to have a ligand-to-metal ratio of 2:1 based on Job plot analysis and isosbestic point. However, a slight turn-on effect was observed from Zn^{2+}, whereas Ni^{2+}, Co^{2+}, Cu^{2+}, Fe^{2+}, and Fe^{3+} were found to be quenchers of this fluorescence sensor.

Scheme 1.8 Possible sensing mechanism of **1** with Al^{3+}. [48]

In 2019, Wang et. al. reported a "turn on" fluorescent chemosensor **2** [49] that has a similar structure to compound **1** with the additional hydroxyl group on the aromatic ring (**Figure 1.8**). The results suggested that this additional hydroxyl group affected the emission wavelength by shifting to a longer wavelength when compared with **1**. Interestingly, Job's plot analysis validates the stoichiometry between the probe and Al^{3+} to be 1:1 and the detection limit of compound **2** was calculated to be 0.66 µM which is below than detection limit of compound **1** (0.5 nM).
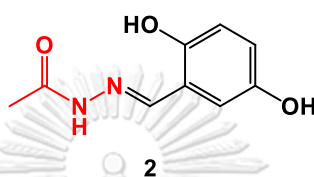
Figure 1.8 Structure of sensors **2**.

Wu et. al. investigated quinoline containing Schiff bases **3** [50] for the recognition of Zn^{2+} in living cells. Compound **3** displayed a fluorescence ''turn on'' response in the presence of Zn^{2+} with a detection limit of 89.3 nM. Initially, the free Schiff base sensor **3** exhibits weak fluorescence primarily due to C=N isomerization. Binding with Zn^{2+} inhibits the isomerization of the imine bond, thereby increasing the fluorescence intensity through the MCEF mechanism. The characterization experiments confirmed the enolization and deprotonation of the carbonyl group and the participation of the quinoline nitrogen atom in the coordination complex (**Scheme 1.9**). The study of coexisting metal cations indicated that Co^{2+} and Cu^{2+} interfere in the detection of Zn^{2+} due to the high coordination affinity and inherent magnetic properties. Moreover, the strong Lewis acidity of Cr^{3+} may induce the hydrolytic cleavage of the imine bond.
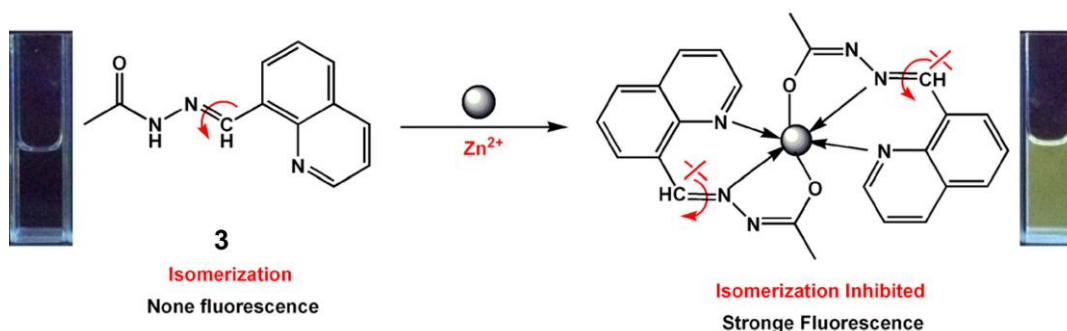
Scheme 1.9 Possible sensing mechanism of **3** with Zn^{2+}. [50]

However, compound **1**-**3** has some limitations such as a few competitive metal ions and a short-conjugated system, so the researchers have designed novel fluorescence sensors by extending the conjugated system or adding more donor atoms to increase the sensing ability. **Table 1.2** shows the comparison of some properties of sensors **1**-**3**.

Table 1.2 Some parameters of fluorescent probe **1**-**3**.

No.	Analyte	Solvent	$\lambda_{ex} / \lambda_{em}$ (nm)	Interference	Mode
1 [48]	Al^{3+}	water	352 / 441	Ni^{2+}, Co^{2+}, Cu^{2+}, Fe^{2+}, Fe^{3+}	Turn on
2 [49]	Al^{3+}	water	350 / 500	Ga^{3+}, Cu^{2+}, Fe^{3+}	Turn on
3 [50]	Zn^{2+}	EtOH/HEPES (pH 7.40, 3/7, v/v)	360 / 525	Co^{2+}, Cr^{3+}, Cu^{2+}	Turn on

จุฬาลงกรณ์มหาวิทยาลัย

CHULALONGKORN UNIVERSITY

1.6.2 Derivatives derived from benzohydrazide.

Schiff bases **4** [51, 52] and **5** [53] have a similar structure with a benzohydrazide moiety but **5** had more steric hindrance than **4** because of two tert-butyl groups on the salicylaldimine moiety (**Figure 1.9**). Both compounds were good indicators for Zn^{2+} in aqueous ethanol. In the absence of Zn^{2+}, the fluorescence emission of **4** and **5** were very weak. Upon the addition of Zn^{2+} to the sensor solutions, there was a significant enhancement in the fluorescence emission band. The selectivity mechanism of **4** and **5** for Al^{3+} is based on a combinational effect of proton transfer (ESPT), C=N isomerization, and MCEF. Job's plot analysis revealed the coordination mode of probe **4** with Zn^{2+} is 2:1 and probe **5** with Zn^{2+} is 1:1 stoichiometry, it is apparently due to the steric effect of compound **5**.
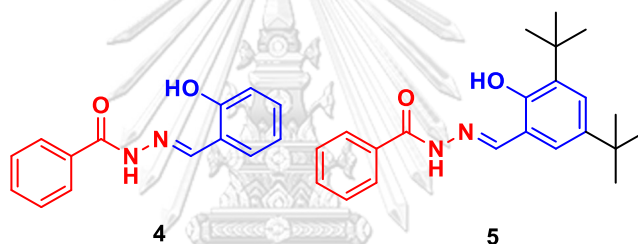
Figure 1.9 Sensors **4** and **5** derived from benzohydrazide.

Huang et. al. reported the on-off coumarin-based fluorescent chemosensor (**6**). [54] This chemosensor had a quantum yield of 0.289 in H_2O/DMSO (9:1, v/v). Only Cu^{2+} caused a significant fluorescence decrease (ϕ_{fl} = 0.024). This process involved the complexation of Cu^{2+} with the tautomeric enol form which can be confirmed by the crystal structure (**Scheme 1.11**). This compound showed a detection limit of 0.1 µM for Cu^{2+}, an association constant estimated to be 6.4×10^5 M^{-1}, and a response time of 2 min upon the addition of 1 equivalent of Cu^{2+}.
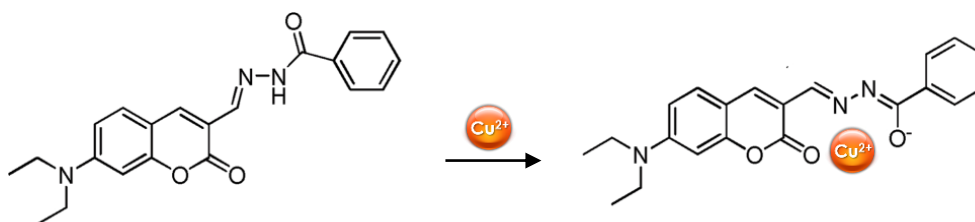
Scheme 1.10 Possible sensing mechanism of **6** with Cu^{2+}. [54]

In 2012, Hou et. al. reported the development of a fluorescein-based chemosensor (**7**). [55] The chemosensor **7** displayed on–off–on type fluorescence change with alternately added Cu^{2+} and H_2S to the media along with reversible forming–separating of the complex. In the absence of metal ions, a strong emission peak was observed at 523 nm, after adding 1 equivalent of Cu^{2+}, it displayed 28-fold fluorescence quenching. The complex **7**-Cu^{2+} (**Scheme 1.11**) was confirmed by ESI-MS, elemental analysis, and UV-vis spectrum, and supported by DFT calculation.
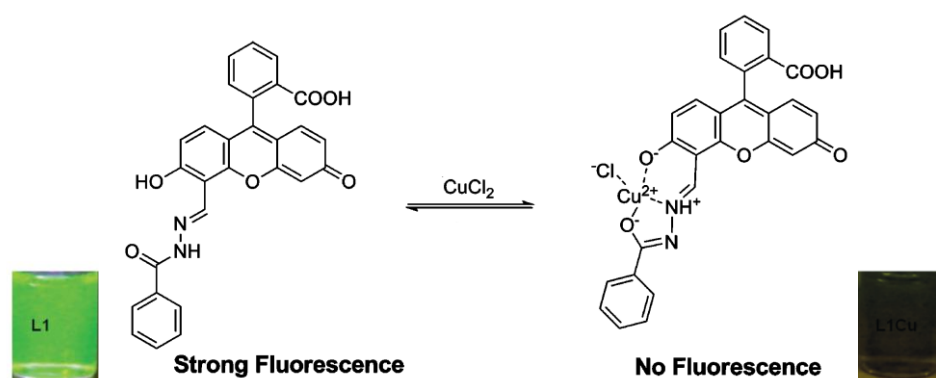
Scheme 1.11 Possible sensing mechanism of **7** with Cu^{2+}. [55]

In 2013, Zhao et. al. designed and synthesized a 1,8-naphthalimide-based chemosensor **8** [56] as a new turn-on fluorescent probe for the detection of Zn^{2+} with high selectivity over other metal ions (**Figure 1.10**). Apparently, the sensing mechanism is attributed to the replacement of the protons of the O–H groups by Zn^{2+} at the binding site which was confirmed by ^{1}H NMR spectroscopic analysis. It appeared that this event blocked the PET process. The fluorescence intensity of **8** is linearly proportional to Zn^{2+} concentrations of 0–4 µM, and the detection limit is as low as 1.03 µM. Sensor **8** was successfully applied to the fluorescence imaging of zinc ions in different cells and the cytokinesis-block micronucleus assay.
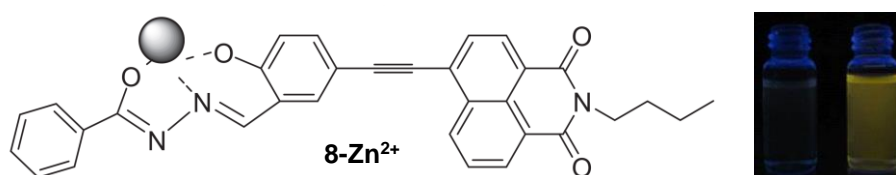
Figure 1.10 Sensors **8** derived from benzohydrazide. [56]

Liao et. al. investigated a fluorescent turn-on chemosensor **9** based on methyl pyrazinyl ketone. [57] The free probe does not show any fluorescence in common solvents, including DMF, THF, DMSO, EtOH, MeOH, acetone, and acetonitrile. The PET appears to have been facilitated by the lone pair of electrons from the nitrogen atom in the Schiff base which suppressed the fluorescence emission of **9**. However, the addition of Al^{3+} to the solution of **9** led to the great enhancement of yellow-green fluorescence due to the formation of a 1:1 complex between **9** and Al^{3+} (**Scheme 1.12**). It is noticeable that the addition of Ga^{3+} and In^{3+}, which are in the same group as Al^{3+}, could produce feeble fluorescence emission. The association constant K_a of the complex was calculated to be $1.24 \times 10^7 \, M^{-1}$.
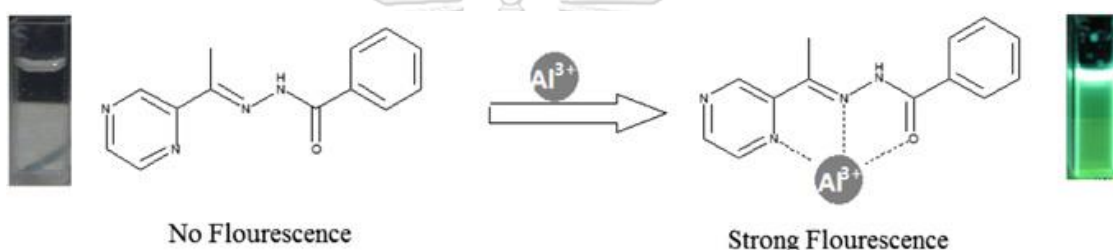
Scheme 1.12 Possible sensing mechanism of **9** with Al^{3+}. [57]

In 2014, Lee et. al. developed a fluorescence sensor **10** [58] by integrating the 8-hydroxyjulolidine and the acylhydrazone functionality. Chemosensor **10** exhibited little emission with a low fluorescence quantum yield (ϕ_{fl} = 0.035). This chemosensor exhibited selectivity and sensitivity towards Al^{3+} by fluorescent intensity enhancement (ϕ_{fl} = 0.502). This fluorescence enhancement could be explained by an ESIPT mechanism, C=N isomerization, and MCEF (**Scheme 1.13**). Apparently, paramagnetic properties of Cr^{3+}, Cu^{2+}, and Fe^{3+} promoted dissipation of the excited state energy in a non-radiative process.
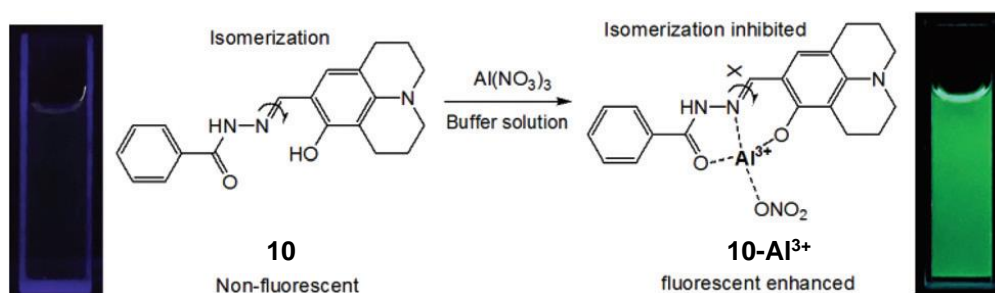
Scheme 1.13 Possible sensing mechanism of **10** with Al^{3+}. [58]

In 2016, Liu et. al. [59] and JI et. al. [60] synthesized compound **11** via the simple condensation reaction of benzohydrazide and 2-hydroxy-1-naphthaldehyde. The first research carried out experiments under acetonitrile/H_2O media, whereas another researcher did it in EtOH/H_2O solution. However, the chemosensor showed effective fluorescent selectivity and high sensitivity for Al^{3+} with fluorescence enhancement. A Job's plot of two works indicated a 1:1 stoichiometric complexation of **11** with Al^{3+}. The detection limit for Al^{3+} was determined as 8.87×10^{-7} M in Liu's work and as 1.3×10^{-7} M in JI's work. The binding pattern between **11** and Al^{3+} was examined by ^1H NMR titration experiments in Lui's work. The phenolic OH proton peak disappeared upon the addition of Al^{3+}, indicating the ligand's deprotonation in the presence of Al^{3+}. Meanwhile, the imine proton shifted because the C=N group and carbonyl group coordinated with Al^{3+}, which changes the electron distribution in the sensor (**Scheme 1.14**).
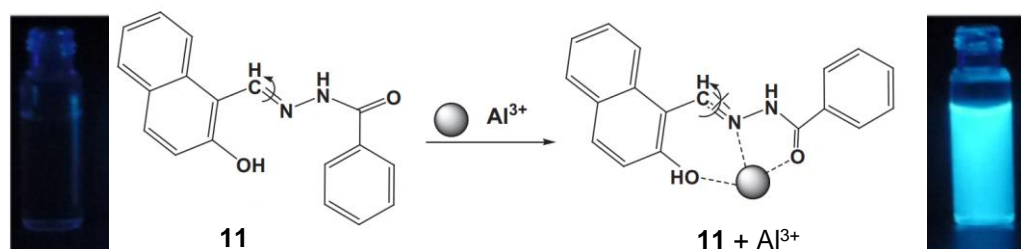
Scheme 1.14 Possible sensing mechanism of **11** with Al^{3+}. [59, 60]

In 2017, Nan et. al. synthesized chemodosimeter **12** [61] bearing benzohydrazide and dimethyl aminobenzylidene moiety. As a solution, compound **12** emitted weak fluorescence at 409 nm with a total fluorescence quantum yield of 0.0079 in CH_3CN. When exposed to Cu^{2+}, sensor **12** produced a remarkable fluorescence enhancement. Mechanism investigations revealed that the highly selective behavior of these receptors towards Cu^{2+} could be attributed to the Cu^{2+}-mediated oxidative cyclization of these compounds to the corresponding 1,3,4-oxadiazoles as shown in **Scheme 1.15**. Quantum calculations and solvent effects proved that the sensor might have an intramolecular charge transfer process, which could be prevented by the oxidative cyclization mechanism. Cu^{2+} in the drug sample was determined using sensor **12** with a low detection limit of 22 nM.
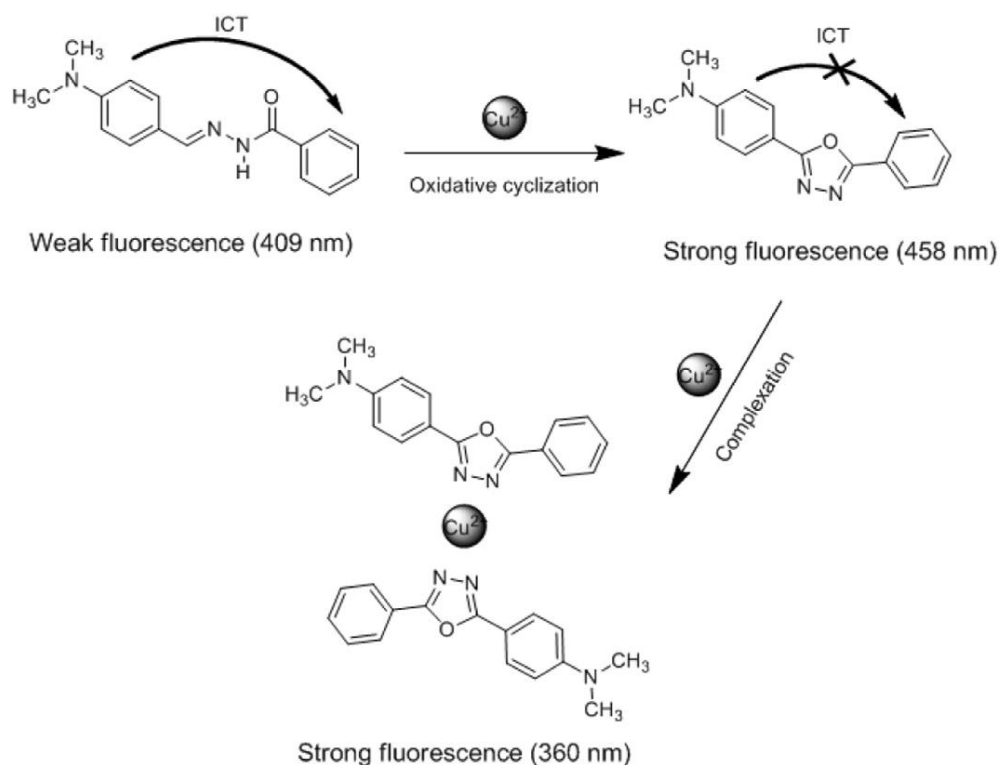
Scheme 1.15 Possible sensing mechanism of **12** with Cu^{2+}. [61]

Moreover, a series of *N*-acylhydrazones **13** and **14** [62] (**Figure 1.11**) was synthesized and found to be "turn-on" fluorescent chemodosimeters for Cu^{2+} with the same mechanism as compound **12**.
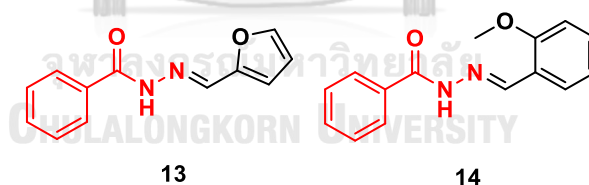
Figure 1.11 Sensors **13** and **14** derived from benzohydrazide.

It is noteworthy that the building block of the chelating site of most compounds has a similar structure to compound **1** because it provides a hydroxyl oxygen atom in position 3 from the terminal nitrogen of the hydrazone group which can serve as the donor atoms together with carbonyl oxygen and imine nitrogen of acyl hydrazone group. As a result, these sensors have the selectivity to Zn^{2+} or Al^{3+} by turn-on response. However, Cu^{2+} could quench their fluorescence signal except for compound **8**. Interestingly, three reported chemosensors without a hydroxyl group **12**, **13**, and **14** exhibit turn-on response to Cu^{2+} via reaction mode.

Table 1.3 Some parameters of fluorescent probe **4 - 14**.

No.	Analyte	Solvent	λ_{ex} / λ_{em} nm	Interference	Mode
4 [51]	Zn^{2+}	EtOH : H_2O (9:1 v/v)	390 / 495	No data	Turn on
5 [53]	Zn^{2+}	EtOH:Tris-HCl buffer (pH 7.13, 8:2 v/v)	336 / 505	Cr^{3+}, Fe^{3+}, Cu^{2+} (Turn off)	Turn on
6 [54]	Cu^{2+}	DMSO : H_2O (9:1 v/v)	450 / 523	No interference	Turn off
7 [55]	Cu^{2+}	CH_3CN : HEPES (pH 7.0, 6:4 v/v)	494 / 523	Fe^{3+}, Ni^{2+} (Turn off)	Turn off
8 [56]	Zn^{2+}	CH_3CN : HEPES (pH 7.4, 6:4 v/v)	410 / 556	No interference	Turn on
9 [57]	Al^{3+}	EtOH	390 / 506	Fe^{3+}, Cu^{2+} (Turn off)	Turn off
10 [58]	Al^{3+}	MeOH : bis-tris buffer ((pH 7.0, 999:1 v/v).	410 / 483	Cu^{2+}, Fe^{2+}, Fe^{3+}, Cr^{3+} (Turn off)	Turn on
11 [59]	Al^{3+}	CH_3CN : H_2O (1:1 v/v)	365 / 468	Fe^{3+}, Cu^{2+}	Turn on
12 [60]	Cu^{2+}	CH_3CN	310 / 360	No interference	Turn on
13 [61]	Cu^{2+}	CH_3CN	- / 360	No interference	Turn on
14 [62]	Cu^{2+}	CH_3CN	- / 355	No interference	Turn on

1.6.3 Derivatives derived from 2-hydroxybenzohydrazide (Salicyloyl hydrazide)

According to previous derivatives, most chemosensors have a significant increase in fluorescence which can be explained by the stable chelation with certain metal ions, the inhibition of C=N isomerization, and the prevention of the ESIPT process. However, a series of *N*-acylhydrazones derived from salicyloyl hydrazide mentioned below also use the same strategy. Therefore, this section will discuss the influence of additional hydroxyl groups on salicyloyl moiety in terms of structure and their selectivity for metal ions. The first three similar structures of *N*-acylhydrazones derived from salicyloyl hydrazide bearing with three different fluorophores: salicylaldehyde (**15**) [51], naphthalene (**16**) [63], and pyrene (**17**) [64] were shown in **Figure 1.12**.

The experimental condition of **15** was performed in aqueous ethanol and the other two were performed in aqueous CH$_3$CN. Compounds **15** and **17** had selectivity for Zn^{2+}, whereas compound **16** had high selectivity for Al^{3+} through the turn-on response. Interestingly, changing the solvent from aqueous ethanol to aqueous DMF allowed **15** to change its ion selectivity from Zn^{2+} to Mg^{2+} as shown in **Figure 1.13**. Notably, DFT and NMR studies of compounds **16** and **17** substantiated that phenolic oxygen on salicyloyl moiety participated in the chelation with metal ions, whereas phenolic oxygen on salicyloyl moiety of **15** did not.
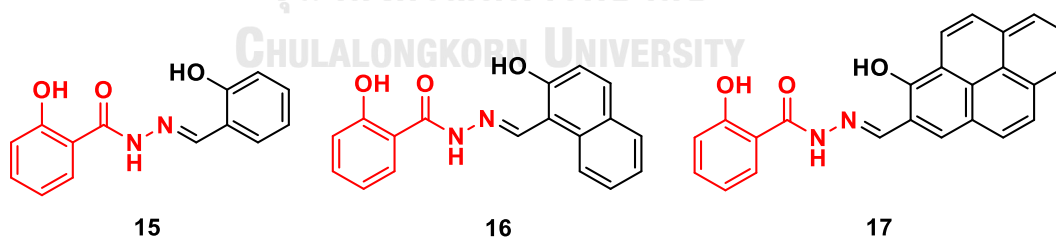
Figure 1.12 Sensors **15, 16**, and **17** derived from salicyloyl hydrazide.
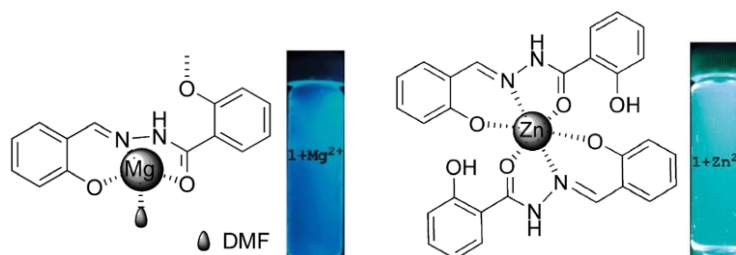
Figure 1.13 Possible binding mode of **15** with Mg^{2+} and Zn^{2+}. [51]

In 2016, Zhang et. al. designed and synthesized a new Schiff base fluorescence probe **18** [65] which has a similar structure to **15** with the extended conjugation of the allyl group on position 3 of salicylaldehyde moiety. As expected, the fluorescence of **18** was enhanced by Mg^{2+} in DMF/water like **15**. The difference between **15** and **18** is the binding ratio for Mg^{2+} of **18** is 2:1 (**Scheme 1.16**), while **15** is 1:1. Moreover, the binding constant of **18** was determined to be 1.02×10^{7} M^{-1} which was more than **15** (2.96×10^{4} M^{-1}). However, Cu^{2+} and Fe^{3+} were also found to be the competitive metal ions for Mg^{2+} detection.
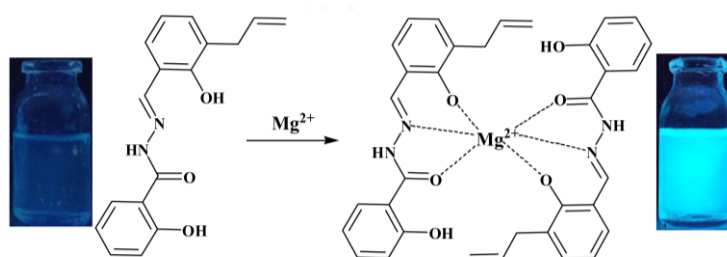
Scheme 1.16 Possible sensing mechanism of **18** with Mg^{2+}. [65]

To expand the conjugated system like compound **18**, in 2019, Liu et. al. designed and synthesized a fluorescent probe **19** [66] derived from triphenylamine. In CH_3CN/water, the fluorescence of **19** at 540 nm was significantly enhanced only by Zn^{2+} with a larger Stokes shift (210 nm), but the fluorescence of **19** was quenched in the existence of Co^{2+} and Cu^{2+}. Meanwhile, when Zn^{2+} was added, it was seen by the naked eye that the solution turned from colorless to yellow. The chelating site of **19** towards Zn^{2+} was characterized indicating that the N atom of C=N, the O atom of C=O and –OH (of salicylaldehyde moiety), and the Cl^- and H_2O from the solution coordinated with the center Zn^{2+} to form a complex (**Scheme 1.17**).

Scheme 1.17 Possible sensing mechanism of **19** with Zn^{2+}. [66]

Next, hydroxypyrazole derivative **20** [67] and 1,2,3-triazole derivative **21** [68] can be used as a "turn-on" fluorescent chemosensor to detect Al^{3+} in ethanol. The detection limit of Al^{3+} was estimated to be 2.5 x 10^{-8} for **20** and 1.2 x 10^{-8} M for **21**. Job's plot suggested a 1:1 stoichiometry for both compounds (**Figure 1.14**). ^{1}H NMR titration experiments revealed that **21** can chelate Al^{3+} through interactions with imine nitrogen and oxygen of the phenolic hydroxyl group. However, **20** did not provide data about this interaction.
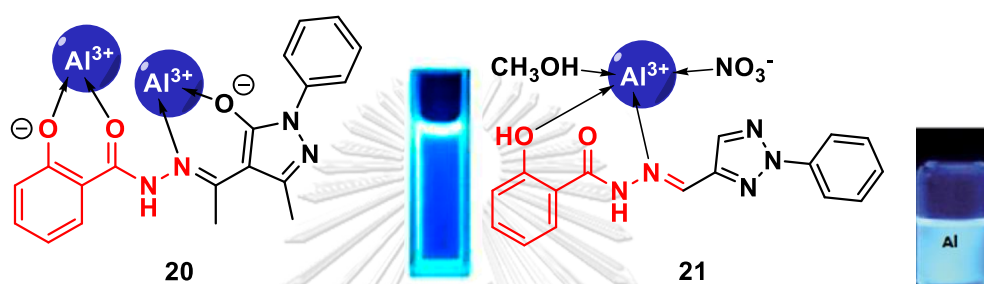
Figure 1.14 Possible binding mode of sensors **20** with Al^{3+} [67] and **21** with Al^{3+} [68].

The next pair of compounds is a good example to demonstrate the influence of the position of the hydroxyl group on the selectivity for metal ions. Compounds **22** [69] and **23** [70] are the derivatives of benzothiazole which have sulfur and nitrogen as the additional donor atoms (**Figure 1.15**). Both molecules have a similar structure, but the position of the hydroxyl group highlighted blue of both molecules is different. Remarkably, this hydroxyl group of **22** could exhibit ESIPT with C=N in both the hydrazone unit and the benzothiazole unit, whereas **23** could exhibit ESIPT only with the benzothiazole unit. With this difference in structure, **22** was accomplished in the determination of Zn^{2+} and Al^{3+} via fluorescence ratiometric responses, whereas **23** showed dual functionality including sensing changes in pH with a turn-on response and detecting Cu^{2+} with a ratiometric response. The sensing experiments of both derivatives were performed in DMF/H_2O. In the case of **22**, the limit of detection for Zn^{2+} and Al^{3+} was 0.127 µM and 0.1 µM, respectively and the binding ratio of a probe with Zn^{2+} and Al^{3+} were determined as 1:1 and 2:1, respectively. In the case of **23**, the limit of detection for Cu^{2+} was calculated as 1.35 µM and the ratio of the probe to the Cu^{2+} was 1:2. However, the design of the copper turn-on sensor is interesting because almost all of the aforementioned *N*-acylhydrazone sensors are quenched fluorescence

signal by Cu^{2+}. The researchers proposed the sensing mechanism of **23** for Cu^{2+} as follows: Cu^{2+} first coordinated with the benzothiazole moiety which led to the drop in fluorescence intensity due to the paramagnetic nature of Cu^{2+}. When the amount of Cu^{2+} added was greater than 1 equivalent, excess Cu^{2+} further coordinated with the oxygen atom of the hydroxyl in the ortho-position of the hydrazide, which resulted in the ICT process from the oxygen atom of the hydroxyl to the benzothiazole core was inhibited.
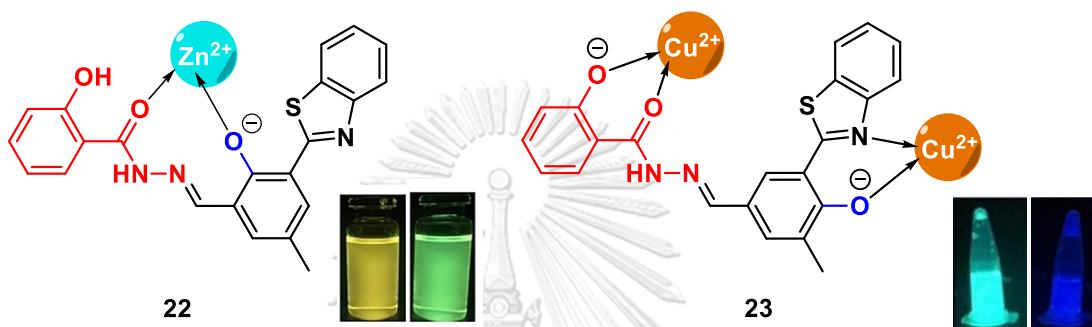
Figure 1.15 Possible binding mode of sensors **22** with Zn^{2+} [69] and **23** with Cu^{2+} [70].

In 2020, Chen et. al. introduced two kinds of fluorophores sensors, including coumarin (**24**) and triphenylamine (**25**), for Cu^{2+} detection [71]. Predictably, both compounds could recognize Cu^{2+} with a fluorescence turn-off mechanism. The strength of this work is the proposed binding mode was confirmed by Job's plot and the single-crystal structure of the **24**-Cu^{2+} complex (**Figure 1.16**). Density functional theory (DFT) calculation was carried out to get insight into the mechanism of Cu^{2+} sensors. The result suggested that the ICT of sensors was blocked after binding Cu^{2+}, which leads to fluorescence quenching.
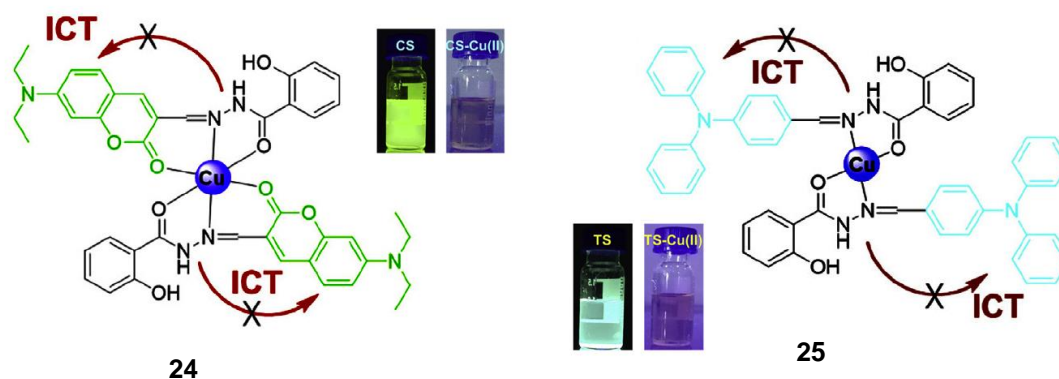
Figure 1.16 Possible binding mode of sensors **24** with Cu^{2+} and **25** with Cu^{2+}. [71]

Finally, Fan et. al. reported a new BODIPY derivative bearing salicyloyl hydrazide moieties as a ratiometric fluorescence chemodosimeter **26** for Cu^{2+} in DMF-H_2O. [72] The solution of probe **26** displays a single emission band centered at 555 nm upon excitation at 525 nm. Upon the addition of Cu^{2+}, the emission band around 505 nm increased, whereas the emission band centered at 555 nm decreased. Meanwhile, the excitation wavelength changed to 450 nm upon the addition of Cu^{2+}. The sensing mechanism of the chemodosimeter **26** toward Cu^{2+} was proved by the ^{1}H NMR experiments. It suggests that the C=N bond in the hydrazone unit of probe **26** was hydrolyzed in the presence of Cu^{2+} to generate the green fluorescence product BODIPY-CHO (**Scheme 1.18**). The ratiometric response F_{505}/F_{555} was not induced any change with any competitive metal ions. The detection limit of this sensor was determined to be 0.2 μM.
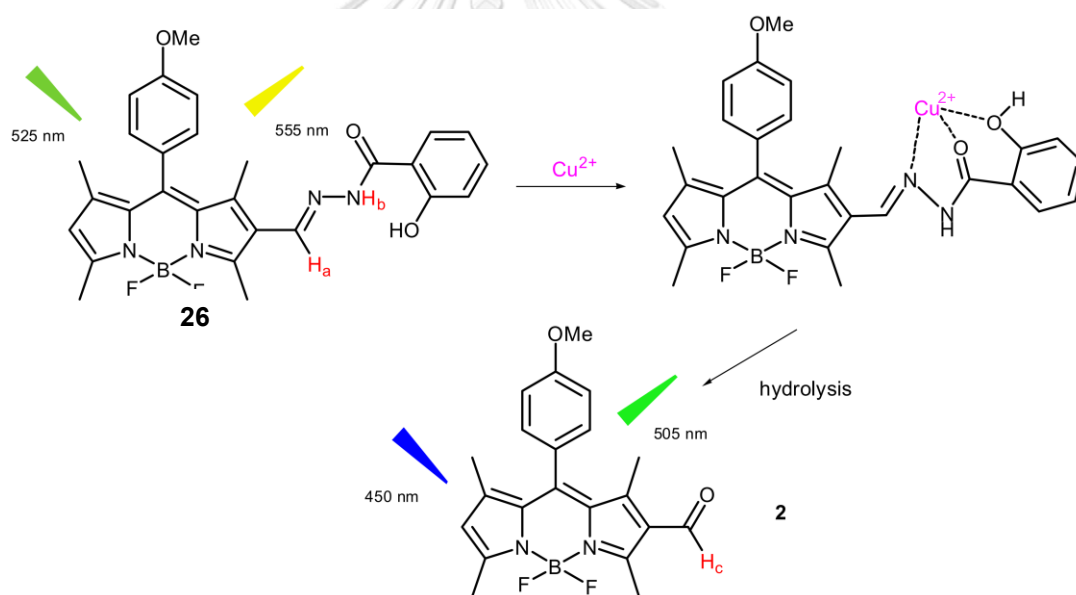
Scheme 1.18 Possible sensing mechanism of **26** with Cu^{2+}. [72]

Table 1.4 Some parameters of fluorescent probe 15 - 26.

No.	Analyte	Solvent	λ_{ex} / λ_{em} nm	Interference	Mode
15[51]	Zn^{2+}	90% EtOH/H$_2$O	390 / 488	Fe^{3+}, Co^{2+}, Cu^{2+}	Turn on
	Mg^{2+}	90% DMF/H$_2$O	410 / 453	Fe^{3+}, Co^{2+}, Ni^{2+}, Cu^{2+}	Turn on
16[63]	Al^{3+}	80% CH$_3$CN/H$_2$O	425 / 472	No interference	Turn on
17[64]	Zn^{2+}	50% CH$_3$CN/H$_2$O	490 / 556	Co^{2+}, Cu^{2+}	Turn on
18[65]	Mg^{2+}	80% DMF/H$_2$O	391 / 465	Fe^{3+}, Bi^{2+}, Cu^{2+}	Turn on
19[66]	Zn^{2+}	60% CH$_3$CN/H$_2$O	330 / 540	Co^{2+}, Cu^{2+}	Turn on
20[67]	Al^{3+}	EtOH	381 / 396, 419	Mn^{2+}, Zn^{2+}, Hg^{2+}, Fe^{3+}, Ba^{2+}, Ni^{2+}, Co^{2+}, Cu^{2+}.	Turn on
21[68]	Al^{3+}	EtOH	358 / 442	No interference	Turn on
22[69]	Al^{3+}	50% DMF/H$_2$O	420 / 494	No interference	Turn on
	Zn^{2+}	50% DMF/H$_2$O	420 / 508	No interference	Turn on
23[70]	Cu^{2+}	30% DMF/H$_2$O (pH 13)	390 / 451, 498	No interference	Ratio-metric
24[71]	Cu^{2+}	50% DMSO/H$_2$O	460 / 518	No interference	Turn off
25[71]	Cu^{2+}	50% DMSO/H$_2$O	370 / 476	No interference	Turn off
26[72]	Cu^{2+}	70% DMF/H$_2$O	450 / 505, 555	No interference	Ratio-metric

1.6.4 Derivatives derived from 2-aminobenzohydrazide.

To compare the influence of hydroxyl and amino groups on the selectivity of the sensor according to the Hard-Soft Acid-Base principle, the previously reported fluorescence sensors derived from 2‑aminobenzohydrazide are presented in **Figure 1.17** to compare the properties with 2-hydroxybenzohydrazide derivatives. However, the selectivity to metal ions of these derivatives is not significantly different from that of 2‑hydroxybenzohydrazide derivatives because they still have selectivity towards Zn^{2+}, Mg^{2+}, and Cu^{2+} as well (**Table 1.5**).
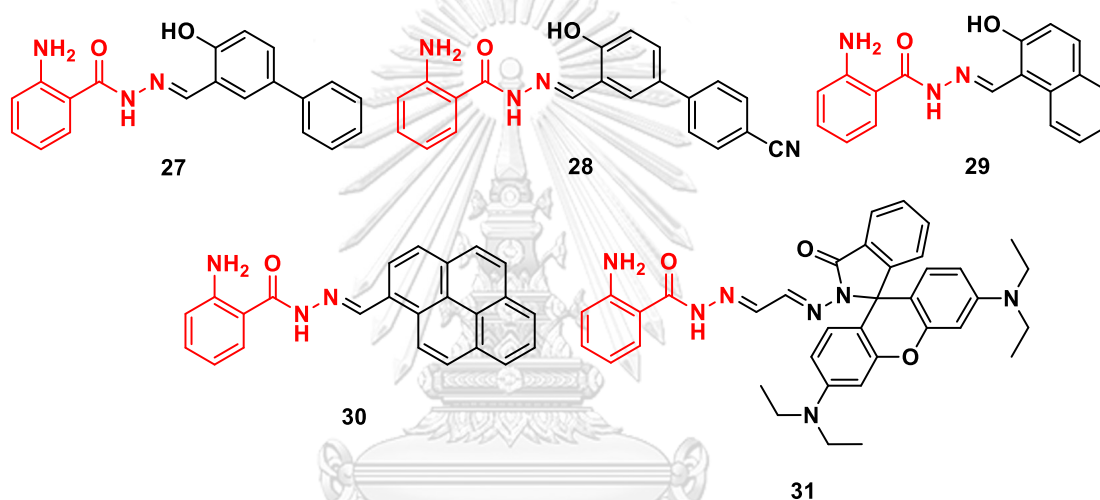
Figure 1.17 Sensors **27 – 31** derived from 2-aminobenzohydrazide.

Table 1.5 Some parameters of fluorescent probe **27 - 31**.

No.	Analyte	Solvent	λ_{ex} / λ_{em} (nm)	Mode
27 [73]	Zn^{2+}	30% CH_3CN/HEPES (pH 7.4)	360 / 485	Turn on
28 [74]	Zn^{2+}	40% THF/HEPES (pH 7.4)	360 / 467	Turn on
29 [75]	Mg^{2+}	90% EtOH/HEPES (pH 10)	415 / 482	Turn on
30 [76]	Cu^{2+}	80% EtOH/HEPES (pH 6.3)	350 / 393, 215	Turn on
31 [77]	Cu^{2+}	40% EtOH/HEPES (pH 7.4)	520 / 556	Turn on

*No interference was observed from all derivatives.

1.6.5   Derivatives derived from 2-Pyridinecarbohydrazide (Picolinohydrazide).

Picolinohydrazide is the pyridine substituted at the C-2 position with the carbohydrazide functional group. The nitrogen on the pyridine ring can serve as an additional donor atom for metal chelation. One characteristic of picolinohydrazide is it can undergo the intramolecular hydrogen bond through a five-membered ring between N-H of hydrazide unit (hydrogen bond donor) and nitrogen on pyridine (hydrogen bond acceptor).

In 2019, Peng et al. designed and synthesized two derivatives of picolinohydrazide **32** and **33** [78] via the condensation with salicylaldehyde and 2-hydroxynaphthalaldehyde, respectively to compare their ability for metal ion detection (**Figure 1.18**). Both probes exhibited a turn-on fluorescence response toward Al^{3+} in DMF/H_2O. In addition, probe **33** was reported by Qin et. al. in 2015 [79] and Dey et. al. in 2019 [80] again.

Noteworthy, Qin et. al. and Peng et al. differently proposed the plausible binding mode of **33** and Al^{3+} as shown in **Figure 1.19**. One showed that the nitrogen atom on pyridine precipitates in coordination, while another does not. However, their proposed binding modes were unclear because they did not carry out an experiment to explain about the nitrogen of the pyridine ring before and after the complex formation. However, the sure results from ^{1}H NMR was the oxygen atom of the -OH group was deprotonated when it coordinated to Al^{3+} and the absence of a signal owing to a tautomeric -OH proton suggests that they only exist in keto forms.
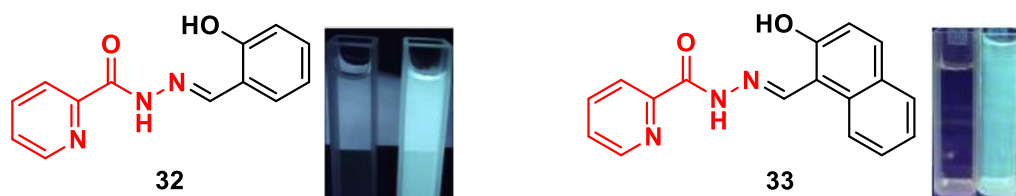
Figure 1.18 Sensors **32** and **33** [78] derived from picolinohydrazide.
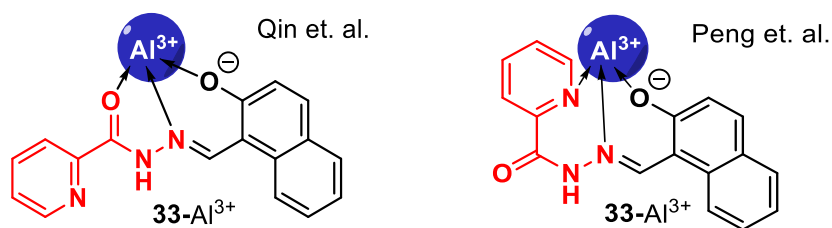
Figure 1.19 Possible binding mode of sensors **33** with Al^{3+}.

Next, **34** which is derived from 2,4-dihydroxysalicylaldehyde can be used as a turn-on fluorescent probe for Al^{3+} in DMF/H$_2$O. [81] Interestingly, both hydroxyl groups on the aromatic ring of **34** were found to be involved in the chelation of Al^{3+}. Moreover, the hydrazide unit transformed to the enolic from in metal complex as shown in **Figure 1.20**. This proposed binding mode was confirmed by the presence of a peak at m/z = 340.70 [**34** + Al^{3+} + 2H$_2$O + 3H$^+$ + Na$^+$]$^+$ in the mass spectrum and ^{1}H NMR spectrum of **34**-Al^{3+}. It suggested that the peaks of protons of its -NH, and two -OH disappeared after the addition of excess Al^{3+}.
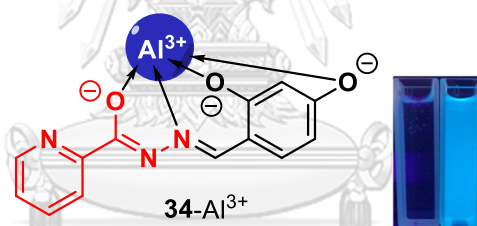
Figure 1.20 Possible binding mode of sensors **34** with Al^{3+}. [81]

In 2019, Purkait et. al. reported vanilinyl-picolinyl hydrazide Schiff base **35** [82] as shown in **Figure 1.21**. When compared in terms of structure, the para hydroxyl group of **34** was converted to a methoxy group to become **35**, it remained specific to Al^{3+}. Interestingly, not only Al^{3+} could turn on the fluorescence signal of **34** but Mg^{2+} also turn on as well. The peculiarities were that Mg^{2+} reported a yellow emission at 522 nm (LOD = 45 nM) in DMSO, whereas a strong blue emission was remarked for Al^{3+} in pure water at 460 nm (LOD = 7.4 nM). In addition, Job's plot revealed a 1:1 for Al^{3+} and 1:2 for Mg^{2+} for the complexes. Remarkably, ^{1}H NMR titration experiment showed both phenolic–OH and hydrazide–NH in **35**-Mg^{2+} indicating that deprotonation and tautomerization did not occur which is unlike **35**-Al^{3+}.
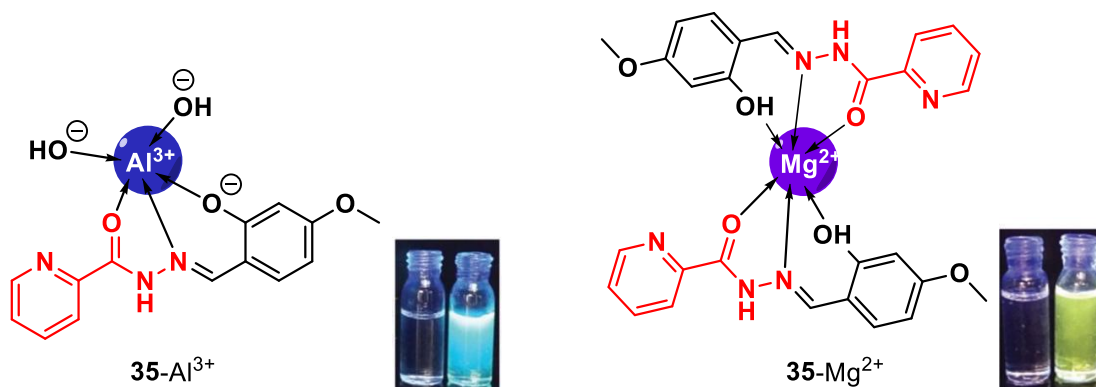
Figure 1.21 Possible binding mode of sensors **35** with Al^{3+} and Mg^{2+}. [82]

In 2018, Liu et. al. developed a fluorescent sensor **36** [83] derived from 4-(diethylamino) salicylaldehyde. In 2022, Gong et. al. constructed a fluorescent sensor **37** from natural camphor [84]. Both derivatives **36** and **37** (**Figure 1.22**) have a similar binding site to previous sensors **32-35** and showed obvious fluorescence enhancement after binding to Al^{3+} and Zn^{2+} at two different emissive channels where Zn^{2+} gives a greater red shift of emission wavelength in both probes. The selectivity study of **36** was performed in CH_3OH/HEPES buffer (1/4, v/v, pH 7.2), whereas **37** was achieved in CH_3CN/HEPES buffer (v/v, 3/7, 10 mM, pH = 7.4). Interestingly, ^1H NMR titration experiment revealed that the protons of the pyridine unit of **36** shifted downfield upon addition of Al^{3+} and Zn^2 suggesting that the N atoms of the pyridine unit might coordinate to the central Al^{3+}/Zn^{2+}. On the contrary, the disappearance of a proton -NH of **37** was found after the addition of Al^{3+} or Zn^{2+} indicating that tautomerization occurred in the metal complex and the carbonyl oxygen is likely involved in the binding sites.
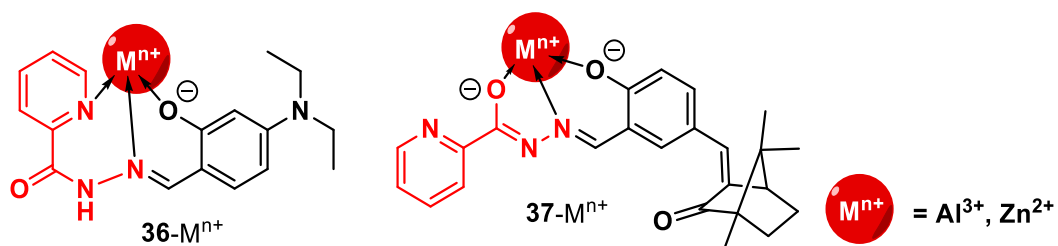
Figure 1.22 Possible binding mode of sensors **36** and **37** with Al^{3+} and Zn^{2+}.

Tang et. al., Wang et. al., and Zhao et. al. developed new fluorescence sensors which bear quinazolinone (**38**) [85], benzothiazole (**39**) [86], and 3-hydroxylflavone (**40**) [87], respectively. Since there are many heteroatoms on these three structures, the expected result of these probes is probably the selectivity for other metal ions that might not be Al^{3+} or Zn^{2+}. However, all compounds show ability in the recognition of Al^{3+} with turn-on fluorescence as well.

Interestingly, the binding stoichiometry of **38** with Al^{3+} was proved by Job's plot analysis to be 1:2 which is a rare case in which two metal ions can bind to one acylhydrazone unit as shown in **Figure 1.23**. In the case of **39**, nitrogen and sulfur atoms on benzothiazole did not involve in the binding of Al^{3+} which can be proved ^{1}H NMR. It can be assumed that the position of nitrogen and sulfur on benzothiazole is not suitable for metal chelation. Remarkably, Al^{3+} preferred to be bound to the two oxygen on flavone of **40** rather than to the acylhydrazone units.
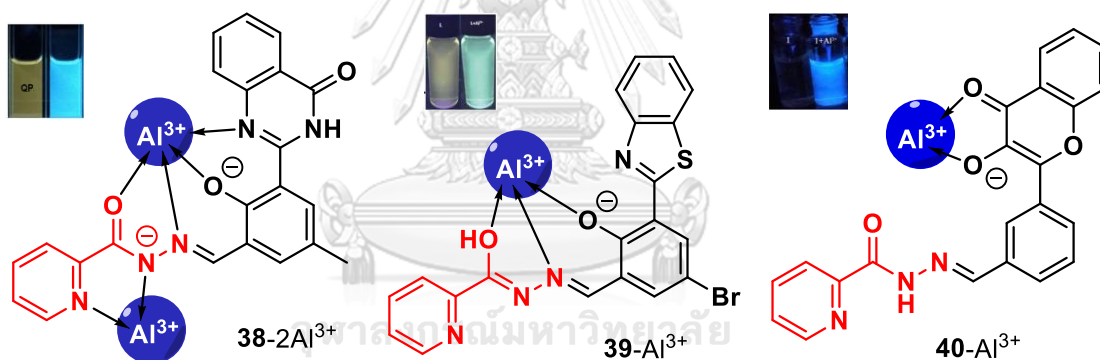
Figure 1.23 Possible binding mode of sensors **38 – 40** with Al^{3+}. [85-87]

Purkait et. al., Guo et. al., and Xie et. al. developed fluorescent probes which are derivatives of coumarin **41** [88] and **42** [89, 90]. Due to the hydroxyl group at the binding site, **41** shows selectivity to Al^{3+} as in previous probes. However, when carbonyl oxygen of coumarin is in the binding site, it promoted **42** to selective only Cu^{2+} with fluorescence quenching (**Figure 1.24**).
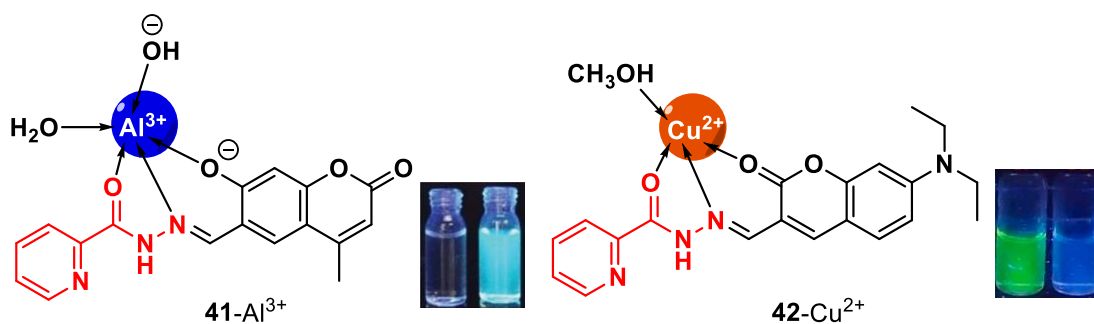
Figure 1.24 Possible binding mode of sensors **41** with Al^{3+} [88] and **42** with Cu^{2+} [89].

Quinoline-based fluorescent probes **43** [91] and **44** [92] were designed and synthesized by Wang et. al. and Tang et. al., respectively. Both probes were studied in DMSO/HEPES buffer at pH 7.4. Interestingly, in the absence of 8-methoxy group on the quinoline unit, **43** responded to Zn^{2+} with fluorescence enhancement, whereas **44** which has an 8-methoxy group did not show fluorescence enhancement with any metal ions. However, **44** manifested the selective quenching response to Cu^{2+}. Moreover, Cu^{2+} was found to be able to extinguish the signal enhancement of **43** with Al^{3+}. The highlight of Tang's work is they can crystalize the **44**-Cu^{2+} complex. This clearly explained the binding pattern of Cu^{2+} and the picolinohydrazide unit. Apparently, the nitrogen atoms in the pyridine and amide groups participated in coordination with Cu^{2+} as shown in **Figure 1.25**. Notably, the hydrogen atom on amide is deprotonated by Cu^{2+} interaction. This is the reason why Cu^{2+} tends to compete with the target metal ions in many picolinohydrazide-based probes.
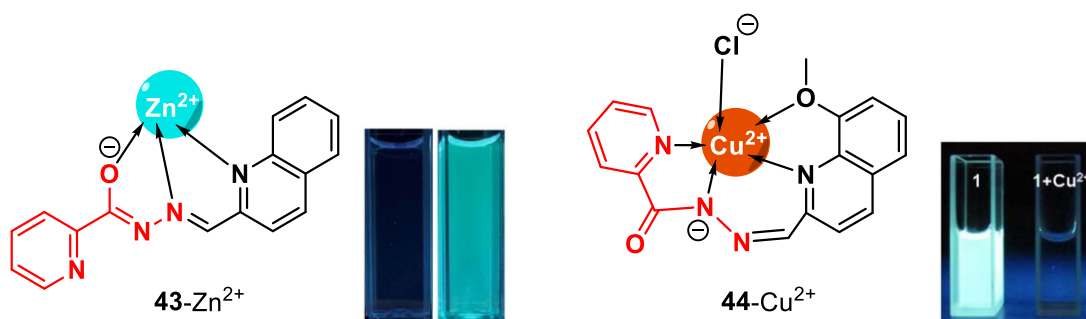
Figure 1.25 Possible binding mode of sensors **43** with Zn^{2+} [91] and **44** with Cu^{2+} [92].

The same binding pattern between the probe and Cu^{2+} was also proposed in probe **45** which contains a pyrene unit and picolinohydrazide. [93] Interestingly, Cu^{2+} was the only metal ion that caused an enhancement of the blue emission signal in CH_3OH/H_2O. The binding structure of the **45**-Cu^{2+} complex was investigated by ^{1}H NMR. Upon the addition of Cu^{2+}, the amide NH proton signal decreased and the adjacent proton signals of nitrogen at pyridine disappeared. These observations indicated the binding of Cu^{2+} with an amide group and pyridine (**Figure 1.26**).
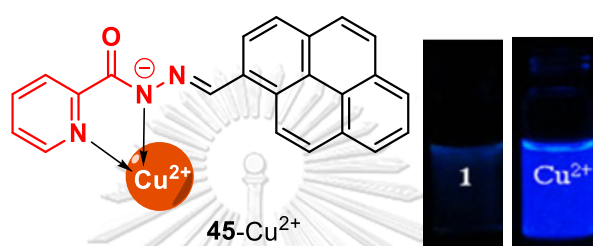
Figure 1.26 Possible binding mode of sensors **45** with Cu^{2+}. [93]

In 2015, Kar et. al. prepared Schiff base **46** from 4-(dimethylamino) cinnamaldehyde and picolinohydrazide. [94] Exceptionally, the fluorescence intensity increased after Cd^{2+} was added to the solution of **46**. Since **46** is the only picolinohydrazide-based probe that is selective to Cd^{2+}, it is noteworthy that only heteroatom in the picolinohydrazide unit is the important binding site for Cd^{2+}. According to X-ray crystallographic investigations, a 2:1 binding stoichiometry is preferred in the solid state, whereas a 1:1 stoichiometry is demonstrated in solutions (**Figure 1.27**).
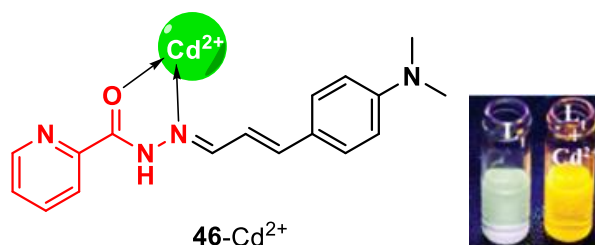
Figure 1.27 Possible binding mode of sensors **46** with Cd^{2+}. [94]

The last two probes based on carbazole (**47**) [95] and naphthalimide (**48**) [96] displayed a turn-on fluorescence recognition of Cu^{2+}. The fluorescence responses of the **47/48** to Cu^{2+} were studied in buffer solution (pH 7.4 for **47** and pH 5.0 for **48**) which is diluted with a little volume of DMSO from the stock solution of the probe. Interestingly, the mechanism of the probe in sensing Cu^{2+} could be deduced that the Cu^{2+} promoted hydrolysis reaction to generate the aldehyde fluorophore with high fluorescence signal after coordination with the carbonyl oxygen and imine nitrogen atoms of the probe (**Scheme 1.19**). This can be confirmed by ^{1}H NMR titration, mass spectroscopy, and comparing UV-vis and fluorescence spectra of the probe after adding Cu^{2+} with a pure aldehyde. The strength of these works is no interference in the detection of Cu^{2+} and the detection could perform in 99% aqueous media.
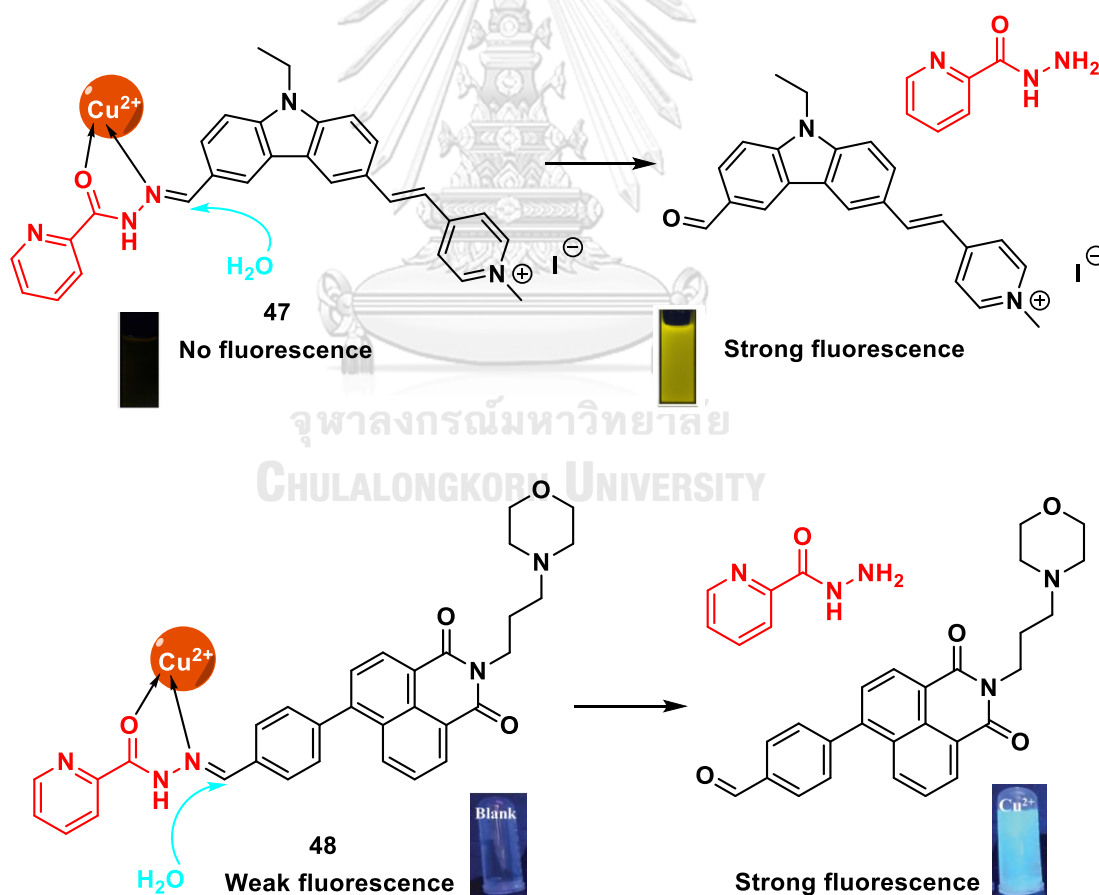
Scheme 1.19 Possible sensing mechanism of **47** [95] and **48** [96] with Cu^{2+}.

Table 1.6 Some parameters of fluorescent probe **32** - **48**.

No.	Analyte	Solvent	λ_{ex} / λ_{em} nm	Interference	Mode
32 [78]	Al^{3+}	DMF/H_2O (1:9 v/v)	300 / 467	Cu^{2+}, Hg^{2+}	Turn on
33 [78]	Al^{3+}	DMF/H_2O (1:9 v/v)	360 / 483	Cu^{2+}	Turn on
34 [81]	Al^{3+}	DMF/H_2O (1:9 v/v)	370 / 456	Co^{2+}, Fe^{3+}, Cr^{3+}, Hg^{2+}, Cu^{2+}	Turn on
35 [82]	Al^{3+}	H_2O	340 / 460	Hg^{2+}, Cu^{2+}, Pb^{2+}, Fe^{3+}	Turn on
	Mg^{2+}	DMSO	340 / 522	Pd^{2+}, Ba^{2+}, Fe^{3+}, Al^{3+}, Co^{2+}, Ni^{2+}, Mn^{2+}	Turn on
36 [83]	Al^{3+}	CH_3OH/HEPES (pH 7.2, 1:4 v/v)	390 / 504	no interference	Turn on
	Zn^{2+}	CH_3OH/HEPES (pH 7.2, 1:4 v/v)	390 / 575	no interference	Turn on
37 [84]	Al^{3+}	ACN/HEPES (pH 7.4, 3:7 v/v)	365 / 500	no interference	Turn on
	Zn^{2+}	ACN/HEPES (pH 7.4, 3:7 v/v)	365 / 555	no interference	Turn on
38 [85]	Al^{3+}	EtOH/Tris buffer (pH 7.4, 9:1 v/v)	371 / 473	Co^{2+}, Cu^{2+}, Fe^{2+}, Fe^{3+}, Ni^{2+}	Turn on
39 [86]	Al^{3+}	MeOH/water (pH 6.0, 1:1 v/v)	403 / 473	Ni^{2+}, Cu^{2+}	Turn on
40 [87]	Al^{3+}	DMSO/H_2O (1:9 v/v)	350 / 453	Hg^{2+}, Cu^{2+}, Mn^{2+}, Co^{2+}	Turn on
41 [88]	Al^{3+}	HEPES buffer pH 7.2	400 / 470	Hg^{2+}, Cu^{2+}, Cr^{3+}, Fe^{3+}, Zn^{2+}, Ba^{2+}	Turn on

No.	Analyte	Solvent	λ_{ex} / λ_{em} nm	Interference	Mode
42 [89]	Cu^{2+}	PBS buffer (pH = 7.2)	470 / 525	no interference	Turn off
43 [91]	Zn^{2+}	DMSO/HEPES (pH 7.4, 3:2, v/v)	375 / 484	Co^{2+}, Cu^{2+}, Ni^{2+}, Hg^{2+}	Turn on
44 [92]	Cu^{2+}	1% DMSO/HEPES (pH 7.4)	340 / 523	no interference	Turn off
45 [93]	Cu^{2+}	CH_3OH/HEPES (pH 7.0, 7:3 v/v)	360 / 455	no interference	Turn on
46 [94]	Cd^{2+}	CH_3OH/HEPES (pH 7.3, 1:4 v/v)	405 / 578	no interference	Turn on
47 [95]	Cu^{2+}	0.5% DMSO/PBS (pH 7.4)	422 / 539	no interference	Turn on
48 [96]	Cu^{2+}	1% DMSO/AcOH buffer (pH 5.0)	360 / 440	no interference	Turn on

1.6.6   Derivatives derived from other heterocyclics.

In addition to pyridine, other heterocyclics have also been synthesized as fluorescent sensors for metal ions, such as furans, thiophenes, and pyrroles as shown in **Figure 1.28**. However, these derivatives have been studied relatively little and their detection results are not significantly different from those of pyridine derivatives, except for **55** which shows the selectivity for In^{3+}.

I.   **2-Furancarbohydrazide**
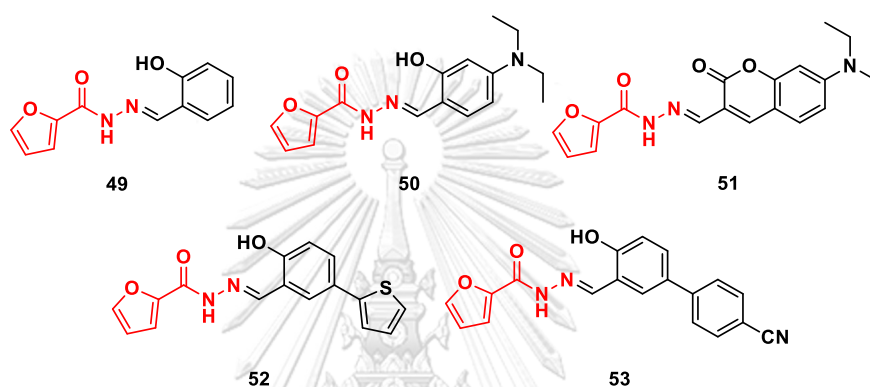
II.   **2-Thiophenecarbohydrazide**
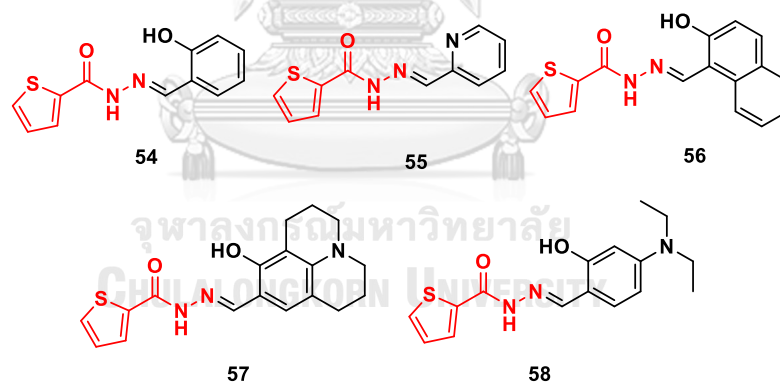
III.   **2-Pyrrolecarbohydrazide**
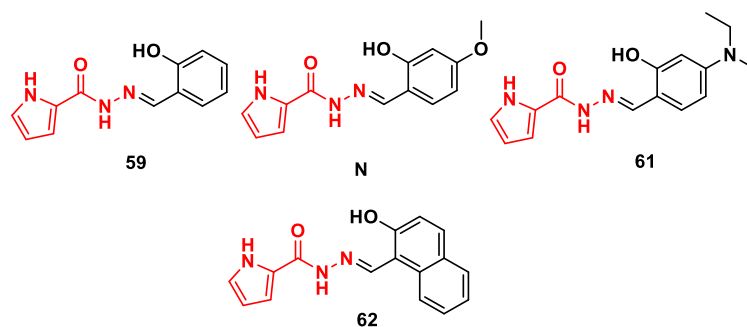
Figure 1.28 *N*-acylhydrazone-based fluorescent sensors **49-62**

Table 1.7 Some parameters of fluorescent probe **49** - **62**

No.	Analyte	Solvent	λ_{ex} / λ_{em} (nm)	Interference
49 [97]	Al^{3+}	0.1% $DMSO/H_2O$ (pH 5.5)	369 / 458	Cu^{2+}, Fe^{2+}
50 [98]	Al^{3+}	Bis–Tris buffer (pH 7.0)	390 / 452	Cu^{2+}, Fe^{2+}, Fe^{3+}, Cr^{3+}
51 [99]	Zn^{2+}	90% $EtOH/H_2O$	322 / 511	Co^{2+}, Cu^{2+}, Fe^{3+}, Ni^{2+}
52 [100]	Zn^{2+}	99% $H_2O/EtOH$	375 / 493, 534	Co^{2+}, Cu^{2+}, Fe^{3+}, Ni^{2+}
53 [101]	Al^{3+}	80% CH_3CN/H_2O (pH 7.0)	355 / 464	Cu^{2+}, Fe^{3+}
	Zn^{2+}	80% CH_3CN/H_2O (pH 7.0)	355 / 512	Fe^{2+}, Ca^{2+}, Cu^{2+}, Fe^{3+}
54 [102, 103]	Al^{3+}	50% $DMSO/H_2O$	320 / 463	None
55 [104]	In^{3+}	EtOH	379 / 465	Cu^{2+}, Pb^{2+}, Ni^{2+}
56 [105]	Al^{3+}	20% $EtOH/H_2O$	407 / 476	None
57 [106]	Al^{3+}	CH_3CN	420 / 521	Cu^{2+}
58 [107, 108]	Al^{3+} Zn^{2+}	50% $DMSO/H_2O$	375 / 475	None
59-62 [109]	Al^{3+}	0.3% $DMSO/H_2O$ (pH 7.4)	372/446 (**59**), 385/448 (**60**), 398/453 (**61**), 425/480 (**62**)	Hg^{2+}, Cu^{2+}, Fe^{2+}, Fe^{3+}

[*]All derivatives show turn-on responses to the analyte.

1.6.7 Objectives of this research (Part A)

In previous research [58, 106], the design and synthesis of julolidine-based fluorescent chemosensors usually started from 8-hydroxyjulolidine-9-carboxaldehyde condensing with hydrazide to generate molecular sensors with acylhydrazone unit as shown in **Scheme 1.20**.
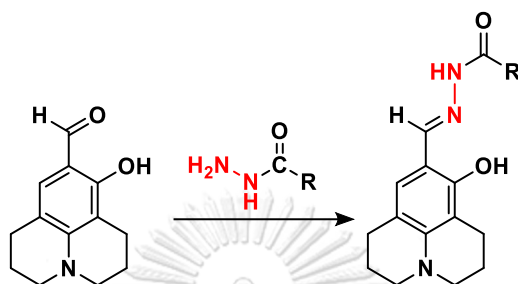
Scheme 1.20 Synthesis of sensors from 8-hydroxyjulolidine in previous research [58, 106].

Since the presence of a hydroxyl group on julolidine, it promotes the sensing mechanism to be the coordination mode which can observe and describe in **10** and **57**. Moreover, other probes containing a similar binding site with 8-hydroxyjulolidine also show similar selectivity and sensing mechanism. However, julolidine without a hydroxyl group at position 8 has never been studied for metal ion detection. Meanwhile, several acylhydrazone-based sensors without hydroxyl group show interesting selectivity for metal ions such as **45** (Cu^{2+}), **46** (Cd^{2+}), and **55** (In^{3+}) and can support the sensing mechanism to be the reaction mode as mentioned in **12**, **13**, **14**, **26**, **47**, and **48**. Therefore, three julolidine derivatives without hydroxyl groups **JA**, **JS**, and **JP** were designed and synthesized and investigated their sensory response for metal ions in this work (**Figure 1.29**).
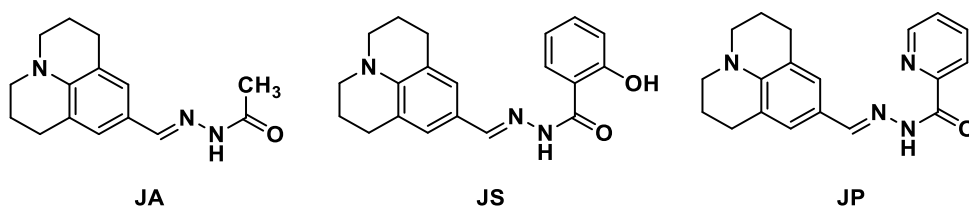
Figure 1.29 Target compound

1.7 Aza Crown Ether

Crown ethers are heterocyclic compounds containing cyclic polyethers. Due to the fixed size of the crown cavity, which allows only cations with similar ionic radii to enter, the crown ethers behave as selective complexing agents. Simple members of the crown ether family, including 12-crown-4, 15-crown-5, and 18-crown-6 are generally capable of binding alkali metal ions as shown in **Figure 1.30**.
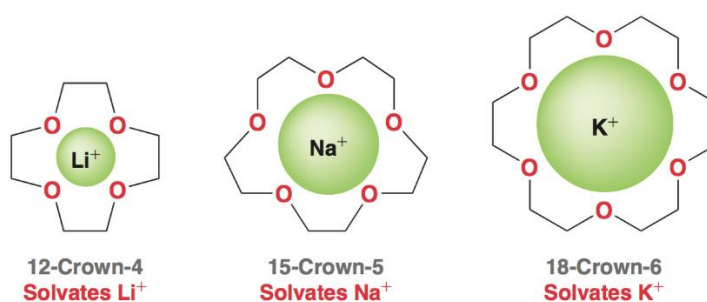
Figure 1.30 Simple members of the crown ether family. [110]

Nevertheless, each oxygen atom on crown ether can be substituted by other heteroatoms such as nitrogen called aza crown ethers or sulfur called thia crown ether (**Figure 1.31a**). These heteroatoms have a significant impact on coordinating ability even though the cavity's size remains the same because the metal binding affinity of each atom is different. [111, 112] Lariat ethers are modified crown ethers that have one or more sidearms appended to the ring (**Figure 1.31b**). The sidearms generally contain Lewis basic donor groups to improve the properties for binding cations. [113]

Based on sensing mechanisms, ICT and PET processes are usually utilized for the design of fluorescence sensors from the aza-crown ether.
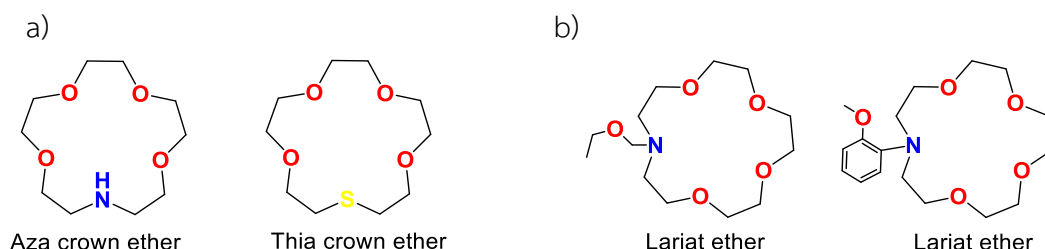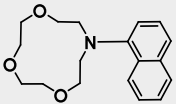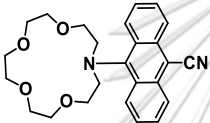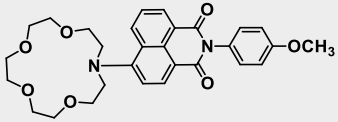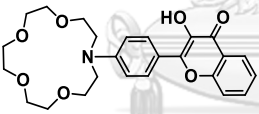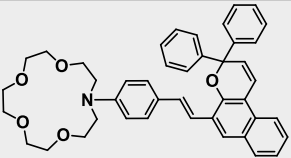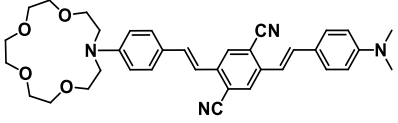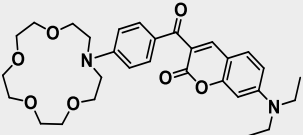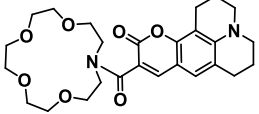
Figure 1.31 (a) The structure of aza crown ethers and thia crown ether (b) The structure of lariat ethers

1.7.1 ICT-based fluorescent sensors from the aza-crown ether

In ICT-based fluorescence probes, the nitrogen of aza-crown ether is normally bonded directly to fluorophore as the same conjugated system. Hypsochromic and bathochromic shifts of the emission bands can occur after complexation, depending on how the metal cation induces the electronic distribution in the molecule. [114] Typical examples of ICT-based fluorescence sensors are shown in **Table 1.8**.

Table 1.8 Typical examples of fluorogenic ICT sensor
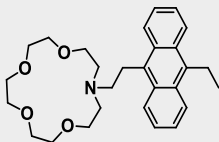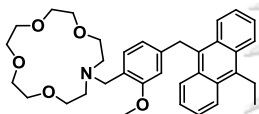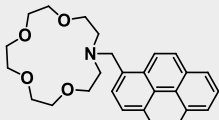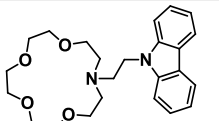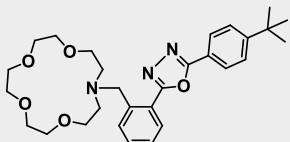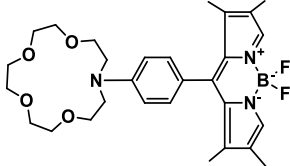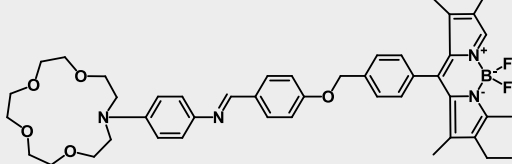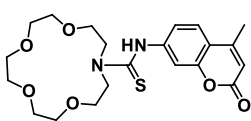
No.	Compound	Analyte	FE[a]	λ_{fl} [nm][b]	Ref.
109		Li^+	-105	337	[115]
110		Li^+	-40	545	[116]
111		Hg^{2+}	-22	515	[117]
112		Ba^{2+}	-44	536	[118]
113		Mg^{2+}	-65	440	[119]
114		Mg^{2+}	+40	665	[120]
115		Pb^{2+}	+15	491	[121]
116		Mg^{2+} Ca^{2+}	+15 +13	498 496	[122]

[a] Blue (–)/red (+) shift of the initial fluorescence. [b] λ_{max} after cation binding.

1.7.2 PET-based fluorescent sensors from the aza-crown ether

If the aza-crown ether moiety and fluorophore are linked by a spacer, chelation will induce fluorescence enhancement. Because PET from nitrogen in aza-crown ether to fluorophore unit causes the fluorescence quenching, chelation with metal ion will restrict the electron transfer from nitrogen atom. Typical examples of PET-based fluorescence sensors are shown in **Table 1.9**.

Table 1.9 Typical examples of fluorogenic PET sensor

No.	Compound	Analyte	FE[a]	Ref.
116		Li^+ Na^+	3	[123]
117		Na^+	8	[124]
118		Ba^{2+}	17	[125]
119		Fe^{3+}	Turn off	[126]
120		Mg^{2+} Zn^{2+}	15 30	[127]
121		Mg^{2+} Ca^{2+} Sr^{2+}	2250 1700 1250	[128]
122		Hg^{2+}	5	[129]
123		Hg^{2+}	29	[130]

[a]FE: Fluorescence enhancement.

In 2017, Schwarze et. al. introduced different aza-15-crown-5 ether derivatives which have the same backbone as anilino-triazole-coumarin to investigate the influences of probe structure towards stabilities of Na^+-complex (**Table 1.10**). [131] The stabilities of Na^+-complex were determined as K_d values in CH_3CN and water. Comparing between **124** and **125**, when the methoxy group is introduced at the ortho position, the K_d in CH_3CN decrease from 867 to 5 µM suggesting that the methoxy groups in the ortho position are involved in the coordination sphere with Na^+. However, **126** and **127** which have a lariat structure as **125** show a lower K_d than **124** as well. Moreover, the influence of fluorophore, diethylaminocoumarin (**125**), two 6-membered rings fused coumarin (**126**), and π-extended coumarin derivatives (**127**) was observed. Apparently, **126** shows to be most stable Na^+-complex with a K_d value of 48 mM in water. This evidence suggests that not only the lariat structure supports the Na^+-complex stability and Na^+ selectivity, but also the fluorophore moiety influences the Na^+-binding properties.

Table 1.10 Some photophysical properties of **124** - **127**

	124	125	126	127
[a]FE in CH_3CN	46.5	2.2	1.5	1.6
FE[a] in H_2O	-	5.0	10.9	2.0
[b]K_d in CH_3CN	867 µM	5 µM	6 µM	7 µM
K_d in H_2O	-	117 mM	48 mM	223 mM

[a] FE: Fluorescence enhancement, [b] K_d: Dissociation constants

Noteworthy, a "Saturn-like" complex is the common form when crown ether encapsulates ions of appropriate size. However, if a metal ion is too large to be bound in a Saturn-like manner by a particular crown ether, it is still possible for complexation to occur to generate ''half-sandwich'' with a single ligand, or ''sandwich'' complexes with two ligands (**Figure 1.32**). [132]
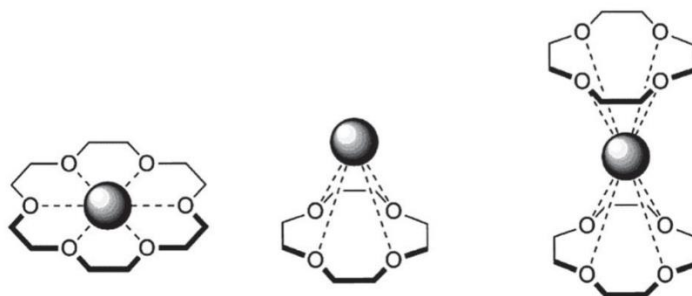
Figure 1.32 Typical modes of complexation of a metal ion to a crown ether. [132]

1.7.3 Objective of this work (Part B)

Herein, we focus on the design of lariat aza crown ether-based fluorescence sensors because nitrogen can be easily further functionalized, and the lariat structure provides greater complex stability. Three target compounds are shown in **Figure 1.33**. Because each crown ether can selectively capture a cation of a specific size, the objective of this plan is to compare the photophysical properties and selectivity of the sensor bearing different cavity sizes of aza crown ether including aza-9-crown-3 (**JB1**), aza-12-crown-4 (**JB2**), and aza-15-crown-5 (**JB3**).
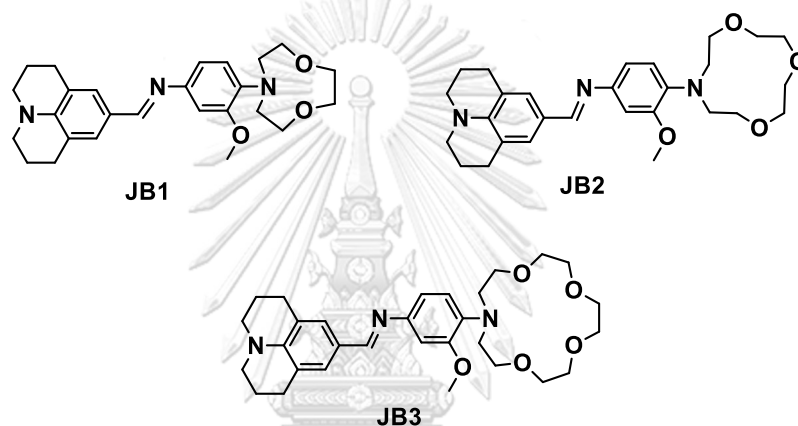
Figure 1.33 Target compound **JB1**, **JB2**, and **JB3**

In addition, the 4 target compounds with different linker between julolidine part and crown ether part were also designed to investigate their sensing ability for metal ion detection.
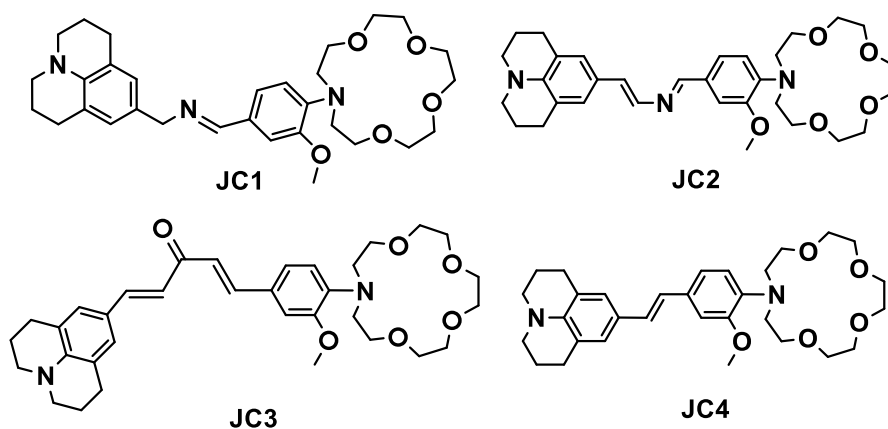
Figure 1.34 Target compound **JC1**, **JC2**, **JC3**, and **JC4**

CHAPTER II

EXPERIMENTAL

2.1   Chemicals and Materials

All reagents and solvents were purchased from commercial companies (Merck, TCI, and Sigma-Aldrich). All column chromatography was operated using silica gel 60 (70-230 mesh) and aluminium oxide 90 active neutral (70-230 mesh). Thin layer chromatography (TLC) was performed on silica gel plates F245. Water used in all spectroscopic experiments was deionized with a Milli-Q reference water purification system to a specific resistivity of 18.2 MΩ.cm.

2.2   Analytical instruments

All ^{1}H and ^{13}C NMR spectra were performed on a JEOL NMR spectrometer operating at 500 MHz for ^{1}H and 125 MHz for ^{13}C. The chemical shifts (δ) and the coupling constants in all NMR spectra were calculated by using MestReNova program. High-resolution mass spectra were obtained from a JEOL AccuTOF^{TM}-DART^{TM}. FTIR spectra were obtained from a Bruker Alpha II FTIR spectrometer with a Diamond Crystal ATR. Melting points were measured on a Stuart analogue melting point apparatus SMP11. Absorption spectra were recorded at room temperature using a UV-2550 UV–vis spectrophotometer (SHIMADZU). Emission spectra were recorded on a Carry Eclipse Fluorescence Spectrophotometer (Agilent Technologies) and EnSight™ multimode plate reader (Perkin Elmer). The pH buffers were measured from an Ohaus pH meter. Inductively coupled plasma-optical emission spectrometer (ICP-OES) (iCAP 6500, Thermo Scientific) was used in the experiment of quantitative analysis for Cu^{2+}.

PART A: Fluorescence chemosensors from hydrazide derivatives of julolidine

2.3 Synthesis and Characterization of JA, JS, and JP

2.3.1 *N'*-((2,3,6,7-tetrahydro-1*H*,5*H*-pyrido[3,2,1-*ij*]quinolin-9-yl)methylene) acetohydrazide (JA)
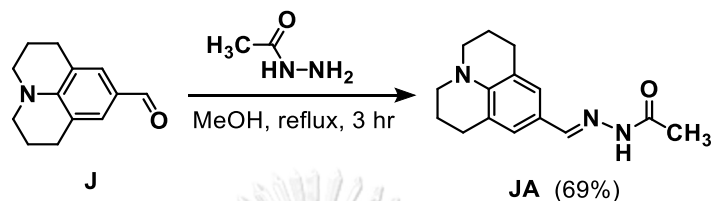
A mixture of acetohydrazide (0.04 g, 0.54 mmol) and julolidine-9-carboxaldehyde (0.1 g, 0.5 mmol) in 2 mL of MeOH was stirred and refluxed at 80 °C for 3 hours until a light-yellow precipitate appeared. The resulting precipitate was filtered and washed several times with hexane and diethyl ether. The white solid product was obtained in 0.11 g (68.8%). Mp. > 200 °C (decomp.). ^{1}H NMR (CDCl$_3$, 500 MHz): δ 9.02 (s, 1H), 7.54 (s, 1H), 7.07 (s, 2H), 3.21 (t, 4H), 2.75 (t, 4H), 2.35 (s, 3H), 1.96 (tt, 4H). ^{13}C NMR (CDCl$_3$, 126 MHz,): δ 173.16, 144.75, 144.68, 126.29, 121.20, 120.42, 50.06, 27.85, 21.82, 20.64. HRMS: m/z calcd. for C$_{15}$H$_{19}$N$_3$O+H$^+$ ([M + H$^+$]), 258.1606; found, 258.1203.

2.3.2 *N'*-((2,3,6,7-tetrahydro-1*H*,5*H*-pyrido[3,2,1-*ij*]quinolin-9-yl)methylene) picolinohydrazide (JP)
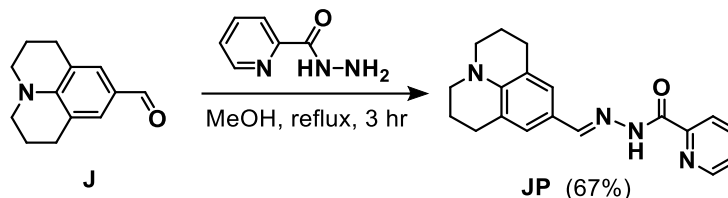
A mixture of julolidine-9-carboxaldehyde (0.1 g, 0.5 mmol) and picolinohydrazide (0.07 g, 0.51 mmol) in MeOH (2 mL) was stirred and refluxed at 80 °C for 3 hours. The bright yellow precipitate was filtered by suction and rinsed with diethyl ether and hexane. The yellow solid product was obtained in 0.12 g (66.7%). Mp. > 170 °C (decomp.). ^{1}H NMR (DMSO, 500 MHz): δ 11.76 (s), 8.68 (m, 1H), 8.34 (s, 1H), 8.09 (m, 1H), 8.03 (td, 1H), 7.63 (m, 1H), 7.06 (s, 2H), 3.19 (t, 4H), 2.70 (t, 4H), 1.87 (tt, 4H). ^{13}C NMR (DMSO, 126 MHz): δ 159.67, 150.03, 149.95, 148.39, 144.37, 137.95, 126.69, 126.13, 122.44, 120.53, 120.45, 49.20, 27.09, 21.18. HRMS: m/z calcd. for $C_{19}H_{20}N_4O+H^+$ ([M + H$^+$]), 321.1715; found, 321.1754.

2.3.3 2-hydroxy-N'-((2,3,6,7-tetrahydro-1H,5H-pyrido[3,2,1-ij]quinolin-9-yl)methylene)benzo-hydrazide (JS)
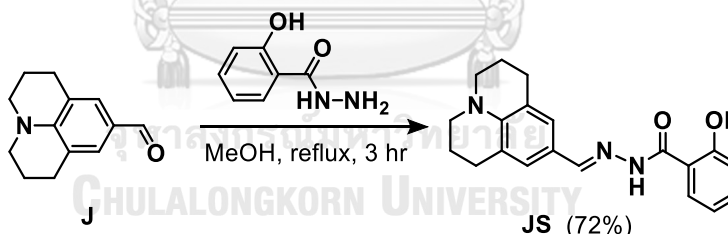
A mixture of salicylohydrazide (0.08 g, 0.53 mmol) and julolidine-9-carboxaldehyde (0.1 g, 0.5 mmol) in MeOH (2 mL) was stirred and refluxed at 80 °C for 3 hours. The yellow product was collected by filtration and washed with diethyl ether and hexane. The yellow solid product was obtained in 0.13 g (72.2%). Mp. > 140 °C (decomp.). ^{1}H NMR (DMSO, 500 MHz): δ 8.18 (s, 1H), 7.90 (d, 1H), 7.41 (t, 1H), 7.09 (s, 2H), 6.93 (m, 2H), 3.18 (t, 4H), 2.69 (t, 4H), 1.86 (tt, 4H). ^{13}C NMR (DMSO, 126 MHz): δ 165.00, 160.17, 150.38, 145.01, 134.11, 128.58, 126.73, 121.05, 120.63, 119.16, 117.87, 116.03, 49.72, 27.62, 21.68. HRMS: m/z calcd. for $C_{20}H_{21}N_3O_2+H^+$ ([M + H$^+$]), 336.1712; found, 336.1738.

2.4   Photophysical property study of JA, JP, and JS

2.4.1   Preparation of the stock solutions and experimental condition

JA, JP, and JS were prepared as stock solutions in DMSO of 1.0 mM. The stock solutions were pipetted and diluted with DMSO to the desired concentration before the spectroscopic measurement. The absorption, excitation, and emission spectra were recorded at ambient temperature.

2.4.2   Molar absorptivity (ε) calculation

The molar absorptivity (ε) is defined as the ratio of absorbance to the molar concentration of a solution which can be represented in the following equation:

$$\varepsilon = \frac{A}{bc}$$

Where: A = absorbance

b = path length of the beam in the sample

c = concentration of the solution

Since the absorbance is directly proportional to the concentration of the solution, molar absorptivity can be calculated by measuring the absorbance (at a maximum absorption wavelength) through varying concentrations of solution (three to five concentrations of one solution) and plotting the concentration versus the absorbance on a graph. The slope of the graph is used to estimate molar absorptivity.

2.4.3   Quantum calculation method

The quantum calculations were performed using Gaussian 16. [133] Avogadro was used for molecular orbital visualization. [134] All the calculation was done in def2-SVP/M062X level of theory with SMD solvation model. [135] All the structure was optimized with free bond rotations, and the resulting structures were validated by checking positive vibrational frequencies. All the conformers were compared to find the most stable conformer and would be used to calculate in TD-DFT. The molecular visualization was done using Avogadro software. This calculation is an approximation from M062X functional. The functional and solvation model could be benchmarked for better correlation.

2.4.4 Fluorescence quantum yield ($\boldsymbol{\phi}_{fl}$) calculation

The fluorescence quantum yield ($\boldsymbol{\phi}_{fl}$) is defined as the ratio of photons absorbed to photons emitted through fluorescence. The $\boldsymbol{\phi}_{fl}$ can be measured using two methods: the absolute method and the relative method. Here, the $\boldsymbol{\phi}_{fl}$ of target compounds is calculated by the relative method. In the calculation, it is possible to estimate that $\boldsymbol{\phi}_{fl}$ refers to the ratio of integrated fluorescence intensities (I) to absorbance (A) at the same concentration of solution when integrated fluorescence intensities can be observed from the area of the emission band. The ratio I/A can be abbreviated as m. Therefore, providing the experimental conditions remain the same, the ratio of m value of the two solutions can be related to the ratio of the $\boldsymbol{\phi}_{fl}$ values. The m_R from the standard reference and m_S form the sample are further calculated using the following equation:

$$\frac{\phi_S}{\phi_R} = \left(\frac{m_S}{m_R}\right)\left(\frac{n_S}{n_R}\right)^2$$

Where:

m = Gradient of the plot of integrated fluorescence intensity against absorbance

n = Refractive index of the solvent

Subscripts 'S' and 'R' refer to the sample and reference, respectively.

However, the m value is not measured from one concentration but over a range of absorbances at the excitation wavelength. The finding of m value from the slope on a graph of the emission band area against the absorbance at several fluorophore concentrations enhances the accuracy of the calculation. In this work, quinine sulfate was used as a reference standard with known $\boldsymbol{\phi}_{fl}$ values of 0.52 in 0.05 M H_2SO_4 solution [136] because its optical properties closely match the sample. Noteworthy, a suitable sample concentration must be prepared since quantum yield measurements require the solution's absorbance to be less than 0.1 at the absorption maxima. By keeping the absorbance below 0.1, non-linear effects from inner filter (re-absorption) effects are reduced to a minimum, which prevents the resulting quantum yield from being unreliable.

2.4.5 Effect of solvent on excitation and emission spectra

The 16 solvents which have different polarity were used to investigate the influence on excitation and fluorescence spectra of target compounds including toluene, hexane, acetone, tetrahydrofuran, diethyl ether, acetonitrile, chloroform, dichloromethane, dimethyl carbonate, methanol, ethanol, 2-propanol, ethylene glycol, dimethyl formamide, dimethylacetamide, and ethyl acetate. The stock solutions in DMSO were pipetted and diluted with each solvent to the concentration of 10 μM.

2.4.6 Effect of water on emission spectra

DMSO was chosen as the primary solvent, and the water content was gradually adjusted in 10% v/v increments up to 100% v/v. To achieve the desired final concentration of the probe, 10 μL of probe stock solution was pipetted into a cuvette and diluted with water and DMSO to the desired proportions in the final volume of 1 mL.
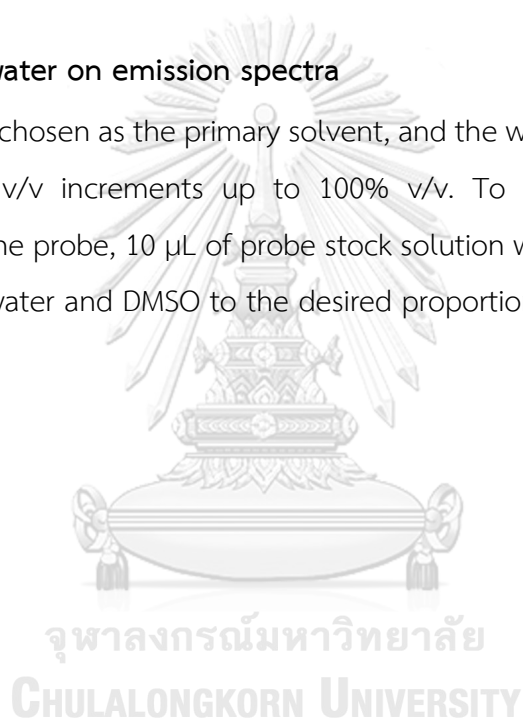
2.5   Metal ion selectivity

2.5.1   Preparation of the metal ion stock solutions

The stock solutions of metal ions were prepared in Milli-Q water to a concentration of 10 mM using the following commercially available salts: $LiNO_3$, $NaNO_3$, KNO_3, $CsNO_3$, $Mg(NO_3)_2$, $Ca(NO_3)_2$, $SrCl_2$, $Ba(NO_3)_3$, $Al(NO_3)_3$, $Ga(NO_3)_3$, $Pb(NO_3)_2$, $Cr(NO_3)_3$ $Mn(OAc)_2$, $Fe(OAc)_2$, $Fe(OAc)_3$, $Co(NO_3)_2$, $Ni(NO_3)_2$, $Cu(NO_3)_2$, $Zn(NO_3)_2$, $Cd(NO_3)_2$, $Hg(OAc)_2$, and $AgNO_3$.

2.5.2   Screening Test

The three julolidine derivatives were freshly prepared as a solution in DMSO with a concentration of 20 µM for diluting metal ions. The experiment was conducted by pipetting the 20 µL of each metal ion stock solution into different vials and followed by adding the 500 µL of the probe solution. The stoichiometric ratio of the probe with metal ions was 1/10. The screening of the emission signal was followed under blacklight (365 nm). After that, 500 µL of Milli-Q water was added to each mixture to produce 50% v/v DMSO/water media and the fluorescence signals of all solutions were observed again. Moreover, other common solvents were also used instead of DMSO to observe the change in fluorescence signal.

2.5.3   Condition optimization: aqueous buffer content

The microplate technique was used to measure the fluorescence signal in this study. The experiments were conducted by adding 2 µL of the probe's stock solution (1 mM) into the well and followed by adjusting the volume of the solution with the aqueous buffer and DMSO. The proportions of aqueous buffer in DMSO in this study were 10% v/v increments up to 100% v/v. In each well, the concentration of the probe was fixed at 10 µM in the final volume of 200 µL. The fluorescence signal of each proportion was measured repeatedly and averaged from 8 wells. After the above-mentioned measurements has been completed, the plate was removed from the instrument. Then, the exact volume of $Cu(NO_3)_2$ stock solution was added to the same plate to measure the fluorescence signal again. The final equivalents of Cu^{2+} were calculated to be 10 in the experiments of **JA** and **JS**, and 5 in the experiment of **JP**.

2.5.4 Condition optimization: pH effect

The buffer solutions were prepared at 100 mM using the following chemicals: pH 3-5 from acetic acid/sodium acetate and pH 6-8 from HEPES and NaOH. The experimental method was carried out in the same way as the water effect experiment which includes the condition with and without Cu^{2+}, but the solution was adjusted volume by a 1:1 v/v mixture of aqueous buffer at various pHs and DMSO instead.

2.5.5 Selectivity study at the optimized condition

The 10 µM of each probe solution were prepared in 50% v/v DMSO/HEPES buffer solution (**JA** and **JP** = pH 7.0, **JS** = pH 8.0). The prepared probes solution was divided into two portions. One portion was carried out with a fluorescence spectrophotometer to collect the emission spectra, whereas another portion was measured with a microplate reader to find the average intensity. Since the final volume adjusted in the cuvette was 1000 µL and the maximum volume that can be contained in a well is not more than 250 µL, the volume of each pipetted solution was calculated to be reduced by about 5 times for the experiment on the microplate.

I.   Fluorescence spectrophotometer method

The 10 µL of each metal ion stock solution was pipetted into a quartz cuvette, followed by placing the 1000 µL of the prepared probes solution (10 µM) and repeated with other metal ions.

II.   Microplate method

The 2 µL of each metal stock solution was pipetted in each well on the microplate and followed by placing the 200 µL of probes solution. The fluorescence signal of each metal ion solution was measured repeatedly and averaged from 4 wells. A total of 23 metal ions were measured simultaneously on the same plate. The samples on a plate were set to be measured repeatedly 3-5 times every 10 minutes until the emission signals in all wells were stable.

2.5.6 Interference study

Under the same measurement conditions for the experiment of metal ion selectivity, the competitive signaling behavior of probes toward Cu^{2+} in the presence of the coexistence of metal ions as the background was studied. The only two julolidine derivatives, **JS** and **JP**, were prepared as the solution of 10 µM in 30 mL of 50% v/v DMSO/HEPES buffer solution (pH 7.0: **JP** and pH 8.0: **JS**). The 2 µL of each stock solution, including $Cu(NO_3)_2$ and competing metal ions, were pipetted and mixed in each well before adding the 200 µL of the probe solution.

2.6 Sensitivity study for Cu^{2+} detection

2.6.1 Fluorescence titration

Fluorescence emissions of **JP** and **JS** with different concentrations of Cu^{2+} were investigated. According to the selectivity study, a fluorescence spectrophotometer and a microplate reader were used to collect the emission spectra and find the average intensity, respectively.

I. Fluorescence spectrophotometer method

The stock solution of $Cu(NO_3)_2$ was freshly prepared in Milli-Q water with a concentration of 1 mM. Meanwhile, the **JP** and **JS** were also freshly prepared as a stock solution in DMSO with a concentration of 20 µM.

The titrated solutions were prepared in 21 vials by pipetting the stock solution of $Cu(NO_3)_2$ in 1 µL increment from 0 – 20 µL and followed by adjusting the volume of all solutions to 20 µL with Milli-Q water. Then, HEPES buffer solution (**JA** and **JP** = pH 7.0, **JS** = pH 8.0) was added to make the volume of the titrated solution to be 500 µL. Finally, 500 µL of the probe stock solution was placed in the vial to give the volume of the titrated solution to 1,000 µL.

At the final condition, the concentration of probe solution was fixed at 10 µM and the range of concentrations of Cu^{2+} ion was 0 - 20 µM in 50% DMSO/HEPES buffer. All titrated solutions in vials were left for about 30 minutes to allow the solution to come to equilibrium.

II.   Microplate method

The stock solution of Cu(NO$_3$)$_2$ was freshly prepared in Milli-Q water with a concentration of 200 µM. Meanwhile, the stock solutions of **JS** and **JP** were also freshly prepared in DMSO at a concentration of 20 µM.

The titrated solutions were prepared in the well by pipetting the stock solution of Cu(NO$_3$)$_2$ in 1 µL increment from 0 – 20 µL and followed by adjusting the volume of all solutions to be 20 µL with Milli-Q water. Then, HEPES buffer solution was added to adjust the volume of the titrated solution to 100 µL. Finally, 100 µL of the probe stock solution was added to the well to give the final volume of the titrated solution to be 200 µL.

At the final condition, the concentration of probe solution was fixed at 10 µM and the range of concentrations of Cu^{2+} ion was 0 - 20 µM in 50% DMSO/HEPES buffer. The fluorescence signal of each concentration of Cu^{2+} was measured repeatedly and averaged from 5 wells. All concentrations of Cu^{2+} in the tested range were measured simultaneously in the same plate.

2.6.2 Time dependent

According to fluorescence titration on microplate experiment, fluorescence emissions of **JS** and **JP** at different concentrations were investigated every 10 minutes after the addition of Cu^{2+} until the emission signals in all wells were stable (90 minutes).

2.6.3 Detection limit

Detection limits of **JS** and **JP** to Cu^{2+} were obtained from the fluorescence titration experiment using the following equation:

$$\text{Detection limit} = \frac{3SD}{\text{slope}}$$

Where SD is the standard deviation of 10 blank solutions of each sensor before the addition of the metal ions and the slope is from the fluorescence titration experiment in the linear range.

2.7 Studied of sensing mechanism of JP with Cu^{2+}

2.7.1 UV-Vis titration

UV-Vis titration was performed in the same cuvette of the fluorescence titration experiment as mentioned before to find the change of species in the solution when the Cu^{2+} was added into **JP**.

2.7.2 Reversibility of JP+Cu^{2+} by EDTA addition

The EDTA stock solution was prepared and used to investigate the nature of the reversible reaction of **JP** with Cu^{2+}. The reaction was carried out in 50% DMSO/HEPES solution pH 7.0 with the final concentration of **JP** and **Cu^{2+}** to be 10 μM and 15 μM, respectively. Then, the EDTA stock solution was pipetted into **JP**+Cu^{2+} solutions with a final concentration of 100 μM. The solution before and after the addition of EDTA was analyzed by UV-Vis and fluorescence spectrophotometer.

2.7.3 TLC analysis

TLC analysis was carried out to observe the product from the reaction of **JP** with Cu^{2+} and to confirm the reversibility of the **JP**+Cu^{2+} complex. The five solutions including 1) **JP**, 2) **JP**+Cu^{2+}, 3) **JP**+Cu^{2+}+EDTA, 4) free julolidine-9-carboxaldehyde (**J**), and 5) free picolinohydrazide (**P**) were spotted on the plate, and investigated the rate of flow. The ethyl acetate/hexane (3:1 v/v) were used as mobile phases.

2.7.4 ^{1}H NMR experiment

The mixture of **JP** (10 μM) and Cu^{2+} (20 μM) was stirred for 1 hour in the 20 mL of 50% DMSO/aqueous HEPES pH 7 solution at room temperature. After that, the mixture was extracted with ethyl acetate. The ethyl acetate layer was separated and evaporated to dryness. Then, DMSO-d6 was added to dissolve the residue for a further ^{1}H NMR experiment.

2.7.5 Mass spectrometry analysis

The mixture of **JP+**Cu^{2+} was prepared with the same procedure as the selectivity study. The prepared solution **JP**+Cu^{2+} must be extracted with a small amount of ethyl acetate before measurement.

2.8   Studied of sensing mechanism of JS with Cu^{2+}

2.8.1   Temperature-dependent quenching of the fluorescence signal

The difference between static and dynamic quenching is determined by their temperature dependency. The experiment was performed as the fluorescence titration of **JS** with Cu^{2+} at two different temperatures, $25^{\circ}C$, and $50^{\circ}C$. The I_0/I is considered to be linearly dependent on the concentration of Cu^{2+}. The results were shown as the graph of I_0/I versus $[Cu^{2+}]$ in the range of Cu^{2+} concentration between $0 - 5$ µM. The slopes of the two lines were compared and interpreted.

2.8.2   Fluorescence quenching constants of JS

In the case of **JS**, the fluorescence quenching efficiencies and the sensitivity of the sensor can be quantified using the Stern-Volmer equation as shown in the following equation:

$$\frac{I_0}{I} = 1 + K_{sv}[Q]$$

Where:

I_0 =   the fluorescence intensity of the free ligand **JS**,

I =   the fluorescence intensity of the **JS**-Cu^{2+} complex

Q = $[Cu^{2+}]$

K_{sv} =   Stern-Volmer constant

According to the result from the fluorescence titration experiment of **JS** with Cu^{2+}, when the reciprocal of I_0/I was plotted as a function of the $[Q]$ concentration, a linear relationship was obtained, ($y = A + Bx$), $y = I_0/I$, $A = 1$, $x = [Q]$, and K_{sv} was calculated from B.

2.8.3   UV-Vis titration

UV-Vis titration was performed in the same cuvette of the fluorescence titration experiment to find the change of species in the solution when the Cu^{2+} was added into **JS**.

2.8.4 TLC analysis

TLC analysis was carried out to detect the **JS**+Cu^{2+} complex and to confirm the reversibility of **JS**+Cu^{2+} by EDTA. The three solutions including 1) free **JS**, 2) **JS**+Cu^{2+}, and 3) **JS**+Cu^{2+}+EDTA were spotted on the plate and investigated the rate of flow. The CHCl$_3$/hexane (3:1 v/v) was used as the mobile phase.

2.8.5 ^{1}H NMR experiment

The Cu(NO$_3$)$_2$ was dissolved in DMSO-d6 to prepare a Cu^{2+} stock solution. At the same time, **JS** was dissolved in DMSO-d6 and placed in two NMR tubes. One is without Cu^{2+} and the other is with 1 equivalent of Cu^{2+}.

2.8.6 Mass spectrometry analysis

The small-volume solution of **JS**+Cu^{2+} was prepared with the same procedure as the selectivity study. The prepared solution could be measured directly.

2.8.7 IR Spectroscopy

The precipitate of **JS**+Cu^{2+} can be observed when the excess aqueous Cu(NO$_3$)$_2$ solution was dropped into the solution of **JS** in acetonitrile. The precipitate **JS**+Cu^{2+} was filtered and evaporated to dryness. The pure solid **JS** and precipitate **JS**+Cu^{2+} were measured to compare the change of transmittance pattern.

2.8.8 Job's plot

The fluorescence emissions of 10 solutions that have [**JS**] + [Cu^{2+}] at 20 μM were studied. The mole fraction (χ) of the sensors that were used in this experiment was 0.1, 0.2, 0.3, 0.4, 0.5, 0.6, 0.7, 0.8, 0.9, and 1.0. The data were plotted between χ_{JS} and $(\Delta I)(\chi_{JS})$ to determine a stoichiometry of **JS**+Cu^{2+} complex. This experiment was carried out by a microplate reader and the fluorescence intensity (I) of each mole faction was measured repeatedly and averaged from 5 wells.

2.9 Reversibility of JS+Cu^{2+} study

2.9.1 Preparation of the amino acid stock solutions and JS+Cu^{2+} solution

The 21 amino acids including alanine, arginine, aspartic, cystine, cysteine, glutamic, glutamine, glycine, histidine, isoleucine, leucine, lysine, methionine, phenylalanine, proline, serine, trans proline, tryptophan, tyrosine, threonine, and valine were prepared as a stock solution in Milli-Q water with the concentration of 2 mM. The **JS**+Cu^{2+} solution was prepared in 50% DMSO/HEPES buffer pH 8.0 with the concentration of **JP** and Cu^{2+} to be 10 μM and 10 μM, respectively.

2.9.2 Screening Test

The 1 mL of **JS**+Cu^{2+} solutions were pipetted repeatedly into 22 small vials (2 mL) according to the number of amino acids and a control solution (only **JS**+Cu^{2+} in the solution). After that, the stock solutions of each amino acid were pipette into each vial to a final concentration of 50 μM. The screening of the emission signal was followed under blacklight (365 nm).

2.9.3 Selectivity study

The microplate technique was used to measure the fluorescence signal in this study. The 5 μL of each amino acid stock solution was pipetted into each well on the microplate and followed by the addition of 200 μL of **JS**+Cu^{2+} solution.

In this condition, the final volume was fixed at 205 μL and the concentration of amino acid was calculated to be 5 times greater than **JS**+Cu^{2+}. Each amino acid was repeated in 4 wells to calculate the average value of fluorescence intensity.

2.9.4 Interference study

The microplate technique was used to measure the fluorescence signal in this study. The 5 μL of histidine and each amino acid stock solution were pipetted and mixed into each well. Then, the 200 μL of **JS**+Cu^{2+} solution was added.

In this condition, the final volume was fixed at 210 μL and the concentration of amino acid was calculated to be 5 times greater than **JS**+Cu^{2+}. Each amino acid was repeated in 4 well to calculate the average value of fluorescence intensity.

2.9.5   Histidine titration

The microplate technique was used to measure the fluorescence signal in this study. The stock solution of $JS+Cu^{2+}$ was freshly prepared with the concentration of both JS and Cu^{2+} to be 11 µM in 50% DMSO/HEPES buffer pH 8.0.

The histidine stock solution was pipetted into each well in 1 µL increments from 0 µL to 20 µL and followed by adjusting with Milli Q water to give the final volume of solution in each well to be equal (20 µL). Finally, 200 µL of $JS+Cu^{2+}$ solution was added to each well.

In this condition, the final volume was fixed at 220 µL and the final concentration of both JS and Cu^{2+} was 10 µM. The concentration of histidine in the titrated solution was in the range of 0 µM to 200 µM. Each concentration was repeated in 4 wells to calculate the average value of fluorescence intensity. Fluorescence signals were investigated every 10 minutes after the addition of $JS+Cu^{2+}$ solution until the emission signals in all wells were stable.

2.9.6   EDTA titration

The experiment was conducted as the histidine titration experiment, but EDTA was used to titrate instead of histidine. In this experiment, EDTA was prepared as a stock solution in Milli-Q water with a concentration of 2 mM.

2.9.7   Application of JP for detecting Cu^{2+} in the real water sample

The experiment was carried out on the microplate. In each well, the 5 µL of real water sample was pipetted down and followed by spiking with the exact volume of $Cu(NO_3)_2$ stock solution. Then, 200 µL of 10 µM JP in 50% DMSO/aqueous HEPES pH 7 was added to the mixture. The final concentration of Cu^{2+} was determined to be 4 µM and 8 µM and each concentration was repeated from four wells. The percent recovery of Cu^{2+} in real water samples, including canal water, pond water, rainwater, and drinking water, was calculated by comparing with the fluorescence intensity which was measured from the control solution (The 5 µL of Milli Q water was used instead). Moreover, ICP-OES technique was used to confirm the accuracy and precision from the fluorescence measurement by JP.

PART B: Fluorescence chemosensors from crown ether derivatives of julolidine

2.10   Synthesis and characterization of JB1, JB2, and JB3.

According to the synthetic plan, three final target compounds **JB1**, **JB2**, and **JB3** could not be synthesized as expected. Therefore, the information in this section shows only the obtained product in the synthetic pathway.

2.10.1 Triethylene glycol di(*p*-toluenesulfonate)
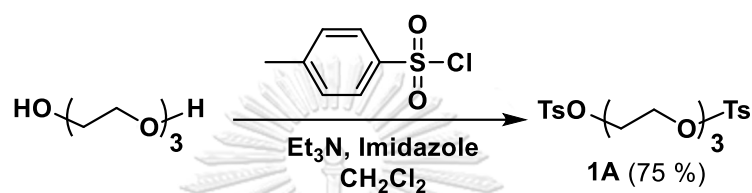
The *p*-toluenesulfonyl chloride (53.4 g, 280 mmol) was added slowly into the mixture of imidazole (76 mg, 1.12 mmol), triethylamine (41 mL) and CH_2Cl_2 (70 mL) which was cooled at 0 °C with an ice bath. After the mixture was stirred until *p*-toluenesulfonyl chloride was completely dissolved, triethylene glycol (15 mL, 112 mmol) was added dropwise. The reaction mixture was stirred at 0 °C for 3 hours and left at room temperature for 1 day. The crude was added water (20 mL) and poured into a separating funnel for extraction. The CH_2Cl_2 layer was separated and dried with Na_2SO_4. A rotatory evaporator was used to concentrate the crude solution before the purification by column chromatography technique. The 2:1 v/v hexane/EtOAc was used as a mobile phase and silica gel was used as a stationary phase. The white solid product **1A** was obtained in 38.6 g (75 %). The spectroscopic data match with the reported in the literature. [137]

2.10.2 Tetrathylene glycol di(*p*-toluenesulfonate)
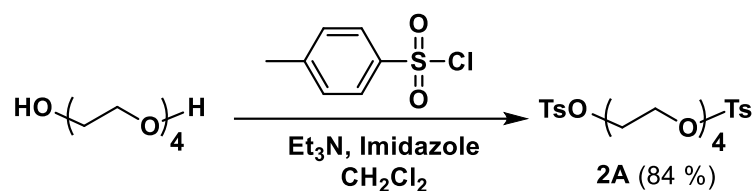
The *p*-toluenesulfonyl chloride (14.7 g, 77.1 mmol) was added slowly into the mixture of imidazole (40 mg, 0.59 mmol), triethylamine (24 mL), and CH_2Cl_2 (20 mL) which was cooled at 0 °C with an ice bath. After the mixture was stirred until *p*-toluenesulfonyl chloride was completely dissolved, tetraethylene glycol (5 mL, 29.1 mmol) was added dropwise. The reaction mixture was stirred at 0 °C for 3 hours and left at room temperature for 1 day. The crude was added water (20 mL) and poured into a separating funnel for extraction. The CH_2Cl_2 layer was separated and dried with Na_2SO_4. A rotatory evaporator was used to concentrate the crude solution before the purification by column chromatography technique. The 2:3 v/v hexane/EtOAc was used as a mobile phase and silica gel was used as a stationary phase. The viscous colorless liquid of **2A** was obtained in 12.2 g (84 %). The spectroscopic data match with the reported in the literature. [137]

2.10.3 Pentaethylene glycol di(*p*-toluenesulfonate)
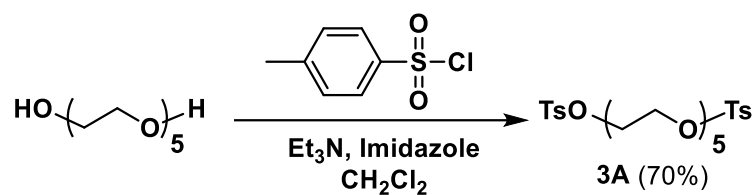
The *p*-toluenesulfonyl chloride (13.5 g, 71.1 mmol) was added slowly into the mixture of imidazole (40 mg, 0.59 mmol), triethylamine (16.5 mL) and CH_2Cl_2 (16 mL) which was cooled at 0 °C with an ice bath. After the mixture was stirred until *p*-toluenesulfonyl chloride was completely dissolved, pentaethylene glycol (5 mL, 23.7 mmol) was added dropwise. The reaction mixture was stirred at 0 °C for 3 hours and left at room temperature for 1 day. The crude was added water (20 mL) and poured into a separating funnel for extraction. The CH_2Cl_2 layer was separated and dried with Na_2SO_4. A rotatory evaporator was used to concentrate the crude solution before the purification by column chromatography technique. The 1:1 v/v hexane/EtOAc was used as a mobile phase and silica gel was used as a stationary phase. The light-yellow liquid product was obtained in 9 g (70%). The spectroscopic data match with the reported in the literature. [137]

2.10.4 *N*-(2-methoxyphenyl)acetamide

1B (92 %)
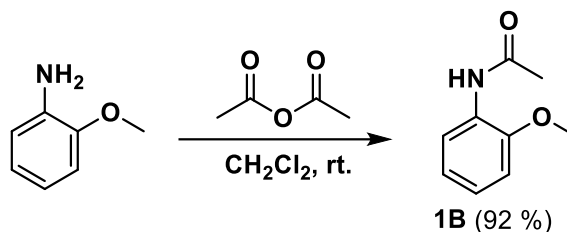
The *o*-anisidine (20 mL, 177 mmol) was added to dry CH_2Cl_2 (20 mL) in a round-bottom flask that was fitted with a rubber septum via a syringe. Then, acetic anhydride (30 mL, 317 mmol) was added dropwise to the above mixture. The reaction mixture was stirred at room temperature and monitored by TLC. The crude was washed with a saturated solution of $NaHCO_3$ after the reaction was complete. The CH_2Cl_2 layer was separated and dried with Na_2SO_4. A rotatory evaporator was used to concentrate the crude solution before the purification by column chromatography technique. The 1:2 v/v hexane/EtOAc was used as a mobile phase and silica gel was used as a stationary phase. The white solid product was obtained in 17.9 g (92 %). The spectroscopic data match the reported in the literature. [138]

2.10.5 *N*-(2-methoxy-4-nitrophenyl)acetamide

2B (83 %)
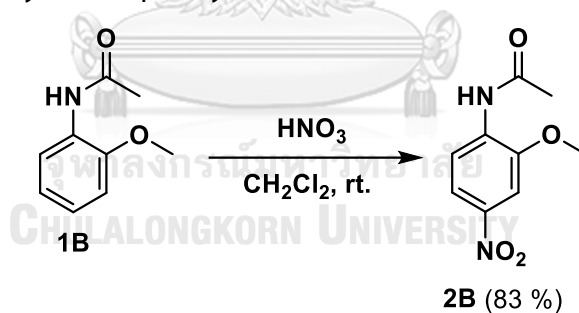
The solution of **1B** (400 mg, 2.14 mmol) in CH_2Cl_2 (1 mL) was added dropwise into the 65% HNO_3 (3 mL) in a round-bottom flask. The reaction mixture was stirred at room temperature for 3 hr. The crude was washed with a saturated solution of $NaHCO_3$. The CH_2Cl_2 layer was separated and dried with Na_2SO_4. A rotatory evaporator was used to concentrate the crude solution before the purification by column chromatography technique. The 3:1 v/v hexane/EtOAc was used as a mobile phase and silica gel was used as a stationary phase. The light-yellow solid product **2B** was obtained in 373 mg (83 %). The spectroscopic data match the reported in the literature. [139]

2.10.6 2-methoxy-4-nitroaniline

2B   **3B** (75 %)
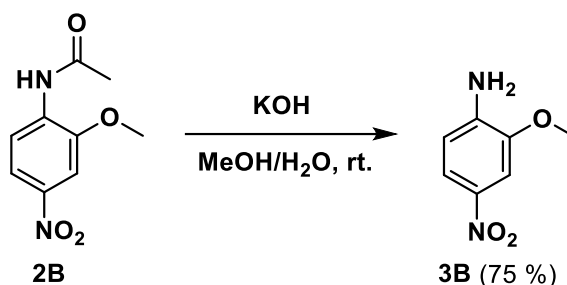
A mixture of **2B** (350 mg, 1.67 mmol) and KOH (280 mg, 5 mmol) in 10 mL of 50% MeOH/H_2O was stirred at room temperature for 1 day. The crude was evaporated under reduced pressure to remove MeOH. The mixture was extracted with ethyl acetate and dried with Na_2SO_4. After evaporation, the mixture was purified by the column chromatography technique. The 2:1 v/v hexane/EtOAc was used as a mobile phase and silica gel was used as a stationary phase. The yellow solid of **3B** was obtained in 210 mg (75 %). The spectroscopic data match the reported in the literature. [140]

2.10.7 2,2'-((2-methoxy-4-nitrophenyl)azanediyl)bis(ethan-1-ol)

3B   **4B** (43 %)
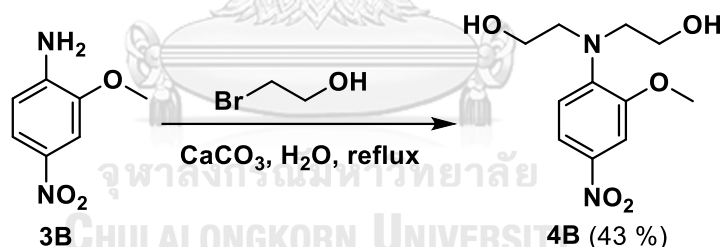
A mixture of **3B** (506 mg, 3 mmol), calcium carbonate (722 mg, 6 mmol), and 2-bromoethanol (2.14 mL, 30 mmol) in 1 mL of H_2O was stirred and refluxed at 110 ^{o}C for 1 day. The mixture was extracted with ethyl acetate and dried with Na_2SO_4. After evaporation, the mixture was purified by the column chromatography technique. The 1:2 v/v hexane/EtOAc was used as a mobile phase and silica gel was used as a stationary phase. The yellow oil of **4B** was obtained in 330 mg (43 %). The spectroscopic data match the reported in the literature. [141]

2.10.8 13-(2-methoxy-4-nitrophenyl)-1,4,7,10-tetraoxa-13-azacyclopentadecane
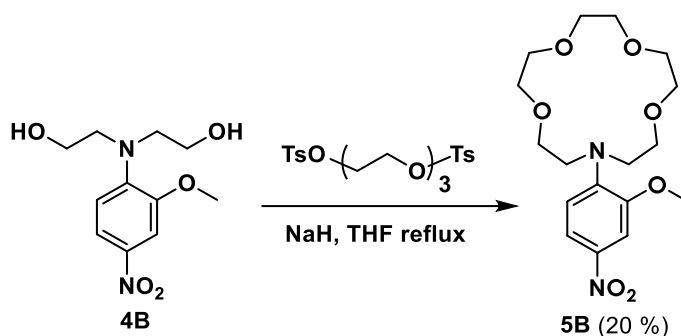
Under a nitrogen atmosphere, 60% NaH in mineral oil (0.32 g, 8 mmol) was added into dry THF (400 mL) in the three-neck flask and the mixture was heated to reflux at 70 °C. Then, a solution of **4B** (100 mg, 0.4 mmol) and **1A** (0.18 g, 0.4 mmol) in 20 mL of THF was slowly added dropwise into the reaction mixture. The reaction mixture was stirred and refluxed at 70 °C for 1 day. The distilled water was slowly added dropwise into the reaction mixture to remove the excess NaH. The crude was evaporated under reduced pressure to remove THF. The mixture was extracted with ethyl acetate and dried with Na_2SO_4. After evaporation, the mixture was purified by the column chromatography technique. The CH_2Cl_2 was used as a mobile phase and alumina was used as a stationary phase. The light-yellow oil of **5B** was obtained in 30 mg (20 %). The spectroscopic data match the reported in the literature. [141]

2.10.9 2,2'-((2-methoxyphenyl)azanediyl)bis(ethan-1-ol)
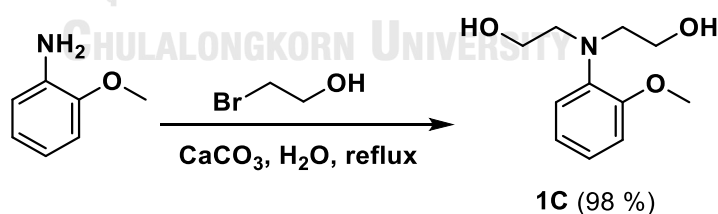
A mixture of *o*-anisidine (0.67 mL, 6 mmol), calcium carbonate (1.54 g, 15.4 mmol), and 2-bromoethanol (1 mL, 14 mmol) in 1 mL of H_2O was stirred and refluxed at 110 °C for 1 day. The mixture was extracted with ethyl acetate and dried with Na_2SO_4. After evaporation, the mixture was purified by the column chromatography technique. The 1:1 v/v hexane/EtOAc was used as a mobile phase and silica gel was used as a stationary phase. The brown oil of **1C** was obtained in 1.24 g (98 %). The spectroscopic data match the reported in the literature. [142]

2.10.10 13-(2-methoxyphenyl)-1,4,7,10-tetraoxa-13-azacyclopentadecane
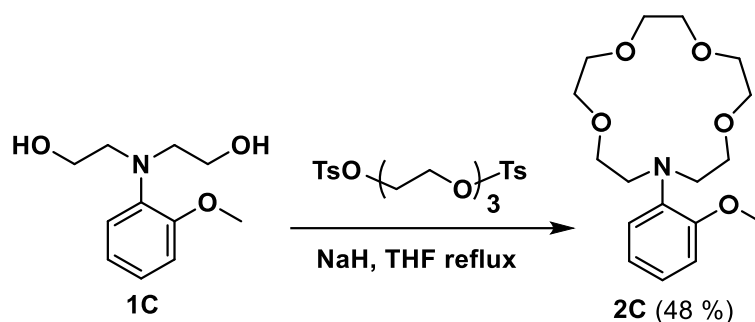
Under a nitrogen atmosphere, 60% NaH in mineral oil (0.48 g, 12 mmol) was added into dry THF (250 mL) in the three-neck flask and the mixture was heated and stirred to reflux at 70 °C. Then, a solution of **1C** (180 mg, 0.8 mmol) and **1A** (370 mg, 0.8 mmol) in 100 mL of THF was slowly added dropwise into the reaction mixture. After 1 day, the distilled water was slowly added dropwise into the reaction mixture to remove the excess NaH. The crude was evaporated under reduced pressure to remove THF. The mixture was extracted with ethyl acetate and dried with Na_2SO_4. After evaporation, the mixture was purified by the column chromatography technique. The 5% MeOH in CH_2Cl_2 was used as a mobile phase and alumina was used as a stationary phase. The pale-yellow oil of **5B** was obtained in 125 mg (48 %). The spectroscopic data match the reported in the literature. [142]

2.10.11 4-(1,4,7,10-tetraoxa-13-azacyclopentadecan-13-yl)-3-methoxy

benzaldehyde

2C

$POCl_3$

DMF

3C (78 %)
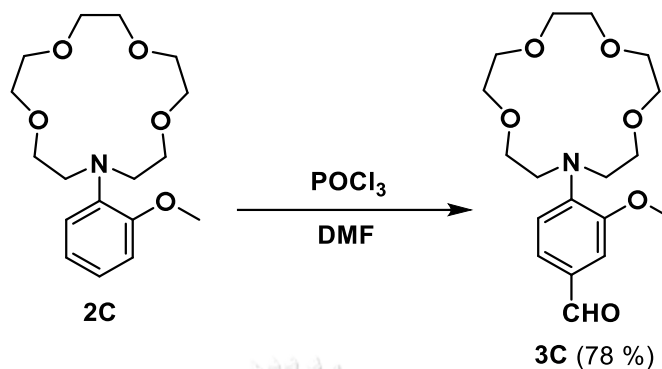
Compound **2C** (325 mg, 1 mmol) was dissolved in DMF (1.55 mL, 20 mmol) in a three-neck flask and cooled to 0 °C in the ice bath. $POCl_3$ (0.93 mL, 10 mmol) was added dropwise via a syringe. After stirring at room temperature for 16 h, the solution was heated to 60 °C for 1 hour and poured into 20 mL of cooled water. The solution was extracted with ethyl acetate, and the organic layer was dried with Na_2SO_4. After evaporation, the mixture was purified by the column chromatography technique. The ethyl acetate was used as a mobile phase and alumina was used as a stationary phase. The light-yellow oil of **2C** was obtained in 276 mg (78 %). The spectroscopic data match the reported in the literature. [142]

จุฬาลงกรณ์มหาวิทยาลัย

CHULALONGKORN UNIVERSITY

CHAPTER III

RESULTS AND DISCUSSION

PART A: Fluorescence chemosensors from hydrazide derivatives of julolidine

3.1 Synthesis and characterization

The synthesis of target julolidine derivatives relies on a condensation reaction between julolidine-9-carboxaldehyde (**J**) and a variety of hydrazides (**Scheme 3.1**). Upon simple heating under refluxed conditions in methanol for 3 h, the products were obtained in moderate yields between 67 and 72 %. The products were isolated with ease by simple filtrations and purified by washing them with hexane and diethyl ether. These compounds are stable in solid form upon storage in a refrigerator. They are also stable in DMSO solutions at room temperature for at least 1 month.

JA : R = Methyl

JS : R = 2-hydroxyphenyl

JP : R = 2-pyridinyl
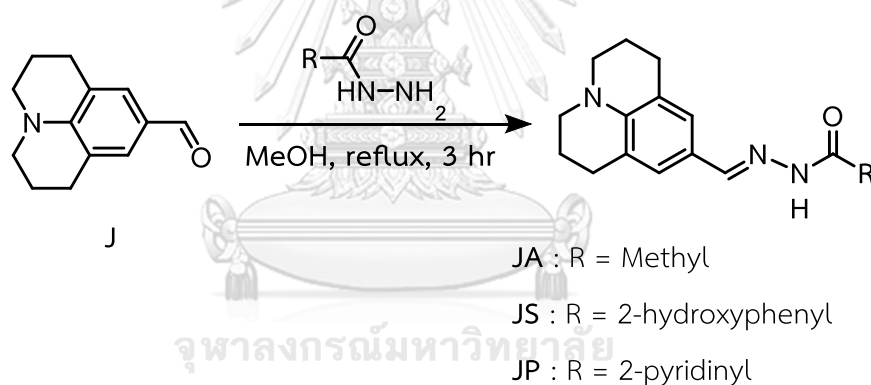
JA (69 %)   JS (72 %)   JP (67 %)

Scheme 3.1 Synthesis of **JA**, **JS**, and **JP** and their physical appearance.

All derivatives were characterized using ^{1}H NMR spectroscopy as shown in **Figure 3.1**. The singlet signals which were labeled by alphabet " **e** " confirmed the appearance of imine proton. The integration ratio of each type of proton in the spectrum corresponded to their structures.
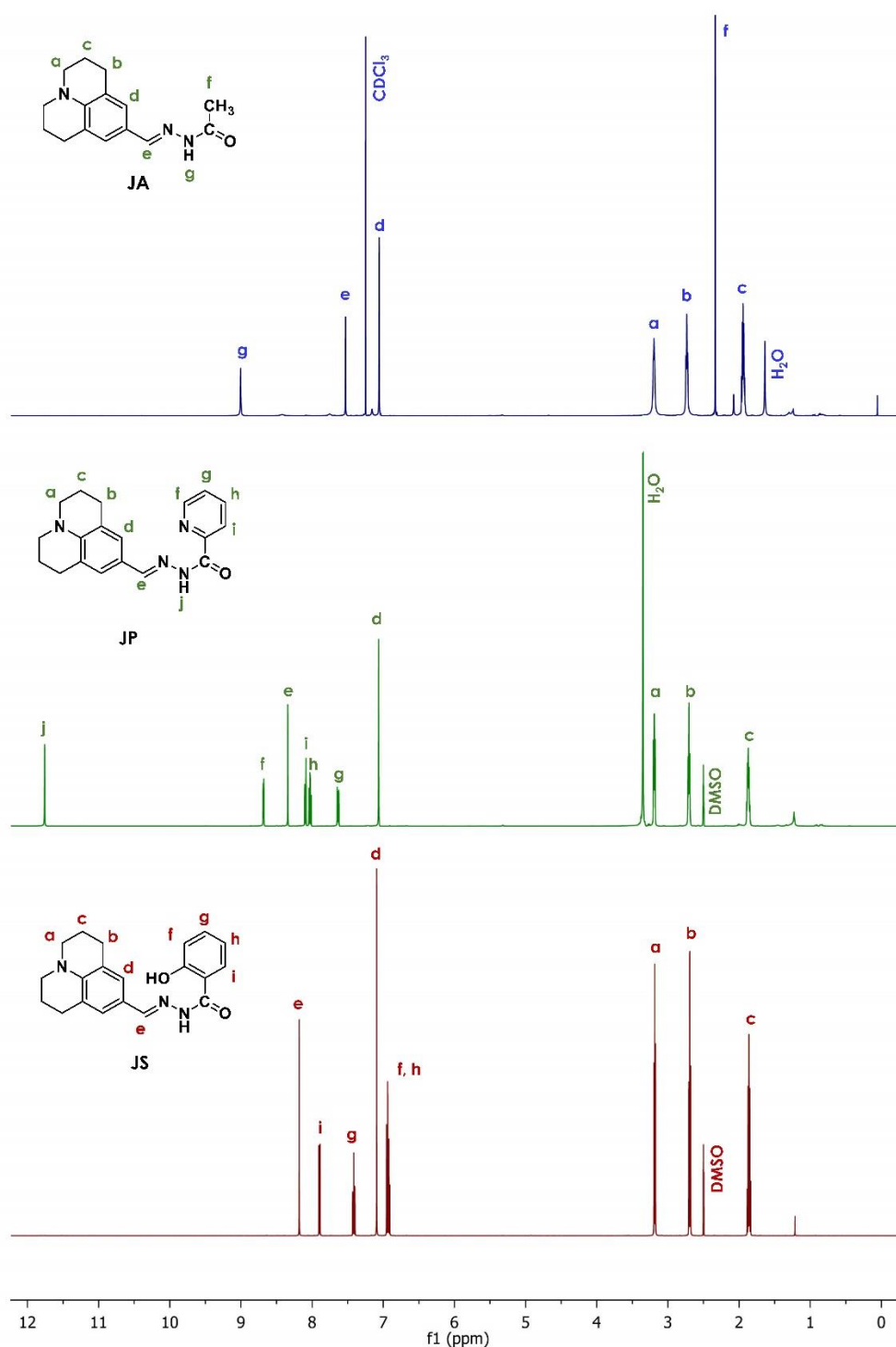
Figure 3.1 ^{1}H NMR spectra of **JA**, **JP**, and **JS**

The exact masses of **JA**, **JS**, and **JP** were determined by an atmospheric pressure ionization, high-resolution time-of-flight mass spectrometer (API-HRTOFMS). The spectra were showed in **Figure 3.2 – 3.4.** It is noteworthy that, besides the peaks of molecular mass, peaks of its dimer were also found.
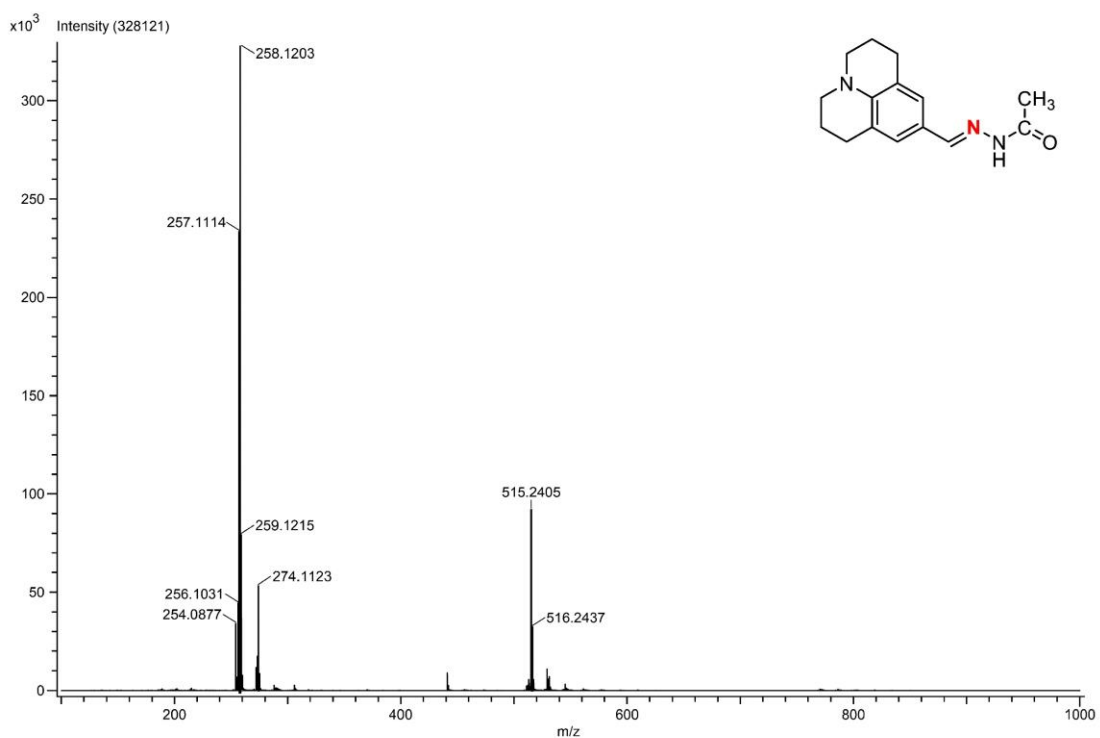
Figure 3.2 HRMS spectrum of **JA**
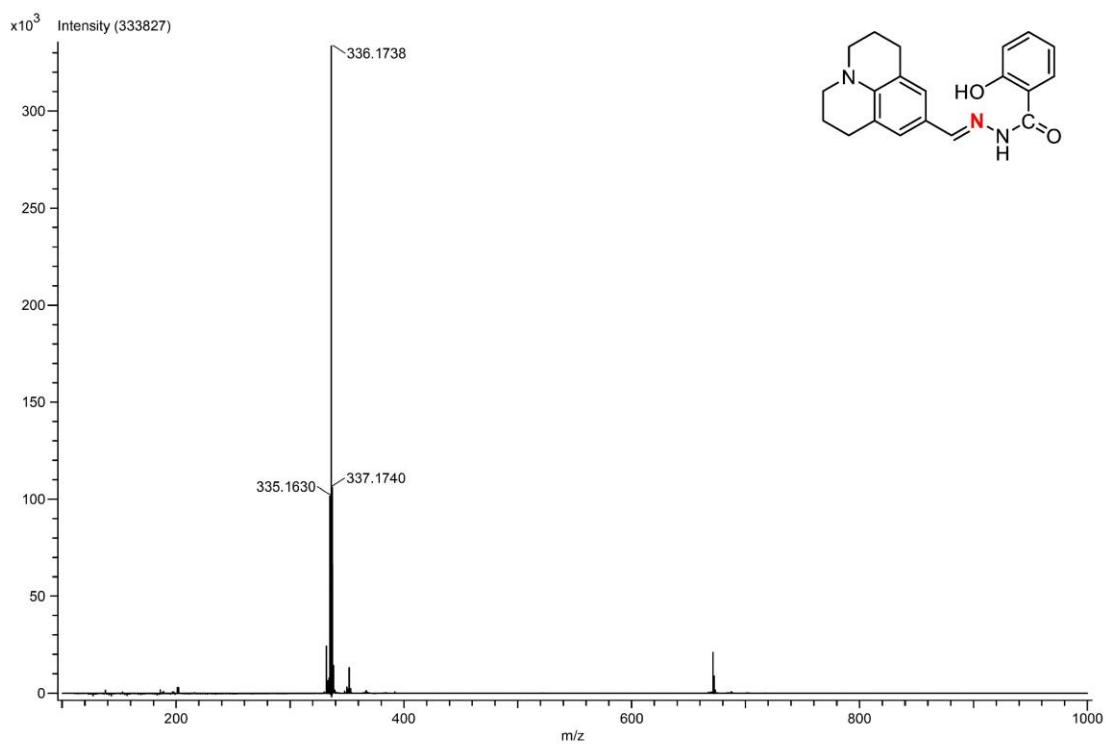
Figure 3.3 HRMS spectrum of JS
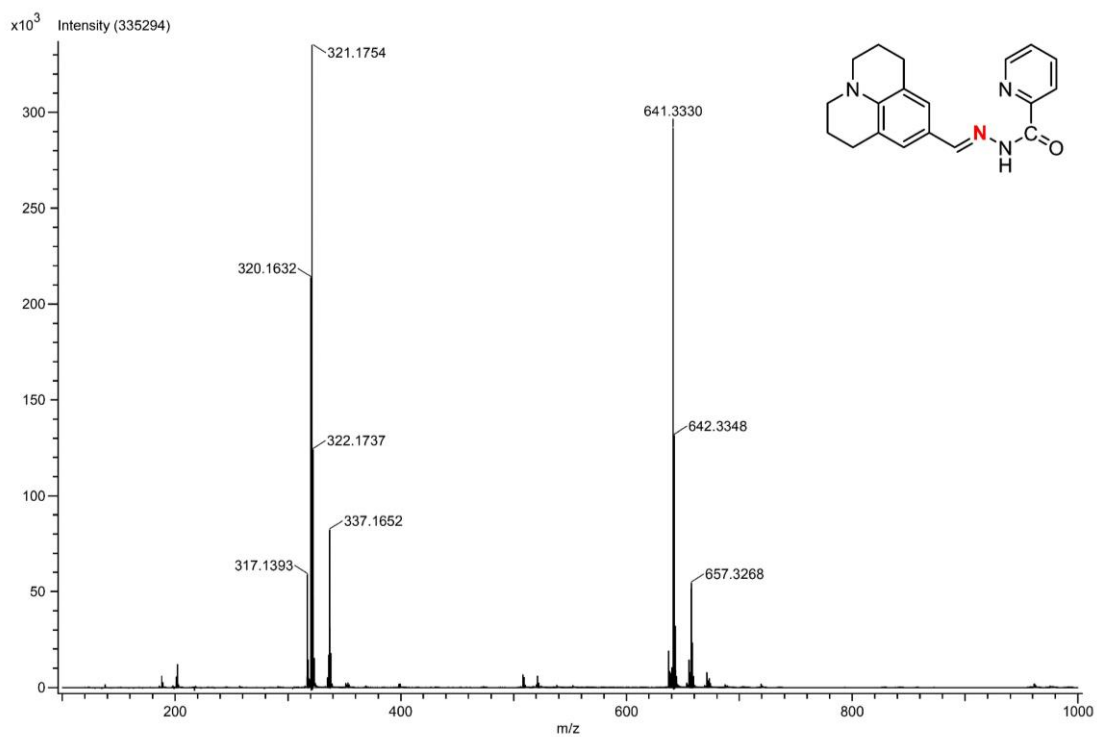
Figure 3.4 HRMS spectrum of JP

3.2   Photophysical properties

DMSO was chosen as a solvent to study the photophysical properties of the target molecule due to the relatively high solubility of the three compounds in DMSO. The photophysical properties of the three julolidine derivatives in DMSO are summarized in **Table 3.1**.

Table 3.1 Photophysical properties of **JA**, **JS**, and **JP** in DMSO (10 µM).

Compound	Absorption		Emission		Stokes Shift
	λ_{max} (nm)	ε (M^{-1} cm^{-1})	λ_{max} [a] (nm)	ϕ_{fl} [b]	(cm^{-1})
JA	359	12,700	416	0.053	3,817
JS	385	11,700	482	0.016	5,227
JP	383	27,300	436 | 603	0.001	3,174 | 9,526

3.2.1   Absorption

It is apparent that the higher degree of conjugation in the molecule, the longer the maximum absorption wavelength is observed. [143] Among the three compounds, **JA** has the shortest conjugation system, thus it has the shortest maxima absorption wavelength of 359 nm. The absorption bands of **JS** and **JP** appear at longer wavelengths due to the presence of a phenolic and a pyridyl group.

The absorption peak of **JA** which is shorter than those of **JS** and **JP** by about 24 nm was also revealed by a TD-DFT calculation (**Figure 3.5**). The calculation results are highly correlated with the experimental results. In the deeper details of molecular transition (**Figure 3.6**), it was found that the HOMO and LUMO transition of **JA** occurs only within the julolidine-Schiff base fragment, whereas, the HOMO-to-LUMO transition in **JS** and **JP** also involved the aromatic ring fragment resulting in the decrease of the energy gap of HOMO and LUMO.

However, the position of the simulated spectra is quite different from the experimental spectra. This may be because the molecular geometry generated in the program may not be exactly the same as the actual molecular structure, or the solvent relaxation may not be calculated correctly.
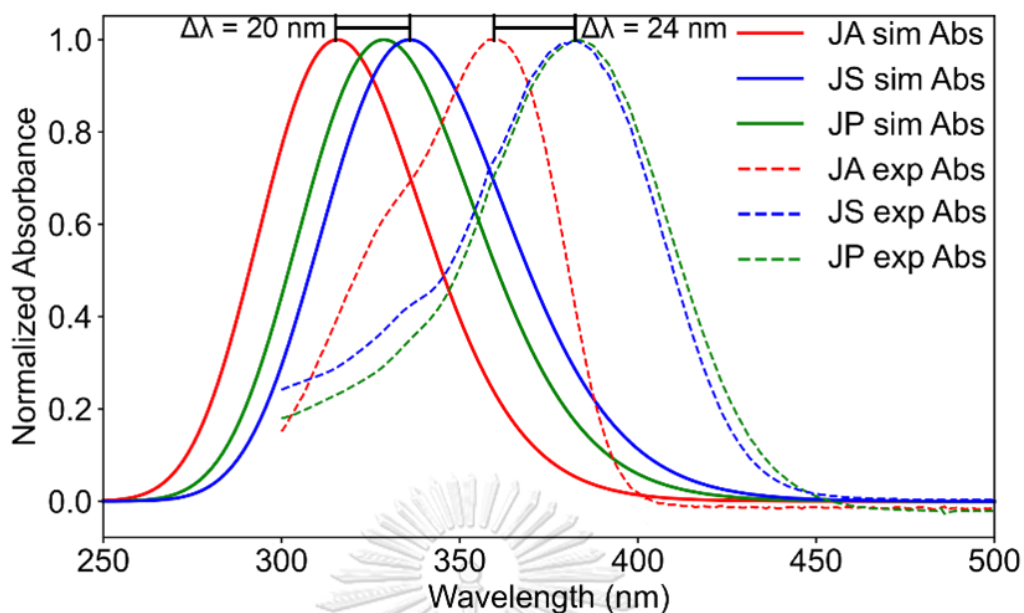
Figure 3.5 Experimental absorption spectra of **JA**, **JS**, and **JP** in DMSO (dashed lines) and simulated absorption spectra of **JA**, **JS**, and **JP** in DMSO using SMD solvation model (solid lines).
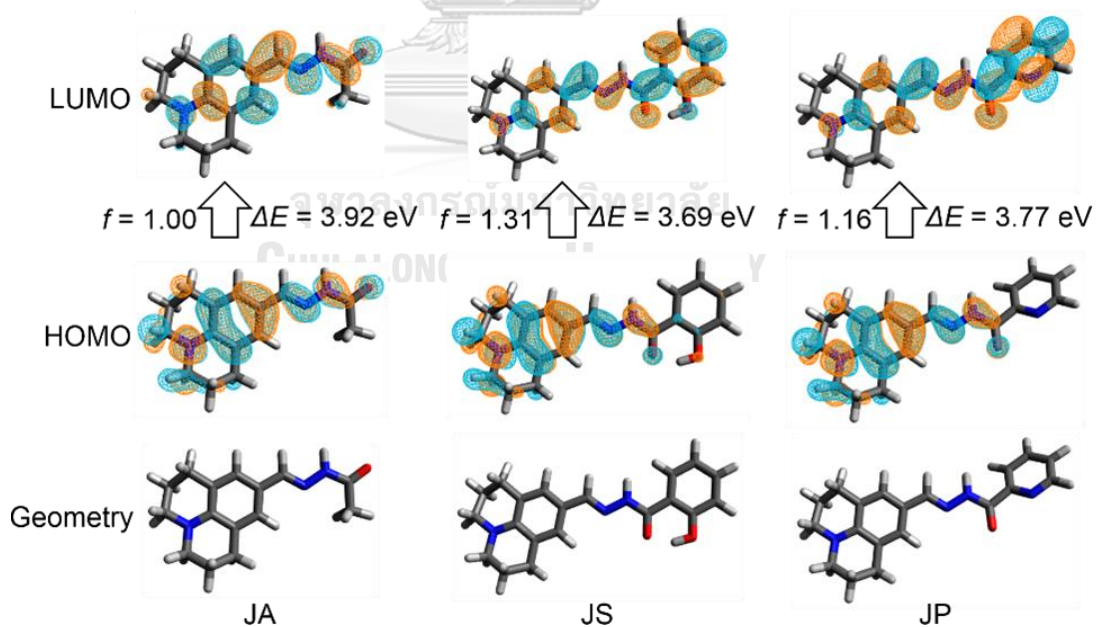
Figure 3.6 The molecular transition of **JA**, **JS**, and **JP** regarding TD-DFT calculation in DMSO with oscillator strength as f and the energy difference of HOMO and LUMO as ΔE

3.2.2 Emission

Upon the excitation at the maxima absorption wavelength, **JA** and **JS** have only one emission maxima at 416 and 482 nm, respectively. Interestingly, **JP** has dual emission maxima at 438 and 603 nm as shown in **Figure 3.7**. Moreover, the excitation spectra of the three compounds were also investigated at the fixed emission maxima (**Figure 3.8**). It appears that the wavelengths of light that each compound absorbed to emit the fluorescence signal at their emission maxima are closely similar to their absorption maxima. These results confirmed that these emission signals result from a relaxation process of the excited molecules.
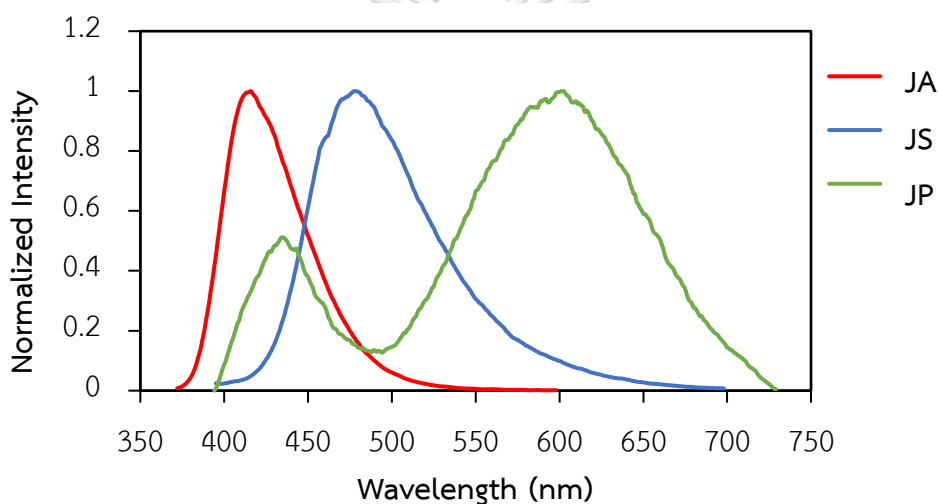
Figure 3.7 Normalized emission spectra of **JA JP** and **JS** in DMSO.
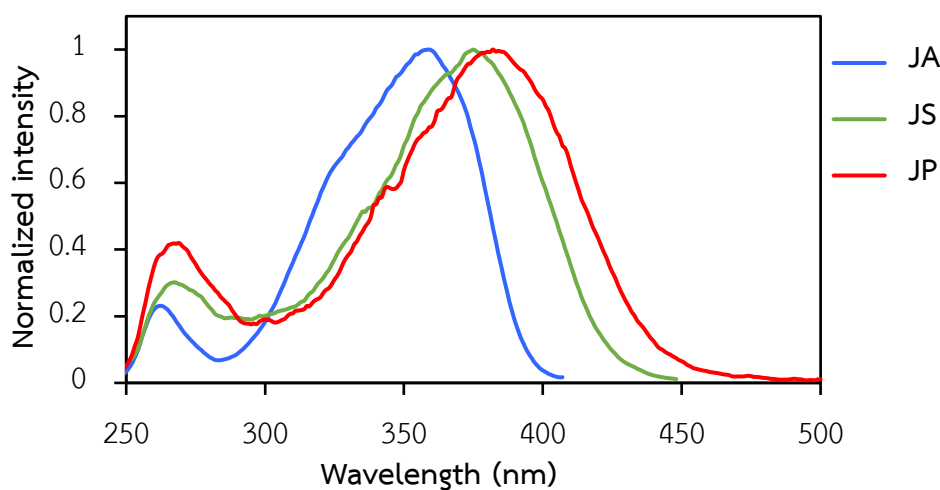
Figure 3.8 Normalized excitation spectra of **JA** (λ_{em} = 416 nm), **JS** (λ_{em} = 483 nm), and **JP** (λ_{em} = 603 nm) in DMSO.

The appearance of dual emission maxima of **JP** is probably due to the excited-state intramolecular proton transfer (ESIPT) that results in two forms in the excited state (amide form and amidic acid form) as shown in **Figure 3.9**. This hypothesis was based on the literature reported by Chen et. al. [144].

To get some information about the ESIPT phenomenon, a quantum calculation was also carried out for the emission spectra to investigate the emission of **JP** in an amide and amidic form (**Figure 3.10**) with the integrated corrected linear response (cLR) for excited state relaxation. [145] The results showed that the total energy of the amide form in the ground state is 0.23 eV lower than the amidic form but the amidic is slightly more stable in the excited state (0.05 eV) meaning the ESIPT mechanism is preferable for **JP** upon photoexcitation. The TD-DFT also confirms that the longer wavelength region is due to the emission of the amidic form.

Nevertheless, all three compounds exhibited low fluorescence quantum yields in DMSO because C=N isomerization of the imine double bond is responsible for nonradiative deactivation. [146]
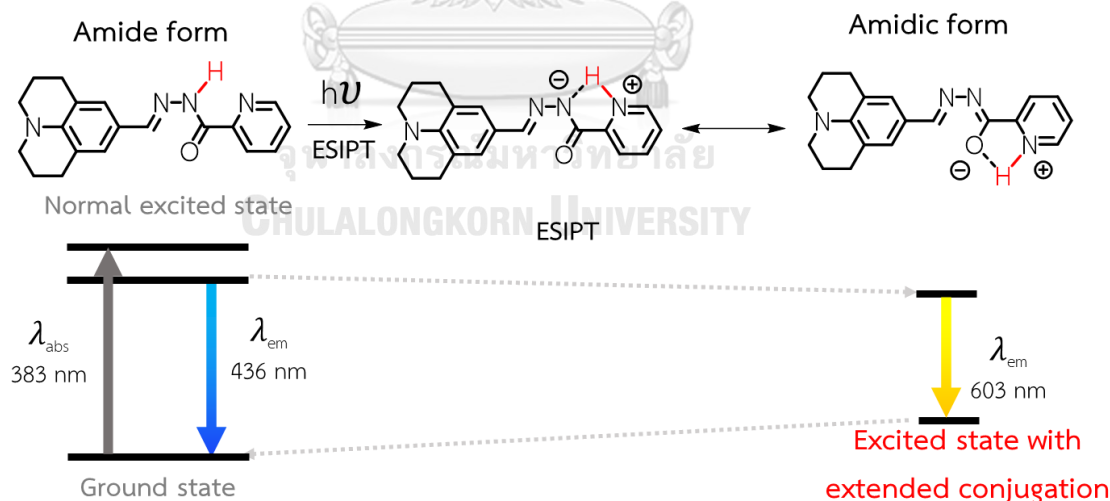
Figure 3.9 Plausible amide and amidic formation of **JP** via ESIPT
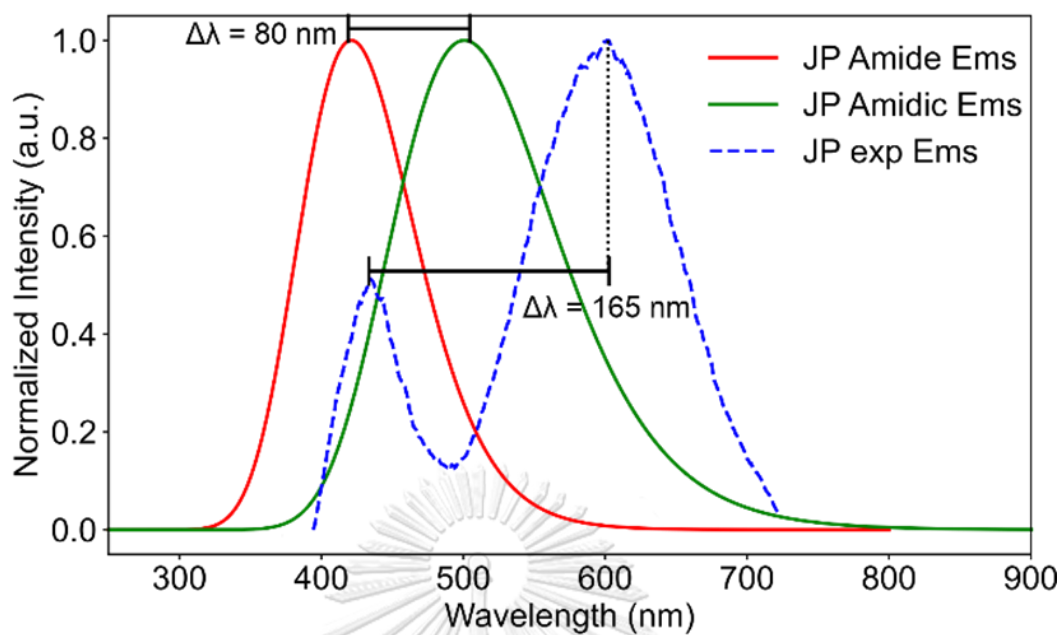
Figure 3.10 Experimental emission spectra of **JP** in DMSO (blue dashed lines) and simulated absorption spectra of **JP** in DMSO using SMD solvation model (solid lines).

3.2.3 Effect of water on emission spectra

The emission spectra of these derivatives were studied in mixed solvents of DMSO and water.

In the case of **JA** (**Figure 3.11**), the amount of water had little effect on the fluorescence intensity, suggesting that **JA** has a high solubility and stability in water. Noteworthy, a bathochromic shift of emission wavelength was found when the amount of water increased. This could be affected by the solvent relaxation from water which is the high polar solvent. This phenomenon is the common nature of ICT-based molecules. The excited state of the ICT-based molecule is more polar as compared to its ground state, so the polar solvents could stabilize the excited state more than the ground state resulting in a decrease in the energy gap between the excited and ground state.

However, in the case of **JP** (**Figure 3.12**) and **JS** (**Figure 3.13**), the fluorescence signal was almost completely extinguished with 99% water content in the co-solvent mixture. Commonly, the main reasons are the reduction of solubility or the aggregation of the compound in water.
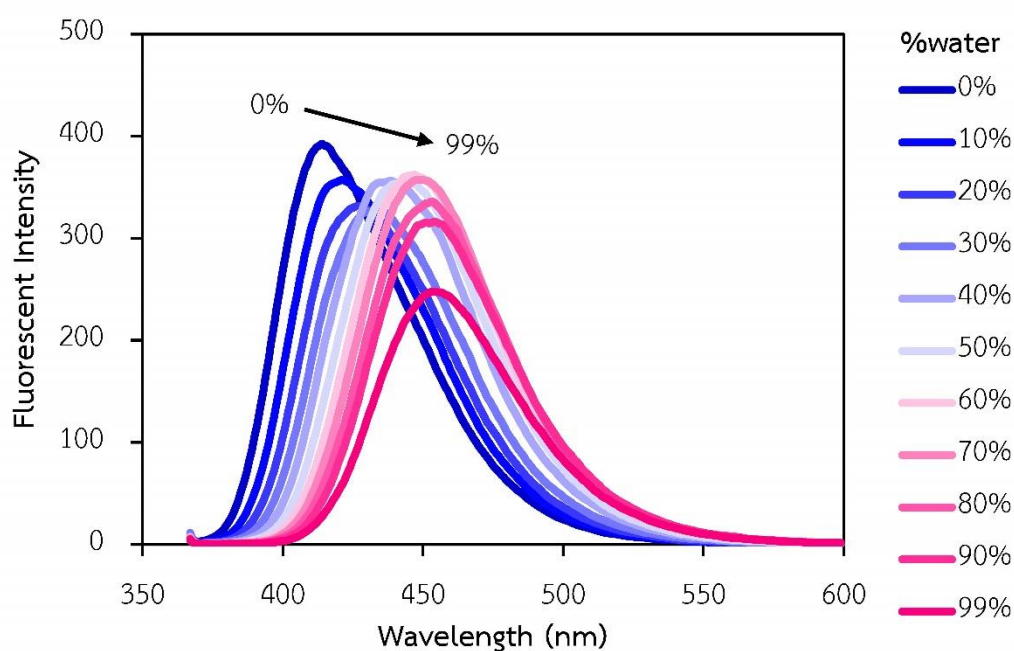
Figure 3.11 Effect of water content on fluorescence of **JA**.

Condition: [**JA**] = 10 μM, λ_{ext} = 359 nm.
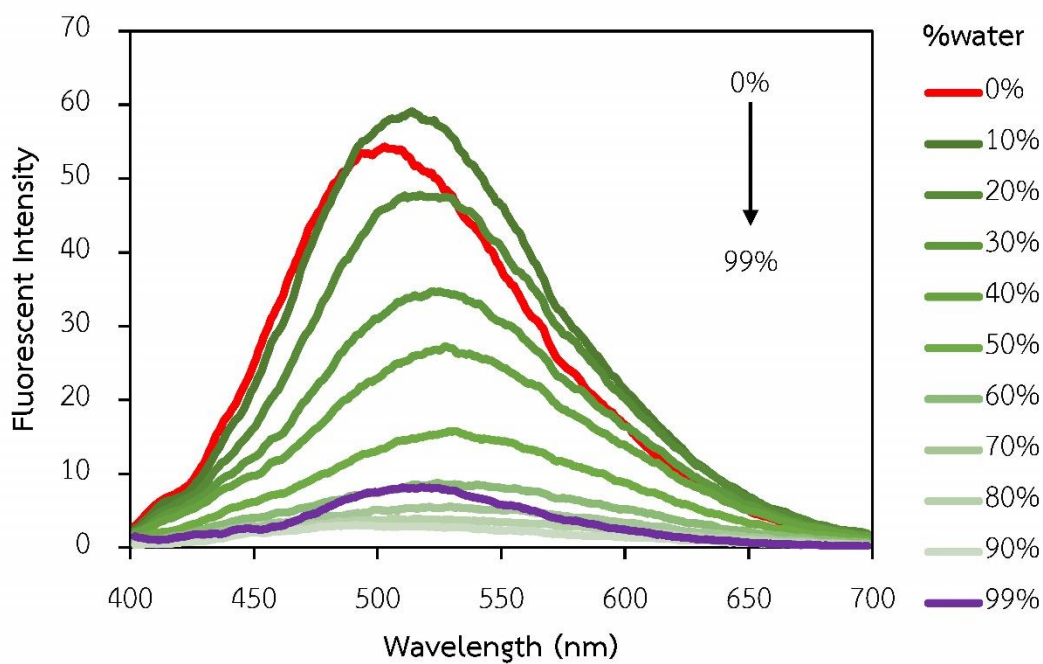
Figure 3.12 Effect of water content on fluorescence of **JS**.

Condition: [**JS**] = 10 µM, λ_{ext} = 385 nm.
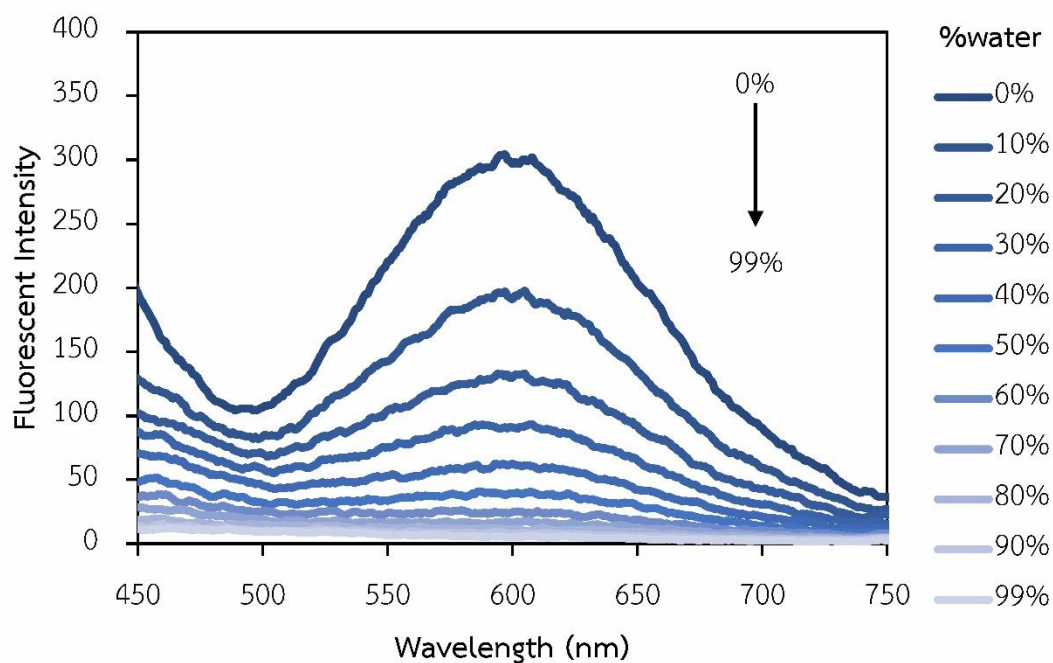
Figure 3.13 Effect of water content on fluorescence of **JP**.

Condition: [**JP**] = 10 µM, λ_{ext} = 383 nm.

3.2.4 Effect of pH on fluorescence intensity

The pH effect on the emission properties of the three julolidine derivatives was studied in a 1:1 (v/v) mixture between DMSO and aqueous buffer at various pHs. The fluorescence emission signals of **JA** and **JP** were steady under a pH range between 3 to 8 (**Figure 3.14**). These results suggest that the acid or base-catalyzed hydrolysis reaction may proceed slowly and the protonation of the pyridine group in **JP** may have a minor effect on its emission properties.
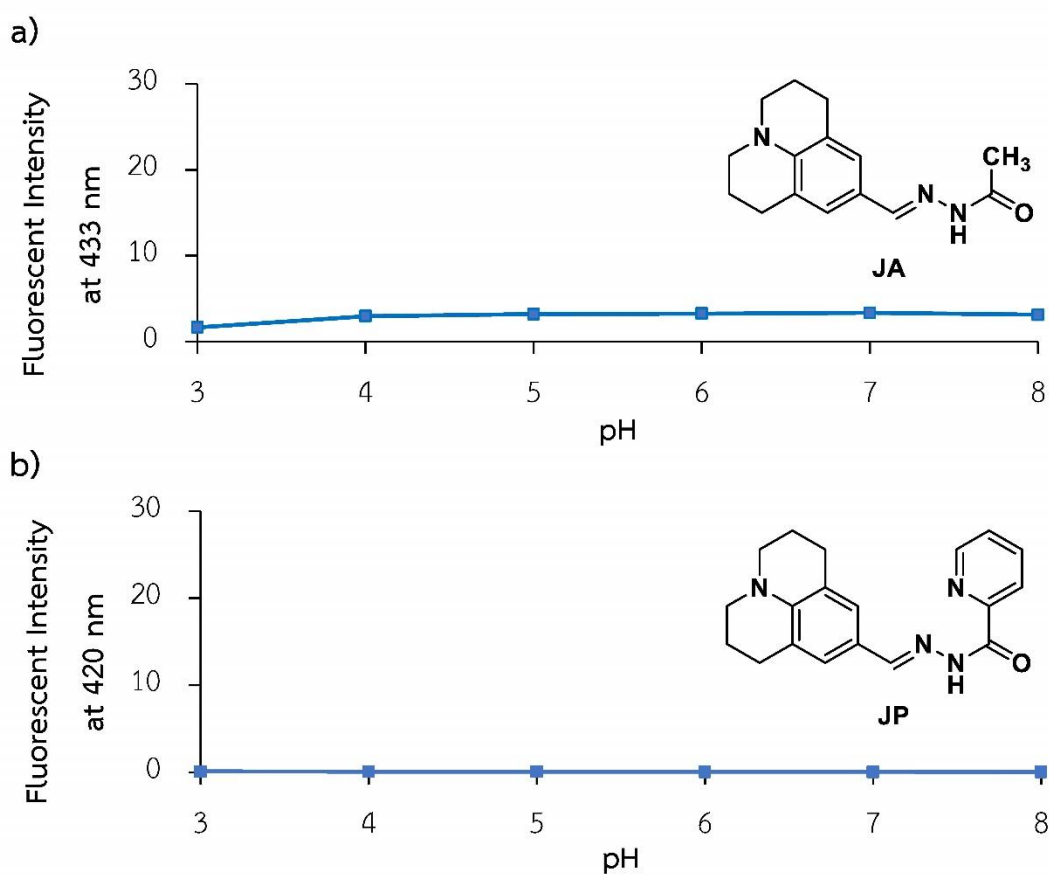
Figure 3.14 Effect of pH on fluorescence of a) **JA**. Condition: [**JA**] = 10 µM, λ_{ex} = 359 nm. b) **JP**. Condition: [**JP**] = 10 µM, λ_{ex} = 383 nm.

Interestingly, the fluorescence intensity of **JS** gradually increased along with the pH (**Figure 3.15**). The results may be related to a previous report by Zhuang et. al. that the emission intensity of deprotonated salicylaldehyde derivatives increased dramatically compared to the nondeprotonated ones. [147] From the structure of **JS**, it can be seen that carbonyl and hydroxyl groups can exhibit ESIPT, which is a process that can reduce the relaxation energy from the excited state. In the non-deprotonated form, the ESIPT process between C=O and O-H group was broken, resulting in an increase in fluorescence signal at 480 nm.
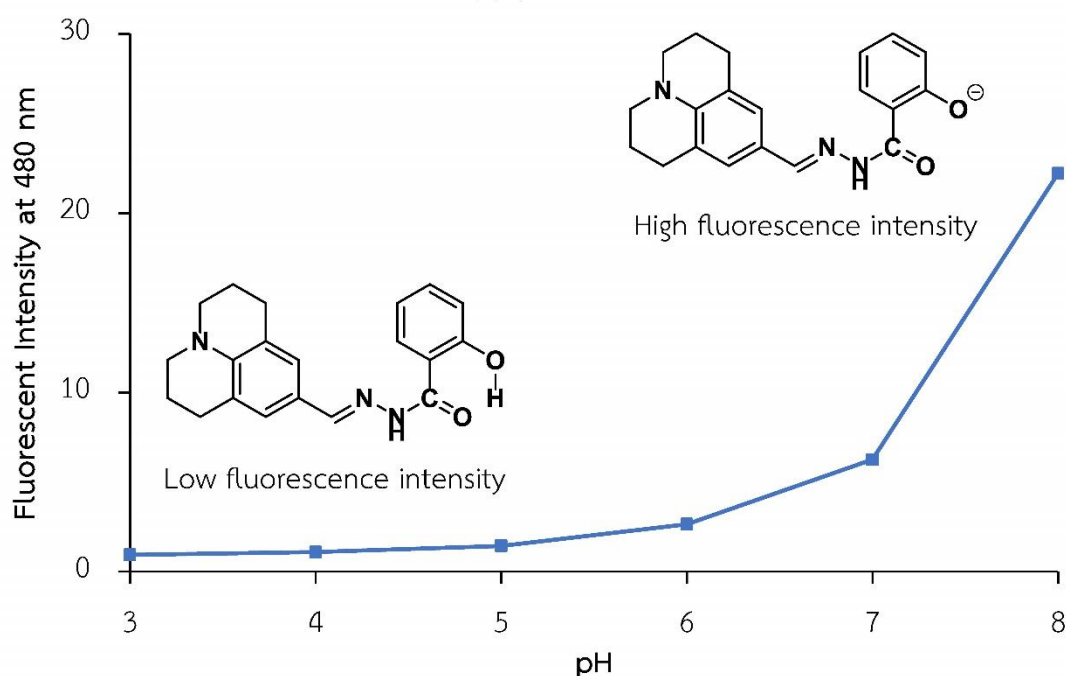
Figure 3.15 Effect of pH on fluorescence of **JS**

Condition: [**JS**] = 10 μM, λ_{ex} = 385 nm

3.2.5   Effect of solvent on emission spectra

Every spectrum of three derivatives in the 13 solvents showed different emission maxima or fluorescence intensity or both. The dipole moments of each solvent [148] are shown below for consideration of the tendency of the solvent polarity effect.

THF (ε=7.58)   DMF (ε=36.7)   DMSO (ε=46.7)   ACN (ε=37.5)

MeOH (ε=32.7)   2-propanol (ε=17.9)   DMAc (ε=37.8)   DMC (ε=3.087)

Chloroform (ε=4.81)   DCM (ε=8.93)   EtOH (ε=24.5)   Acetone   (ε=20.7)

EtOAc (ε=6.02)

1) JA

The emission spectra of **JA** in various solvents were divided into 4 groups with different shades of color (**Figure 3.16**). The emission spectra of **JA** in the low polar solvents (THF, DMC, and EtOAc) and the medium polar solvent (DMAc, Acetone, DCM, 2-propanol, and chloroform) gave the emission maxima in the range of 402 - 404 nm and 409 – 412 nm, respectively. The emission spectra of **JA** in DMSO, DMF, and ACN which are the high polar aprotic solvents caused the emission maxima of **JA** to be in the range of 415 - 417 nm. The emission maxima of **JA** in EtOH, and MeOH which are the high polar protic solvents were 423, and 433 nm respectively. These results indicate that the higher polar solvents cause the longer emission maxima of **JA**. The reason for this can be explained in the same way as the effect of water content.

Nevertheless, the solubility of **JA** in each solvent is probably the main cause that affects the different fluorescence intensities. DMSO (high polar solvent) is a solvent that provides the highest fluorescence intensity, whereas chloroform (low polar solvent) is a solvent that provides the lowest fluorescence intensity.

2) JS

Fluorescence enhancement of **JS** (**Figure 3.17**) was observed especially in the protic solvents. These results supported the results of the pH study. It is most probably connected with the dissociation of proton at the hydroxyl group. The more polar solvents, the more molecules can ionize better.

3) JP

The emission spectra of **JP** in various solvents (**Figure 3.18**) were divided into 2 groups including the low polar aprotic solvents which have a dipole moment (ε) less than 10 and the high-medium polar solvent which have a dipole moment of more than 10. The evidence suggested that the emission intensity of **JP** visibly decreased with a slight red shift on increasing the solvent polarity. It's probably due to the ESIPT characteristic of **JP**, the fluorescent molecules have a larger dipole moment in the excited state than in the ground state. Increasing the solvent polarity produces a correspondingly larger reduction in the energy level of the excited state.

a)

b)
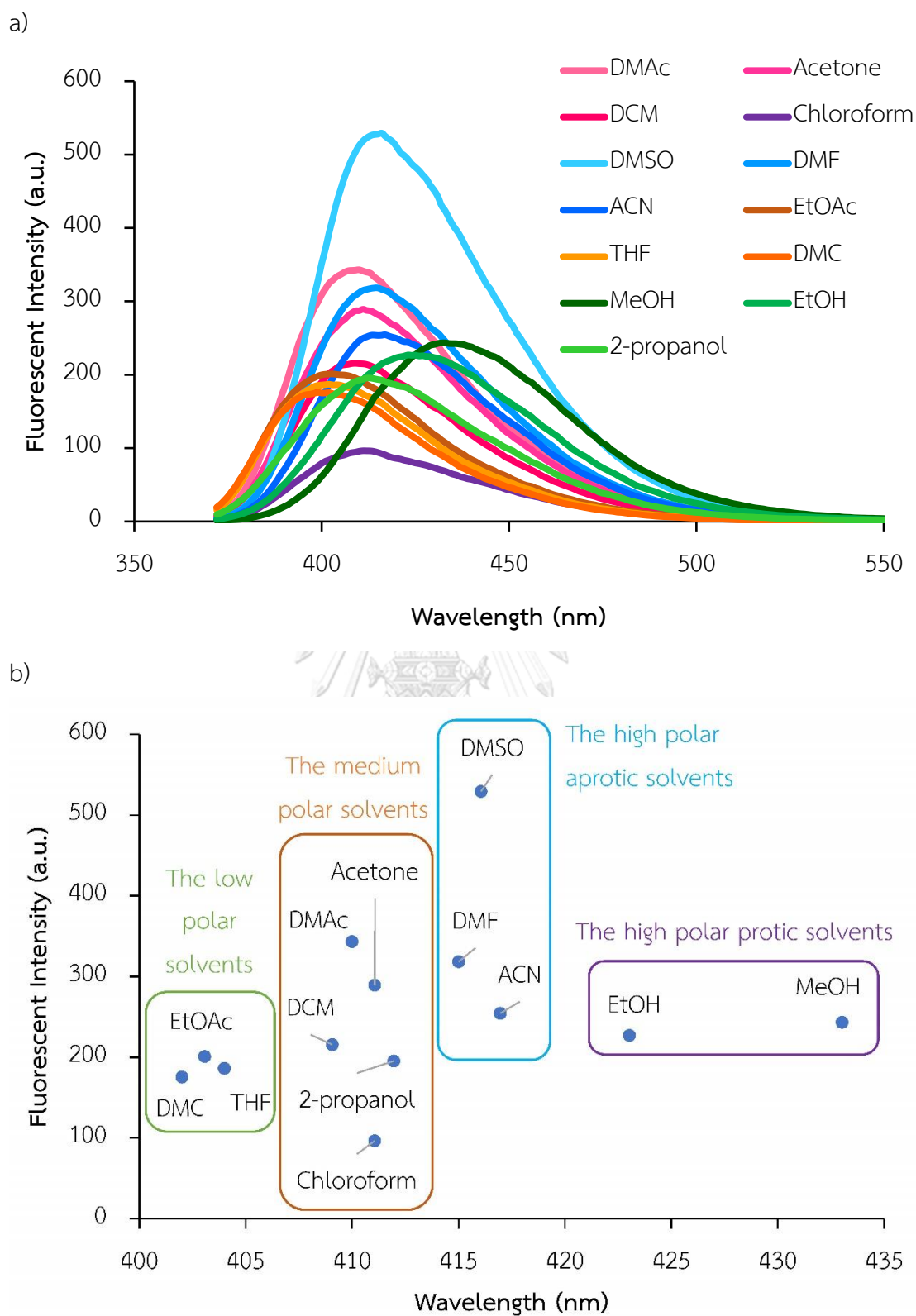
Figure 3.16 (a) Emission spectra, (b) Fluorescence intensity at emission maxima of **JA** in each solvent.

a)

b)
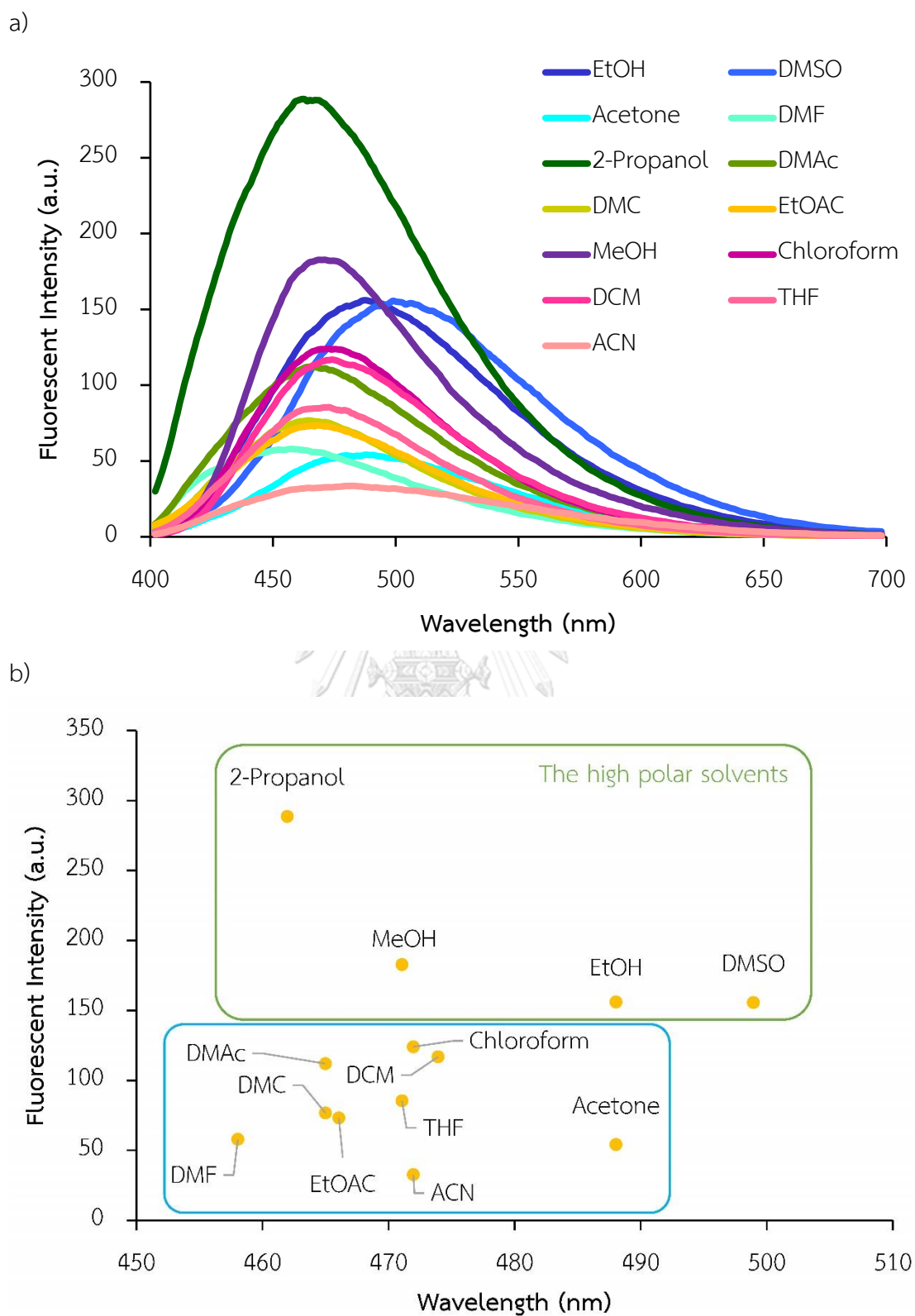
Figure 3.17 (a) Emission spectra, (b) Fluorescence intensity at emission maxima of **JS** in each solvent.

a)

b)
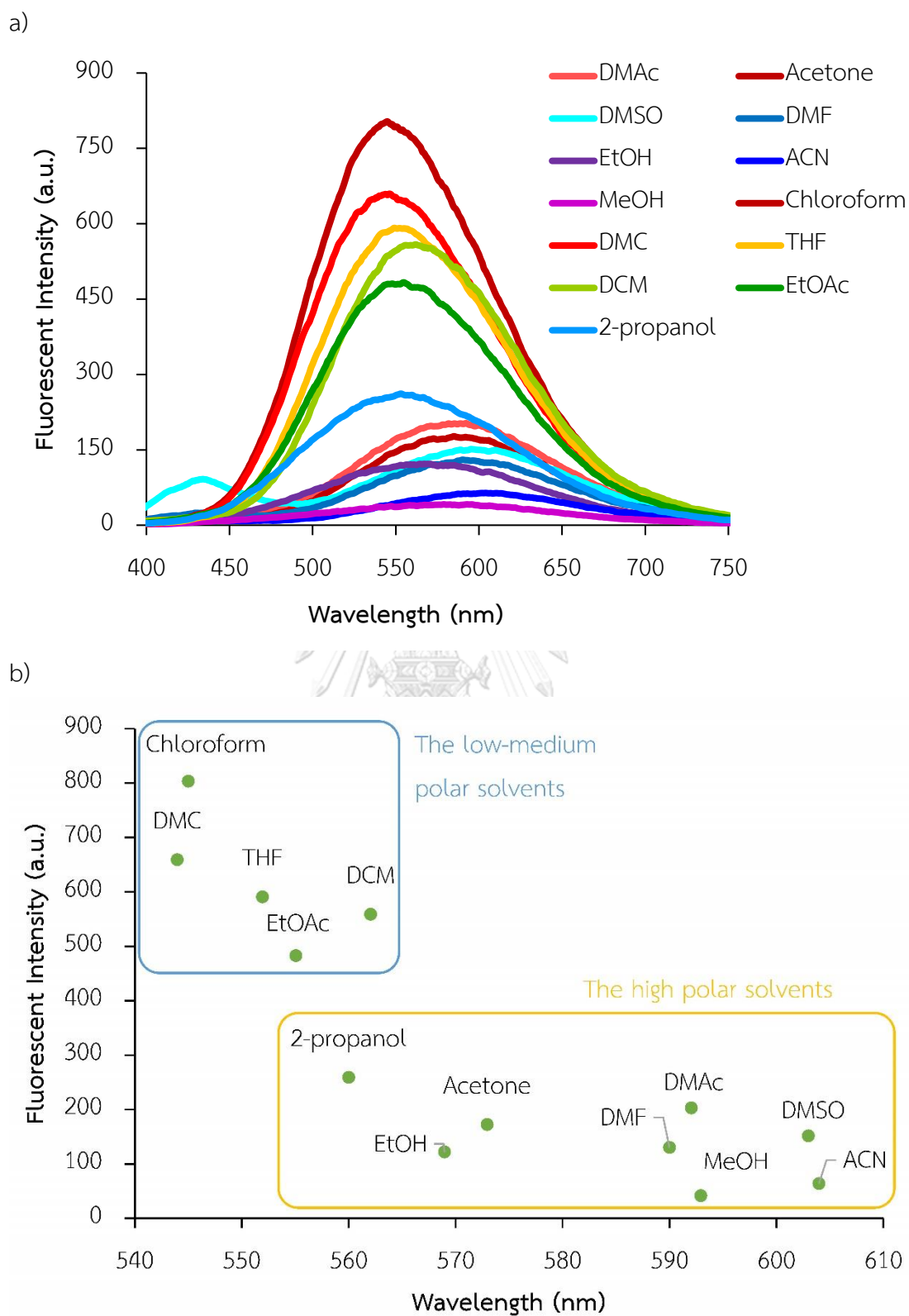
Figure 3.18 (a) Emission spectra, (b) Fluorescence intensity at emission maxima of **JP** in each solvent.

3.3 Metal ion sensing of JA

3.3.1 Selectivity study

Based on the data from the preceding section, a 1:1 (v/v) mixture between DMSO and 50 mM HEPES buffer pH 7.0 were studied for the selectivity test of **JA**. The fluorescence signal of **JA** did not change significantly by the testing metal ions as shown in **Figure. 3.19**. This could be assumed that the acetyl hydrazone unit is incapable of interacting with any metal ions in such a way that it alters the fluorescence signal of the molecule. The acyl moiety should probably bear other functional groups at a suitable position to modulate the properties of metal chelation.

However, it was found that Cu^{2+} has a slight tendency to quench the emission signal. Therefore, the effect of pH in the presence of Cu^{2+} has been studied further. The results were shown in **Figure 3.20**. However, there was no significant difference in I_0/I at any pH, except for pH 3. The main reason was probably due to the hydrolysis of **JA** at the low pH, resulting in the decrease of emission signal in both the absence and presence of Cu^{2+} condition.
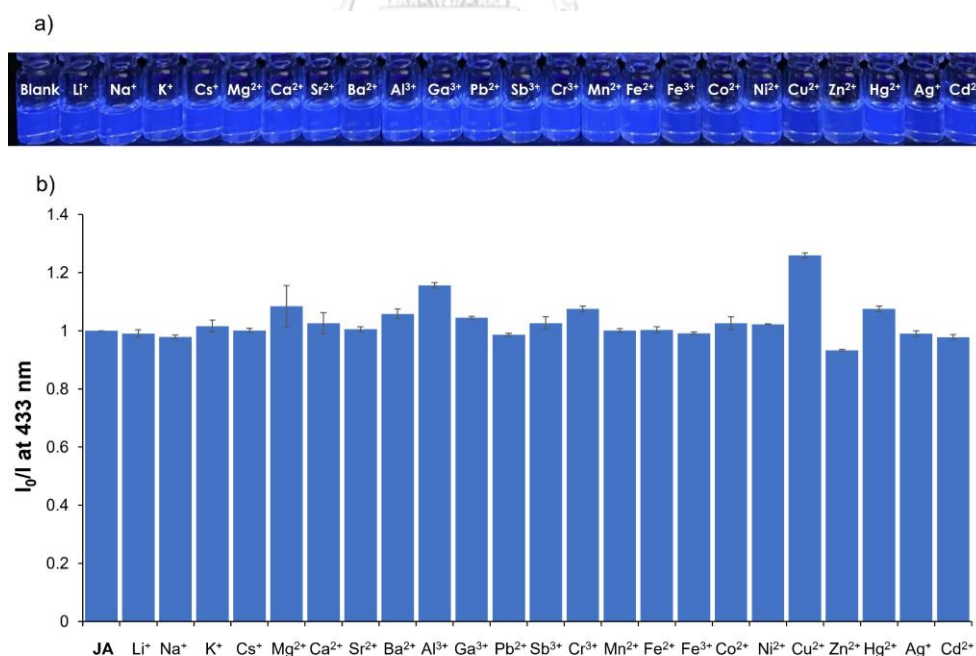
Figure 3.19 a) Photographed images and b) fluorogenic responses at 433 nm of **JA** (10 μM) towards various metal ions (100 μM) in 1:1 (v/v) DMSO and 50 mM HEPES buffer pH 7.0.
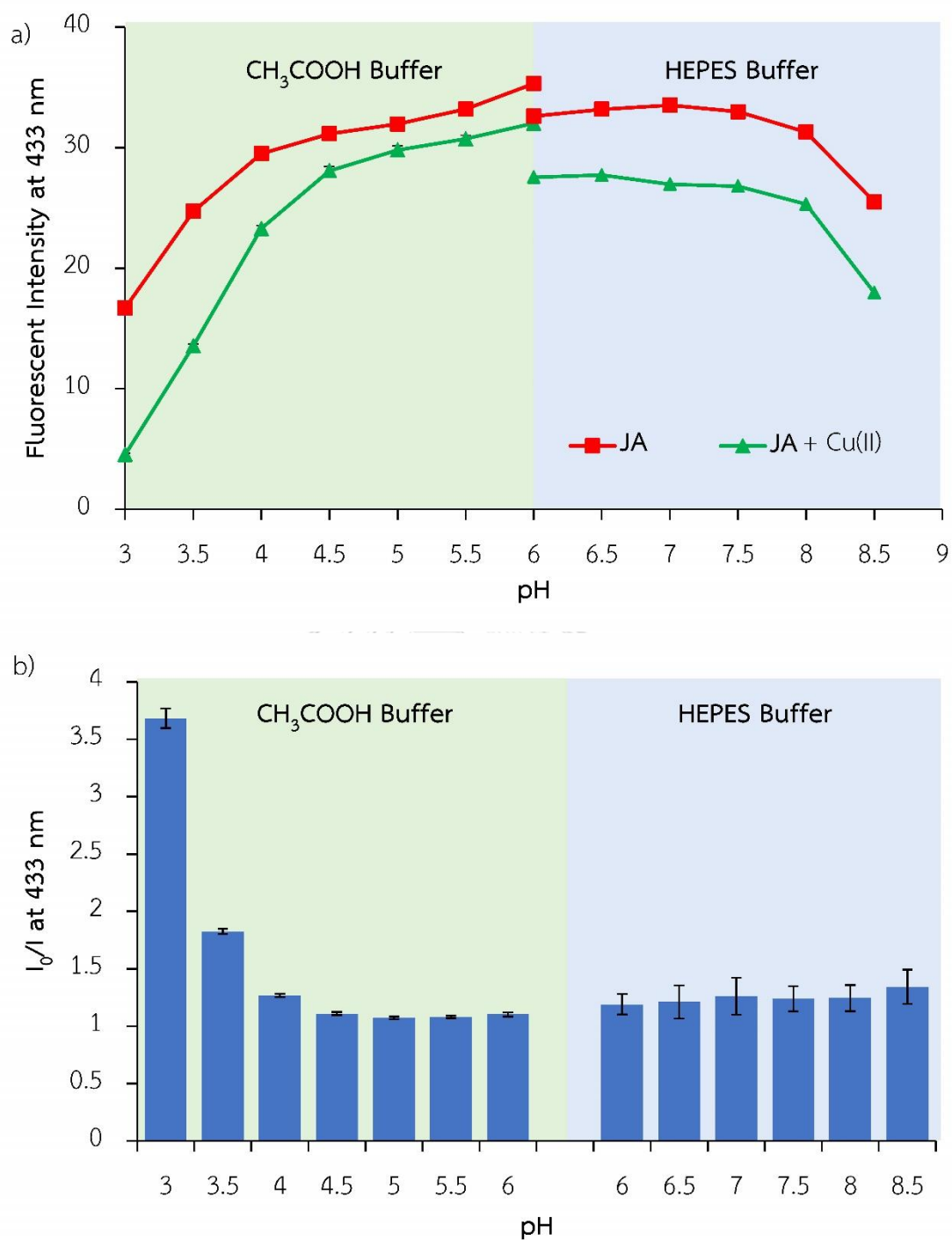
Figure 3.20 Effect of pH of JA on (a) fluorescence intensity and (b) I_0/I at 433 nm in 50% (v/v) DMSO/water.

3.3.2 Sensing mechanism

TLC analysis (**Figure. 3.21**) and Cu^{2+} titration experiments (**Figure. 3.22**) were carried out to investigate the interaction between **JA** and Cu^{2+}. However, the addition of Cu^{2+} into the **JA** solution did not generate a new spot on the TLC plate and Cu^{2+} titration could not change the absorption spectrum of **JA**.
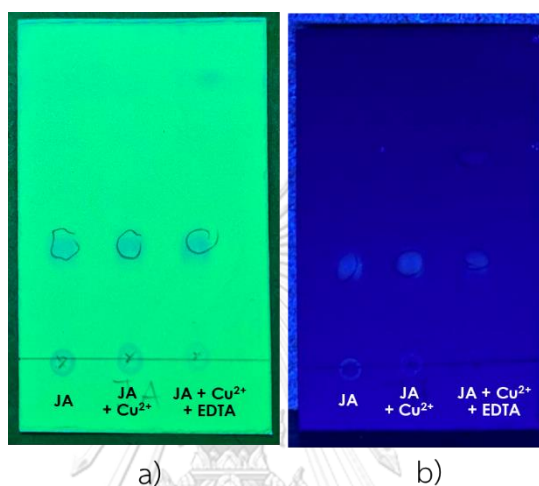
Figure 3.21 The thin layer chromatography (TLC) representing **JA**, **JA**+Cu^{2+}, and **JA**+Cu^{2+}+EDTA. Stationary phase: silica G, Mobile phase: EtOAc:Hexane (3:1 v/v). (a) Under 254 nm UV lights and (b) Under 365 nm UV lights
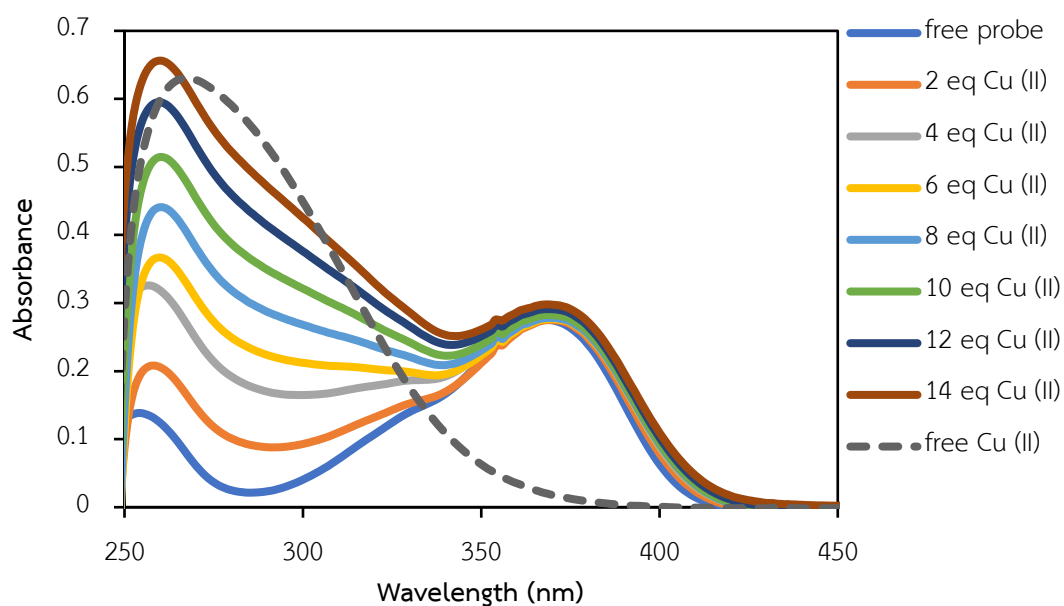
Figure 3.22 UV-Vis titration of **JA** (10 μM) with Cu^{2+} in 50% (v/v) DMSO/HEPS buffer pH 7.0.

3.4 Metal ion sensing of JS

3.4.1 Screening Test & Selectivity study

EtOH As depicted in **Figure 3.23**, the **JS** in EtOH gave a weak green emission signal under black light. After the addition of tested metal ions, many metal ions could alter the fluorescence signal indicating that EtOH might not be a suitable solvent for metal ion detection.
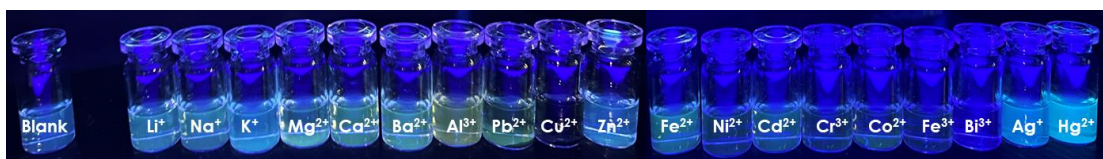
Figure 3.23 Image of **JS** (10 µM) towards various metal ions (100 µM) in EtOH.

In acetonitrile (**Figure 3.24**), the emission signal of **JS** was relatively low. Upon the addition of tested metal ions, the addition of Al^{3+} and Hg^{2+} could enhance the green fluorescence signal under blacklight.
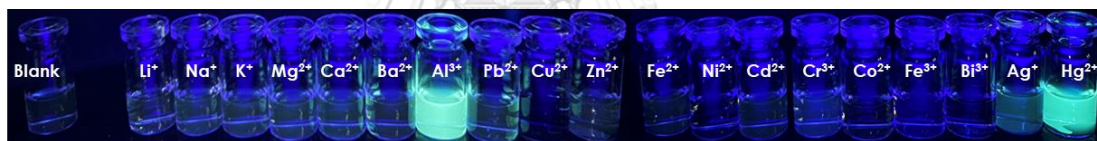
Figure 3.24 Images of **JS** (10 µM) towards various metal ions (100 µM) in ACN.

Unfortunately, the fluorescence enhancement phenomenon of **JS** with Al^{3+} and Hg^{2+} in ACN was restricted upon adding a little of an aqueous solution of the HEPES buffer pH 7.0. As shown in **Figure 3.25**, the fluorescence spectra revealed that only Cu^{2+} could cause the fluorescence quenching in the 1:1 (v/v) ACN/50 mM HEPES buffer pH 7.0 condition.

The study of pH was performed again in ACN to find the suitable pH for the "turn off" fluorescence sensors (**Figure 3.26**). The pH that provides the high fluorescence signal at the beginning could improve the sensitivity of the turn-off sensor. However, the fluorescence intensity of **JS** was relatively low in the range of pH 3-8 and gradually increased in the range of pH 9-10. Inappropriately, the pH 9-10 is too high for the detection of metal ions because some metal ions form precipitation of hydroxide compounds.
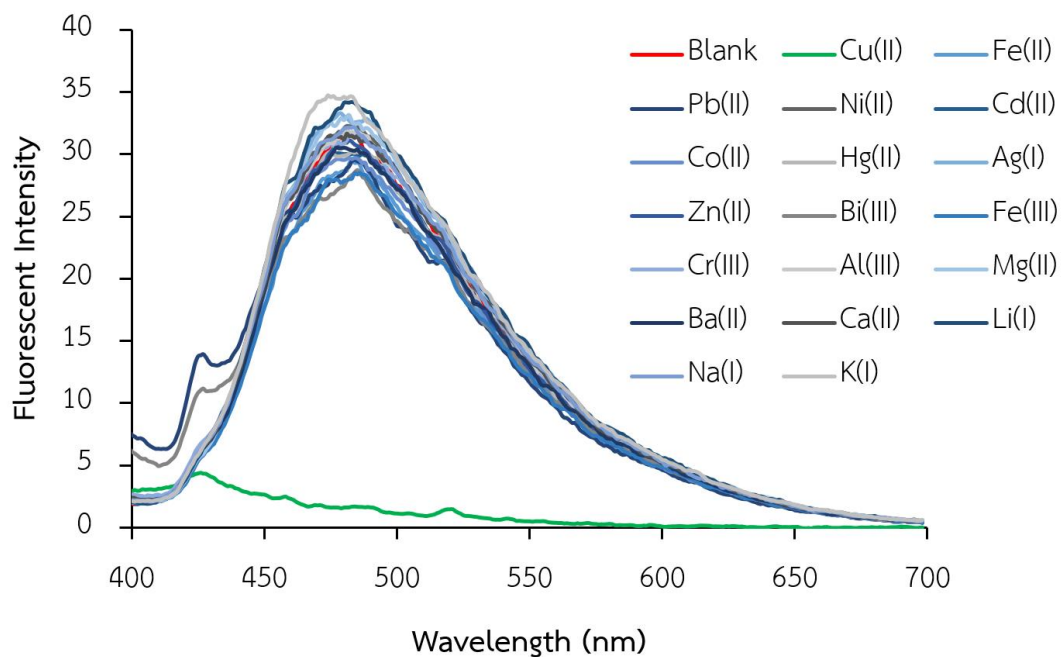
Figure 3.25 The emission spectra of **JS** (10 µM) towards various metal ions (100 µM) in 1:1 (v/v) ACN and 50 mM HEPES buffer pH 7.0
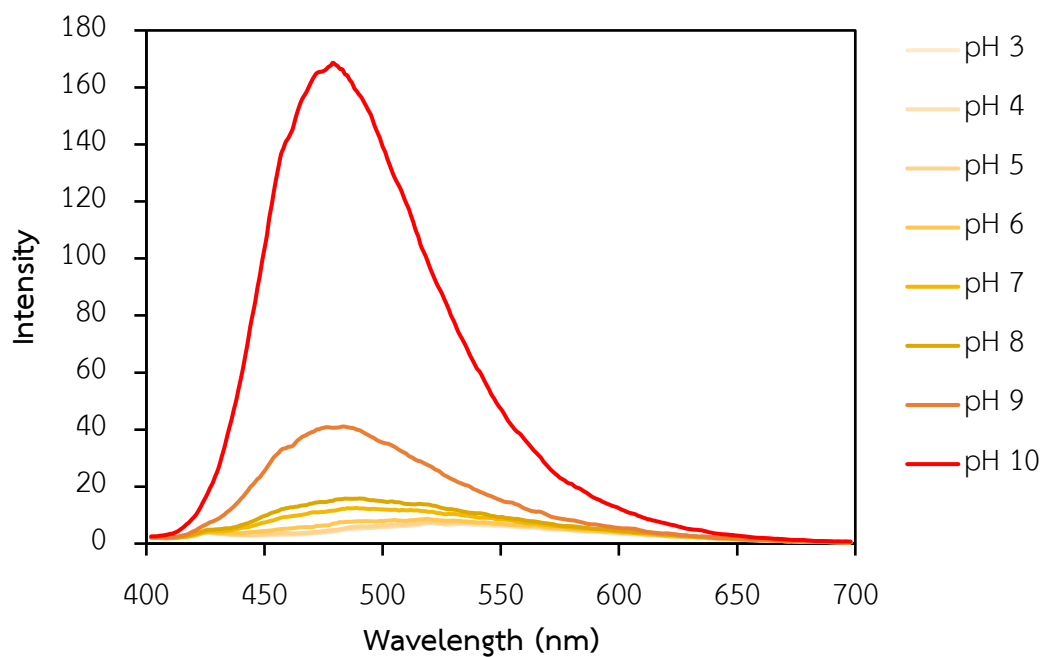
Figure 3.26 The emission spectra of **JS** (10 µM) towards various pH in 1:1 (v/v) ACN and HEPES buffer (50 mM)

The screening test was also investigated in DMSO as depicted in **Figure 3.27**. It was found that the addition of Hg^{2+} could quench the fluorescence signal of **JS** in DMSO. However, when the solution contained 50% v/v HEPES buffer pH 8.0, the results were changed. The color of the emission signal of free **JS** was blue shifted and only Cu^{2+} could cause a fluorescence quenching. This result is similar to the 1:1 (v/v) ACN and 50 mM HEPES buffer condition.

a) DMSO
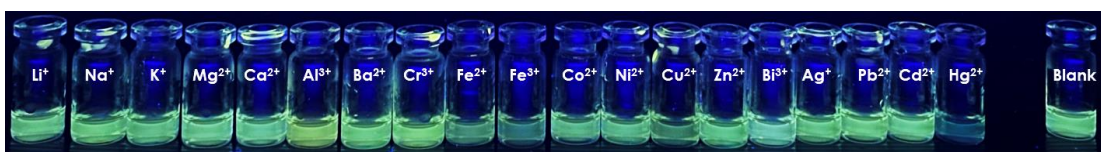
b) 1:1 (v/v) DMSO and 50 mM HEPES buffer pH 8.0

Figure 3.27 Photographed images of **JS** (10 μM) towards various metal ions (100 μM) in (a) DMSO and (b) 1:1 (v/v) DMSO and 50 mM HEPES buffer pH 8.0.

The study of solvent and pH effect indicated that the fluorescence signal of **JS** in DMSO is higher than in ACN at the same pH. Therefore, DMSO was chosen as the tested condition instead of ACN. Meanwhile, the HEPES buffer is more suitable than the CH_3COOH buffer because it could Cu^{2+} showed a better ability in the fluorescence quenching to **JS**.

In addition, it was also found that the higher the pH, the higher I_0/I (**Figure 3.28**) was observed. Therefore, the selectivity was investigated in 1:1 (v/v) DMSO and 50 mM HEPES buffer pH 8.0. The selectivity study suggested that only Cu^{2+} could cause the fluorescence quenching at 480 nm by 100-fold (**Figure 3.29**)

a)

b)
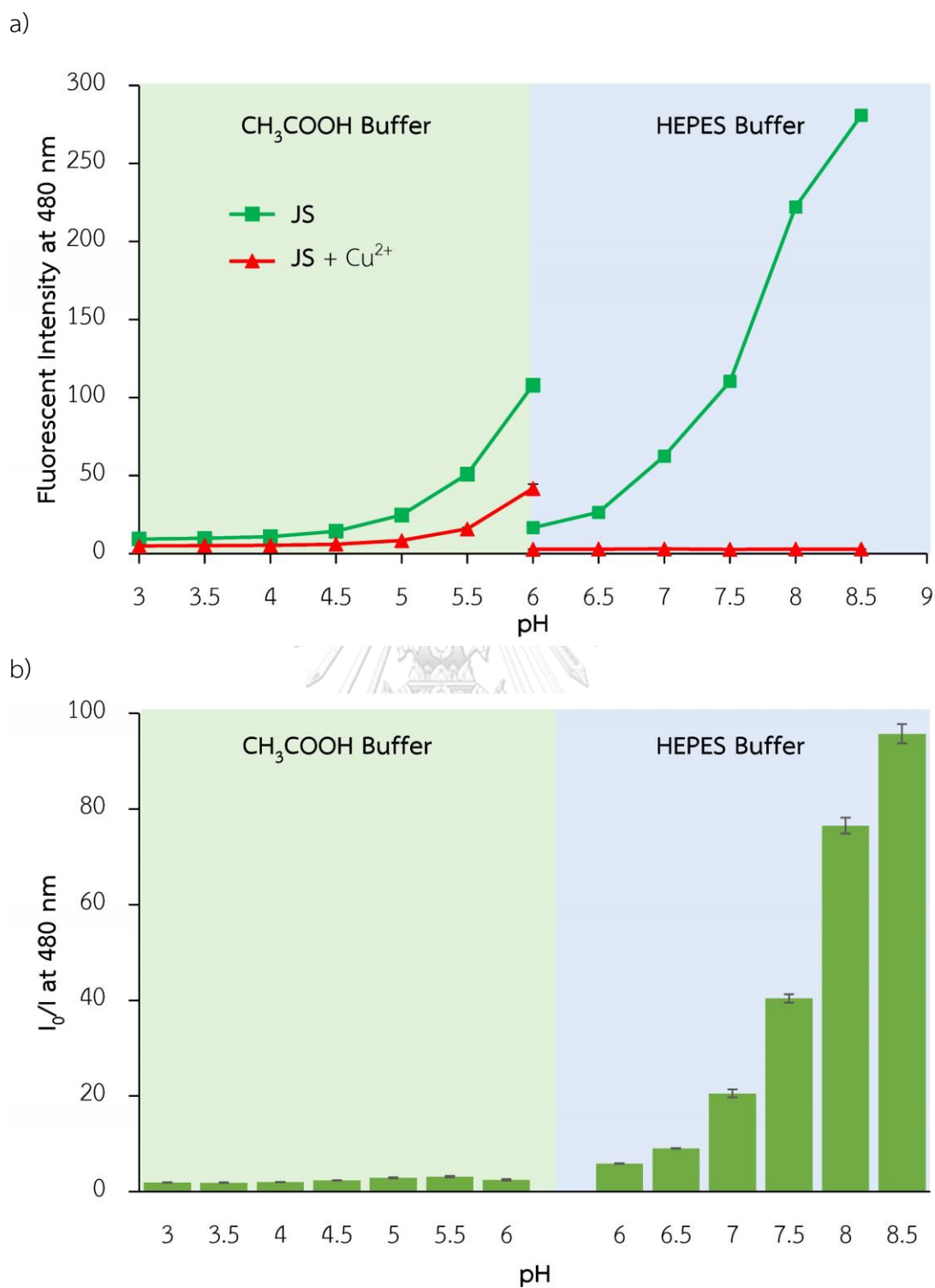
Figure 3.28 The pH effect on a) fluorescence intensity and b) I_0/I at 480 nm of **JS** (10 µM) in the absence and presence of Cu^{2+} (100 µM). Buffer: HEPES pH 6.0-8.0 and acetic/acetate pH 3.0-5.0 (50 mM), 50% (v/v) DMSO/water.
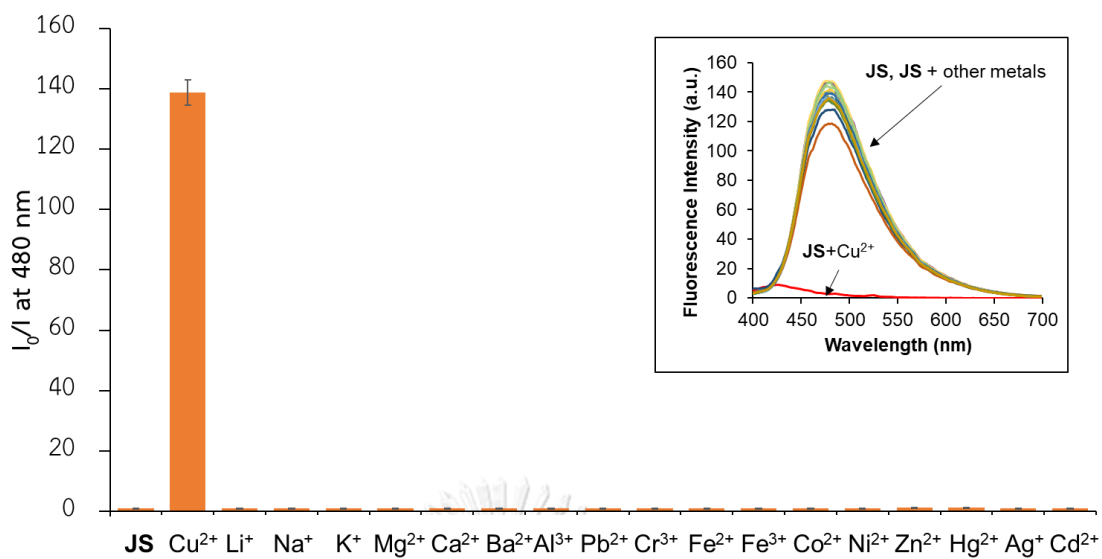
Figure 3.29 Fluorogenic responses (inset: the emission spectra) at 480 nm of **JS** (10 µM) towards various metal ions (100 µM) in 1:1 (v/v) DMSO and HEPES buffer pH 8.0 (50 mM).

3.4.2   Sensitivity study & Time dependent

The sensitivity of **JS** with Cu^{2+} was studied by the fluorescence titration experiments. Upon excitation at 385 nm, the emission intensity at 480 nm gradually decreased as the concentration of Cu^{2+} increased. The experiments were performed at two different pH conditions including pH 7.4 and pH 8.0 (**Figure 3.30**). The results showed that the decrease in fluorescence intensity at 480 nm of **JS** at pH 8.0 was more obvious than at pH 7.5. Therefore, the calibration curve of the change in the emission signal of **JS** over the concentration of Cu^{2+} was plotted at pH 8.0.

a) pH 7.4
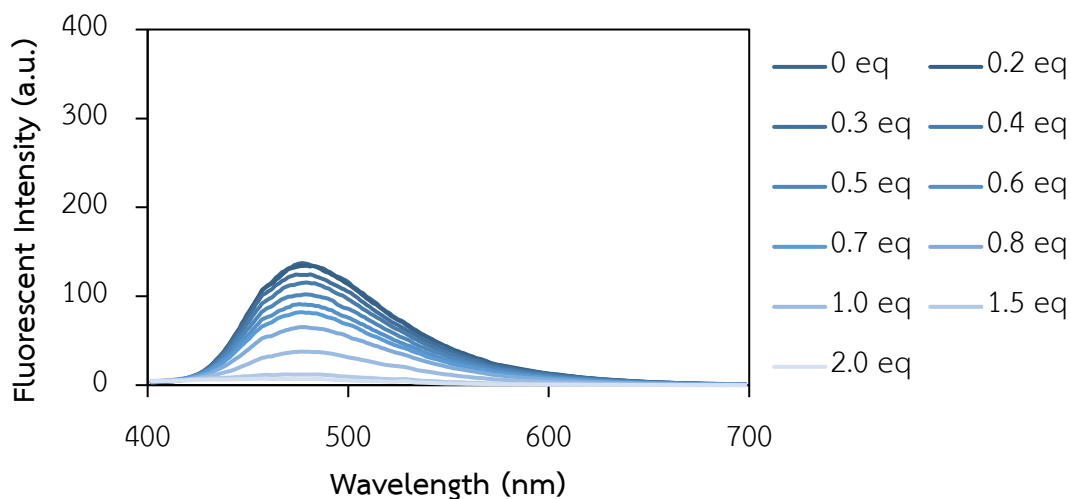
b) pH 8.0
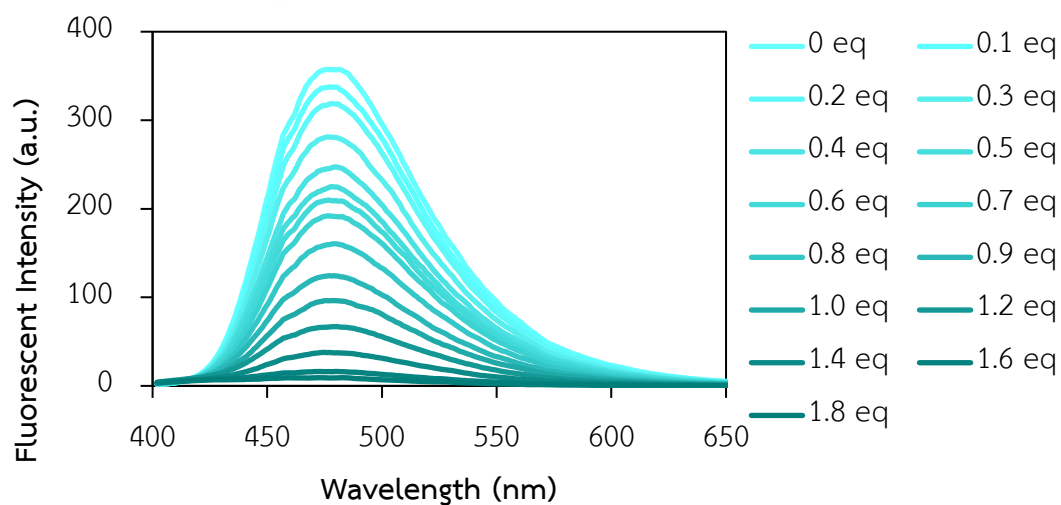
Figure 3.30 The fluorescence titration of **JS** (10 µM) with Cu^{2+} at two different pH
a) pH 7 and b) pH 8.

The time-dependent signal was also investigated to determine the suitable time to plot the calibration curve. As depicted in **Figure 3.31**, the I/I_0 at 480 nm decreases sharply in the first 2 minutes and then gradually constant. Therefore, the calibration curve was plotted 5 minutes after Cu^{2+} was added to **JS**. It is noteworthy that the I/I_0 of free **JS** gradually decreases slowly after 5 minutes indicating that the hydrolysis of **JS** in aqueous might occur.
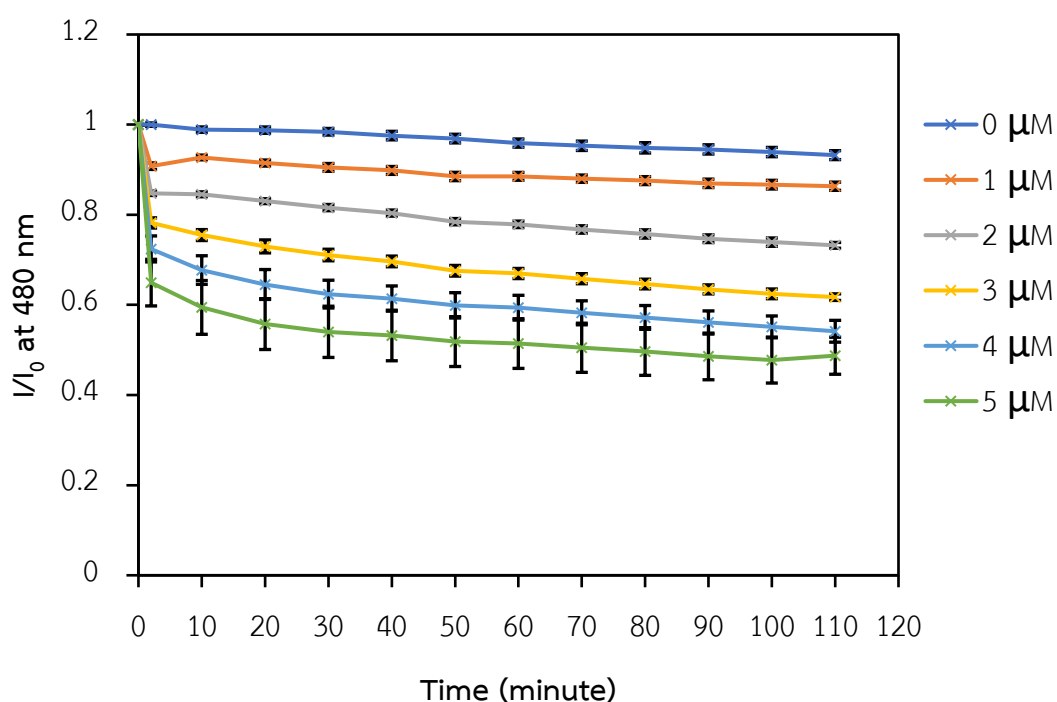
Figure 3.31 Response time of I/I_0 at 480 nm where I_0 is the fluorescence intensity in the absence of Cu^{2+} and I is the fluorescence intensity in the presence of Cu^{2+}. Conditions: [**JS**] = 10 µM, [Cu^{2+}] = 0–5 µM, Buffer: HEPES (50 mM, pH 8.0), 50% (v/v) DMSO/water. λ_{ex} = 370 nm.

The calibration curve was provided by plotting the I_0 - I or ΔI value against the concentration of Cu^{2+} (**Figure 3.32**). The line of best fit is a straight line with a linear range of 0–9 µM and the LOD was calculated to be 1.17 µM.

x 100000
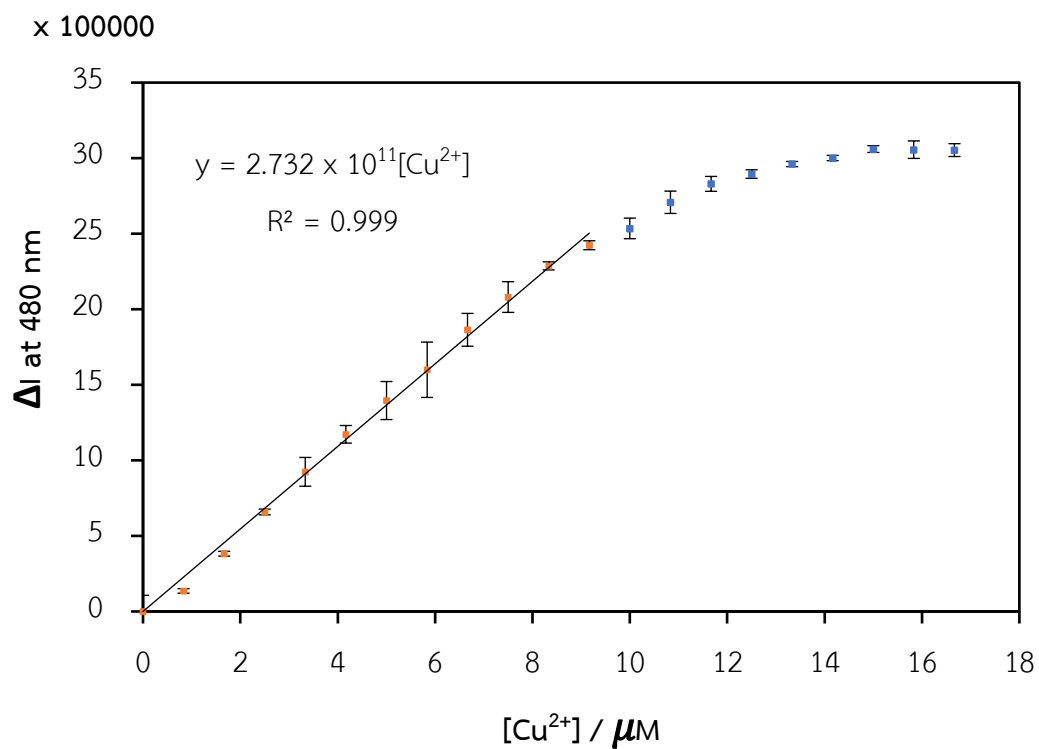
Figure 3.32 The relationship between ΔI at 480 nm and the concentration of Cu^{2+} where ΔI = (Fluorescence intensity before adding Cu^{2+}) – (Fluorescence intensity after adding Cu^{2+}).

3.4.3 Sensing mechanism

As depicted in **Figure 3.33,** the peak at 390 nm in UV-Vis spectra gradually decreased upon the addition of Cu^{2+}, while a new weak band at 420 nm gradually increased indicating that the new substance was generated after the addition of Cu^{2+} into the solution of **JS**.

Data from mass spectroscopy (**Figure 3.34**), and Job's plot (**Figure 3.35**) suggested a formation of a 2:1 complex between **JS** and Cu^{2+}. Since the crystallization of **JS**+Cu^{2+} was not successful, FT-IR spectroscopy and ^{1}H NMR were used to investigate the binding mode of the metal complex. According to ^{1}H NMR spectra (**Figure 3.36**), Cu^{2+} could induce the chemical shifts of all protons on the structure. Noteworthy, the signal of the imine proton of **JS** at 11.6 ppm was shifted and reduced indicating that the Cu^{2+} may induce the deprotonation of the amide proton. In the same way, the IR spectra (**Figure 3.37**) revealed that the peak of N-H stretching ($\approx$3200 cm^{-1}) and the peak around 1580 cm^{-1} which was likely to be C=O stretching of **JS** disappeared in the **JS**+Cu^{2+} complex. It could be inferred that **JS** was in the amidic form when coordination with Cu^{2+}. The plausible complex of **JS**+Cu^{2+} was shown in **Figure 3.38** which is similar to the proposed structure of Shelke et. al. [149].
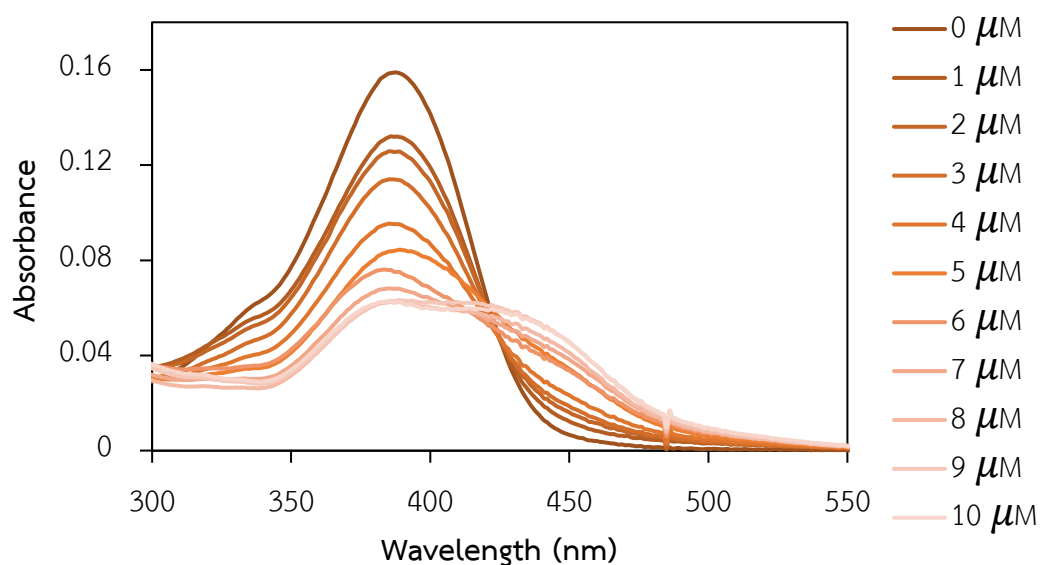
Figure 3.33 The UV-Vis titration of **JS** (10 µM) with Cu^{2+}.
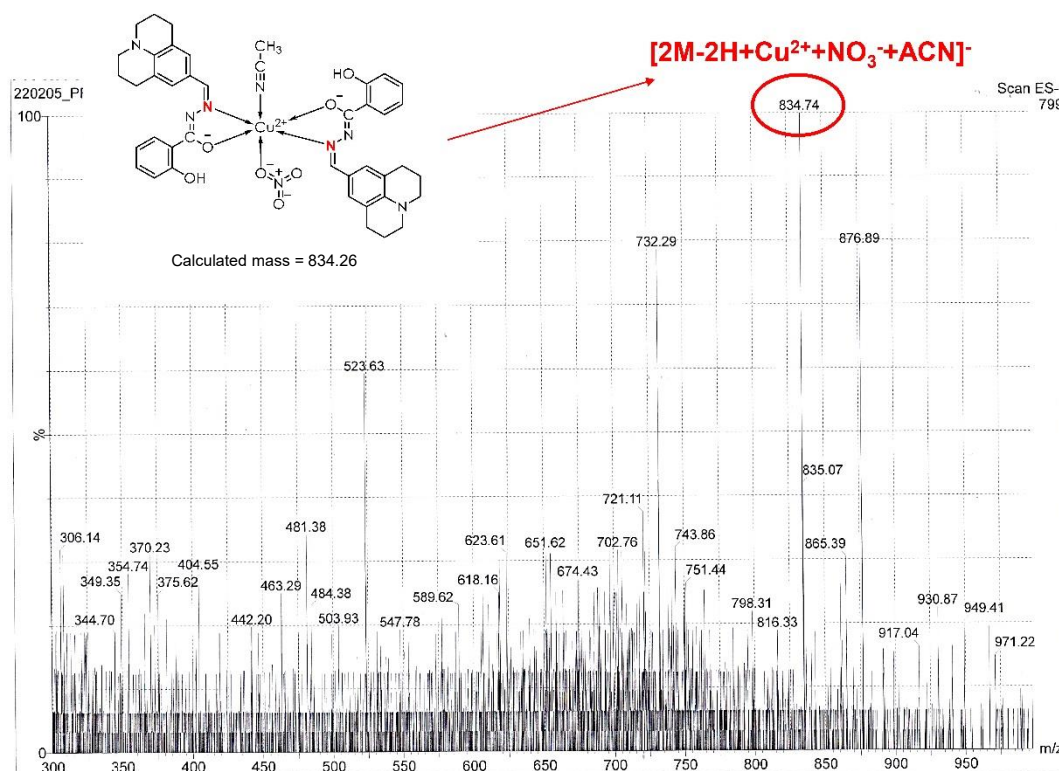
Figure 3.34 ESI-MS spectrum of **JS** + Cu²⁺ complex.
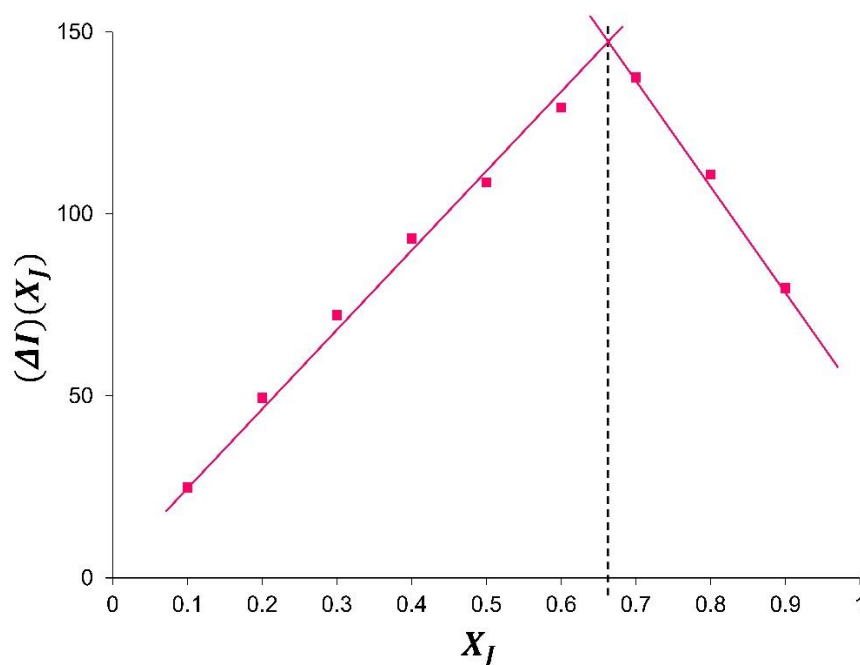
Figure 3.35 Job's plot for the complexation of **JS** with Cu²⁺ (ΔI = change of intensity at 480 nm and χ_J is the mole fraction of **JS**).
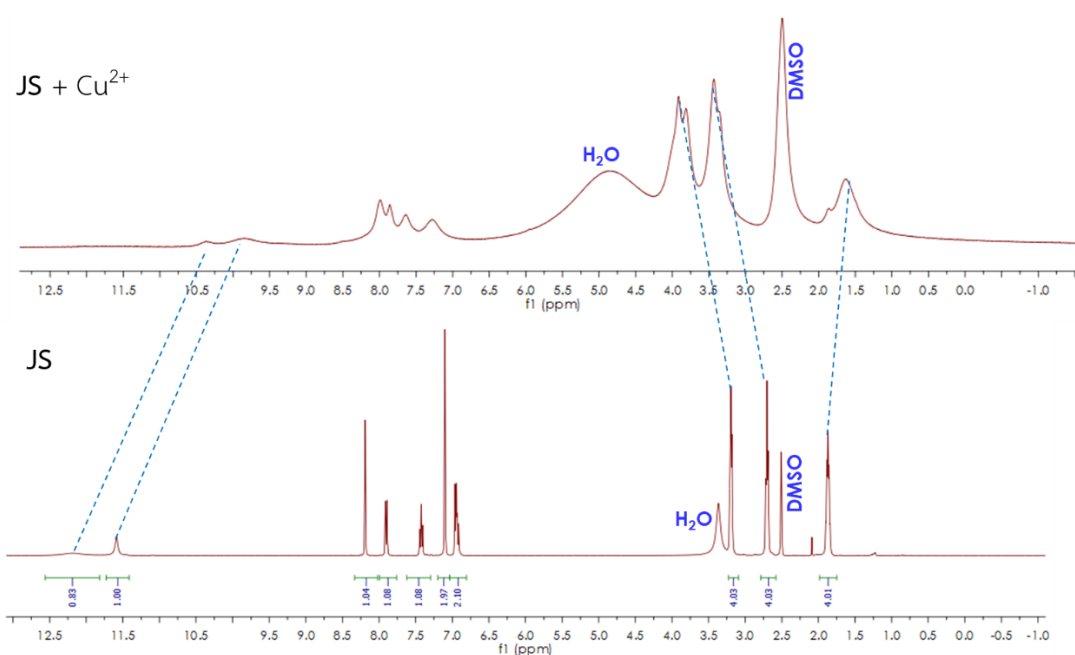
Figure 3.36 ^{1}H NMR spectra of **JS** and **JS**+Cu^{2+} in DMSO-d6
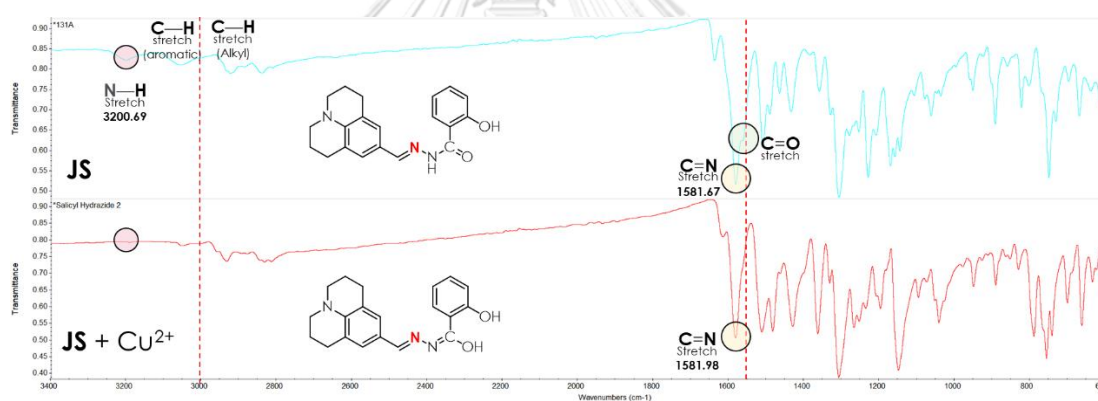
Figure 3.37 IR spectra of **JS** and **JS**+Cu^{2+} in the solid state
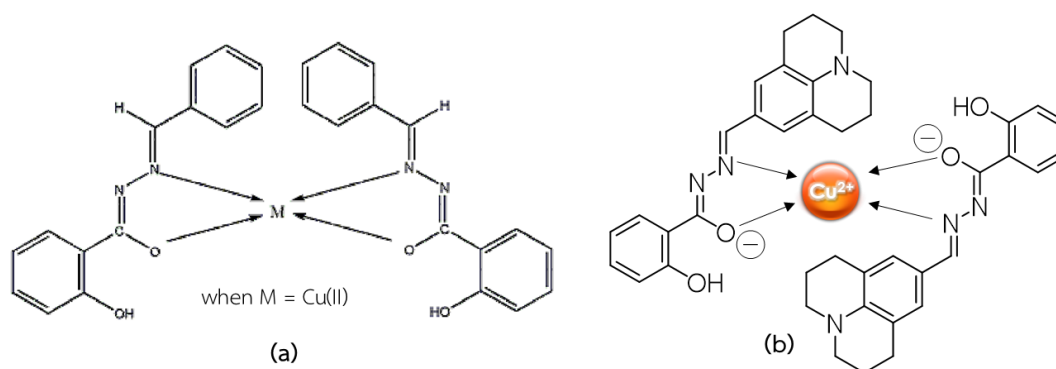
Figure 3.38 (a) The proposed structure of the Cu^{2+} complex by Shelke et. al, [149] (b) The proposed structure in this study

In addition, the Stern-Volmer plots also investigated the quenching mechanism in the detail (**Figure 3.39**). Unexpectedly, the resulting plots showed three linear ranges with different gradients including 0 – 5 μM, 5 - 10 μM, and 10 – 15 μM. From another point of view, the graph looked like an upward curvature in the range of 0 – 15 μM.

According to the equation $I_0/I = 1+K_{sv}[Cu^{2+}]$, the Stern-Volmer constant or K_{sv} (the efficiency and the sensitivity of the turn-off sensor) is equal to the slope of the graph. This result indicated that when the concentration of Cu^{2+} increased, the quenching efficiency increased, and it suggested that more than one mechanism may occur when the concentration of Cu^{2+} increased.
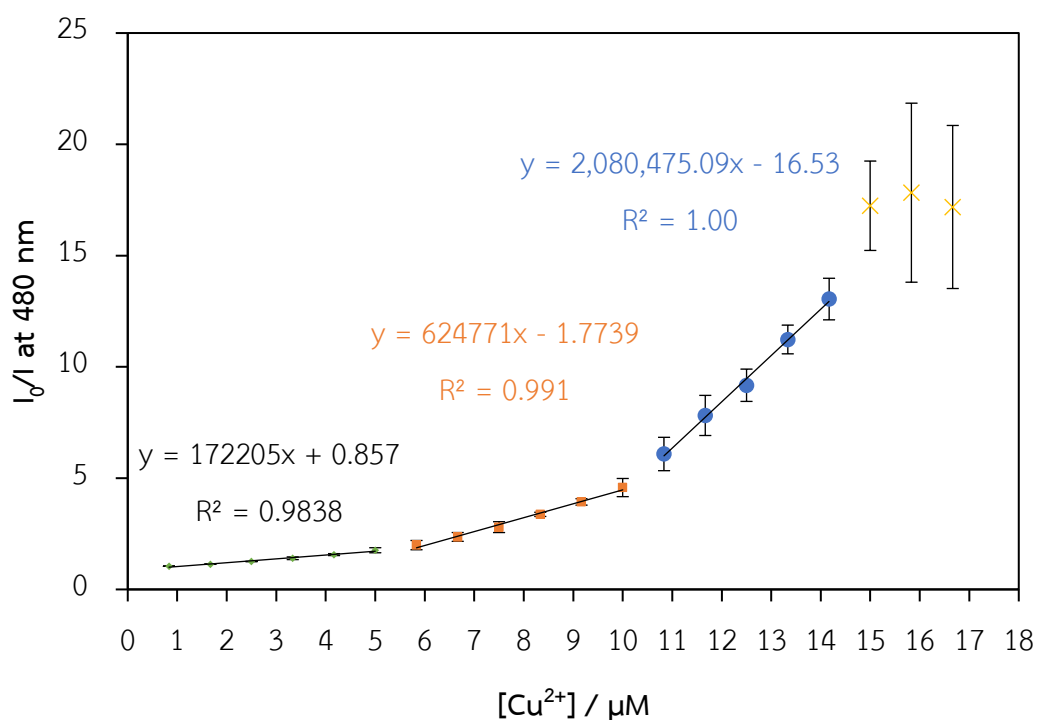
Figure 3.39 The Stern-Volmer plots of quenching of **JS** (10 μM) by Cu^{2+} (0-18 μM)

This hypothesis was proved by the study of temperature-dependent quenching of the fluorescence signal (**Figure 3.40**). The evidence suggested that I_0/I at 50°C was higher than at 25°C, indicating that the higher the temperature, the faster the fluorescence signal quenching occurred. The mechanism may also involve dynamic quenching because the higher temperatures result in faster diffusion and collision.

Therefore, the fluorescence quenching mechanism of **JS** with Cu^{2+} may involve both the formation of a paramagnetic complex and collisional quenching, which lead to a dissipation of the excited state energy into a non-radiative process by spin–orbit coupling. [150]
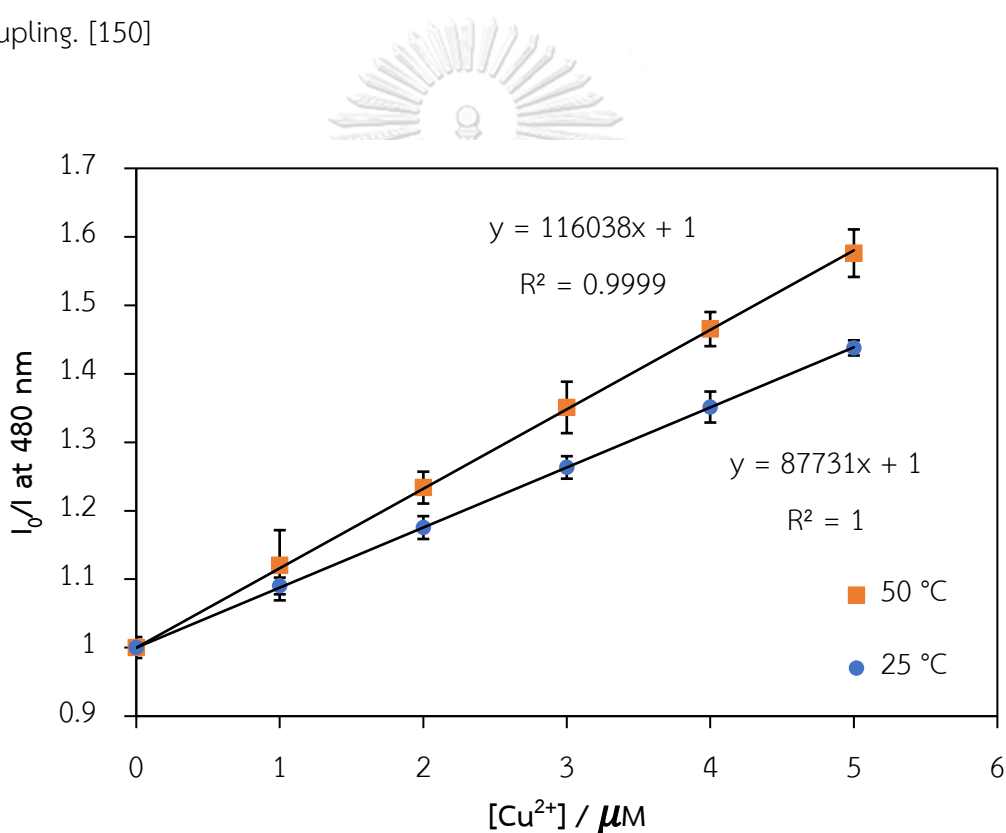
Figure 3.40 The Stern-Volmer plot showing temperature dependence of fluorescence quenching of **JS**+Cu^{2+}

3.4.4   Competitive study

In an interference testing on **JS** (10 µM) with Cu^{2+} (100 µM) and foreign metal ions (100 µM), it was found that the fluorescence quenching was prevented in the presence of Cr^{3+} (**Figure 3.41**). The mass spectrum in **Figure 3.42** indicated that Cr^{3+} could form the complex with **JS** in the ratio of 1:1. Therefore, it could be assumed that the interaction between **JS** and Cr^{3+} may be more preferred than Cu^{2+}, but this interaction did not alter the fluorescence signal of **JS**.
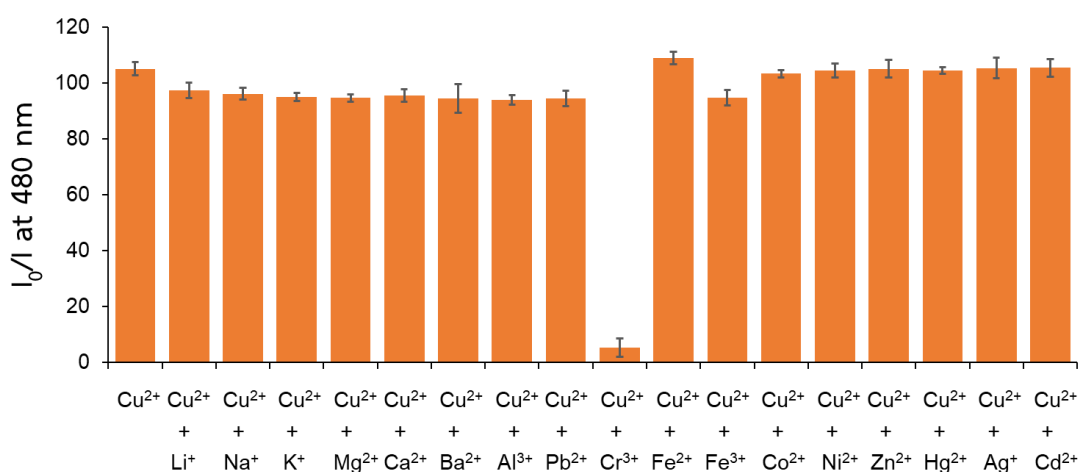
Figure 3.41 Bar chart representing the changes in the relative emission intensities (I_0/I) at 480 nm of **JS**+Cu^{2+} (10 µM/100 µM) in the presence of other metal ions (100 µM) in DMSO/H_2O (1/1, v/v, HEPES pH 8.0)
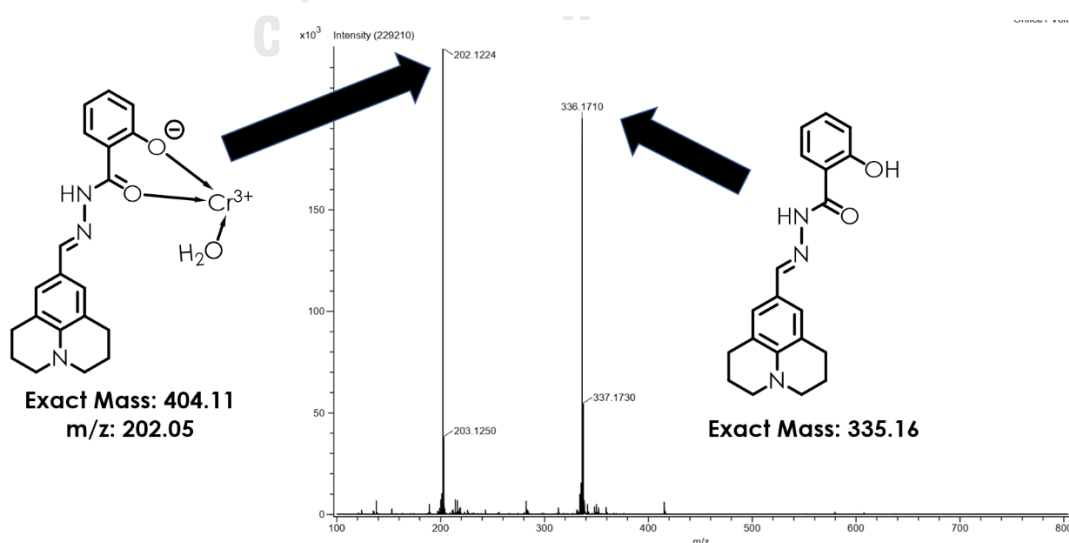
Figure 3.42 DART-MS spectrum of **JS**+Cr^{3+} complex

3.4.5 Reversibility study

3.4.5.1 TLC analysis

From our previous experiences in the development of fluorescent sensors for metal ions, the sensing mechanism usually involved a complex formation between the two species which can be validated by competitive binding with EDTA [151-153].

Upon the addition of Cu^{2+} into **JS**, the newly generated spot which exhibits yellow color under 254 nm UV light did not show the fluorescence properties under 356 nm UV light. After the addition of EDTA, this yellow spot disappeared suggesting that the reaction between **JS** and Cu^{2+} is reversible. Moreover, the julolidine-9-carboxaldehyde (**J**) was also found on the TLC plate indicating that the hydrolysis takes place slowly in the presence of Cu^{2+}.
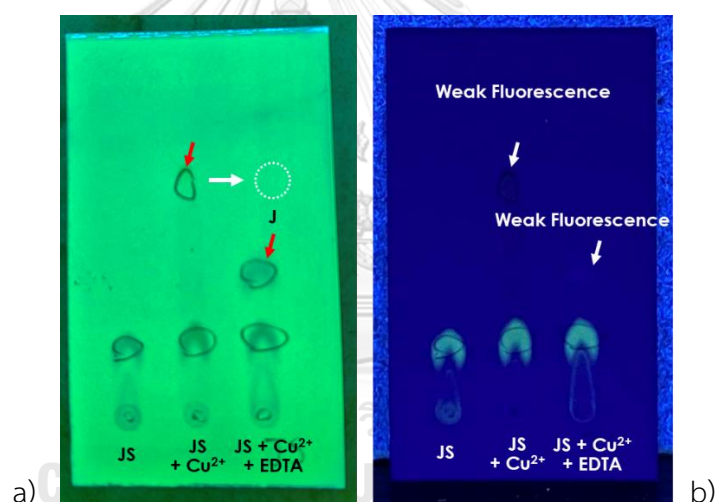
Figure 3.43 The thin layer chromatography (TLC) representing the different R_f values of **JS**, **JS**+Cu^{2+}, and **JS**+Cu^{2+}+EDTA. Stationary phase: silica G, Mobile phase: CH_2Cl_2:Hexane (3:1 v/v). (a) Under 254 nm UV lights and (b) Under 365 nm UV lights.

3.4.5.2   EDTA titration

The EDTA titration experiment was carried out under optimal conditions with a concentration of **JS** and Cu^{2+} to be 10 μM and 15 μM, respectively. The EDTA could recover the fluorescence signal at 480 nm which is the original signal of **JS** indicating that the interaction of Cu^{2+} and **JS** must be reversible. However, EDTA must be consumed up to 90 μM, or 9 equivalents of Cu^{2+}, to reach the maximum signal. This evidence suggests that the binding constant of **JS** with Cu^{2+} is higher than that of Cu^{2+} with EDTA.
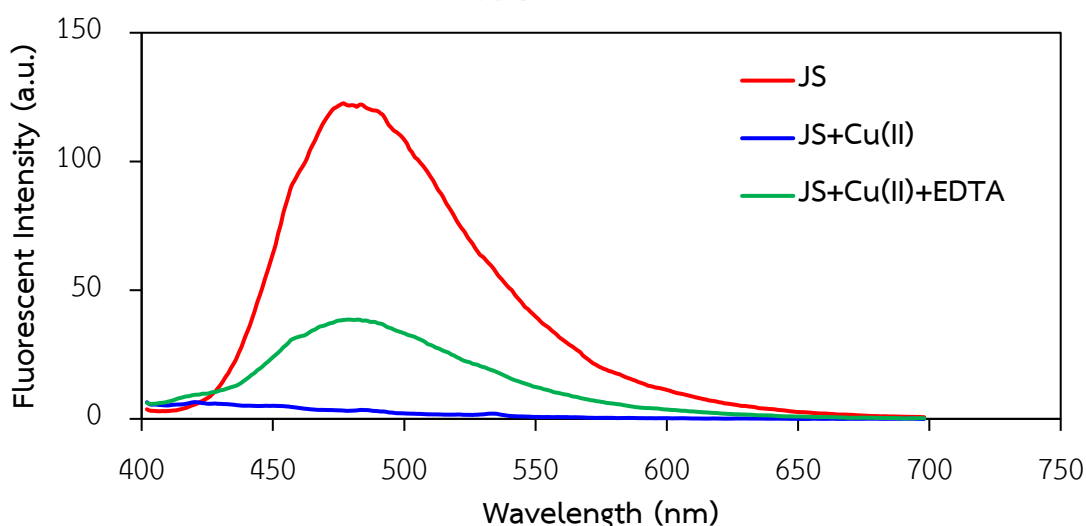
Figure 3.44 Comparison of fluorescence spectra of free **JS**, **JS**+Cu^{2+}, and **JS**+Cu^{2+}+EDTA.
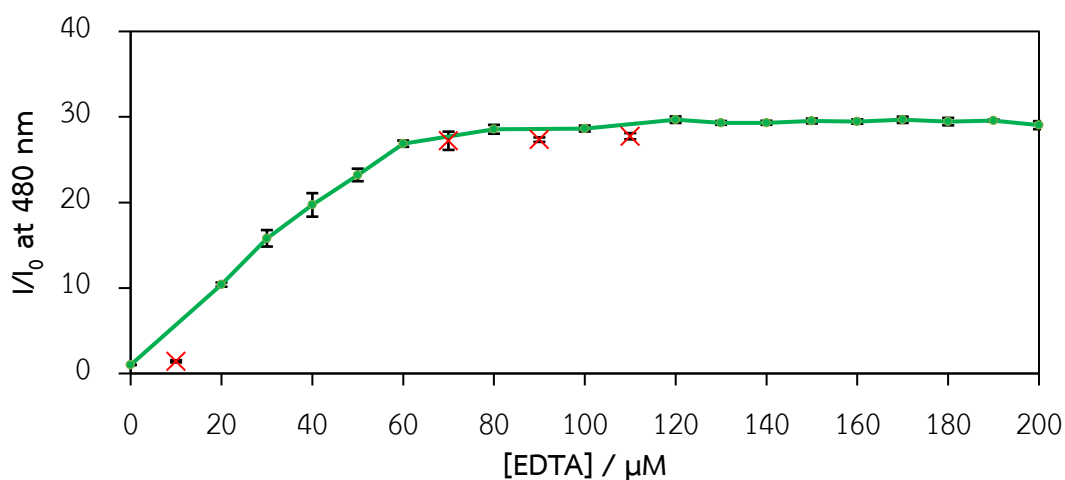
Figure 3.45 EDTA titration of **JS**+Cu^{2+} where "I" is the intensity after the addition of EDTA and "I_0" is the initial signal of **JS**+Cu^{2+}.

3.4.5.3   Histidine titration

As the fluorescent signal of **JS** could be recovered by EDTA, histidine titration was further studied for its application in amino acid sensing. The result from the selectivity study of **JS**+Cu^{2+} with 19 amino acids was showed in **Figure 3.46**. It was found that the addition of histidine into the **JS**+Cu^{2+} solution caused a significant enhancement in the fluorescence signal at 480 nm, whereas the addition of other amino acids slightly brightened the emission signal. The competitive study showed that the enhancement of the emission signal at 480 nm by histidine was not perturbed by any competitive amino acid (**Figure 3.47**).

The linear range of the histidine titration experiment (**Figure 3.48**) was 0-30 µM, and the detection limit was calculated from this equation:

$$\frac{3(0.0516)}{124839} = 24 \text{ µM}$$

The LOD (24 µM) is a relatively high value. Therefore, the application of **JS**+Cu^{2+} to histidine sensing is not appropriate.
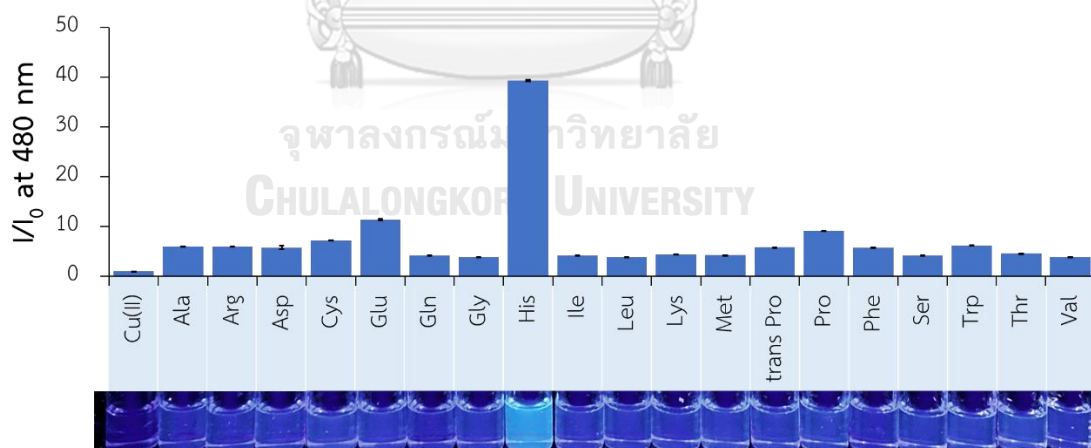
Figure 3.46 Fluorogenic responses at 480 nm of **JS**+Cu^{2+} (10 µM/15 µM) towards various amino acids (50 µM) in 1:1 (v/v) DMSO and 50 mM HEPES buffer pH 8.0.
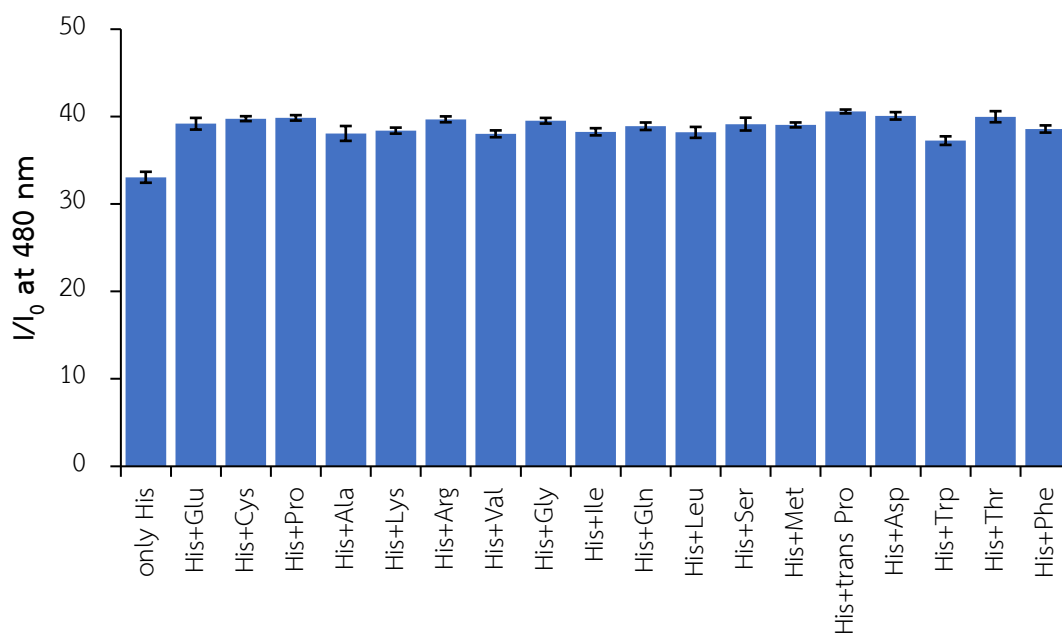
Figure 3.47 Fluorogenic responses at 480 nm of **JS**+Cu^{2+} (10 µM/15 µM) towards the mixture of histidine (50 µM) and other amino acids (50 µM) in 1:1 (v/v) DMSO and 50 mM HEPES buffer pH 8.0.
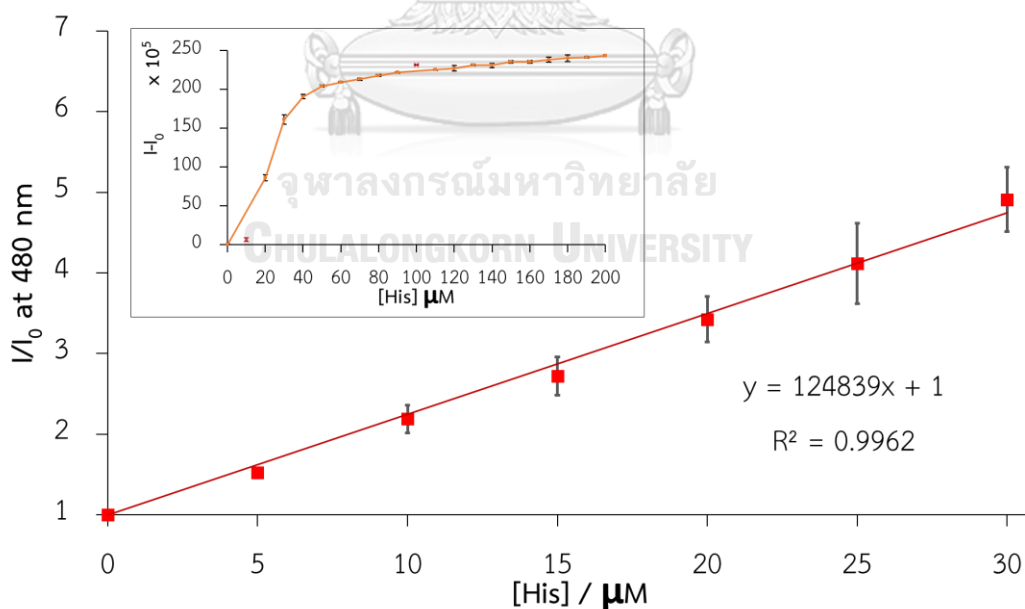
Figure 3.48 Calibration curve for the detection of histidine by **JS**+Cu^{2+} (10 µM/15 µM) in 1:1 (v/v) DMSO and 50 mM HEPES pH 8.0 buffer.

3.5   Metal ion sensing of JP

3.5.1   Screening Test & Selectivity study

The screening tests (**Figure 3.49**) were carried out in different 5 solvents including DMSO, THF, ACN, MeOH, and DMF. The emission color of **JP** solution in each solvent under a blacklight is related to its emission maxima wavelength. However, the emission signal of **JP** in MeOH and ACN under blacklight was relatively low. Upon the addition of testing metal ions, only Hg^{2+} could cause the fluorescence quenching of **JP** in DMSO and THF.
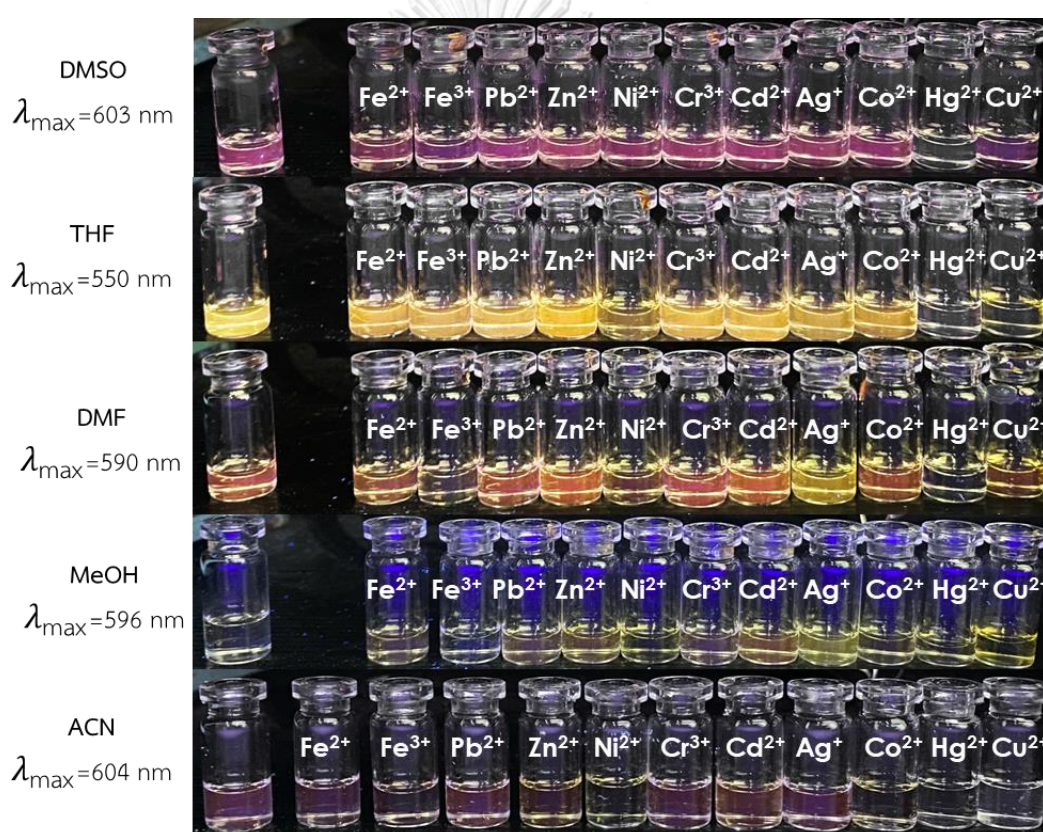
Figure 3.49 Screening test of **JP**

Then, the HEPES buffer pH 7 was added into each mixture to give the 50% v/v of water in DMSO, and the change of signal was observed again. Interestingly, only THF and DMSO could cause the appearance of a blue emission signal. However, we selected DMSO for the selectivity study due to the large stoke shift of the emission signal.

As depicted in **Figure 3.50**, we examined the selectivity of **JP** towards a variety of metal ions in DMSO/H_2O (1:1 v/v, HEPES pH 7.0). The emission signal of **JP** was significantly enhanced and shifted from 440 to 420 nm upon the addition of Cu^{2+}. Under a 365-nm UV irradiation, the original **JP** solution exhibited a weak orange fluorescence. In the presence of Cu^{2+}, a strong blue fluorescence (ϕ = 0.0039) that could be easily observed by the naked eye was emitted from the solution (**Figure 3.5a**). In addition, the interference experiment using a variety of foreign metal ions revealed an exceptional selectivity towards Cu^{2+} (**Figure 3.51**)
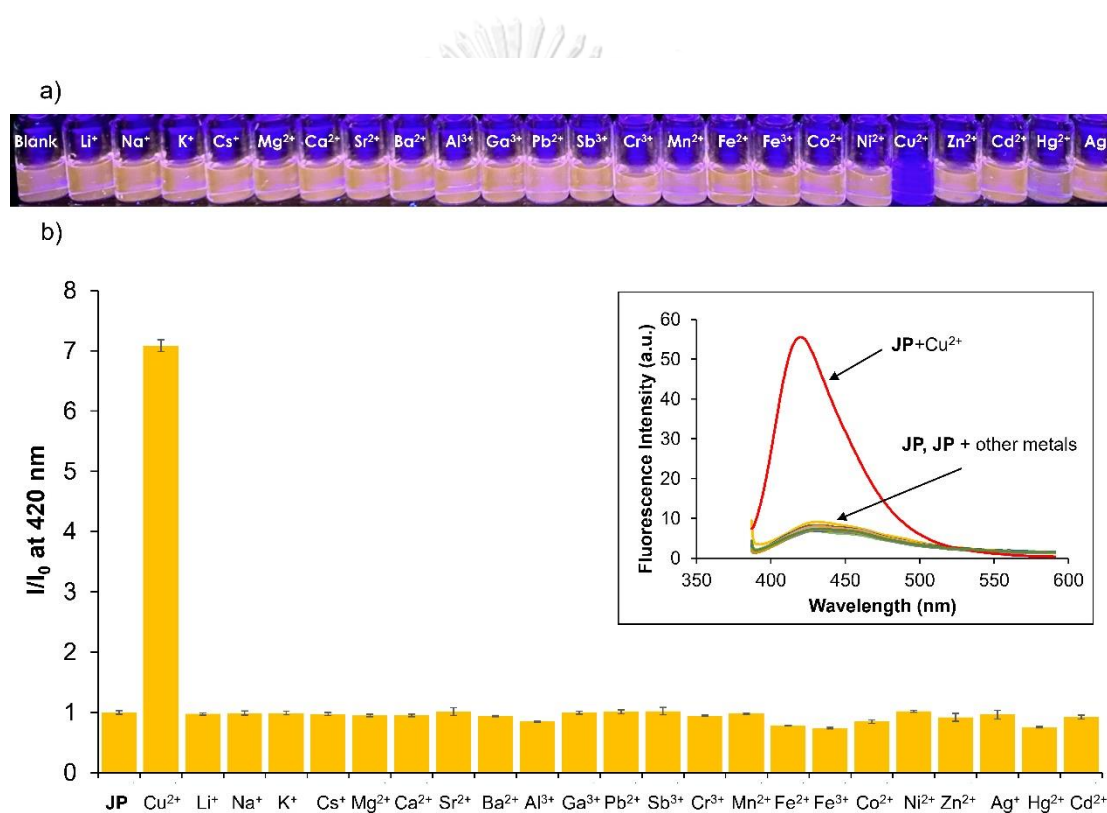
Figure 3.50 a) Photographed images and b) fluorogenic responses (inset: the emission spectra) at 420 nm of **JP** (10 µM) towards various metal ions (100 µM) in 1:1 (v/v) DMSO and 50 mM HEPES pH 7.0 buffer (λ_{ex} = 374 nm).
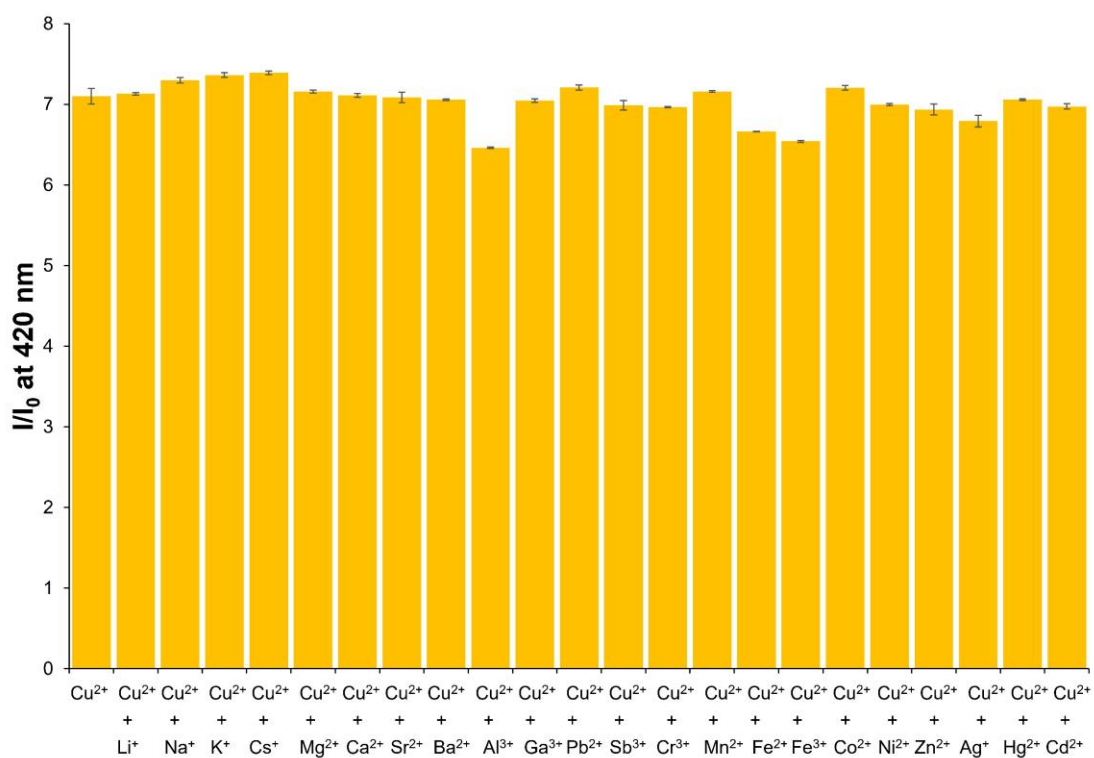
Figure 3.51 Competition selectivity of **JP** (10 μM) toward Cu^{2+} (7.5 equiv.) in the presence of other metal ions (7.5 equiv.) (λ_{em} = 420 nm).

3.5.2 Sensing mechanism

To investigate the sensing mechanism of **JP** for Cu^{2+}, the UV–vis and fluorescence titration experiments were carried out. Upon the addition of Cu^{2+}, the original absorption peak at 393 nm gradually decreased and a new peak at 374 nm immerged (**Figure 3.52**). According to this result, the excitation wavelength for the subsequent fluorescence titration was set at 374 nm. As the amount of Cu^{2+} increased, the fluorescence signal at 420 nm also increased (**Figure 3.53**).

However, the addition of EDTA to the mixture between **JP** and Cu^{2+} did not change both UV absorption and fluorescence spectra to their original wavelengths and intensities (**Figure 3.54 – 3.55**). Results from a TLC analysis, ^{1}H NMR, and mass-spectrometry revealed that the julolidine-9-carboxaldehyde (**J**) was formed when **JP** is mixed with Cu^{2+} (**Figure 3.56 – 3.58**). Moreover, the UV–vis absorption peak at 374 nm and fluorescence signal at 420 nm is the spectral characteristics of **J**.

Therefore, the sensing mechanism may involve an initial complexation in which the picolinohydrazide moiety acts as an "anchoring group" bringing Cu^{2+} near the imine bond. [154] The **JP**-Cu^{2+} complex could then be easily hydrolyzed to generate the fluorescent product **J** and picolinohydrazide (**P**) (**Scheme 3.2**). Interestingly, a catalytic amount of Cu^{2+} ions may be necessary for the hydrolysis of **JP**. However, our data showed that the fluorescence intensity increased along with the concentration of Cu^{2+}. This can be elaborated by the removal of Cu^{2+} from the catalytic cycle due to the formation of a stable complex between Cu^{2+} and **P** as reported by Rodriguez [155].
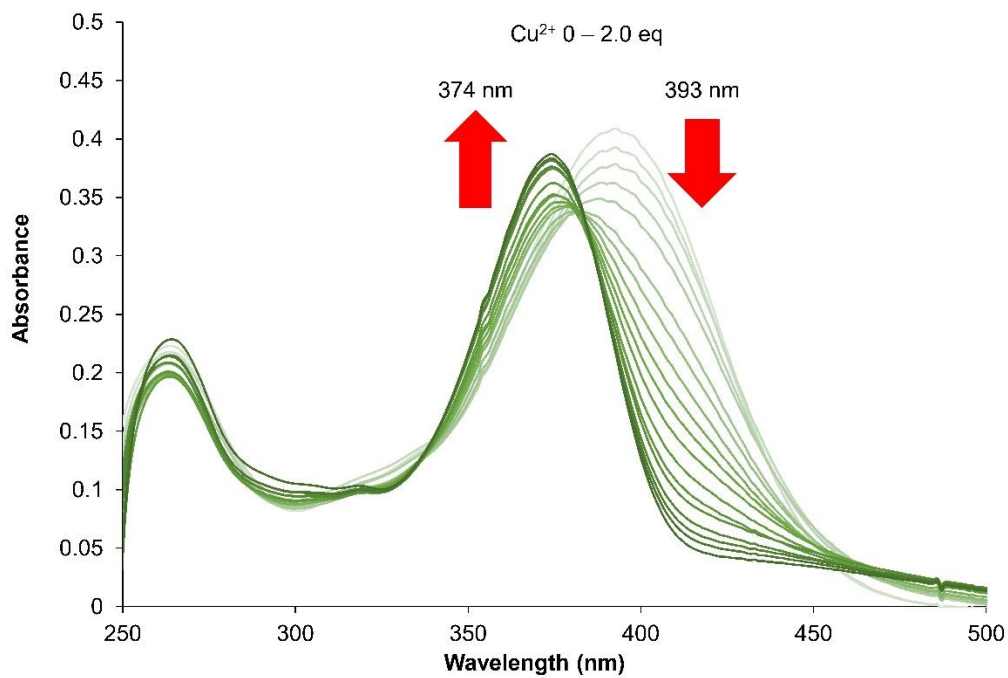
Figure 3.52 UV-Vis titration spectra 60 min after the addition of Cu^{2+} (0 to 20 µM) into **JP** (10 µM) in 1:1 (v/v) DMSO and 50 mM HEPES pH 7.0 buffer
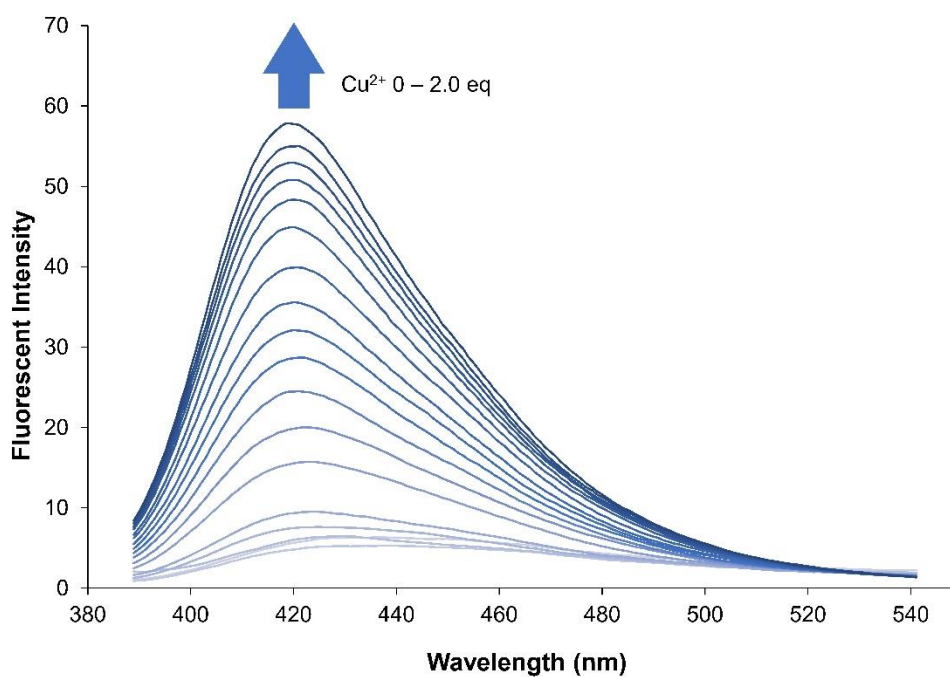
Figure 3.53 Fluorescence titration of **JP** (10 µM) with Cu^{2+} (0 to 20 µM) in 1:1 (v/v) DMSO and 50 mM HEPES pH 7.0 buffer
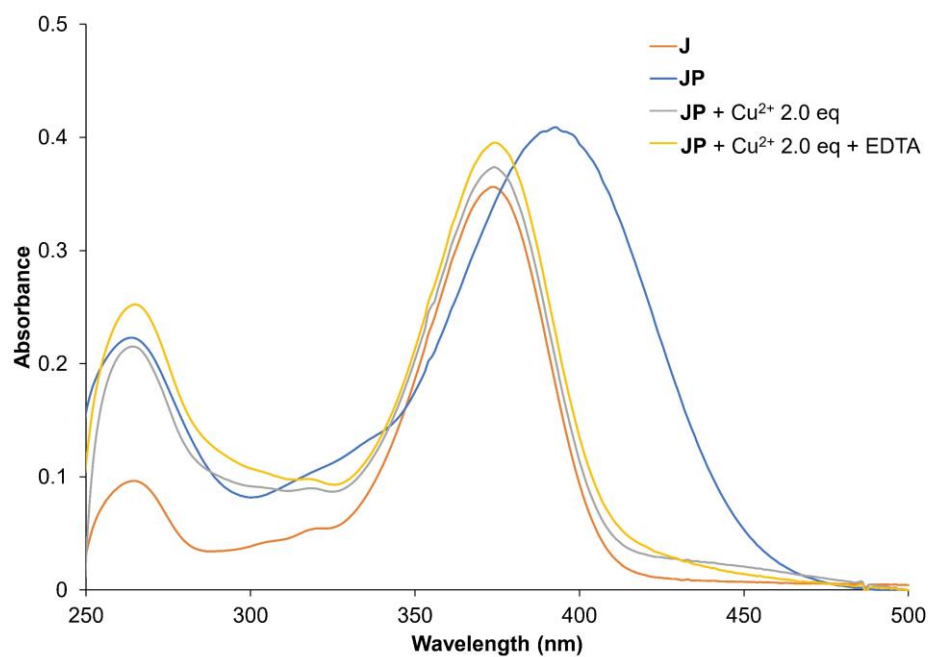
Figure 3.54 Absorption spectra of 10 µM **J**, 10 µM **JP**, 10 µM **JP** + 20 µM Cu^{2+}, and 10 µM **JP** + 20 µM Cu^{2+} + 100 µM EDTA. Buffer: HEPES (50 mM, pH 7.0), 50% (v/v) DMSO/water.
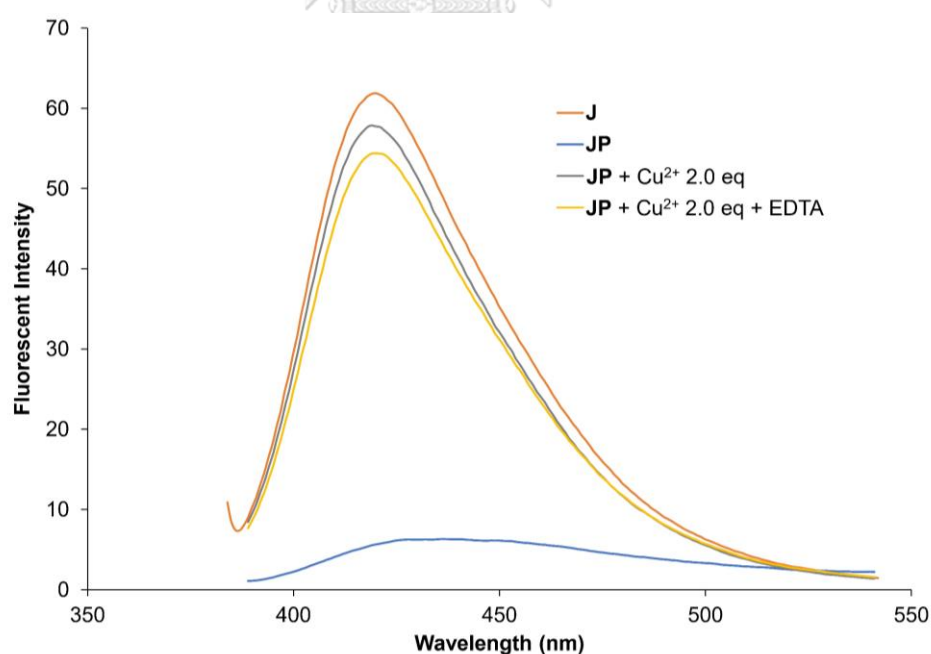
Figure 3.55 Fluorescence emission spectra of 10 µM **J**, 10 µM **JP**, 10 µM **JP** + 20 µM Cu^{2+}, and 10 µM **JP** + 20 µM Cu^{2+} + 100 µM EDTA. Buffer: HEPES (50 mM, pH 7.0), 50% (v/v) DMSO/water. λ_{ex} = 370 nm.
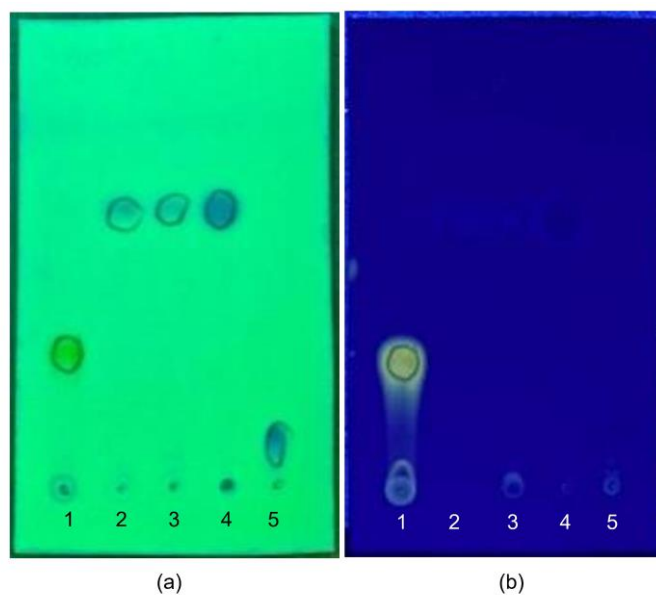
Figure 3.56 Thin layer chromatography (TLC) plates showing: (1) **JP**, (2) **JP**+Cu^{2+}, (3) **JP**+Cu^{2+}+EDTA, (4) **J**, and (5) **P**. Stationary phase: silica G, Mobile phase: n-hexane: Ethyl acetate (1:3 v/v). (a) Under 254 nm UV lights and (b) Under 365 nm UV lights
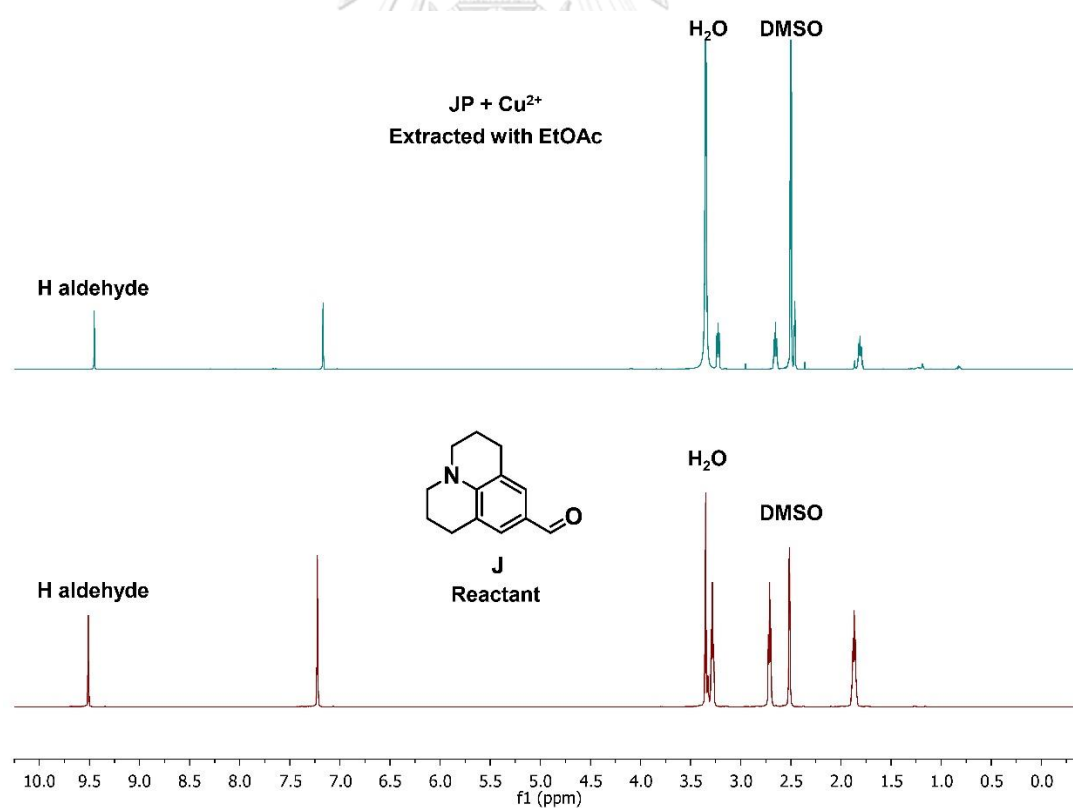
Figure 3.57 ^{1}H-NMR of a crude extract from a mixture between **JP** and Cu^{2+} ion in DMSO-d6 (top), and ^{1}H-NMR of Julolidine-9-carboxaldehyde in DMSO-d6 (bottom).
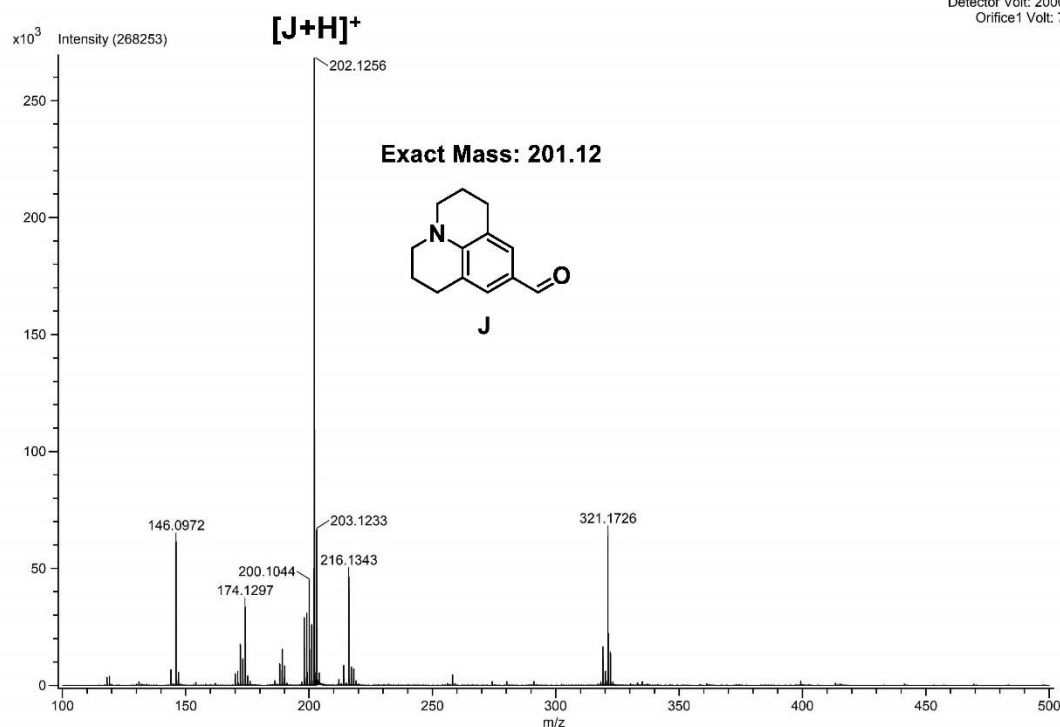
Figure 3.58 Mass spectrum of a crude extract from a mixture between **JP** and Cu^{2+} ion
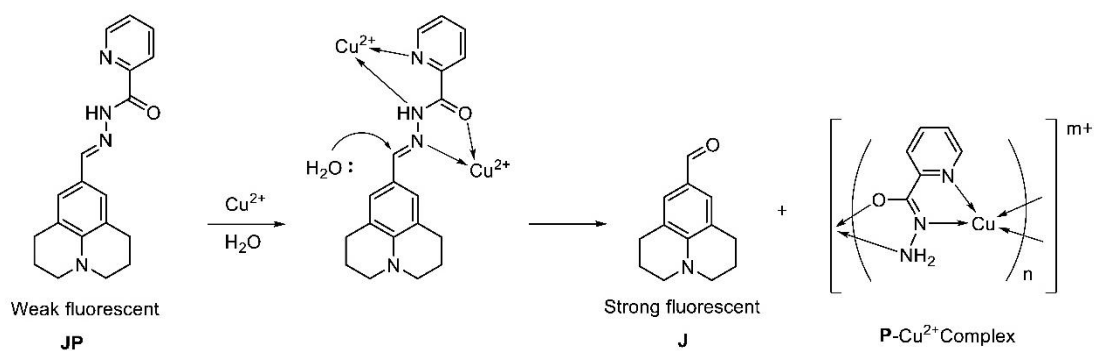
Scheme 3.2 Proposed sensing mechanism of **JP** towards Cu^{2+}

3.5.3 Condition optimization

The influence of pH on the emission response of **JP** to Cu^{2+} ion was examined in a range of buffers with pH values from 3 to 8.5. In the presence of Cu^{2+}, the fluorescence intensity at 420 nm was relatively stable under acidic pH up until pH 8.0 and slightly diminished at pH 8.5 (**Figure 3.59**). This result may involve the precipitation of $Cu(OH)_2$ at higher pHs, which decreased the concentration of free Cu^{2+} ions. In addition, the aqueous buffer content in DMSO was investigated to obtain the optimal condition. When the amount of aqueous buffer increased from 0 to 100 %, the intensity of fluorescence of **JP**+Cu^{2+} at 420 nm decreased significantly as shown in **Figure 3.60**. However, the signal ratio is not much different in the range of 0–50 % of water. Based on the results, we selected 50 % of the aqueous buffer pH 7.0 because it is nearly the environmental sample's condition.
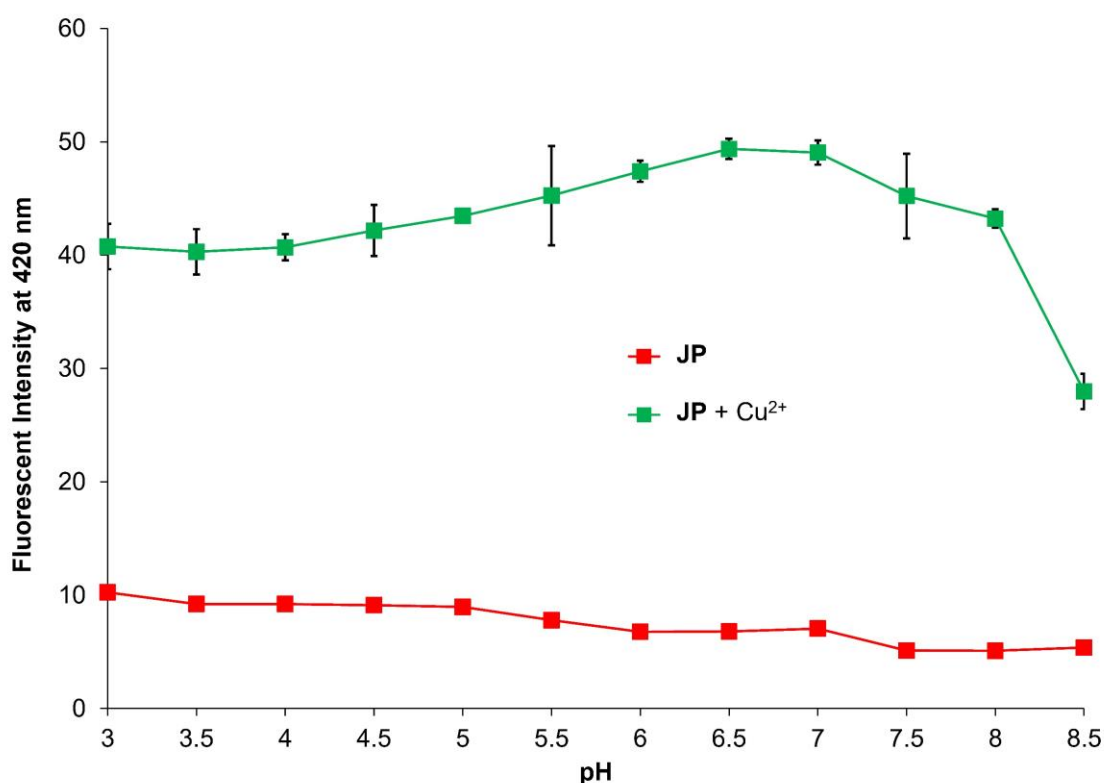
Figure 3.59 pH effect on the hydrolysis of 10 µM **JP** in the absence (red) and presence (green) of 20 µM Cu^{2+}. Buffer: HEPES pH 6.0-8.0 and acetic/acetate pH 3.0-5.0 (50 mM), 50% (v/v) DMSO/water.
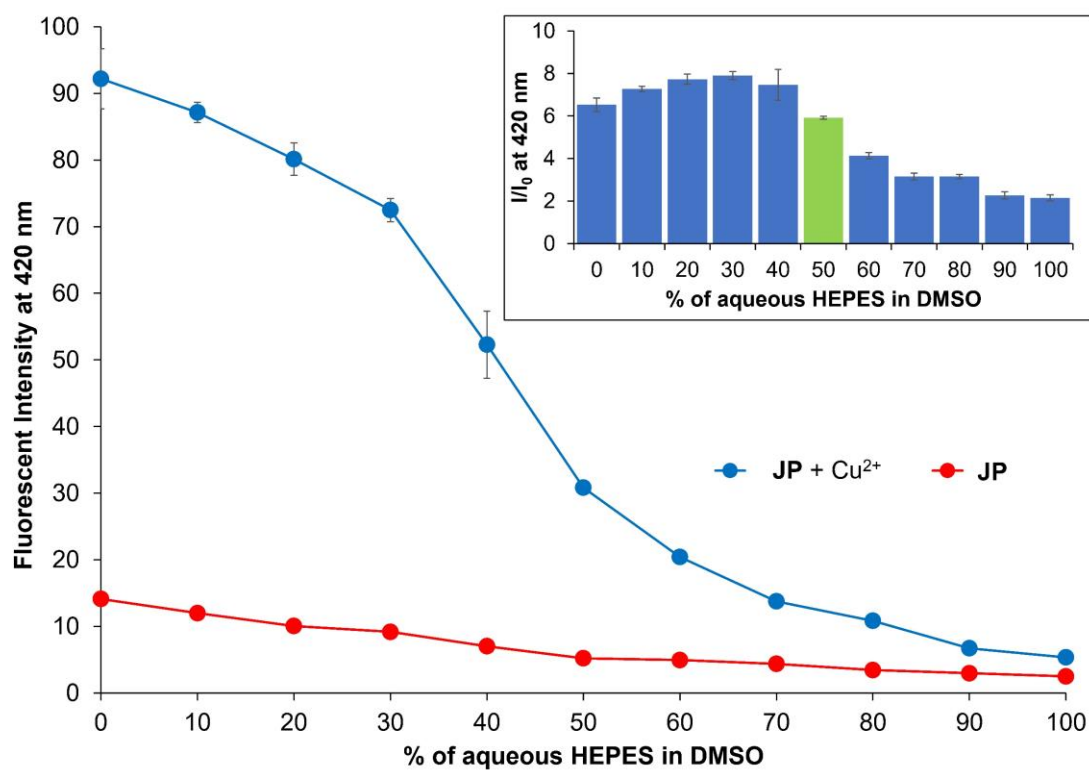
Figure 3.60 Fluorescence intensity at 420 nm of 10 µM **JP** in the absence (red) and presence (blue) of 20 µM Cu^{2+} with varying % aqueous HEPES from 0% to 99%. Inset: Plots of relative emission intensity (I/I_0) versus different % aqueous HEPES

3.5.4 Sensitivity study & Time dependent

Since the mechanism of sensing involves a hydrolysis reaction, it is important to investigate the fluorescence signal change as a function of time at various concentrations of Cu^{2+}. As shown in **Figure 3.61**, the fluorescence enhancement ratio at 420 nm sharply increased during the first 20 min, then reached its plateau at around 60 min. Based on this information, for the optimal conditions, the emission signal will be observed 60 min after **JP** is added into a water sample. When a calibration curve was created from the fluorescence enhancement ratios at 420 nm and Cu^{2+} concentrations (**Figure 3.62**), the detection limit could be estimated at 163 nM or 0.1 ppm. The sensitivity of **JP** is better or comparable to some hydrolysis-based Cu^{2+} fluorescent sensors previously reported in the literature (**Figure 3.63** & **Table 3.2**).
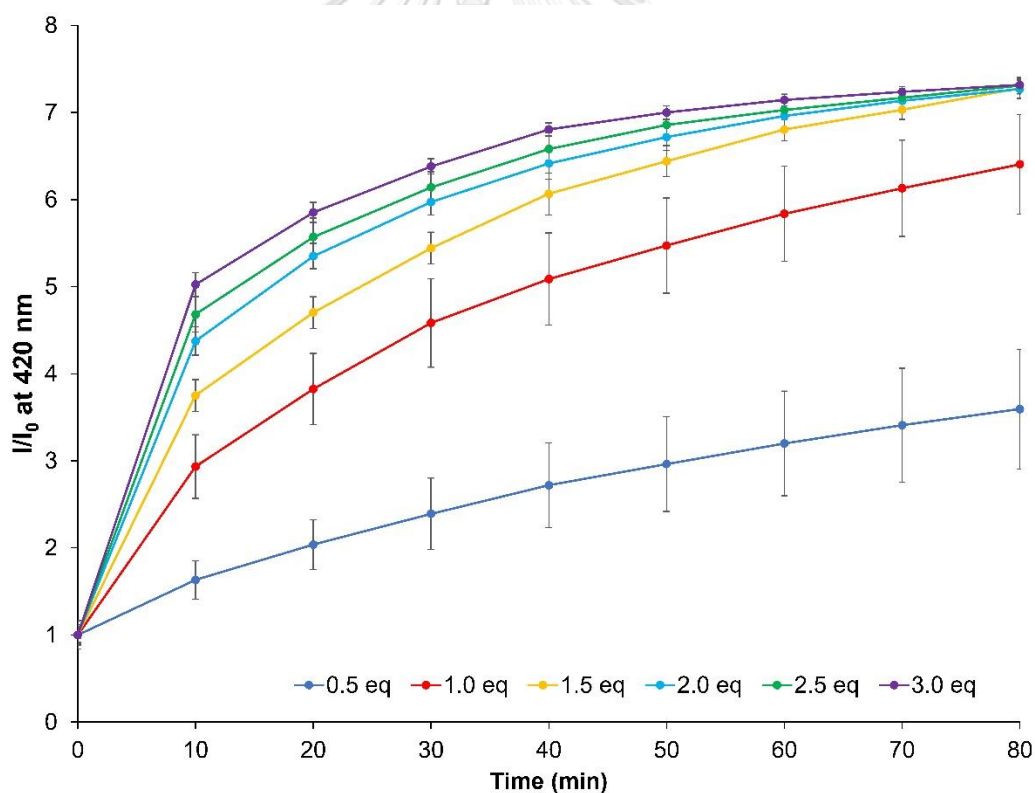
Figure 3.61 Response time of fluorescence enhancement at 420 nm by Cu^{2+}-promoted hydrolysis. Conditions: [**JP**] = 10 μM, [Cu^{2+}] = 0–30 μM, Buffer: HEPES (50 mM, pH 7.0), 50% (v/v) DMSO/water. λ_{ex} = 370 nm.
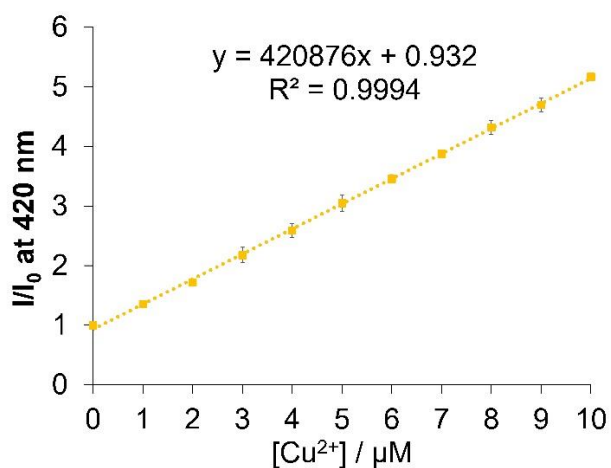
Figure 3.62 Calibration curve for the detection of Cu^{2+} by **JP** (10 µM) in 1:1 (v/v)

DMSO and 50 mM HEPES pH 7.0 buffer
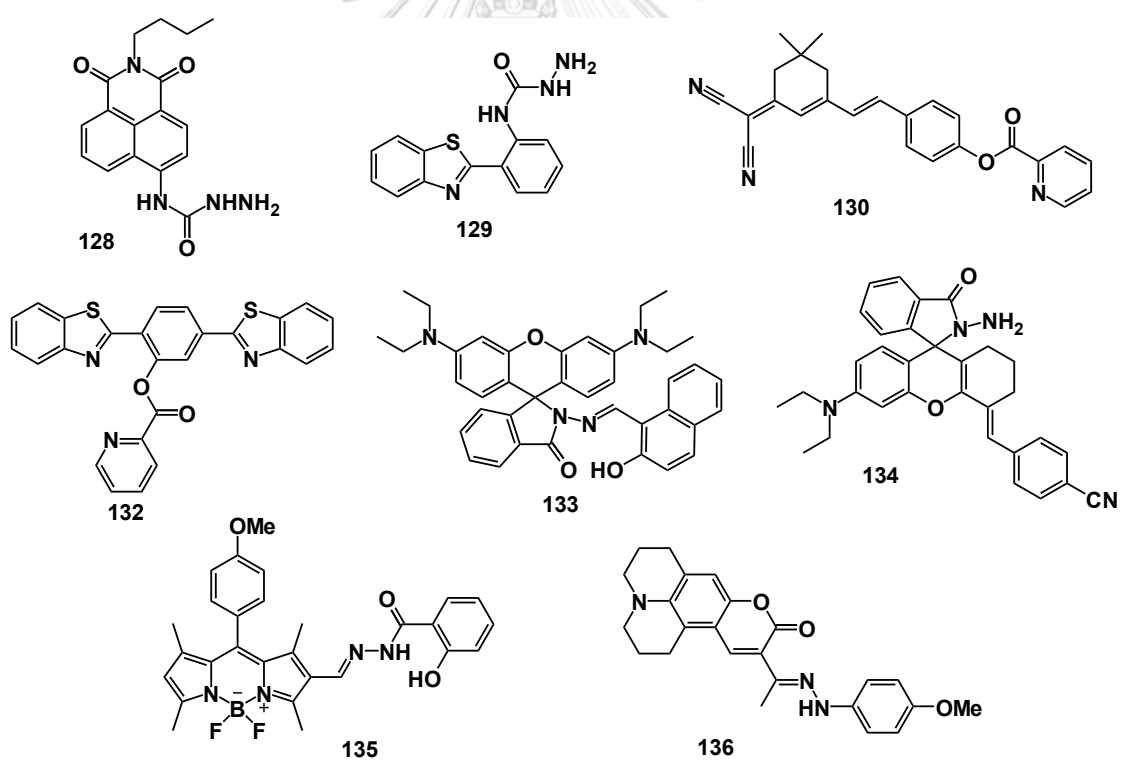
Figure 3.63 The structure of hydrolysis-based Cu^{2+} fluorescent sensors from the

literature.

Table 3.2 Hydrolysis-based Cu^{2+} fluorescent sensors from the literature.

No.	Conditions	Sensing mode	LOD (µM)	Linear range (µM)	Ref
128	MeCN/dimethylglutaric acid-NaOH buffer (pH 7.4, 1:4, v/v)	Turn on	0.052	0.1-10	155
129	DMSO/HEPES buffer (pH 7.0, 8:2, v/v)	Turn on	0.017	-	156
130	MeCN/HEPES buffer (pH = 7.4, 1:4, v/v)	Turn on	0.2	0.5-10	157
131	DMF/HEPES buffer (pH = 7.4, 2:3, v/v)	Ratiometric	0.02	2 – 6	158
132	MeCN/H_2O (1:1 v/v)	Turn on	1.8	0-20	159
133	MeCN	Turn on	0.15	0.5-4	160
134	DMF/H_2O (7:3, v/v)	Ratiometric	0.2	0-1	161
135	MeCN/Acetate buffer (pH = 5.0, 1:1, v/v)	Turn on	0.1	-	162
136	DMSO/HEPES buffer (pH 7.0, 1:1, v/v)	Turn on	0.16	0-10	This work

3.5.5 Analysis in a real water sample

To demonstrate the practicality of **JP** as a selective sensor for Cu^{2+}, four water samples from various sources were spiked with different concentrations of Cu^{2+} (4.00 and 8.00 µM) and analyzed by the optimized method. The result in **Table 3.3** shows that the recovery concentrations of Cu^{2+} analyzed by **JP** were excellent, which means that **JP** can detect Cu^{2+} in water samples with high accuracy and precision.

Table 3.3 Analysis of Cu^{2+} in real samples

Sample	Cu(II) added (µM)	Cu(II) found (µM)	Recovery (%)	R.S.D. (n=3) (%)
Canal water[a]	4.00	3.96	98.95	0.08
	8.00	8.01	100.12	3.24
Pond water[b]	4.00	3.98	99.54	0.47
	8.00	7.80	97.55	3.14
Rainwater	4.00	4.13	103.36	2.26
	8.00	8.40	104.95	7.86
Drinking water	4.00	4.05	101.32	1.15
	8.00	8.03	100.37	1.43

[a] from Bangkok-noi canal in Bangkok, Thailand

[b] from a pond near the main entrance of Chulalongkorn University

PART B: Fluorescence chemosensors from crown ether derivatives of julolidine

3.6 Synthesis plans of JB1, JB2, and JB3

The synthesis plan of three target compounds **JB1, JB2,** and **JB3** that contain different sizes of aza crown ether was shown in **Scheme 3.3**.
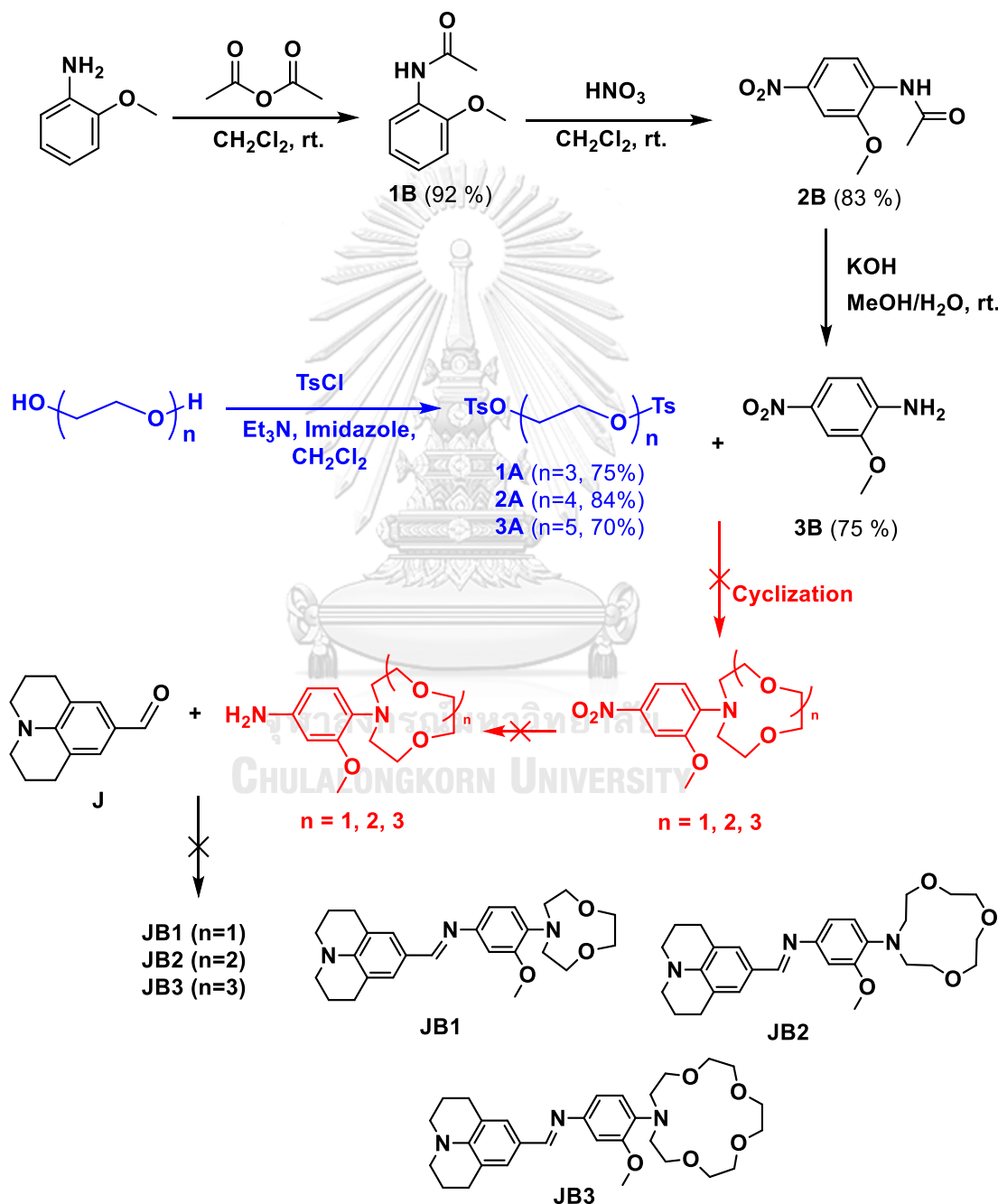
Scheme 3.3 Synthesis plan of target compound **JB1**, **JB2**, and **JB3**.

As depicted in the blue zone of **Scheme 3.3**, tri-, tetra-, and penta ethylene glycol ditosylate was completely synthesized by tosylation of glycol with the tosyl chloride in the mixture of triethylamine and imidazole in dichloromethane. Triethylene glycol ditosylate appeared as a white solid, whereas tetra- and penta ethylene glycol ditosylate appeared as a light-yellow oil. The ^{1}H NMR spectra of these compounds showed a similar pattern of signals (**Figure 3.64**). The integration of proton a b and c revealed that the compound has two toluene moieties. The six equivalents of proton on two methyl groups appear as singlet, while protons b and c on the aromatic ring appear as doublet at around 7.3 and 7.8 ppm, and integration of proton around 3.5 to 4.5 ppm can confirm the number of protons in chain part.
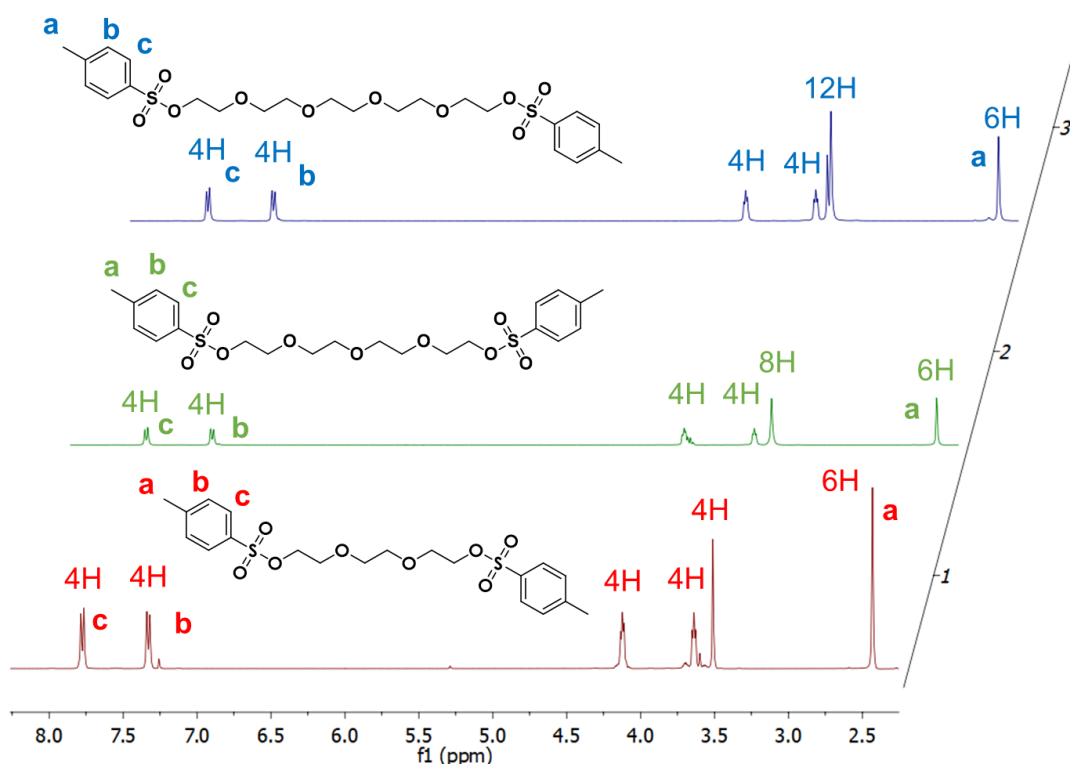
Figure 3.64 ^{1}H NMR spectra of **1A**, **2A**, **3A**.

Meanwhile, the nitration of o-anisidine was successful to generate the nitro compound **3B** (**Scheme 3.3**). Unfortunately, the cyclization step of **1A** - **3A** with **3B** (the red zone in **Scheme 3.3**) was unsuccessful. The ^{1}H NMR spectra of the expected products from the reactions did not correspond to their structures. Although we tried to change the experimental conditions, it did not work.

In addition, the derivative of aza-15-crown-5-ether (**5B**) was synthesized again by another procedure as shown in **Scheme 3.4**. The reaction started with the nucleophilic substitution of 2-bromoethanol with **3B** to produce **4B** and followed by cyclization with triethylene glycol tosylate to produce **5B**. Finally, the ^{1}H NMR spectrum of the product detected from this reaction matched with the literature.

The target sensor **JB3** containing julolidine as a fluorophore and aza-15-crown-5-ether as a chelating unit can be synthesized from the amine **C** and julolidine-9-carboxaldehyde via imination reaction. However, the reduction of nitro group of **5B** to generate compound **C** was not successful because the crude from the reaction decomposed which could be observed by the rapid change of color when expose to the air.
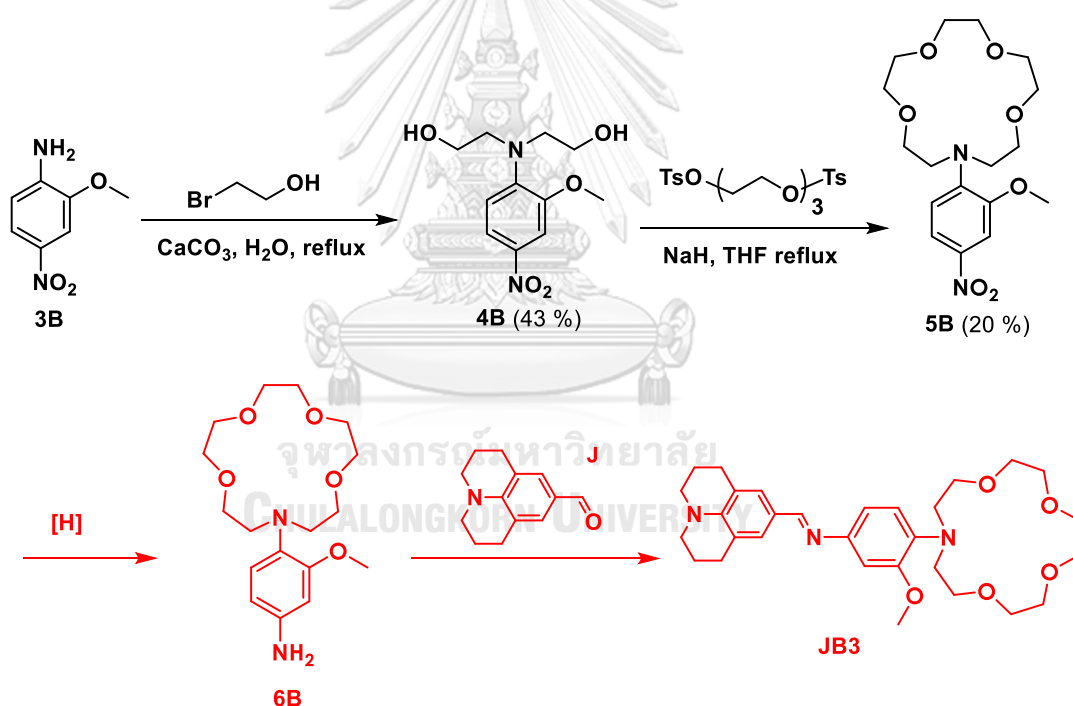
Scheme 3.4 Synthesis of **JB3**.

3.7 Synthesis plans of JC1, JC2, JC3, and JC4

Since the nitro compound **5B** could not be converted to amine, the functionalization plan of o-anisidine was changed from the amino group to aldehyde **3C** for coupling with julolidine-9-carboxaldehyde (**J**). As depicted in **Scheme 3.5**, the aldehyde **3C** was successfully synthesized and confirmed by ^{1}H NMR spectra which match the literature.
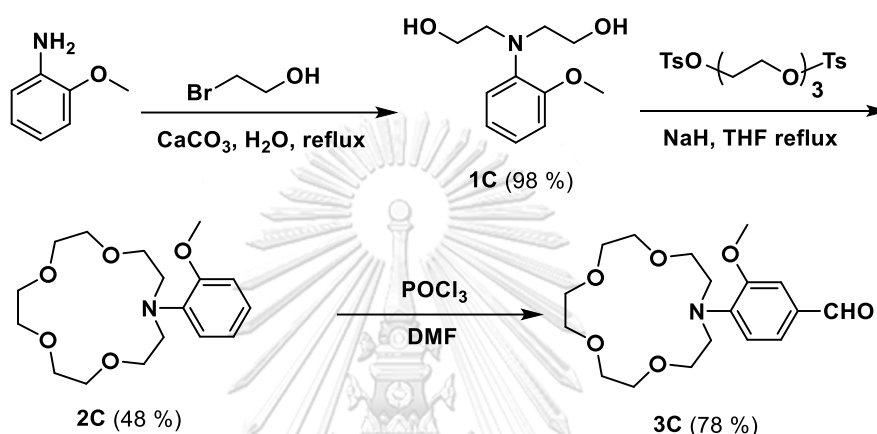
Scheme 3.5 Synthesis of **3C**.

The first target compound **JC1** (**Scheme 3.6**) is theoretically possible to be synthesized from amine **3J** and aldehyde **3C** via an imination reaction. However, the reductive amination of aldehyde **J** to generate amine **3J** was not successful because the reduction of oxime **2J** did not take place by any reducing agents such as Zn in CH_3COOH, $NaBH_3CN$ in HCl and $LiAlH_4$ in THF.
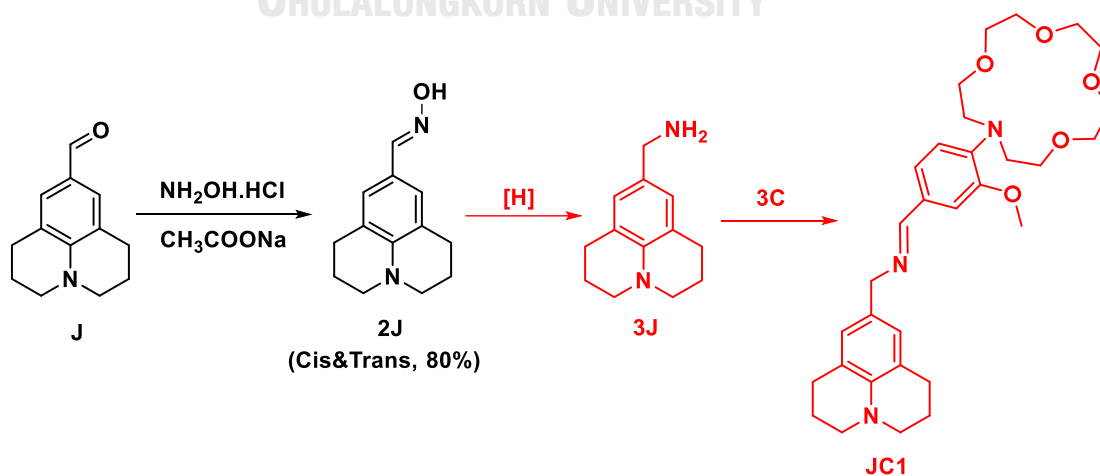
Scheme 3.6 Synthesis plan of **JC1**.

The second target compound **JC2** was designed according to **Scheme 3.7**. This target compound should be synthesized from amine **5J** and aldehyde **3C** via an imination reaction. However, the aldol condensation reaction between **J** and nitromethane to generate the compound **4J** was unsuccessful even though several reactions were tried (**Table 3.4**).
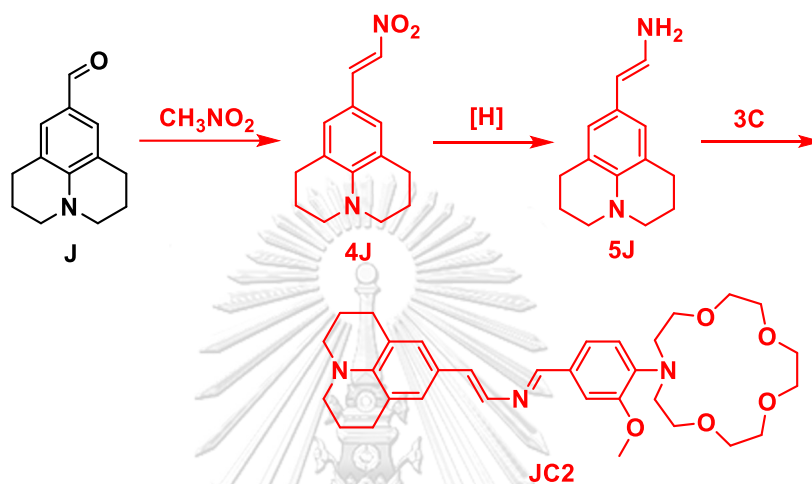
Scheme 3.7 Synthesis plan of **JC2**.

Table 3.4 Synthesis condition of **4J**

No.	J	CH$_3$NO$_2$	Base	Solvent	Temp.	Yield
1	1.2 mmol	excess	K$_2$CO$_3$	-	RT	-
2	0.5 mmol	excess	Cs$_2$CO$_3$	ACN	RT	-
3	1 mmol	excess	NaOH	EtOH	90 °C	-
4	0.5 mmol	excess	Cs$_2$CO$_3$	DMF	RT - 150 °C	Complex mixture

Since the aldol condensation of aldehyde **J** with nitromethane was unsuccessful, the third target compound **JC3** was designed and synthesized by the aldol condensation of **3C** and **J** with acetone instead of nitromethane (**Scheme 3.8**). First step, aldehyde **J** reacted with acetone in an aqueous sodium hydroxide solution to obtain **6J**. After that, methyl ketone **6J** was mixed with aldehyde **3C** in ethanol and an aqueous sodium hydroxide solution to generate **JC3**. The ^{1}H NMR spectrum of **JC3** is shown in **Figure 3.65**. The characteristic peaks of **JC3** appear correctly but there are some noise peaks from decomposition. Noticeably, the color of the **JC3** solution in EtOH gradually changed from yellow to red when it was left in the air.
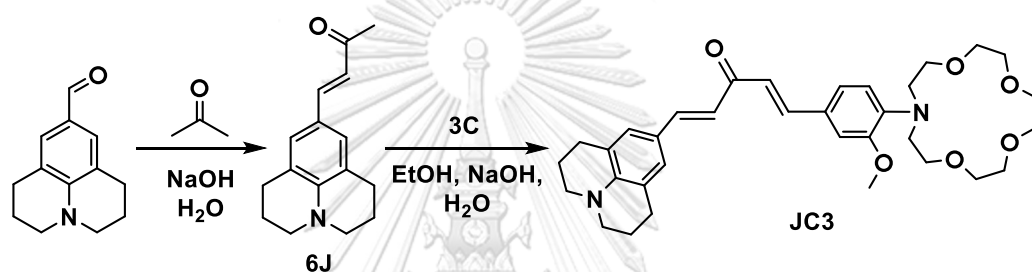
Scheme 3.8 Synthesis of **JC3**.
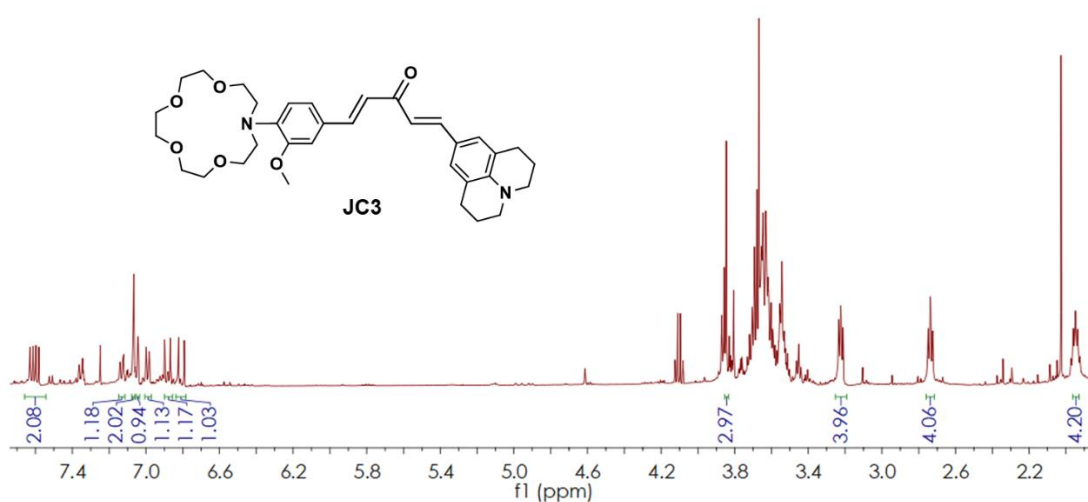
Figure 3.65 ^{1}H NMR spectrum of **JC3**.

Next, the synthesis plan was changed to design the new target compound **JC4.** This compound contains a C=C bond linker between aza crown ether and julolidine moiety. According to the synthetic plan, it can be synthesized by the Wittig reaction between aldehyde **3C** and triphenyl phosphonium ylide **11J** (**Scheme 3.9**). However, ylide **11J** could not be synthesized because the transformation step of **8J** to **9J** did not occur.
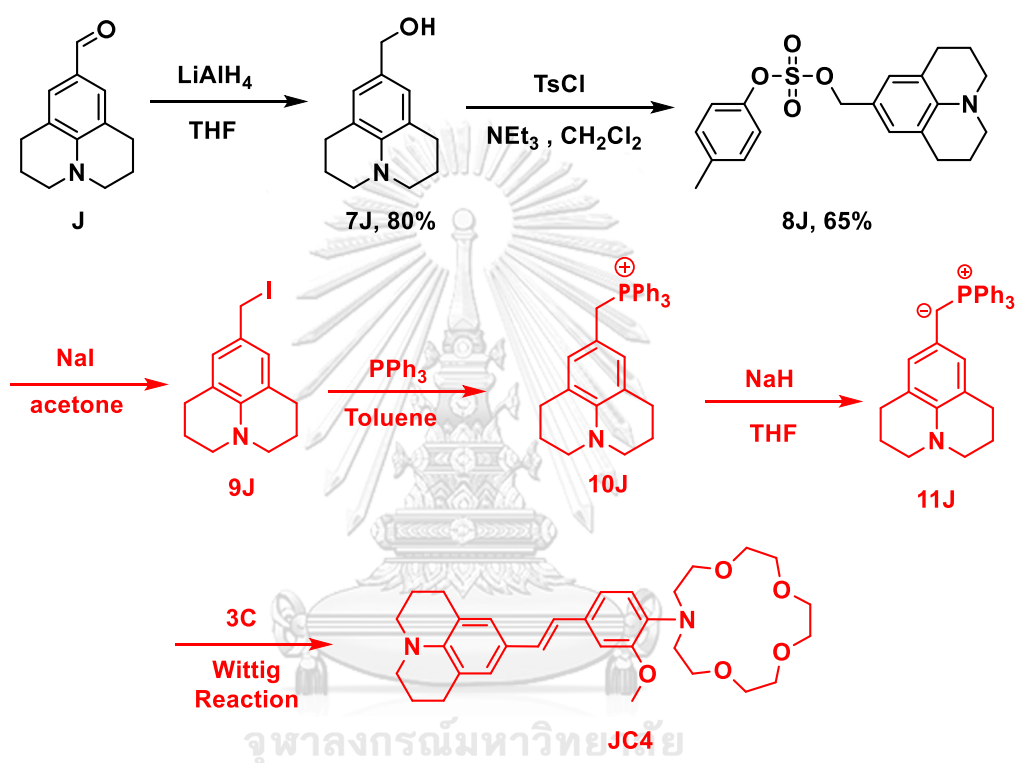
Scheme 3.9 Synthesis plan of **JC4** by Wittig reaction.

In addition, the McMurry coupling method was also carried out for the synthesis of **JC4**. This reaction can be directly accessed to a C=C bond formation between the carbons of the carbonyl groups of compound **J** and **3C** in one step (**Scheme 3.10**). The three possible products from McMerrry reaction between **J** and **3C** include **JJ** from self-coupling of **J**, **CC** from self-coupling of **3C**, and **JC4** from cross-coupling of **J** and **3C**. However, the major product from this reaction is **JJ**, whereas **JC4** was not detected from the crude.
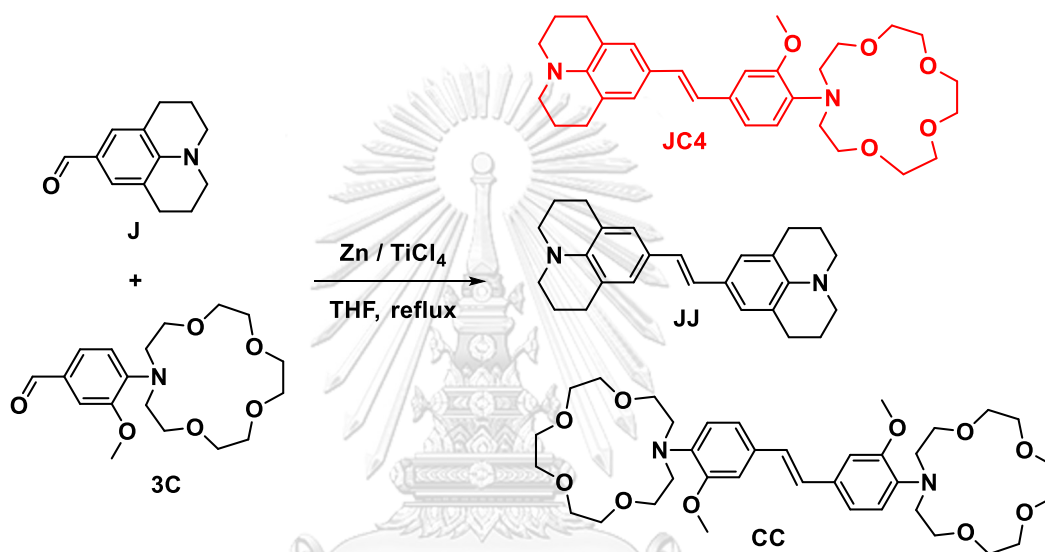
Scheme 3.10 Synthesis plan of **JC4** by McMurry reaction.

None of the synthesis plans have been successful to generate the target compounds. Therefore, the crown ether project has been discontinued.

PART C: Fluorescence chemosensors from hydrazine derivatives of julolidine

3.8   Screening test of JK1, JK2, and JK3

The three hydrazine derivatives **JK1**, **JK2**, and **JK3** were synthesized and investigated in the screening test for metal ion sensing. It was found that only **JK3** showed a change in the fluorescence signal when metal ions were added (**Figure 3.66**). However, the signal changes are not specific to a particular ion. (Note: the characterizations were not provided for all derivatives due to no selectivity for metal ion sensing in the screening test). Therefore, no further study was made.
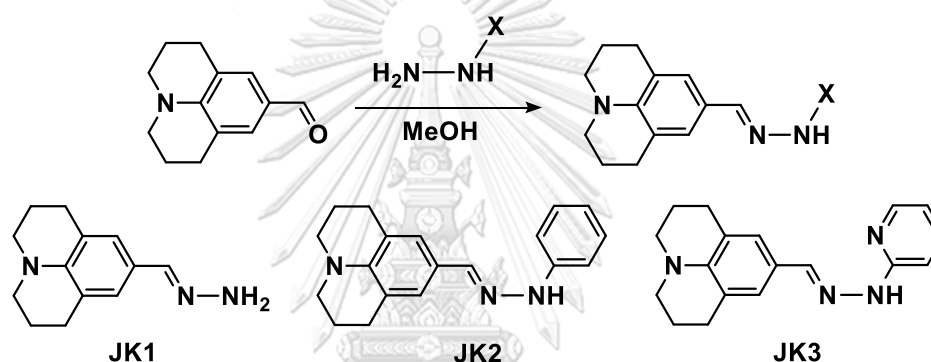
Scheme 3.11 Synthesis of **JK1**, **JK2**, and **JK3**
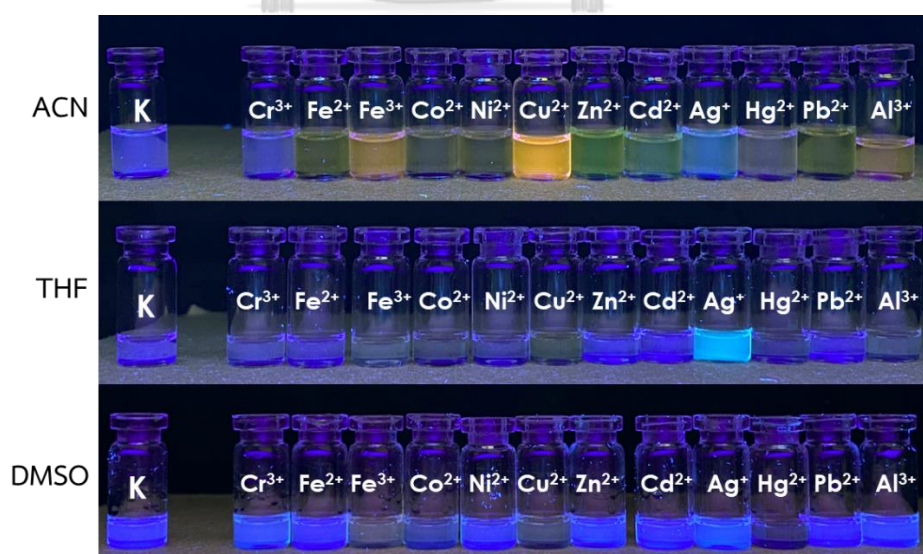
Figure 3.66 The visual changes of **JK3** upon adding various metal ions under a UV light irradiation (365 nm)

CHAPTER IV

CONCLUSIONS

In summary, we have designed and synthesized three new julolidine derivatives and investigated their properties for metal ions detection. The hydrazone from picolinohydrazide (**JP**) exhibits high selectivity and sensitivity towards Cu^{2+} among other competitive metal ions with the enhanced fluorescence emission. All of the spectroscopic data, TLC analysis, and a competitive binding experiment using EDTA indicated that the sensing mechanism involves the Cu^{2+}-triggered hydrolysis reaction of the imine bond. Moreover, **JP** could detect Cu^{2+} across a wide pH range with a detection limit of 0.1 ppm, which was successfully demonstrated in the quantitative analysis of Cu^{2+} in real water samples. This study supports the observation that if the fluorophore used in the sensor design of hydrazide derivatives does not contain hydroxyl groups, the sensing mode takes place via hydrolysis reaction.

In addition, we also designed aza crown ether derivatives of julolidine for metal ion detection. However, there were many obstacles in the coupling steps of the aza crown ether with the julolidine-9-carboxaldehyde. It was found that the reactions on the aldehyde group of the julolidine ring were quite difficult, except for the formation of imines. Therefore, the synthetic plans may have to change the fluorophore to lower the barriers in the synthesis of the desired target molecules.

REFERENCES

REFERENCES

1. *Basic Concepts in Fluorescence. https://micro.magnet.fsu.edu/primer/ techniques/fluorescence /fluorescenceintro.html* (accessed 2023-05-11).

2. Wouterlood, F.; Boekel, A. J., Fluorescence Microscopy in the Neurosciences. 2009; pp 253-260.

3. Deshpande, S. S., Principles and applications of luminescence spectroscopy. *Crit. Rev. Food Sci. Nutr.* **2001**, *41* (3), 155-224.

4. Lakowicz, J. R. *Principles of fluorescence spectroscopy,* 3rd ed. *Springer,* 2006.

5. Pavlova, M.; Panchenko, P., Optical Chemosensors for Cations Based on 1,8-Naphthalimide Derivatives. *INEOS OPEN* **2021**, *4*, 1-16.

6. Sharma, S.; Ghosh, K. S., Overview on recently reported fluorometric sensors for the detection of copper ion based on internal charge transfer (ICT), paramagnetic effect and aggregation induced emission (AIE) mechanisms. *J. Mol. Struct.* **2021**, *1237*, 130324.

7. Liu, Z.; He, W.; Guo, Z., Metal coordination in photoluminescent sensing. *Chem. Soc. Rev.* **2013**, *42* (4), 1568-600.

8. Liu, S.; Wang, Y. M.; Han, J., Fluorescent chemosensors for copper(II) ion: Structure, mechanism and application. *J. Photochem. Photobiol. C: Photochem. Rev.* **2017**, *32*, 78-103.

9. Mohamed, Y.; Müjgan, Y.; Zeynel, S., Optical Chemosensors: Principles, Chemistry, Strategies, and Applications. In *Fluorescence Imaging - Recent Advances and Applications*, Dr. Raffaello, P., Ed. IntechOpen: Rijeka, 2022.

10. Sahoo, S. K.; Sharma, D.; Bera, R. K.; Crisponi, G.; Callan, J. F., Iron(III) selective molecular and supramolecular fluorescent probes. *Chem. Soc. Rev.* **2012**, *41* (21), 7195-227.

11. Li, L.; Wang, J.; Xu, S.; Li, C.; Dong, B., Recent Progress in Fluorescent Probes For Metal Ion Detection. *Front. Chem.* **2022**, *10*, 875241.

12. Balamurugan, R.; Liu, J.-H.; Liu, B.-T., A review of recent developments in fluorescent sensors for the selective detection of palladium ions. *Coord. Chem. Rev.* **2018**, *376*, 196-224.

13. Magri, D. C., Logical sensing with fluorescent molecular logic gates based on photoinduced electron transfer. *Coord. Chem. Rev.* **2021**, *426*, 213598.

14. Misra, R.; Bhattacharyya, S., *Intramolecular Charge Transfer: Theory and Applications*. 2018.

15. Udhayakumari, D., Review on fluorescent sensors-based environmentally related toxic mercury ion detection. *J. Incl. Phenom. Macrocycl. Chem.* **2022**, *102*, 451-476.

16. Bi, X. Synthesis and Characterization of Novel Fluorescent Sensors Based on Terpyridine, Benzoxazole and Benzothiazole Chromophores. University of Akron, Ph.D. Thesis, 2018.

17. Wang, R.; Liu, D.; Xu, K.; Li, J., Substituent and solvent effects on excited state intramolecular proton transfer in novel 2-(2′-hydroxyphenyl) benzothiazole derivatives. *J. Photochem. Photobiol. A: Chem.* **2009**, *205* (1), 61-69.

18. Yang, G.; Li, S.; Wang, S.; Hu, R.; Feng, J.; Li, Y.; Qian, Y., Novel fluorescent probes based on intramolecular charge- and proton-transfer compounds. *Pure Appl. Chem.* **2013**, *85* (7), 1465-1478.

19. Kimuro, Y.; Usui, K.; Karasawa, S.; Hirai, G.; Aso, M., 7-Hydroxy-3-methylene isoindolin-1-one as a new ESIPT-fluorescent probe to monitor aqueous environments. *Chem. Pharm. Bull.* **2017**, *65* (8), 796-800.

20. Cao, Y.; Yu, X.; Sun, C.; Cui, J., Theoretical Investigation on the ESIPT Process and Detection Mechanism for Dual-Proton Type Fluorescent Probe. *Int. J. Mol. Sci.* **2022**, *23* (4). 2132.

21. Ameer-Beg, S.; Ormson, S. M.; Brown, R. G.; Matousek, P.; Towrie, M.; Nibbering, E. T. J.; Foggi, P.; Neuwahl, F. V. R., Ultrafast measurements of excited state intramolecular proton transfer (ESIPT) in room temperature solutions of 3-hydroxyflavone and derivatives. *J. Phys. Chem. A* **2001**, *105* (15), 3709-3718.

22. Sedgwick, A. C.; Wu, L.; Han, H. H.; Bull, S. D.; He, X. P.; James, T. D.; Sessler, J. L.; Tang, B. Z.; Tian, H.; Yoon, J., Excited-state intramolecular proton-transfer

(ESIPT) based fluorescence sensors and imaging agents. *Chem. Soc. Rev.* **2018**, *47* (23), 8842-8880.

23. Wu, J. S.; Liu, W. M.; Zhuang, X. Q.; Wang, F.; Wang, P. F.; Tao, S. L.; Zhang, X. H.; Wu, S. K.; Lee, S. T., Fluorescence turn on of coumarin derivatives by metal cations: A new signaling mechanism based on C=N isomerization. *Org. Lett.* **2007**, *9* (1), 33-36.

24. Ding, S.; Xia, Y.; Lin, X.; Sun, A.; Li, X.; Liu, Y. A theoretical study of the sensing mechanism of a Schiff-Based sensor for fluoride. *Sensors* **2022**, *22*, 3958.

25. Wu, J.; Liu, W.; Ge, J.; Zhang, H.; Wang, P., New sensing mechanisms for design of fluorescent chemosensors emerging in recent years. *Chem. Soc. Rev.* **2011**, *40* (7), 3483-3495.

26. Paul, S.; Das, R.; Banerjee, P., Recent endeavours in the development of organo chromo-fluorogenic probes towards the targeted detection of the toxic industrial pollutants Cu^{2+} and CN^-: recognition to implementation in sensory device. *Mater. Chem. Front.* **2022**, *6* (18), 2561-2595.

27. Chan, J.; Dodani, S. C.; Chang, C. J., Reaction-based small-molecule fluorescent probes for chemoselective bioimaging. *Nat. Chem.* **2012**, *4* (12), 973-984.

28. Kaur, K.; Saini, R.; Kumar, A.; Luxami, V.; Kaur, N.; Singh, P.; Kumar, S., Chemodosimeters: An approach for detection and estimation of biologically and medically relevant metal ions, anions and thiols. *Coord. Chem. Rev.* **2012**, *256*, 1992-2028.

29. Quang, D. T.; Kim, J. S., Fluoro- and chromogenic chemodosimeters for heavy metal ion detection in solution and biospecimens. *Chem. Rev.* **2010**, *110* (10), 6280-6301.

30. Bhatt, R. B. The synthesis of potential anti parasitic compounds. University of Hertfordshire, Ph.D. Thesis, 2001.

31. Nano, A. Towards optical memories: switchable optical systems for electron and energy transfer processes. University of Strasbourg, Ph.D. Thesis, 2015.

32. Anjong, T. F.; Park, Y. M.; Jang, H. Y.; Kim, J., A solvent-dependent fluorogenic probe containing julolidine for Cr(III) and Cu(II). *Kor. Chem. Soc.* **2016**, *37* (6), 905-910.

33.   Choi, Y. W.; Lee, J. J.; You, G. R.; Lee, S. Y.; Kim, C., Chromogenic naked-eye detection of copper ion and fluoride. *RSC Adv.* **2015**, *5* (105), 86463-86472.

34.   Bao, L. Q.; Hai, N. T.; Lee, C. H.; Thogiti, S.; Kim, J. H., Julolidine-based organic dyes with neutral and anion anchoring groups for dye-sensitized solar cells. *J. Nanosci. Nanotechnol.* **2015**, *15* (11), 8813-8819.

35.   Vejdelek, Z.; Protiva, M., Potential antidepressants and tranquillizers: Synthesis of some 9-(aminoalkoxy)-2,3,6,7-tetrahydro-1H,5H-benzo[ij] quinolizines and 1-(substituted amino)-3-(1-naphthoxy)-2-propanols. *Collect. Czech. Chem. Commun.* **1990**, *55*, 1290-1296.

36.   Wang, Z.-S.; Liu, F., Structure-property relationships of organic dyes with D-π-A structure in dye-sensitized solar cells. *Front. Chem. in China* **2010**, *5* (2), 150-161.

37.   Zhu, L. L.; Qu, D. H.; Zhang, D.; Chen, Z. F.; Wang, Q. C.; Tian, H., Dual-mode tunable viscosity sensitivity of a rotor-based fluorescent dye. *Tetrahedron* **2010**, *66* (6), 1254-1260.

38.   Yang, Y.; Liu, F.; Wang, H.; Zhang, M.; Xu, H.; Bo, S.; Liu, J.; Qiu, L.; Zhen, Z.; Liu, X., Synthesis and characterization of a novel second-order nonlinear optical chromophore based on a new julolidine donor. *Phys. Chem. Chem. Phys.* **2014**, *16* (37), 20209-20215.

39.   Abranches, P.; de Paiva, W. F.; de Fatima, A.; Martins, F. T.; Fernandes, S. A., Calix[n]arene-catalyzed three-component Povarov reaction: Microwave-assisted synthesis of julolidines and mechanistic insights. *J. Org. Chem.* **2018,** *83* (4), 1761-1771.

40.   Moss, G. P.; Smith, P. A. S.; Tavernier, D., Glossary of class names of organic compounds and reactivity intermediates based on structure (IUPAC Recommendations 1995). **1995**, *67*, 1307-1375.

41.   Jabeen, M., A comprehensive review on analytical applications of hydrazone derivatives. *J. Turkish chem. soc. sect. chem.* **2022,** *9*, 663-698.

42.   Thiago, M. P.; Arthur, E. K., Hydrazone-based small-molecule chemosensors. In *Computational Biology and Chemistry*, Payam, B.; Nicola, B., Eds. IntechOpen: Rijeka, 2020; p Ch. 6.

43. Su, X.; Aprahamian, I., Hydrazone-based switches, metallo-assemblies and sensors. *Chem. Soc. Rev.* **2014**, *43* (6), 1963-1981.

44. Jabeen, M., Synthesis, characterization and biological studies of some hydrazones and their metal complexes. Thesis, 2016.

45. Maia, R. d. C.; Tesch, R.; Fraga, C. A. M., Acylhydrazone derivatives: a patent review. *Expert Opin. Ther. Pat.* **2014**, *24* (11), 1161-1170.

46. Socea, L. I.; Barbuceanu, S. F.; Pahontu, E. M.; Dumitru, A. C.; Nitulescu, G. M.; Sfetea, R. C.; Apostol, T. V., Acylhydrazones and their biological activity: A review. *Molecules* **2022**, *27* (24), 8719.

47. Wang, J.; Pang, Y., A simple sensitive ESIPT on-off fluorescent sensor for selective detection of Al^{3+} in water. *RSC Adv.* **2014**, *4* (12), 5845-5848.

48. Wang, L.; Yang, J.; Wang, H.; Ran, C.; Su, Y.; Zhao, L., A highly selective turn-on fluorescent probe for the detection of aluminum and its application to bio-imaging. *Sensors* **2019**, *19* (11), 2423.

49. Wu, W. N.; Mao, P. D.; Wang, Y.; Zhao, X.-L.; Xu, Z.-Q.; Xu, Z.-H.; Xue, Y., Quinoline containing acetyl hydrazone: An easily accessible switch-on optical chemosensor for Zn^{2+}. *Spectrochim. Acta A Mol. Biomol. Spectrosc.* **2018**, *188*, 324-331.

50. Wang, L.; Qin, W.; Tang, X.; Dou, W.; Liu, W., Development and applications of fluorescent indicators for Mg^{2+} and Zn^{2+}. *J. Phys. Chem. A* **2011**, *115* (9), 1609-1616.

51. Jun, Z.; Na, L.; Fa, D.; Qing, L.; Yuxiang, J., Synthesis and Characterization of an Al^{3+}-Selective Fluorescent Probe. *Sens. Transducers* **2015**, *186* (3), 125-128.

52. Peng, X.; Tang, X.; Qin, W.; Dou, W.; Guo, Y.; Zheng, J.; Liu, W.; Wang, D., Aroylhydrazone derivative as fluorescent sensor for highly selective recognition of Zn^{2+} ions: syntheses, characterization, crystal structures and spectroscopic properties. *Dalton Trans.* **2011**, *40* (19), 5271-5277.

53. Huang, L.; Cheng, J.; Xie, K.; Xi, P.; Hou, F.; Li, Z.; Xie, G.; Shi, Y.; Liu, H.; Bai, D.; Zeng, Z., Cu^{2+}-selective fluorescent chemosensor based on coumarin and its application in bioimaging. *Dalton Trans.* **2011**, *40* (41), 10815-10817.

54.   Hou, F.; Cheng, J.; Xi, P.; Chen, F.; Huang, L.; Xie, G.; Shi, Y.; Liu, H.; Bai, D.; Zeng, Z., Recognition of copper and hydrogen sulfide in vitro using a fluorescein derivative indicator. *Dalton Trans.* **2012**, *41* (19), 5799-5804.

55.   Zhao, L. Y.; Mi, Q. L.; Wang, G. K.; Chen, J. H.; Zhang, J. F.; Zhao, Q. H.; Zhou, Y., 1,8-Naphthalimide-based 'turn-on' fluorescent sensor for the detection of zinc ion in aqueous media and its applications for bioimaging. *Tetrahedron Lett.* **2013**, *54* (26), 3353-3358.

56.   Liao, Z.-C.; Yang, Z.-Y.; Li, Y.; Wang, B.-D.; Zhou, Q.-X., A simple structure fluorescent chemosensor for high selectivity and sensitivity of aluminum ions. *Dyes Pigm.* **2013**, *97* (1), 124-128.

57.   Lee, S. A.; You, G. R.; Choi, Y. W.; Jo, H. Y.; Kim, A. R.; Noh, I.; Kim, S. J.; Kim, Y.; Kim, C., A new multifunctional Schiff base as a fluorescence sensor for Al^{3+} and a colorimetric sensor for CN^- in aqueous media: an application to bioimaging. *Dalton Trans.* **2014**, *43* (18), 6650-6659.

58.   Liu, Z.; Xu, H.; Sheng, L.; Chen, S.; Huang, D.; Liu, J., A highly selective colorimetric and fluorescent chemosensor for Al(III) based-on simple naphthol in aqueous solution. *Spectrochim. Acta A Mol. Biomol. Spectrosc.* **2016**, *157*, 6-10.

59.   Ji, Y.; Yu, C.; Wen, S.; Zhang, J., Characterization of an Al^{3+}-selective fluorescent probe based on a benzoyl hydrazine derivative and its application in cell imaging. *Turk. J. Chem.* **2016**, *40*, 625-630.

60.   Nan, Q.; Rong, P.; Jiang, Y.; Yang, R., New highly selective turn-on fluorescence receptor for the detection of copper (II). *Spectrochim. Acta A Mol. Biomol. Spectrosc.* **2017**, *174*, 307-315.

61.   Li, A. F.; He, H.; Ruan, Y. B.; Wen, Z. C.; Zhao, J. S.; Jiang, Q. J.; Jiang, Y. B., Oxidative cyclization of *N*-acylhydrazones. Development of highly selective turn-on fluorescent chemodosimeters for Cu^{2+}. *Org. Biomol. Chem.* **2009**, *7* (1), 193-200.

62.   Sharma, S.; Chayawan; Jayaraman, A.; Debnath, J.; Ghosh, K. S., 2-Hydroxy-naphthalene hydrazone based dual-functional chemosensor for ultrasensitive

colorimetric detection of Cu^{2+} and highly selective fluorescence sensing and bioimaging of Al^{3+}. *J. Photochem. Photobiol. A: Chem.* **2023**, *437*, 114408.

63. Gao, C.; Zhu, H.; Zhang, M.; Tan, T.; Chen, J.; Qiu, H., A new highly Zn^{2+}-selective and "off–on" fluorescent chemosensor based on the pyrene group. *Anal. Methods.* **2015**, *7* (19), 8172-8176.

64. Zhang, Q.; Wang, H.; Wang, Y.; Jing, P.; Luo, A.; Huang, Q., A new Schiff base fluorescent indicator for the detection of Mg^{2+} and its application to real samples. *Res. Chem. Intermed.* **2016**, *42* (8), 6681-6693.

65. Liu, B.; Tan, Y.; Hu, Q.; Wang, Y.; Wu, X.; Huang, Q.; Zhang, W.; Zheng, M.; Wang, H., A naked eye fluorescent chemosensor for Zn^{2+} based on triphenylamine derivative and its bioimaging in live cells. *Chem. Pap.* **2019**, *73* (12), 3123-3134.

66. Cheng, X. Y.; Wang, M. F.; Yang, Z. Y.; Li, Y.; Li, T. R.; Liu, C. J.; Zhou, Q. X., A highly sensitive and selective Schiff base fluorescent chemodosimeter for aluminum(III). *J. Coord. Chem.* **2013**, *66* (11), 1847-1853.

67. Ma, J.; Shi, W.; Feng, L.; Chen, Y.; Fan, K.; Hao, Y.; Hui, Y.; Xie, Z., A highly selective and sensitive acylhydrazone-based turn-on optical sensor for Al^{3+}. *RSC Adv.* **2016**, *6* (33), 28034-28037.

68. Liu, T. T.; Xu, J.; Liu, C. G.; Zeng, S.; Xing, Z. Y.; Sun, X. J.; Li, J. L., A novel dual-function probe for recognition and differentiation of Zn^{2+} and Al^{3+} and its application. *J. Mol. Liq.* **2020**, *300*, 112250.

69. Wang, J. X.; Xing, Z. Y.; Tian, Z. N.; Wu, D. Q.; Xiang, Y. Y.; Li, J. L., A dual-functional probe for sensing pH change and ratiometric detection of Cu^{2+}. *Spectrochim. Acta A Mol. Biomol. Spectrosc.* **2020**, *235*, 118318.

70. Chen, H.; Yang, P.; Li, Y.; Zhang, L.; Ding, F.; He, X.; Shen, J., Insight into triphenylamine and coumarin serving as copper (II) sensors with "OFF" strategy and for bio-imaging in living cells. *Spectrochim. Acta A Mol. Biomol. Spectrosc.* **2020**, *224*, 117384.

71. Fan, Z.; Ye, J.-H.; Bai, Y.; Bian, S.; Wang, X.; Zhang, W.; He, W., A new dual-channel ratiometric fluorescent chemodosimeter for Cu^{2+} and its imaging in living cells. *Tetrahedron Lett.* **2016**, *57* (47), 5281-5285.

72. Lu, Z.; Fan, W.; Lu, Y.; Fan, C.; Zhao, H.; Guo, K.; Chu, W.; Lu, Y., A highly sensitive fluorescent probe for bioimaging zinc ion in living cells and zebrafish models. *New J. Chem.* **2018**, *42* (14), 12198-12204.

73. Lu, Z.; Lu, Y.; Fan, W.; Fan, C.; Li, Y., Ultra-fast zinc ion detection in living cells and zebrafish by a light-up fluorescent probe. *Spectrochim. Acta A Mol. Biomol. Spectrosc.* **2019**, *206*, 295-301.

74. Yu, C.; Ji, Y.; Wen, S.; Zhang, J., Synthesis and characterization of a Mg^{2+}-Selective probe based on benzoyl hydrazine derivative and its application in cell imaging. *Molecules* **2021**, *26* (9), 2457.

75. Yu, C.; Yang, M.; Cui, S.; Ji, Y.; Zhang, J., A Ratiometric Selective Fluorescent Probe Derived from Pyrene for Cu^{2+} Detection. *Chemosensors* **2022**, *10* (6), 207.

76. Yu, C.; Wang, T.; Xu, K.; Zhao, J.; Li, M.; Weng, S.; Zhang, J., Characterization of a highly Cu^{2+}-selective fluorescent probe derived from rhodamine B. *Dyes Pigm.* **2013**, *96*, 38-44.

77. Peng, H.; Han, Y.; Lin, N.; Liu, H., Two pyridine-derived Schiff-bases as turn-on fluorescent sensor for detection of aluminium ion. *Opt. Mater.* **2019**, *95*, 109210.

78. Qin, J. C.; Yang, Z. Y.; Yang, P., Recognition of Al^{3+} based on a naphthalene-based "Off–On" chemosensor in near 100% aqueous media. *Inorganica Chim. Acta* **2015**, *432*, 136-141.

79. Dey, S.; Purkait, R.; Pal, K.; Jana, K.; Sinha, C., Aggregation-induced emission-active hydrazide-based probe: Selective sensing of Al^{3+}, HF_2^-, and nitro explosives. *ACS Omega* **2019**, *4*, 8451-8464.

80. Peng, H.; Peng, X.; Huang, J.; Huang, A.; Xu, S.; Zhou, J.; Huang, S.; Cai, X., Synthesis and crystal structure of a novel pyridine acylhydrazone derivative as a "turn on" fluorescent probe for Al^{3+}. *J. Mol. Struct.* **2020**, 1212, 128138.

81. Purkait, R.; Sinha, C., Solvent-tuned discriminant sensing of Al^{3+}, Mg^{2+} and HF_2^- by vanilinyl-picolinyl hydrazide Schiff base. *New J. Chem.* **2019**, *43* (25), 9815-9823.

82. Liu, H.; Liu, T.; Li, J.; Zhang, Y.; Li, J.; Song, J.; Qu, J.; Wong, W. Y., A simple Schiff base as dual-responsive fluorescent sensor for bioimaging recognition of Zn^{2+} and Al^{3+} in living cells. *J. Mater. Chem. B* **2018**, *6* (34), 5435-5442.

83. Gong, S.; Zhang, Y.; Qin, A.; Li, M.; Gao, Y.; Zhang, C.; Song, J.; Xu, X.; Wang, Z.; Wang, S., A novel AIE-active camphor-based fluorescent probe for simultaneous detection of Al^{3+} and Zn^{2+} at dual channels in living cells and zebrafish. *Analyst* **2021**, *147* (1), 87-100.

84. Tang, L.; Ding, S.; Zhong, K.; Hou, S.; Bian, Y.; Yan, X., A new 2-(2'-hydroxyphenyl)quinazolin-4(3H)-one derived acylhydrazone for fluorescence recognition of Al^{3+}. *Spectrochim. Acta A Mol. Biomol. Spectrosc.* **2017**, *174*, 70-74.

85. Wang, J.; Feng, L.; Chao, J.; Wang, Y.; Shuang, S., A new 'turn-on' and reversible fluorescent sensor for Al^{3+} detection and live cell imaging. *Anal. Methods* **2019**, *11* (43), 5598-5606.

86. Zhao, J.; Zhao, Y.; Xu, S.; Luo, N.; Tang, R., A selective fluorescent probe for relay recognition of Al^{3+} and Cu^{2+} through fluorescence "off-on-off" functionality. *Inorganica Chim. Acta* **2015**, *438*, 105-111.

87. Purkait, R.; Dey, A.; Dey, S.; Ray, P. P.; Sinha, C., Design of a coumarinyl-picolinoyl hydrazide Schiff base for the fluorescence turn-on–off sequential sensing of Al^{3+} and nitroaromatics, and electronic device fabrication. *New J. Chem.* **2019**, *43* (37), 14979-14990.

88. Guo, X.; Zhao, Y. R.; Zhang, L. L.; Yan, X. J.; Liu, H. B.; Li, Q. Z.; Xie, C. Z.; Xu, J. Y., Highly selective fluorescent probe in aqueous solution based on coumarin Schiff base for detecting Cu^{2+} and specific biosensing of glutathione in mitochondria. *J. Photochem. Photobiol. A: Chem.* **2023**, *435*, 114350.

89. Xie, Y.; Yan, L.; Li, J., An on-off-on fluorescence probe based on coumarin for Cu^{2+}, cysteine, and histidine detections. *Appl. Spectrosc.* **2019**, *73* (7), 794-800.

90. Wang, J. T.; Pei, Y. Y.; Yan, M. Y.; Li, Y. G.; Yang, G. G.; Qu, C. H.; Luo, W.; Wang, J.; Li, Q. F., A fast-response turn-on quinoline-based fluorescent probe for selective and sensitive detection of zinc (II) and its application. *Microchem. J.* **2021**, *160*, 105776.

91. Tang, L.; Zhou, P.; Qi, Z.; Huang, Z.; Zhao, J.; Cai, M., A new quinoline-based acylhydrazone for highly selective fluorescence recognition of Cu(II) and sulfide in aqueous solution. *Bull. Korean Chem. Soc.* **2013**, *34* (8), 2256-2260.

92. Wu, S. P.; Huang, Z. M.; Liu, S. R.; Chung, P. K., A pyrene-based highly selective turn-on fluorescent sensor for copper(II) ion and its application in live cell imaging. *J. Fluoresc.* **2012**, *22* (1), 253-259.

93. Kar, C.; Samanta, S.; Goswami, S.; Ramesh, A.; Das, G., A single probe to sense Al(III) colorimetrically and Cd(II) by turn-on fluorescence in physiological conditions and live cells, corroborated by X-ray crystallographic and theoretical studies. *Dalton Trans.* **2015**, *44* (9), 4123-32.

94. Li, D.; Sun, X.; Huang, J.; Wang, Q.; Feng, Y.; Chen, M.; Meng, X.; Zhu, M.; Wang, X., A carbazole-based "turn-on" two-photon fluorescent probe for biological Cu^{2+} detection vis Cu^{2+}-promoted hydrolysis. *Dyes Pigm.* **2016**, *125*, 185-191.

95. Xu, T.; Huang, J.; Fang, M.; Sui, M.; Zhu, Y.; Shentu, Y.; Li, C.; Zhu, W., A novel "turn-on" fluorescent probe based on naphthalimide for the tracking of lysosomal Cu^{2+} in living cells. *New J. Chem.* **2020**, *44* (48), 21167-21175.

96. Boonkitpatarakul, K.; Wang, J.; Niamnont, N.; Liu, B.; McDonald, L.; Pang, Y.; Sukwattanasinitt, M., Novel turn-on fluorescent sensors with mega Stokes shifts for dual detection of Al^{3+} and Zn^{2+}. *ACS Sens.* **2015**, *1* (2), 144-150.

97. Hwang, S. M.; Kim, M. S.; Lee, M.; Lim, M. H.; Kim, C., Single fluorescent chemosensor for multiple targets: sequential detection of Al^{3+} and pyrophosphate and selective detection of F^- in near-perfect aqueous solution. *New J. Chem.* **2017**, *41* (24), 15590-15600.

98. Li, C. R.; Li, S. L.; Yang, Z. Y., Development of a coumarin-furan conjugate as Zn^{2+} ratiometric fluorescent probe in ethanol-water system. *Spectrochim. Acta A Mol. Biomol. Spectrosc.* **2017**, *174*, 214-222.

99. Feng, Q.; Li, Y.; Li, K.; Lu, J.; Wang, J.; Fan, P.; Li, D.; Wu, D.; Hou, H., Fluorescent chemosensor for zinc ion detection with significant emission color change in aqueous solution based on AIEgen. *ChemistrySelect* **2017**, *2*, 3158-3162.

100. Aydin, D., A novel turn on fluorescent probe for the determination of Al^{3+} and Zn^{2+} ions and its cells applications. *Talanta* **2020**, *210*, 120615.

101. Yin, P.; Niu, Q.; Wei, T.; Li, T.; Li, Y.; Yang, Q., A new thiophene-based dual functional chemosensor for ultrasensitive colorimetric detection of Cu^{2+} in aqueous solution and highly selective fluorimetric detection of Al^{3+} in living cells. *J. Photochem. Photobiol. A: Chem.* **2020**, *389*, 112249.

102. Zhu, Y.; Gong, X.; Li, Z.; Zhao, X.; Liu, Z.; Cao, D.; Guan, R., A simple turn-on ESIPT and PET-based fluorescent probe for detection of Al^{3+} in real-water sample. *Spectrochim. Acta A Mol. Biomol. Spectrosc.* **2019**, *219*, 202-205.

103. Cho, H.; Chae, J. B.; Kim, C., A thiophene-based blue-fluorescent emitting chemosensor for detecting indium (III) ion. *Inorg. Chem. Commun.* **2018**, *97*, 171-175.

104. Tiwari, K.; Mishra, M.; Singh, V. P., A highly sensitive and selective fluorescent sensor for Al^{3+} ions based on thiophene-2-carboxylic acid hydrazide Schiff base. *RSC Adv.* **2013**, *3*, 12124.

105. Liu, F.; Fan, C.; Tu, Y.; Pu, S., A new fluorescent and colorimetric chemosensor for Al^{3+} and F^-/CN^- based on a julolidine unit and its bioimaging in living cells. *RSC Adv.* **2018**, *8*, 31113-31120.

106. Li, Y.; Niu, Q.; Wei, T.; Li, T., Novel thiophene-based colorimetric and fluorescent turn-on sensor for highly sensitive and selective simultaneous detection of Al^{3+} and Zn^{2+} in water and food samples and its application in bioimaging. *Anal. Chim. Acta* **2019**, *1049*, 196-212.

107. Jeong, H. Y.; Lee, S. Y.; Han, J.; Lim, M. H.; Kim, C., Thiophene and diethylamino phenol-based "turn-on" fluorescence chemosensor for detection of Al^{3+} and F^- in a near-perfect aqueous solution. *Tetrahedron* **2017**, *73*, 2690-2697.

108. Wang, P.; Liu, L.; Meng, F.; Khan, M. A.; Li, H., "Turn-on" fluorescent biosensors for high selective and sensitive detection of Al^{3+} ion. *Front. Chem.* **2020**, 8, 607614.

109. Klein, D., *Organic Chemistry*, 2nd ed. Wiley, 2015.

110. Gokel, G. W.; Leevy, W. M.; Weber, M. E., Crown ethers: sensors for ions and molecular scaffolds for materials and biological models. *Chem. Rev.* **2004**, 104 (5), 2723-2750.

111. Li, J.; Yim, D.; Jang, W.-D.; Yoon, J., Recent progress in the design and applications of fluorescence probes containing crown ethers. *Chem. Soc. Rev.* **2017**, *46* (9), 2437-2458.

112. Dugas, H. *Bioorganic Chemistry Frontiers*. Springer-Verlag, 1990.

113. Minkin, V. I.; Dubonosov, A. D.; Bren, V. A.; Tsukanov, A. V., Chemosensors with crown ether-based receptors. *Arkivoc* **2008**, *4, 90-102*.

114. Kim, H.; Koo, B., Lithium sensors based on photophysical changes of 1-aza-12-crown-4 naphthalene derivatives synthesized via Buchwald–Hartwig amination. *RSC Adv.* **2022**, *12*, 31976-31984.

115. Witulski, B.; Weber, M.; Bergsträsser, U.; Desvergne, J. P.; Bassani, D. M.; Bouas-Laurent, H., Novel alkali cation chemosensors based on *N*-9-anthrylaza-crown ethers. *Org. Lett.* **2001**, *3*, 1467-1470.

116. Hou, C.; Urbanec, A. M.; Cao, H., A rapid Hg^{2+} sensor based on aza-15-crown-5 ether functionalized 1,8-naphthalimide. *Tetrahedron Lett.* **2011**, *52*, 4903-4905.

117. Poteau, X.; Saroja, G.; Spies, C.; Brown, R. G., The photophysics of some 3-hydroxyflavone derivatives in the presence of protons, alkali metal and alkaline earth cations. *J. Photochem. Photobiol. A: Chem.* **2004**, *162*, 431-439.

118. Smolentsev, A. B.; Glebov, E. M.; Korolev, V. V.; Paramonov, S. V.; Fedorova, O. A., Fluorescent properties of an azacrown-containing styryl derivative of naphthopyran: ion-binding response and photochemical switching off. *Photochem. Photobiol. Sci.* **2013**, *12*, 1803-1810.

119. Pond, S. J. K.; Tsutsumi, O.; Rumi, M.; Kwon, O.; Zojer, E.; Brédas, J.-L.; Marder, S. R.; Perry, J. W., Metal-ion sensing fluorophores with large two-photon absorption cross sections: Aza-crown ether substituted donor–acceptor– donor distyrylbenzenes. *J. Am. Chem. Soc.* **2004**, *126* (30), 9291-9306.

120. Chen, C. T.; Huang, W. P., A highly selective fluorescent chemosensor for lead ions. *J. Am. Chem. Soc.* **2002**, *124* (22), 6246-6247.

121. Taziaux, D.; Soumillion, J. P.; Habib Jiwan, J. L., Photophysical and complexing properties of new fluoroionophores based on coumarin 343 linked to rigidified crown-ethers. *J. Photochem. Photobiol. A: Chem.* **2004**, *162* (2), 599-607.

122. Geue, J. P.; Head, N. J.; Ward, A. D.; Lincoln, S. F., Complexation of alkali metal and alkaline earth ions by anthracene based fluorophores with one and two appended monoaza coronand receptors. *Dalton Trans.* **2003**, *4*, 521-526.

123. Gunnlaugsson, T.; Nieuwenhuyzen, M.; Richard, L.; Thoss, V., Novel sodium-selective fluorescent PET and optically based chemosensors: towards Na^+ determination in serum. *J. Chem. Soc., Perkin trans. II* **2002**, *1*, 141-150.

124. Thapa, P.; Arnquist, I.; Byrnes, N.; Denisenko, A. A.; Foss, F. W., Jr.; Jones, B. J. P.; McDonald, A. D.; Nygren, D. R.; Woodruff, K., Barium Chemosensors with dry-phase fluorescence for neutrinoless double beta decay. *Sci. Rep.* **2019**, 9, 15097.

125. Danjou, P.-E.; Lyskawa, J.; Delattre, F.; Becuwe, M.; Woisel, P.; Ruellan, S.; Fourmentin, S.; Cazier-Dennin, F., New fluorescent and electropolymerizable *N*-azacrown carbazole as a selective probe for iron (III) in aqueous media. *Sens. Actuators B Chem.* **2012**, *172*, 1022-1028.

126. Mashraqui, S. H.; Sundaram, S.; Khan, T.; Bhasikuttan, A. C., Zn^{2+} selective luminescent 'off–on' probes derived from diaryl oxadiazole and aza-15-crown-5. *Tetrahedron* **2007**, *63* (45), 11093-11100.

127. Kollmannsberger, M.; Rurack, K.; Resch-Genger, U.; Daub, J., Ultrafast charge transfer in amino-substituted boron dipyrromethene dyes and its inhibition by cation complexation: A new design concept for highly sensitive fluorescent probes. *J. Phys. Chem. A* **1998**, *102* (50), 10211-10220.

128. Kursunlu, A. N.; Deveci, P.; Guler, E., Synthesis and spectroscopic–electrochemical properties of novel ratiometric Hg (II) chemosensor containing Bodipy and the N-phenylaza-15-crown-5 moiety. *J. Lumin.* **2013**, 136, 430-436.

129. Voutsadaki, S.; Tsikalas, G. K.; Klontzas, E.; Froudakis, G. E.; Katerinopoulos, H. E., A "turn-on" coumarin-based fluorescent sensor with high selectivity for mercury ions in aqueous media. *Chem. Commun.* **2010**, *46*, 3292-3294.

130. Schwarze, T.; Müller, H.; Schmidt, D.; Riemer, J.; Holdt, H. J., Design of Na^+-selective fluorescent probes: A systematic study of the Na^+-complex stability and the Na^+/K^+ selectivity in acetonitrile and water. *Chem. Eur. J.* **2017**, *23* (30), 7255-7263.

131. Swidan, A. A.; Macdonald, C. L. B., Polyether complexes of groups 13 and 14. *Chem. Soc. Rev.* **2016**, *45* (14), 3883-3915.

132. M. J. Frisch; G. W. Trucks; H. B. Schlegel; G. E. Scuseria; M. A. Robb; J. R. Cheeseman; G. Scalmani; V. Barone; G. A. Petersson; H. Nakatsuji; X. Li, M. C.; A. V. Marenich; J. Bloino; B. G. Janesko; R. Gomperts; B. Mennucci; H. P. Hratchian; J. V. Ortiz; A. F. Izmaylov; J. L. Sonnenberg; Williams, F. D.; F. Lipparini, F. E.; J. Goings, B. P.; A. Petrone; T. Henderson; D. Ranasinghe; V. G. Zakrzewski; J. Gao, N. R.; G. Zheng; W. Liang, M. H.; M. Ehara; K. Toyota, R. F.; J. Hasegawa, M. I.; T. Nakajima; Y. Honda; O. Kitao; H. Nakai; T. Vreven; K. Throssell; J. A. Montgomery Jr.; J. E. Peralta; F. Ogliaro; M. J. Bearpark; J. J. Heyd; E. N. Brothers; K. N. Kudin; V. N. Staroverov; T. A. Keith, R. K.; J. Normand, K. R.; A. P. Rendell, J. C. B.; S. S. Iyengar; J. Tomasi, M.; Cossi, J. M. M.; M. Klene; C. Adamo; R. Cammi; J. W. Ochterski; R. L. Martin; K. Morokuma; O. Farkas; Foresman, J. B.; Fox, D. J., Journal. 2016.

133. Hanwell, M. D.; Curtis, D. E.; Lonie, D. C.; Vandermeersch, T.; Zurek, E.; Hutchison, G. R., Avogadro: an advanced semantic chemical editor, visualization, and analysis platform. *J. Cheminform.* **2012**, *4* (1), 17.

134. Marenich, A. V.; Cramer, C. J.; Truhlar, D. G., Universal Solvation model based on solute electron density and on a continuum model of the solvent defined by the bulk dielectric constant and atomic surface tensions. *J. Phys. Chem. B* **2009**, *113* (18), 6378-6396.

135. Brouwer, A. M., Standards for photoluminescence quantum yield measurements in solution (IUPAC Technical Report). **2011**, *83* (12), 2213-2228.

136. Mansour, N.; Hriz, K.; Jaballah, N.; Kreher, D.; Majdoub, M., Synthesis, characterization, optical and electrical properties of bis(phenylvinyl) anthracene-based polymers. *Opt. Mater.* **2016**, *58*, 296-305.

137. Xu, J.; Gao, Y.; Li, Z.; Liu, J.; Guo, T.; Zhang, L.; Wang, H.; Zhang, Z.; Guo, K., Chlorotropylium promoted conversions of oximes to amides and nitriles. *Eur. J. Org. Chem.* **2020** (3), 311-315.

138. Xue, L.; Li, G.; Liu, Q.; Wang, H.; Liu, C.; Ding, X.; He, S.; Jiang, H., Ratiometric fluorescent sensor based on inhibition of resonance for detection of cadmium in aqueous solution and living cells. *Inorg. Chem.* **2011**, *50* (8), 3680-3690.

139. McConnell, N.; Frett, B.; Li, H., Microwave-assisted green synthesis of anilines, phenols, and benzenediamines without transition metals, ligands, or organic solvents. *Green Chem. Lett. Rev.* **2018**, *11* (3), 286-295.

140. Gunnlaugsson, T.; Gunaratne, H. Q. N.; Nieuwenhuyzen, M.; Leonard, J. P., Synthesis of functionalised macrocyclic compounds as Na^+ and K^+ receptors: a mild and high yielding nitration in water of mono and bis 2-methoxyaniline functionalised crown ethers. *J. Chem. Soc., Perkin Trans. 1* **2002**, (17), 1954-1962.

141. He, H.; Mortellaro, M. A.; Leiner, M. J. P.; Young, S. T.; Fraatz, R. J.; Tusa, J. K., A Fluorescent chemosensor for sodium based on photoinduced electron transfer. *Anal. Chem.* **2003**, *75* (3), 549-555.

142. Bohlmann, F.; Mannhardt, H., *Chem. Ber.* 1956, 89, 1307.

143. Chen, C. L.; Chen, Y. T.; Demchenko, A. P.; Chou, P. T., Amino proton donors in excited-state intramolecular proton-transfer reactions. *Nature Reviews Chemistry* **2018**, *2* (7), 131-143.

144. Caricato, M.; Mennucci, B.; Tomasi, J.; Ingrosso, F.; Cammi, R.; Corni, S.; Scalmani, G., Formation and relaxation of excited states in solution: A new time dependent polarizable continuum model based on time dependent density functional theory. *J. Chem. Phys.* **2006**, *124*, 124520.

145. Na, Y. J.; Hwang, I. H.; Jo, H. Y.; Lee, S. A.; Park, G. J.; Kim, C., Fluorescent chemosensor based-on the combination of julolidine and furan for selective detection of zinc ion. *Inorg. Chem. Commun.* **2013**, *35*, 342-345.

146. Zhuang, Y. J.; Qu, J. P.; Kang, Y. B., Deprotonated salicylaldehyde as visible light photocatalyst. *The Journal of Organic Chemistry* **2020**, 85 (6), 4386-4397.

147. https://depts.washington.edu/eooptic/linkfiles/dielectric_chart%5B1%5D.pdf.

148. Shelke, V. A.; Jadhav, S. M.; Shankarwar, S. G.; Munde, A. S.; Chondhekar, T. K., *Bull. Chem. Soc. Ethiop.* **2011**, 25 (3), 381-391.

149. Lee, S. A.; You, G. R.; Choi, Y. W.; Jo, H. Y.; Kim, A. R.; Noh, I.; Kim, S. J.; Kim, Y.; Kim, C., A new multifunctional Schiff base as a fluorescence sensor for Al^{3+} and a colorimetric sensor for CN^- in aqueous media: an application to bioimaging. *Coord. Chem. Rev.* **2014**, *43* (18), 6650-6659.

150. Silpcharu, K.; Sam-ang, P.; Chansaenpak, K.; Sukwattanasinitt, M.; Rashatasakhon, P., Selective fluorescent sensors for gold(III) ion from *N*-picolyl sulfonamide spirobifluorene derivatives. *J. Photochem. Photobiol. A* **2020**, 402, 112823.

151. Silpcharu, K.; Soonthonhut, S.; Sukwattanasinitt, M.; Rashatasakhon, P., Fluorescent sensor for copper(II) and cyanide ions via the complexation–decomplexation mechanism with di(bissulfonamido)spirobifluorene. *ACS Omega* **2021**, *6* (25), 16696-16703.

152. Silpcharu, K.; Sukwattanasinitt, M.; Rashatasakhon, P., Novel sulfonamidospiro bifluorenes as fluorescent sensors for mercury(II) ion and glutathione. *RSC Adv.* **2019**, *9* (20), 11451-11458.

153. Zhou, Z.; Li, N.; Tong, A., A new coumarin-based fluorescence turn-on chemodosimeter for Cu^{2+} in water. *Anal. Chim. Acta* **2011**, *702* (1), 81-86.

154. Rodríguez-Hermida, S.; Lago, A. B.; Pino-Cuevas, A.; Hagenbach, A.; Cañadillas-Delgado, L.; Carballo, R.; Abram, U.; Vázquez-López, E. M., A hexameric cationic copper(II) metallacrown as a pertechnetate and perrhenate Scavenger. *Chem. Eur. J.* **2016**, *22* (5), 1847-1853.

APPENDIX
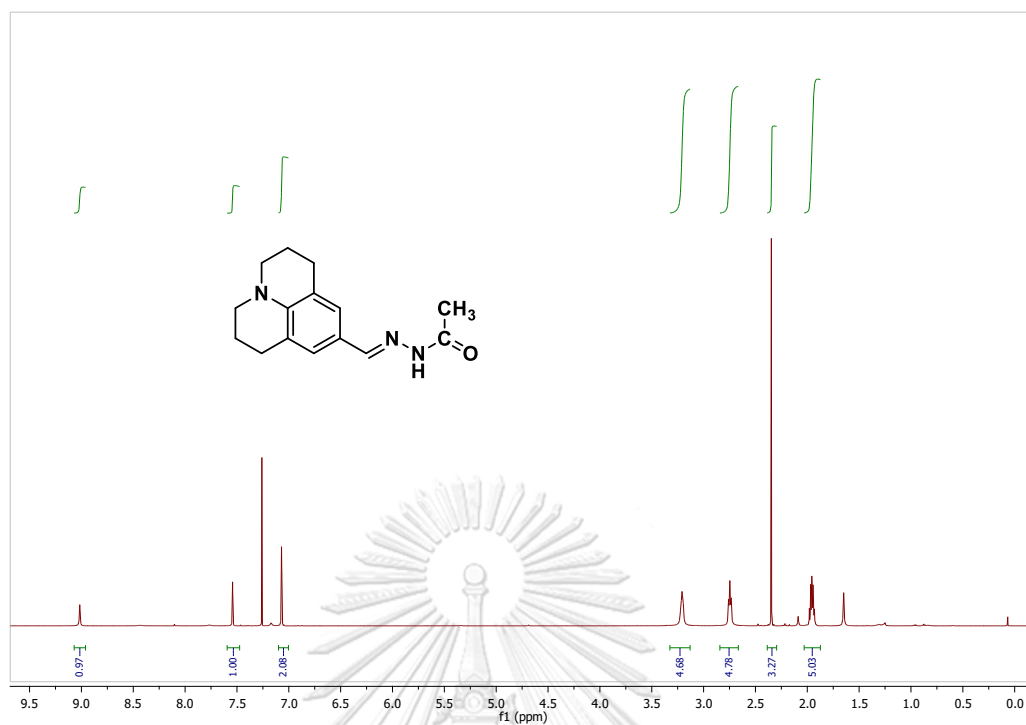
Figure S1 ^{1}H NMR spectrum of **JA** in CDCl$_3$
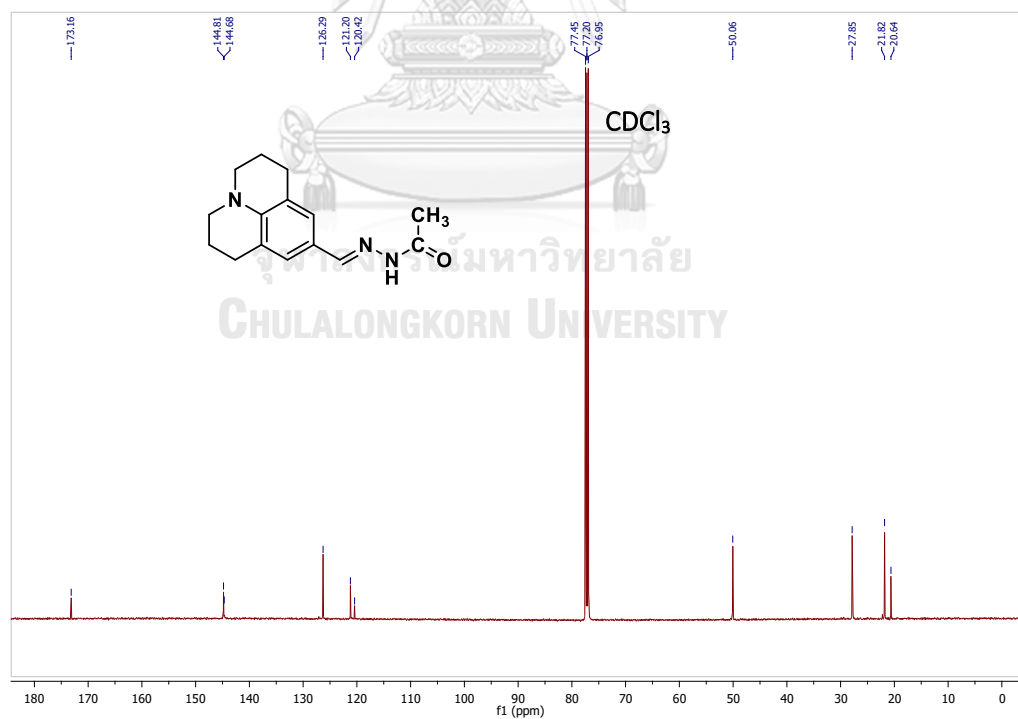
Figure S2 ^{13}C NMR spectrum of **JA** in CDCl$_3$
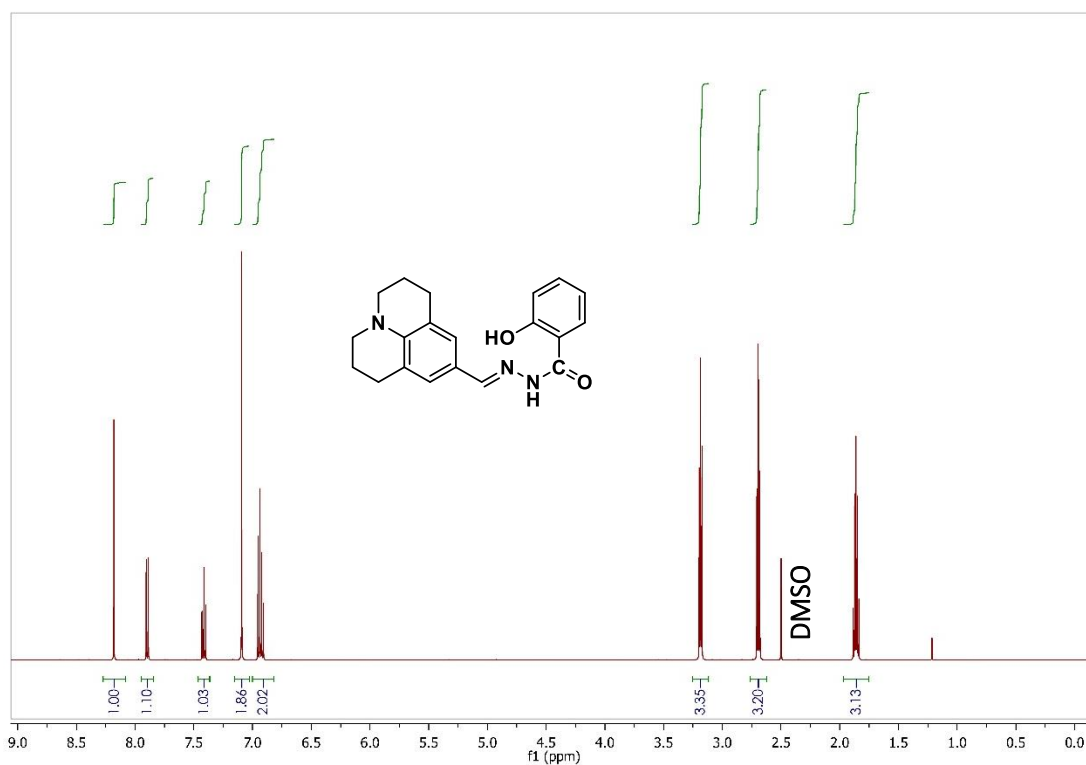
Figure S3 ^{1}H NMR spectrum of **JS** in DMSO-d6
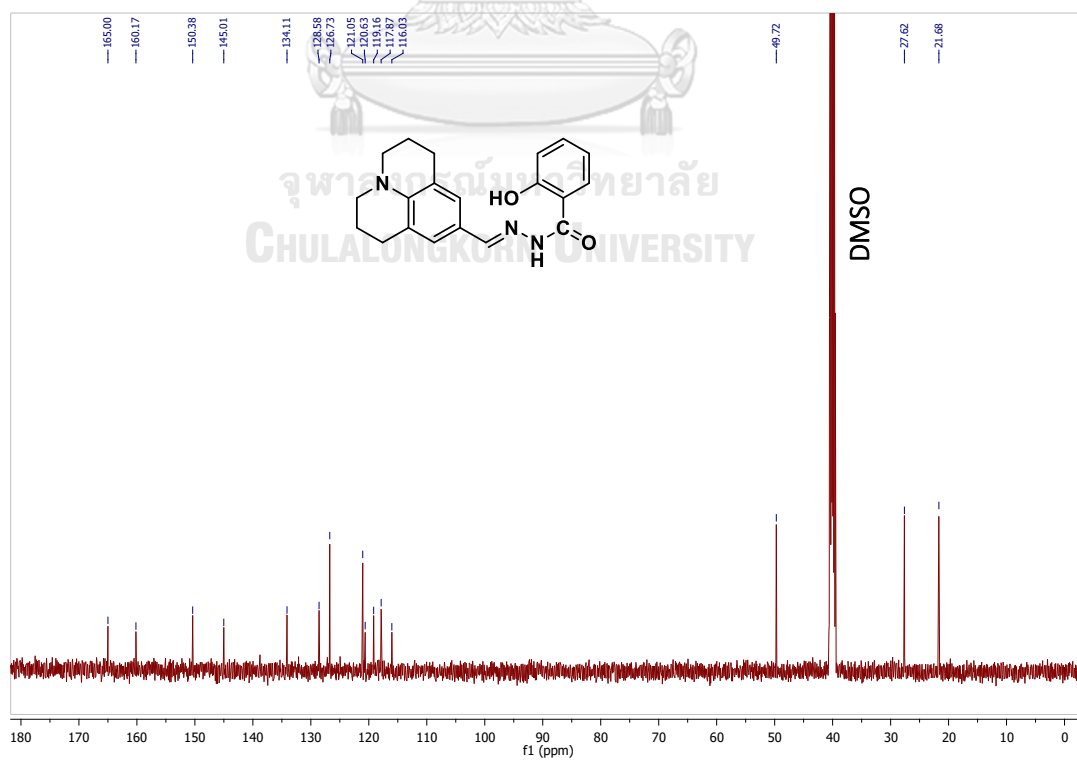
Figure S4 ^{13}C NMR spectrum of **JS** in DMSO-d6
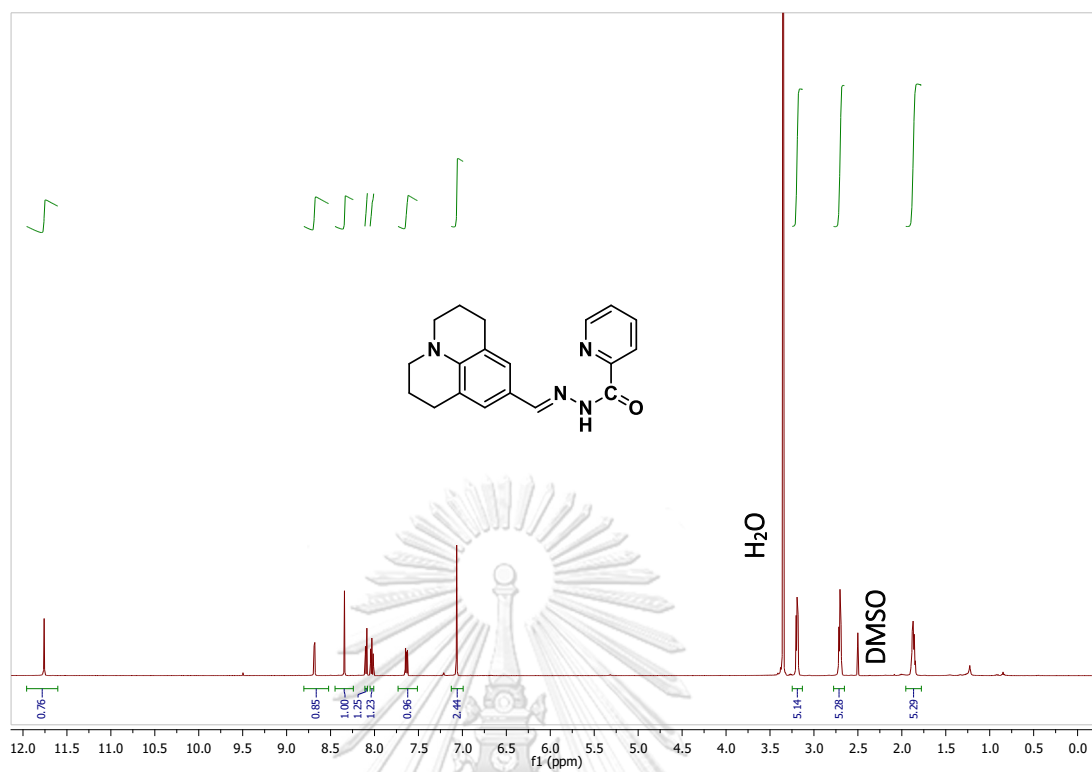
Figure S5 ^{1}H NMR spectrum of JP in DMSO-d6
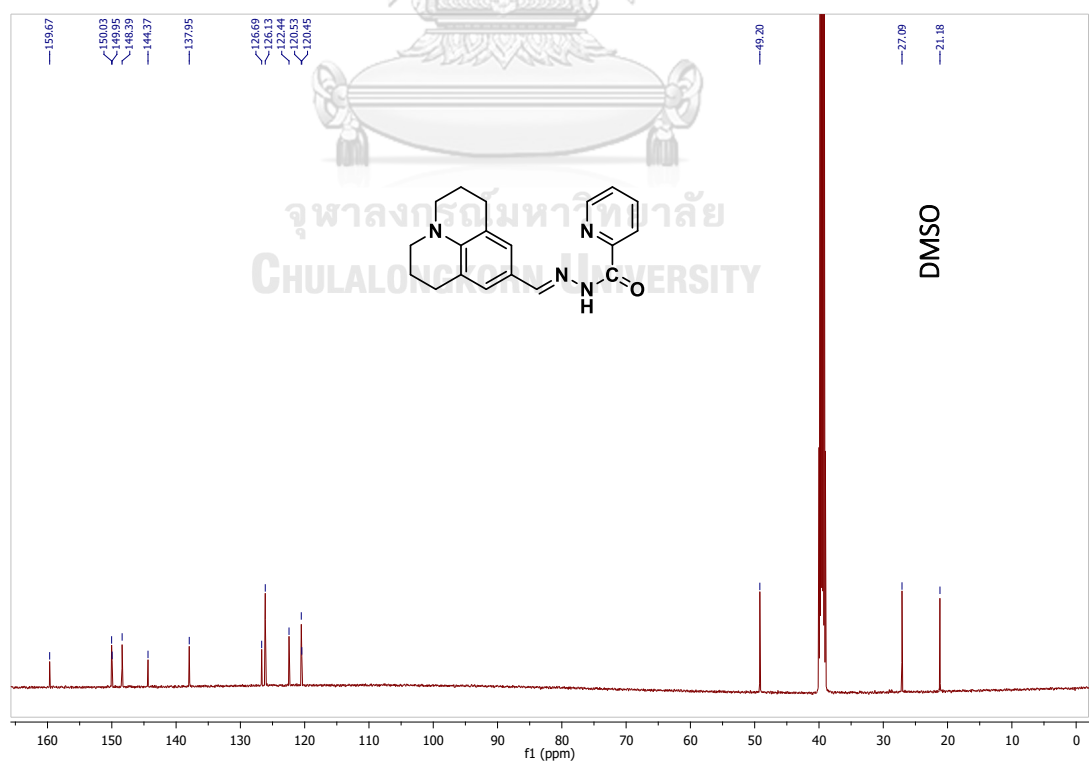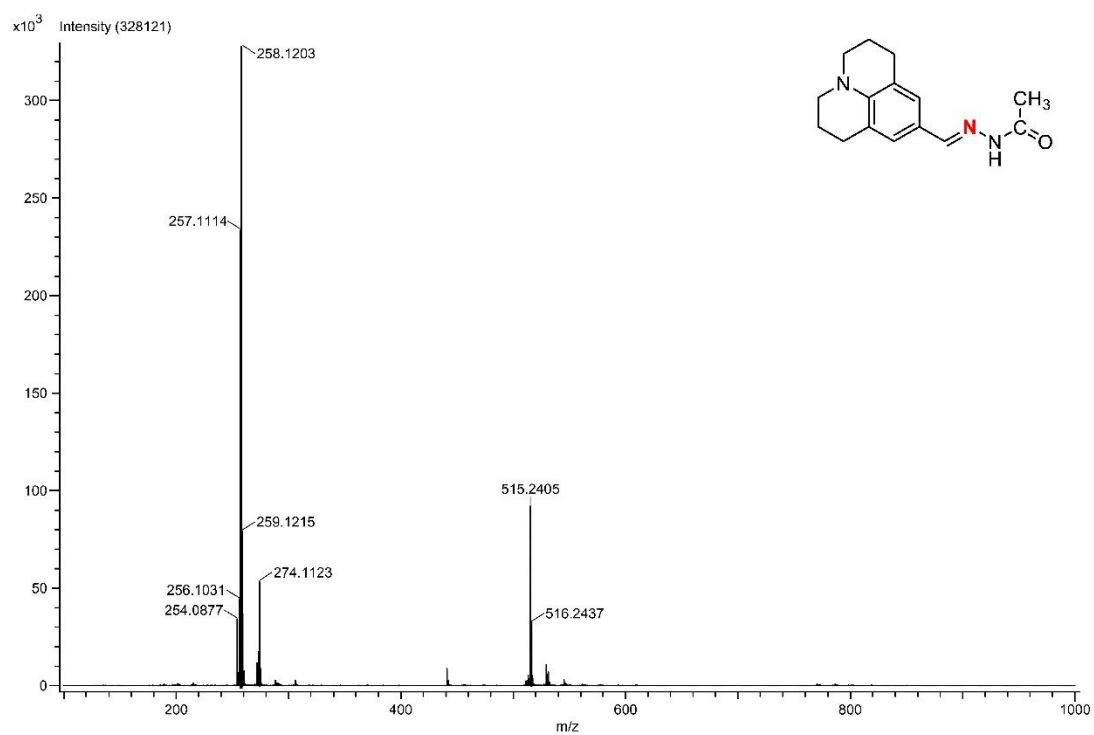

Figure S6 ^{13}C NMR spectrum of JP in DMSO-d6
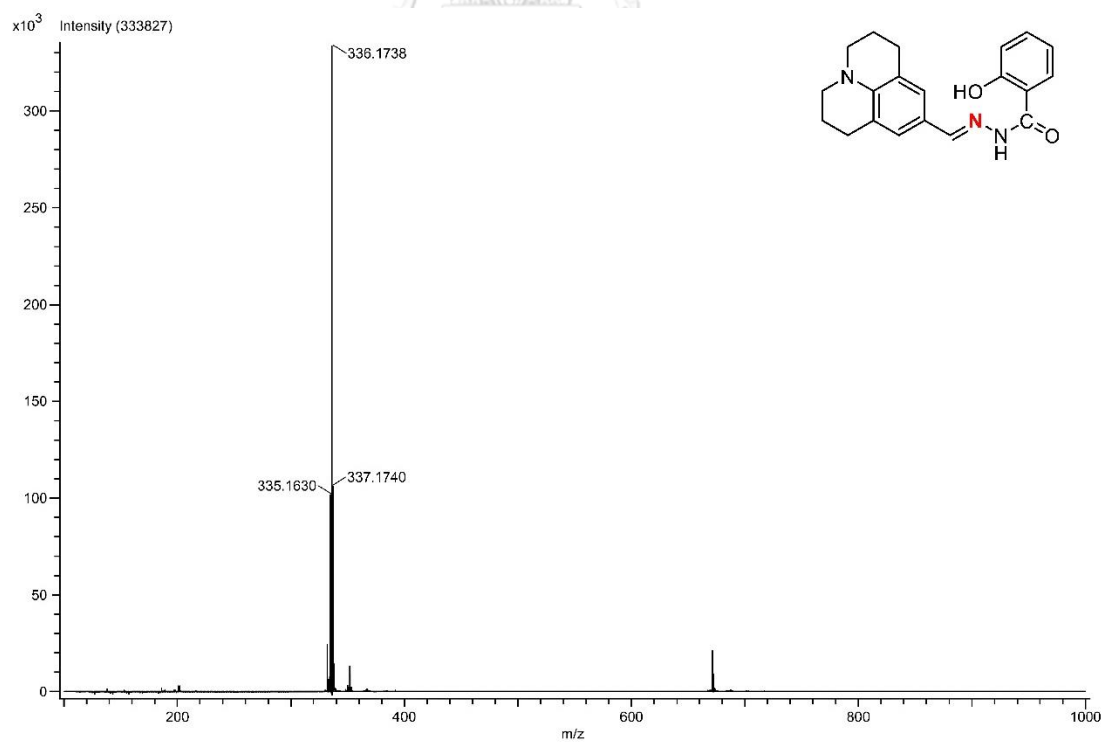
Figure S7 HRMS spectrum of **JA**
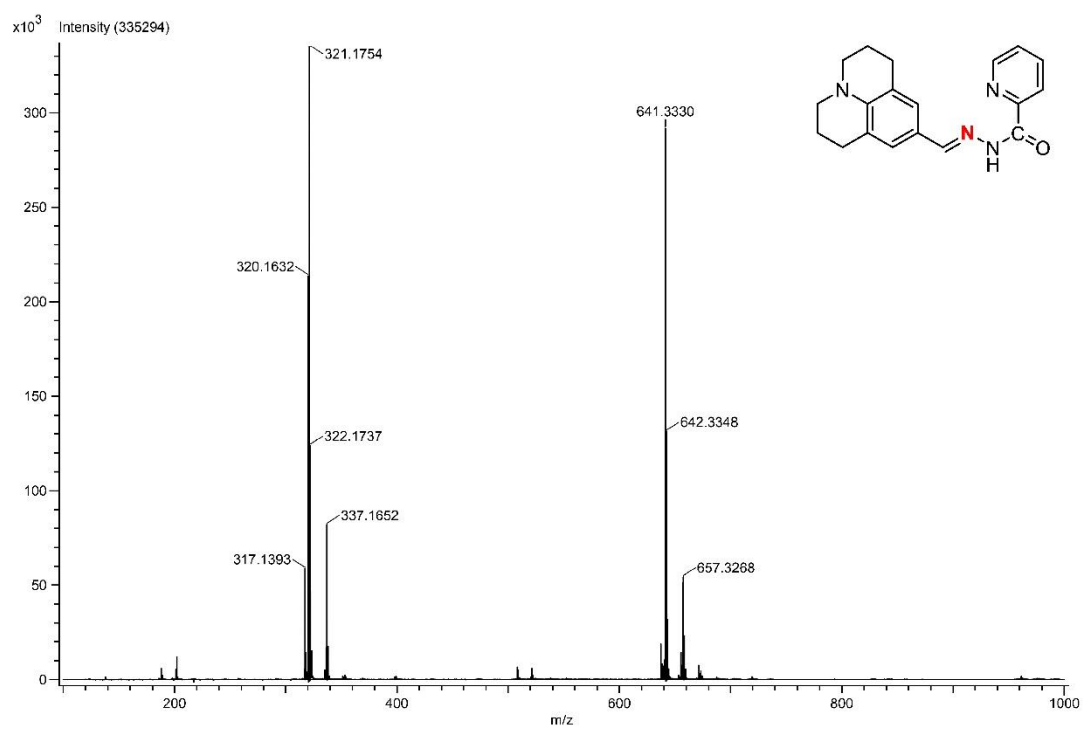

Figure S8 HRMS spectrum of **JS**

Figure S9 HRMS spectrum of **JP**
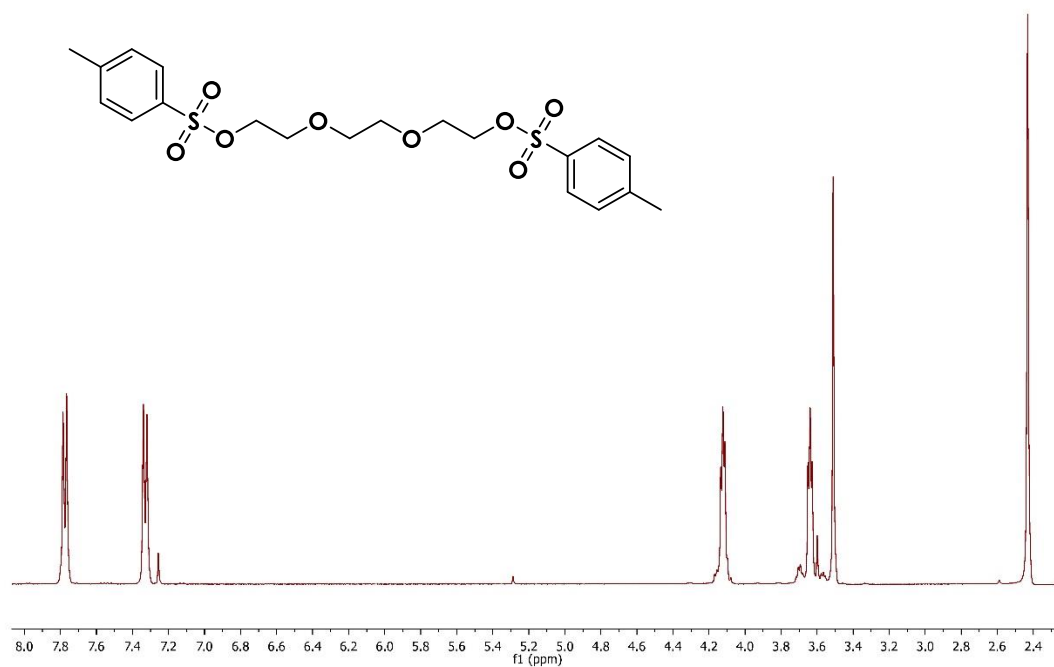
Figure S10 ^{1}H NMR spectrum of **1A** in CDCl$_3$
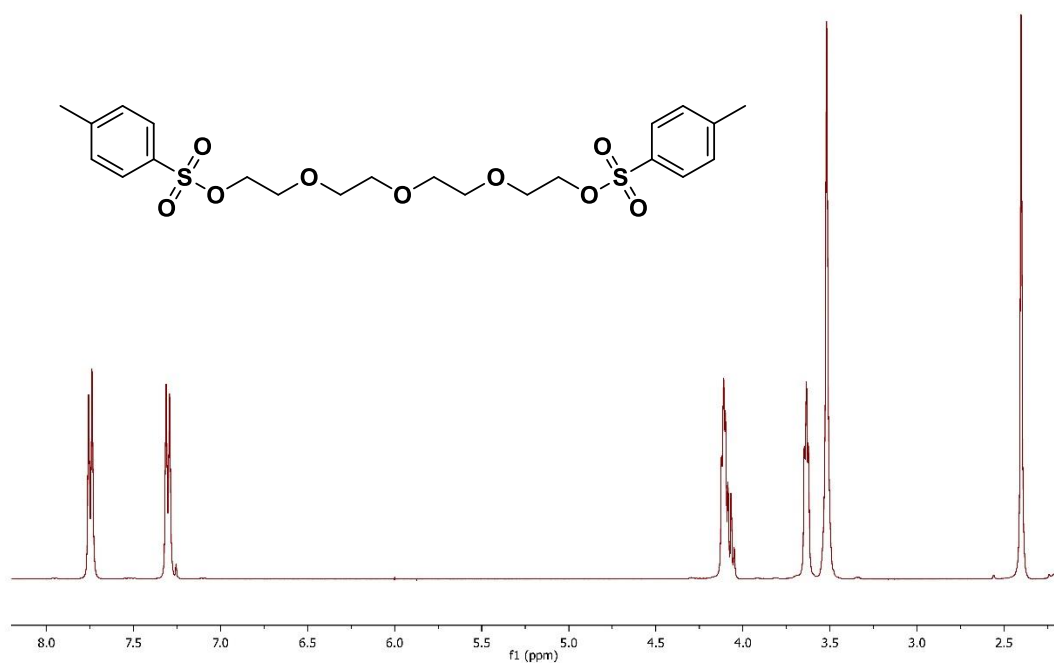
Figure S11 ^{1}H NMR spectrum of **2A** in CDCl$_3$
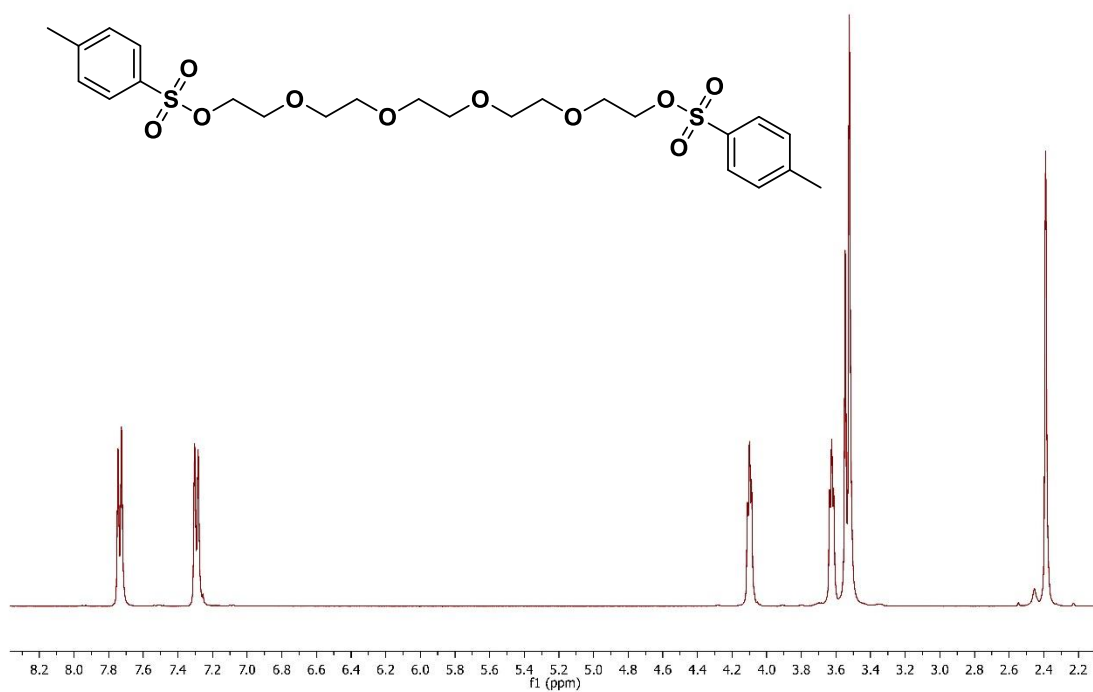
Figure S12 ^{1}H NMR spectrum of **3A** in CDCl$_3$
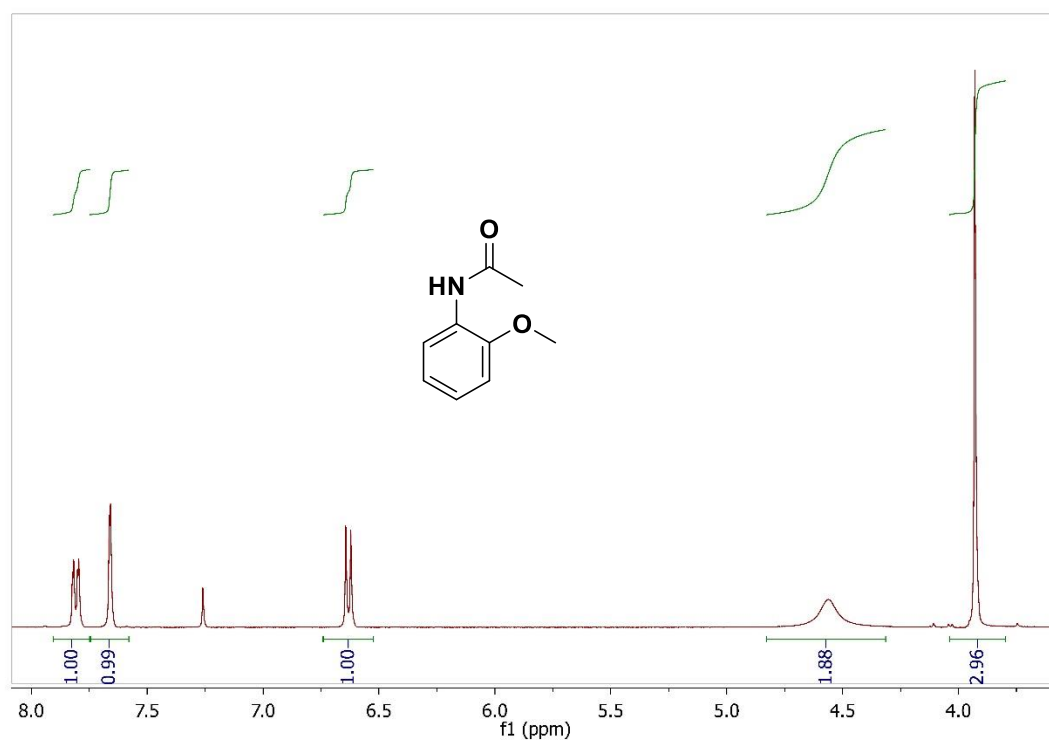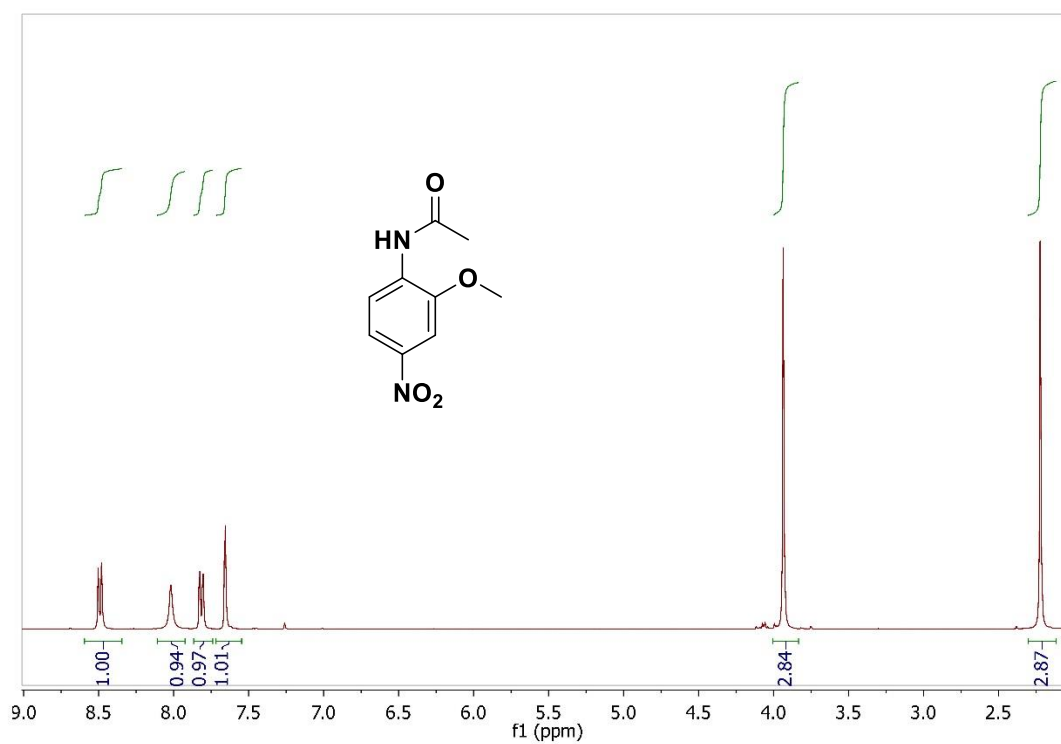

Figure S13 ^{1}H NMR spectrum of **1B** in CDCl$_3$

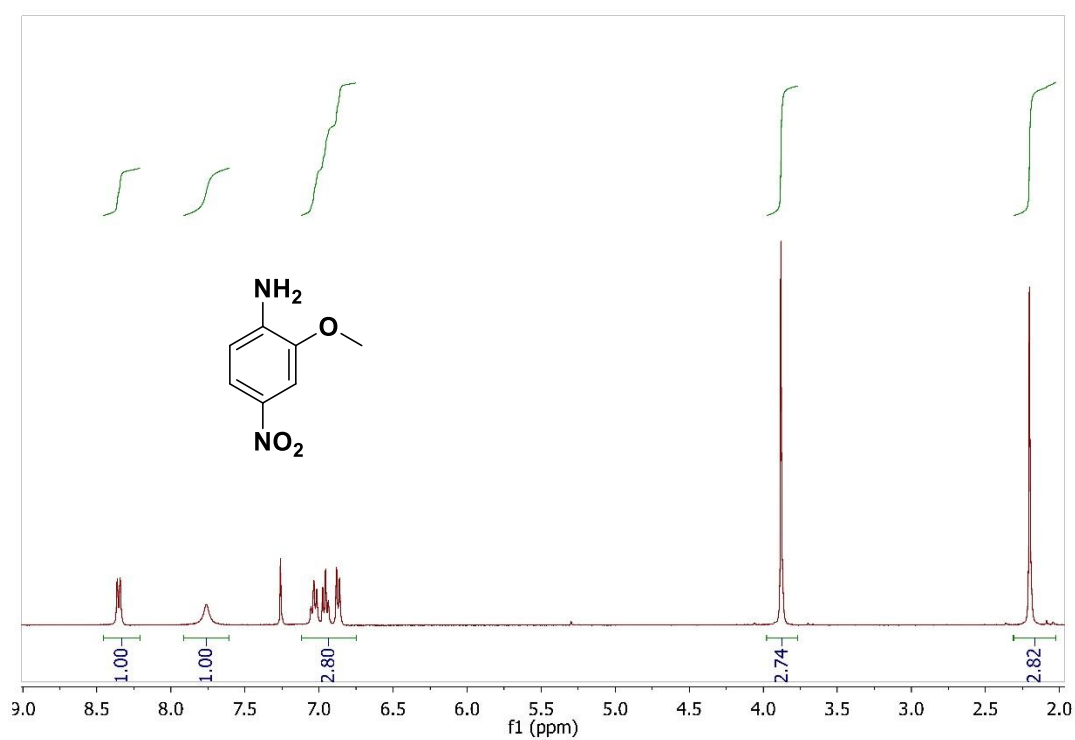**Figure S14** ^{1}H NMR spectrum of **2B** in CDCl$_3$
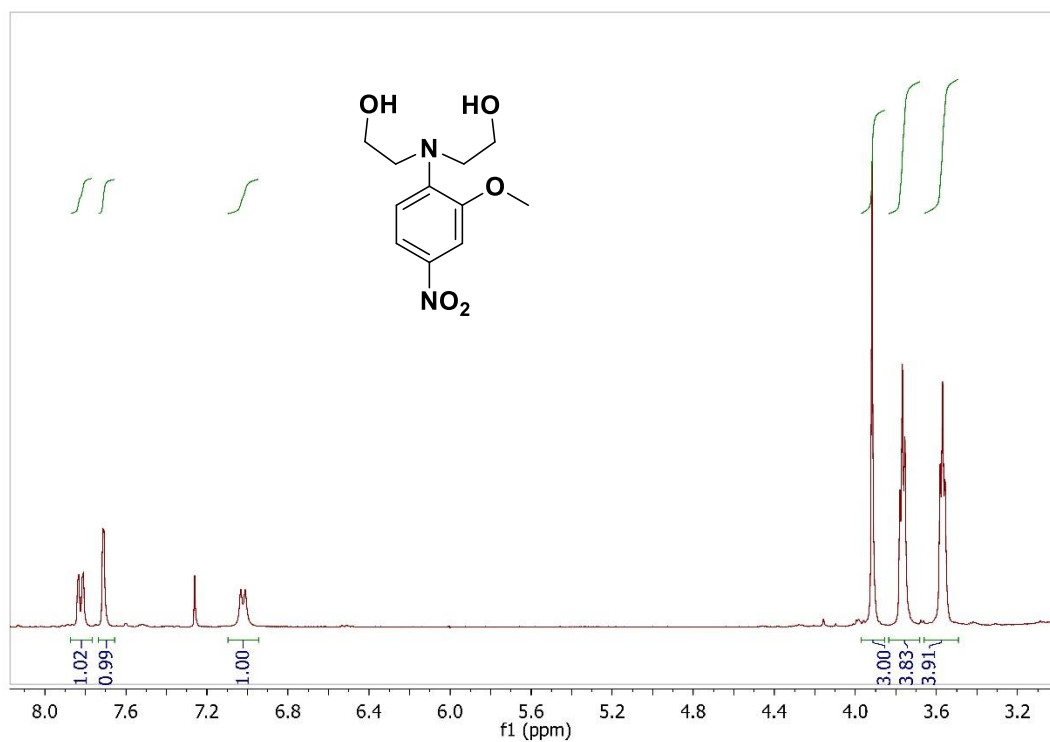

Figure S15 ^{1}H NMR spectrum of **3B** in CDCl$_3$
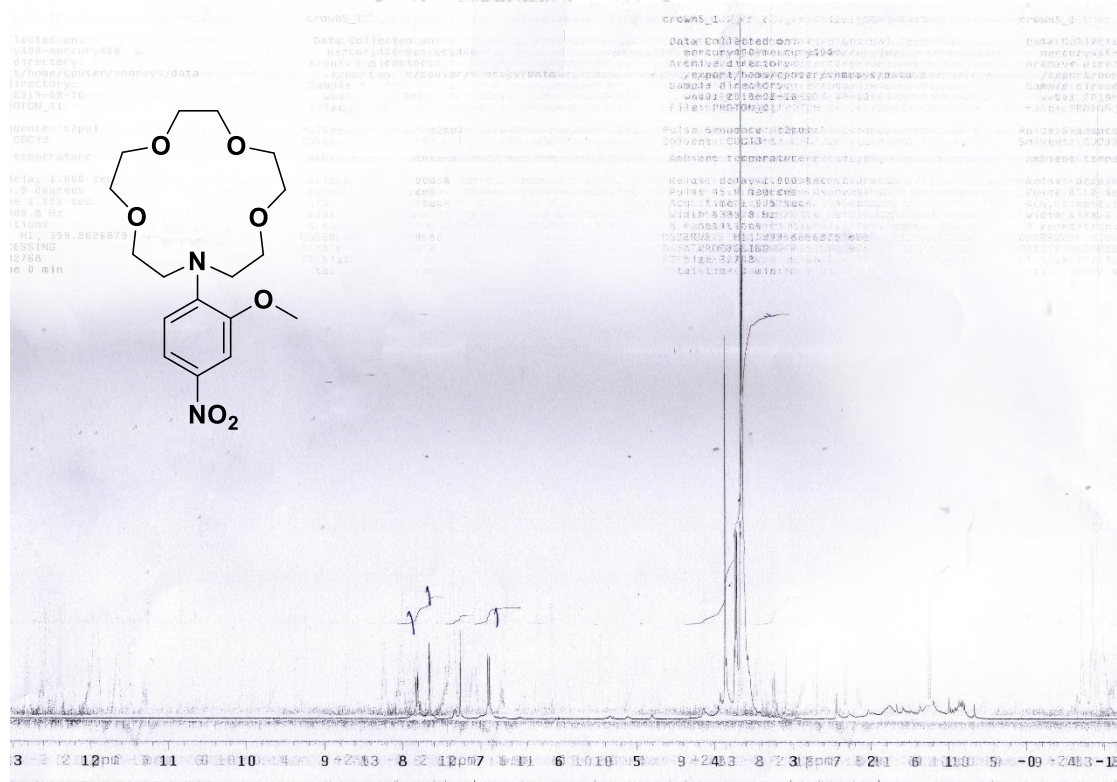
Figure S16 ¹H NMR spectrum of **4B** in CDCl₃

Figure S17 ¹H NMR spectrum of **5B** in CDCl₃
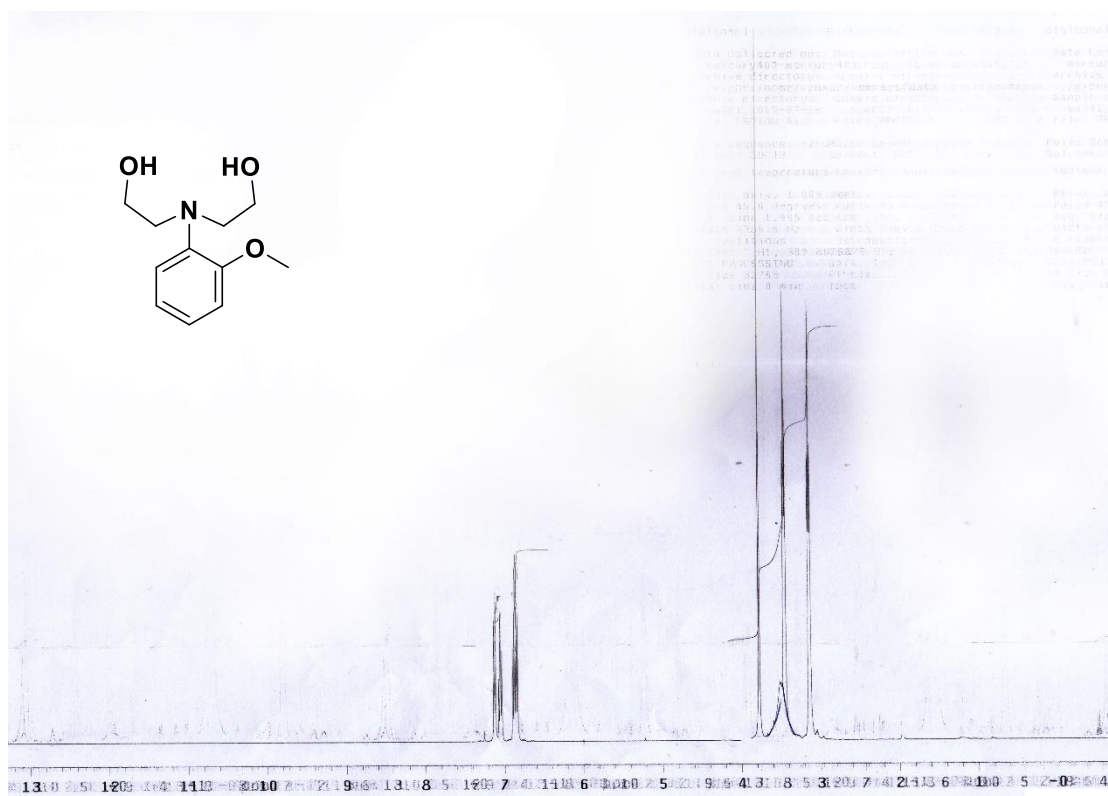
Figure S18 ^{1}H NMR spectrum of **1C** in CDCl$_3$
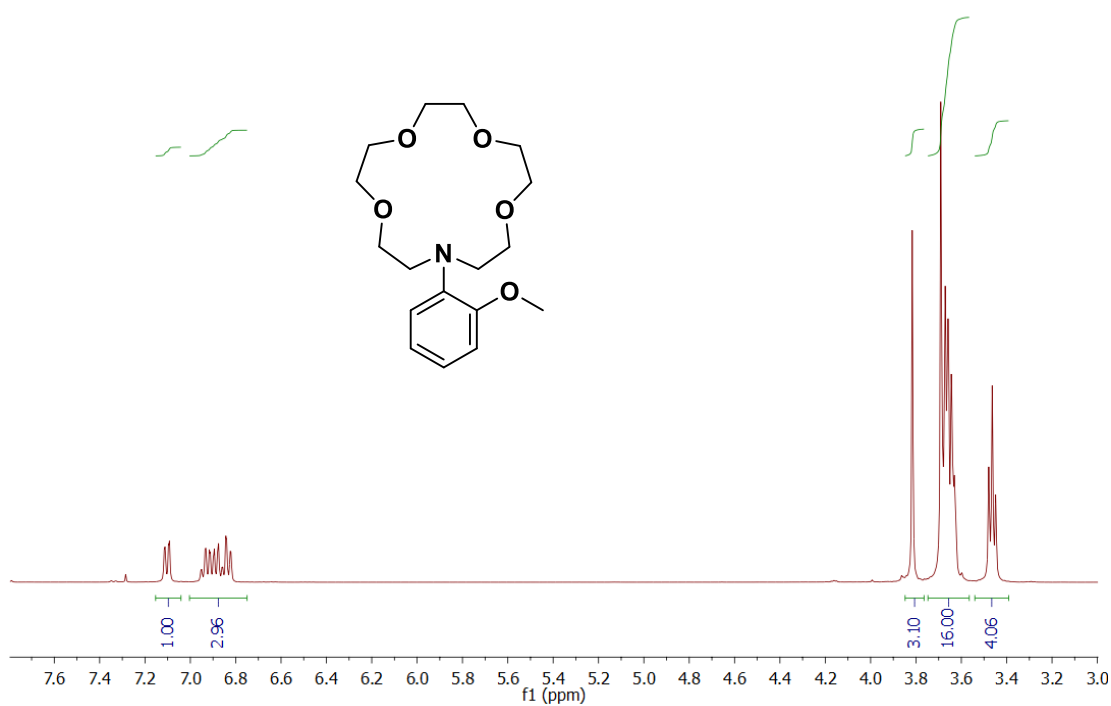
Figure S19 ^{1}H N MR spectrum of **2C** in CDCl$_3$

VITA

NAME	Mr. Warakorn Akarasareenon (นายวรากร อัครเสรีนนท์)
DATE OF BIRTH	18 November 1994
PLACE OF BIRTH	Bangkok, Thailand
INSTITUTIONS ATTENDED	B.Sc. Chulalongkorn University
HOME ADDRESS	48/428 Nimitmai 40 Alley Khwaengsamwatawanok, Khet Khlongsamwa, Bangkok Thailand 10510
PUBLICATION	Akarasareenon, W.; Chanmungkalakul, S.; Xiaogang, L.; Rashatasakhon, P., Selective fluorescent sensors for copper(II) ion from julolidine hydrazone derivatives. Journal of Photochemistry and Photobiology A: Chemistry 2023, 437, 114422.

จุฬาลงกรณ์มหาวิทยาลัย
CHULALONGKORN UNIVERSITY